INDUCED SEISMICITY ANALYSIS FOR RESERVOIR CHARACTERIZATION AT A PETROLEUM FIELD IN OMAN

by

Edmond Kin-Man Sze

B.S., Geophysical Engineering, Colorado School of Mines (1999)

SUBMITTED TO THE DEPARTMENT OF EARTH, ATMOSPHERIC, AND PLANETARY SCIENCES IN PARTIAL FULFILLMENT OF THE REQUIREMENTS FOR THE DEGREE OF

DOCTOR OF PHILOSOPHY IN GEOPHYSICS
AT THE
MASSACHUSETTS INSTITUTE OF TECHNOLOGY

June 2005

Signature of Author.....
Department of Earth, Atmospheric, and Planetary Sciences
May 2, 2005

Certified by.....
Professor M. Nafi Toksöz
Professor of Geophysics
Thesis Advisor

Accepted by.....
Professor Maria Zuber
E.A. Griswold Professor of Geophysics and Planetary Science
Department Head

Induced seismicity analysis for reservoir characterization at a petroleum field in Oman

by

Edmond Kin-Man Sze

Submitted to the Department of Earth, Atmospheric, and Planetary Sciences on April 29, 2005 in partial fulfillment of the requirements for the degree of Doctor of Philosophy in Geophysics

Abstract

This thesis presents the analysis and interpretation of passive seismic data collected in a 20-month monitoring period. The investigation is divided into four studies, each focusing on a different aspect of the seismic data to infer the reservoir properties. First, I applied three different methods (the iterative linearized, nonlinear grid-search, and double-difference methods) to relocate 405 microearthquakes that occurred between October 1999 and June 2001 in a producing field in Oman. A numerical technique is applied to "collapse" the relocated hypocenters and to find the simplest structural interpretation consistent with the data. Comparing the methods, the applicability of waveform correlation methods such as the double-difference in this case is limited by the relatively large number of events with dissimilar waveforms. Unlike the iterative linearized method, the nonlinear grid-search method gives the best results with the smallest average rms error of the absolute locations because it avoids the local minimum problem. The relocated hypocenters clearly delineate nearly vertical, northeast-southwest striking faults near the crest of the field, which is consistent with the graben fault system mapped by surface geologic surveys and reflection seismic interpretations. I also performed statistical tests to estimate location errors, and found that the station geometry is the major factor that limits the accuracy of focal depths.

Secondly, this thesis presents a non-linear wavelet-based approach to linear waveform inversion of high-frequency seismograms for the estimation of a point source mechanism and its time function. For earthquake mechanism inversions, it is important to stabilize the problem by reducing the number of parameters to be determined. Commonly, overlapping isosceles triangles or boxcar functions are used for the parameterization of the moment tensor rate functions (MTRFs). Here, I develop a wavelet-based strategy that allows us to construct an adaptive, problem-dependent parameterization for the MTRFs employing fractional spline wavelets. Synthetic results demonstrate that the adaptive parameterization improves the numerical approximation to the model space and therefore, allows more accurate estimations of the MTRFs. The waveform inversion is performed in the wavelet domain and leads to a multiresolution

sparse matrix representation of the inverse problem. At each resolution level a regularized least-squares solution is obtained using the conjugate gradient method. The wavelet-based waveform inversion method has been applied successfully in three real-data examples: the April 22, 2002 Au Sable Forks, New York earthquake, the September 3, 2002 Yorba Linda, California earthquakes, and 11 M>1 microearthquakes in a producing field in Oman. In the Oman field, the dominant styles of focal mechanism are left-lateral strike-slip for events with focal depths less than 1.5 km, and dip-slip along an obliquely trending fault for those with focal depths greater than 2.0 km.

Thirdly, the covariance matrix method of shear-wave splitting analysis is presented. Different from conventional methods that usually analyze only two horizontal components, this method processes all three components of the seismogram simultaneously, allowing not only orientation but also dip information of fractures to be resolved. Synthetic test results show that this method is stable even for high noise level. The method is applied to the Oman microearthquake records that display distinctive shear-wave splitting and polarization directions. From the polarizations, I estimate the predominant subsurface fracture directions and dipping angles. From the time delays of the split wave I determine the fracture density distributions in the reservoir.

Finally, I examine the spatio-temporal characteristics of the microseismicity in the producing reservoir. The frequency-magnitude distribution measured by the *b*-value is determined using the maximum likelihood method. I found that *b*-values are higher for events below the deeper Shuaiba oil reservoir than those above. Also, the feasibility of monitoring the temporal change of *b*-values is demonstrated. The analysis of production and injection well data shows that seismicity event rates in the field all strongly correlated with gas production from the shallower Natih Formation. Microseismicity, focal mechanisms, GPS analysis, and production / injection well data all suggest the NE-SW bounding graben fault system responds elastically to the gas-production-induced stresses. Normal faulting is enhanced in the reservoirs by the compaction related stresses acting on the graben fault system.

Thesis Advisor: M. Nafi Toksöz
Title: Professor of Geophysics, MIT

Acknowledgements

My metamorphosis from prospective geoscience student to geophysicist was indebted to my three mentors. I must thank Wing-Sun Lo, my high school teacher in Wah Yan College Hong Kong, who fueled my academic interest in solid earth; Ken Larner, my academic advisor in Colorado School of Mines, who introduced me to the fascinating field of seismology; and Nafi Toksöz, my thesis advisor, who counseled and assisted me throughout this investigation. Nafi showed an enthusiastic interest both in the study and in my progress.

I want to express appreciation to Royal Dutch / Shell and Petroleum Development Oman (PDO) for providing the data and supporting this research financially.

Many thanks are due to the members of the Earth Resources Laboratory. Valuable discussions with Dan Burns, Jonathan Kane, Xu Li, and Youshun Sun helped form some of the ideas in this thesis. My graduate school life at MIT would not be the same were it not for the fellowship of Hong Kong Student Bible Study group (HKSBS), with special thanks to Ada Au, Samuel Au, Danielle Chu, Connie Yeh, and Ernie Yeh.

I would like to thank my family. My parents always give me the liberty and resources to pursue my dreams. I wish to express gratitude to my wife and editor, Becky, for her love, encouragement, and personal sacrifice. Above all, I thank God who is the ultimate provider of all the blessings and necessities in my life. Apart from Him I can do nothing to accomplish this work.

Contents

Chapter 1

Introduction

1.1 The Main Goals of the Thesis

The producing oil and gas field in the Sultanate of Oman presented in this thesis has been one of the largest oil-producing fields in the country since its discovery in 1962. It is referred as the Field hereafter. Starting in 1996, increasing seismic activities have been reported by staff working in the Field, and surface subsidence of up to 50 cm in the center of the field has been observed by Interferometric Synthetic Aperture Radar (InSAR) and leveling surveys. Horizontal displacements associated with vertical subsidence have been known to cause damage to well casings in the producing fields (Maury et al., 1992). Although currently there are no obvious manifestations of well damage in the Field, further compaction of the reservoir may lead to problems, such as leakage of the connectors of the well casing or loss of well access due to buckling and bending. The first objective of the seismic and surface subsidence monitoring in the Field is to provide information about the magnitude and spatial variations in Natih Formation compaction. The second objective is the identification of seismic risk to the surface facilities from the largest microseismic tremors that can be expected at the field. This will provide reference for seismic design of buildings and engineering structures on the surface of the field.

The final objective of this study is to integrate passive microseismic monitoring techniques for reservoir characterization. Since earthquakes often are associated with structural weaknesses such as faults, microseismicity in oil fields can be used for detailing structural and dynamic properties of the subsurface reservoir. Reservoir heterogeneity at a variety of scales can be caused by structural complexity, stratigraphy, or pore system continuity. These factors create barriers or baffles to fluid flow, and may significantly hinder fluid production. The interpretation of the microseismic event characteristics increases our understanding of the response of these geologic structures to man-made stress perturbations within the reservoirs, which allows more efficient management of future drilling locations and reservoir production planning. With these objectives in mind, I analyze the passive seismic data to obtain (1) precise locations of the event hypocenters, (2) to gain knowledge of the source processes, (3) to perform seismic waveform inversion, (4) to improve understanding of the triggering mechanisms of the induced seismicity, and (5) to integrate microseismicity and geodetic data.

1.2 Previous Studies of Induced Seismicity in Petroleum Reservoirs

Induced seismicity means earthquakes that are caused directly or indirectly by human engineering activities. Engineering sometimes perturbs the regional stress field that is near to its failure strength and leads to induced seismicity. These earthquakes also occur in different geologic settings. Induced seismicity has been observed during the

fillup of water reservoirs (Piccinelli et al, 1995), oil and gas extraction (Grasso, 1990; Rutledge et al. 1997), enhanced oil recovery (Phillips et al., 2000), mining activity (McGarr et al., 1990), fluid injection and disposal (Tabeli & Cornet, 1987), geothermal operations (Li et al., 1998; Phillips et al, 1997), underground nuclear explosions (Boucher et al, 1969, Hamilton et al., 1969), and large-scale construction works (Milne & Berry, 1976; Grasso, 1992). Hypocenters of this type of earthquake are usually located within or near the rock mass under action, but can also appear at a distance of several kilometers away. Theoretically, induced earthquake energy can reach the maximum for natural seismicity depending on the tectonic stresses in the region. Although many of these earthquakes are small in magnitude, they can still have significant social and economic impact due to the proximity of these events to the engineering constructions that trigger them. In the following I will briefly summarize previous studies of induced seismicity in oil and gas fields.

The problems related to induced seismicity in oil and gas fields have been known since 1920s when geologists detected subsidence and earthquakes in the Goose Creek oil field, Texas (Pratt & Johnson, 1926; Snider, 1927). It was suggested that the subsidence and seismicity were directly related to the oil extraction. Similar observations were reported for the Wilmington field, California, where the rate of oil extraction rose rapidly after 1946 and reached its peak at the end of 1951. Subsidence (Plumlee, 1962) and a series of earthquakes occurred between 1947 and 1961 (Kovach, 1974).

The introduction of injection technology in enhancing oil and gas recovery has also been shown to be a cause of induced seismicity. The Rangely oil field in western Colorado was a famous example. Seismicity monitoring at the Rangely oil field was undertaken in 1967 in a joint venture between the U.S. Geological Survey and Chevron Oil Company, to test the feasibility of controlled earthquake generation. A three-phrase program was undertaken in 1969 to monitor the seismicity during a controlled series of waterfloods. The program, which ran for four years, demonstrated that raising and lowering the injection fluid pressure in the subsurface could turn induced microearthquakes on and off in Rangely. It confirmed that earthquakes could be triggered by the increase of pore pressure and resulting reduction of effective normal stress due to fluid injection (Raleigh et al., 1976). Other recent case studies of induced seismicity in hydrocarbon fields are summarized in Table 2.1.

Area	Cause	Source
Visund field, North Sea, Norway	postglacial rebound, overpressure	Wiprut & Zoback, 1999
Valhall field, North Sea, Norway	depletion	Zoback & Zinke, 2002
Ekofisk field, North Sea, Norway	depletion	Zoback & Zinke, 2002 Teufel et al., 1991
Griddings field, Texas	injection (hydraulic fracturing)	Phillips et al., 2002
Carthage Cotton Valley field, Texas	injection (hydraulic fracturing)	Rutledge & Phillips, 2003
Clinton County, Kentucky	depletion	Rutledge et al., 1998
Lacq field, France	depletion	Segall et al., 1994
Eagle & Eagle West field, BC, Canada	depletion	Horner et al., 1994
Sleepy Hollow field, Nebraska	injection (enhanced recovery)	Evans & Steeples, 1987
Cold Lake field, AL, Canada	injection (enhanced recovery)	Talebi et al., 1998
Strachan field, AL, Canada	depletion	Wetmiller, 1986 Baranova et al., 1999

Table 2.1. Recent case studies of induced seismicity in petroleum reservoirs.

Passive seismic monitoring is the practice of recording, analyzing, and interpreting earthquakes with local magnitudes $M_L \leq 2.5$ (Rieven, 1999). Reservoir characterization nowadays depends on the integration of information from geology, geophysics, and petroleum engineering to improve the description of reservoirs. Key information necessary to describe reservoir characteristics includes the geometry of the reservoir (e.g., faults, fractures, depositional units) and its physical properties (e.g., porosity and permeability). Although passive microseismic monitoring has not been used traditionally in oil and gas fields, it has shown promise as a method to monitor the dynamic behavior of reservoirs during the development phase. Because of this, the value of passive microseismics has been increasingly recognized recently (Fehler et al., 2001; Maxwell & Urbancic, 2001; Pavlis, 2003). It can provide important information on the reservoir at locations as far as several kilometers from boreholes.

In most cases, only weak seismic events are induced in oil and gas fields, and they cannot be felt or detected by regional seismic networks. Earthquakes generally follow a power law distribution, meaning that smaller events are more numerous than the larger ones. Only sensitive local seismic networks inside the field can detect them, preferably with the sensors placed in a downhole environment (Jones & Asanuma, 2004) in order to minimize the influence of signal attenuation and high noise level close to the surface. This results in a significant increase in the number of smaller events recorded. These small seismic events carry important information pertaining to the location of zones of weakness and seismically active faults or fractures in the petroleum reservoirs. Since fractures usually dominate the permeability, especially in carbonate reservoirs, the ability

to map them has direct applications to reservoir development and management. Previous studies (Rutledge et al., 1998; Fehler et al., 2000) have shown that induced seismicity data provide highly detailed information about the fractures systems that most other geophysical methods cannot resolve.

It has been suggested that the gross flow paths affected by hydraulic fracturing can be mapped using the microearthquakes induced during the injection operation. Barton et al. (1995) have shown correlations of high permeability along fractures in crystalline rocks that are oriented such that resolved shear stress is high. Therefore, potentially important reservoir flow paths along critically stressed fractures, and the location of the oil front being displaced by water or gas could be revealed by microseismicity patterns generated by reservoir stress changes. Other recent studies also attempted to estimate time variations of reservoir permeability (Shapiro et al., 1999), porosity, and stress (Baisch & Harjes, 2003; Teanby et al., 2004) from microseismicity patterns.

Also, mapping microseismic events both spatially and temporally can identify those volumes of reservoir reacting to stress change at that particular time. Stress changes can be induced outside the reservoir, where no pore-fluid content changes need to occur, due to reservoir volume changes accompanying pressure and temperature drawdown (Segall, 1989; Segall & Fitzgerald, 1998). Microearthquakes induced above the reservoir could be used for monitoring and characterizing deformation in the overburden. In the case where surface subsidence associated with reservoir compaction occurs, source

mechanisms of microseismic events can help verify geomechanical modeling assessments of the compaction strains and cap rock integrity.

1.3 Thesis Outline

The thesis is organized to develop and demonstrate methods and concepts of reservoir characterization using passive microseismic data. The contents are presented in five chapters. Chapter 1 presents the main objectives of this thesis, and a brief summary of previous studies and advances of passive microseismic monitoring in oil and gas fields.

Processing of passive seismic data begins with estimating the 3-D hypocentral locations and origin times. Chapter 2 presents full descriptions of three location algorithms: the iterative linearization method, nonlinear grid-search method, and relative location methods. The interpretation of the location results is aided by using the collapsing method to simplify the diffusive event "cloud" structure, and by measuring the planarity of the hypocenters using polarization analysis.

To study the dynamic characteristics of a reservoir through the use of passive microseismic data, it is necessary to know the source mechanisms of the events. Chapter 3 presents the theoretical development of a new waveform inversion method for source mechanism based on the wavelet transform. Numerous synthetic tests show that the

method is stable and yields better results compared to the conventional time- and frequency-domain methods that use boxcars and triangular functions for parameterization. The method has been successfully applied to three examples in different geologic settings, including the case of Oman microearthquakes.

Monitoring shear-wave splitting in hydrocarbon reservoirs can be used to determine the orientation and density of subsurface fractures. Chapter 4 demonstrates that this can also be done for passive seismic data. The theoretical development of the covariance-matrix method that processes all three components of the seismogram is presented, and the method is applied both to synthetic data and the Oman passive seismic dataset.

Various aspects of the spatial-temporal characteristics of the Oman microseismicity are presented in Chapter 5, including the Gutenberg-Richter magnitude-frequency relationship, and comparisons of microseismicity patterns with both water injection and gas production. Finally, all the results presented in the previous chapters are summarized, and are interpreted jointly with geodetic data and geomechanical modeling results to give an overall picture of the reservoir structures and dynamic processes in the petroleum field.

An overview of the geology of North-Central Oman, particularly of the Natih and Shuaiba Formations that form the main hydrocarbon reservoirs in the Fahud Salt Basin, are presented in Appendix A. Also, the geology and production history of the producing

fields in the Fahud Salt Basin are discussed. They provide the backbone for the interpretation of the passive microseismic data in the petroleum field in Oman, and show how compartmentalization of the reservoirs due to faults, lithology and petrophysics have controlled the distribution of fluids.

1.4 References

Audigane, P., Royer, J., and Kaieda, H., 2002, Permeability characterization of the Soultz and Ogachi large-scale reservoir using induced microseismicity: Geophysics, **67**, 204 – 211.

Baisch, S. and Harjes, H.-P., 2003, A model for fluid-injection-induced seismicity at the KTB, Germany: Geophys. J. Int., **152**, 160-170.

Baranova, V., Mustaqeem A., and Bell, S., 1999, A model for induced seismicity caused by hydrocarbon production in the Western Canada Sedimentary Basin: Can. J. Earth Sci., **36**, 47-64.

Barton, C.A., Zoback, M.D., and Moos, D., 1995, Fluid flow along potentially active faults in crystalline rock, Geology, **23**, 683-686.

Boucher, G., Ryall, A., and Jones, A.E., 1969, Earthquakes associated with underground nuclear explosion: J. Geophys. Res., **74**, 3808 – 3820.

Evans, D.G. and Steeples, D.W., 1987, Microearthquakes near the Sleepy Hollow oil field, southwestern Nebraska: Bull. Seismol. Soc. Am., **77**, 132 – 140.

Fehler, M., Jupe, A. and Asanuma, H., 2001, More than Cloud, New techniques for characterizing reservoir structure using induced seismicity: The Leading Edge, **20**, 324-330.

Fehler, M., Phillips, W.S., House, L., Jones, R.H., Aster, R., and Rowe, C., 2000, Improved relative locations of clustered earthquakes using constrained multiple event location: Bull. Seismol. Soc. Am., **90**, 775 – 780.

Grasso, J.-R., 1992, Mechanics of seismic instabilities induced by the recovery of hydrocarbons: Pure Appl. Geophys., **139**, 507-534.

Hamilton, R. M., McKeown, F. A., and Healy, J. H., 1969, Seismic activity and faulting associated with a large underground nuclear explosion: Science, **166**, 601 – 604.

Horner, R.B., Barclay, J.E., and MacRae, J.M., 1994, Earthquakes and hydrocarbon production in the Fort St. John area of northeastern British Columbia: Can. J. Expl. Geophys., **30**, 39-50.

Jones, R.H. and Asanuma, H., 2004, Optimal four geophone configuration, vector fidelity and long-term monitoring: 66th EAGE Annual Conference, Paris, Expanded Abstracts, 294

Kovach, R.L., 1974, Source mechanisms for Wilmington oil field, California subsidence earthquakes: Bull. Seism. Soc. Am., **64**, 699-711.

Maury, V.M.R., Grasso, J.R., and Wittlinger, G., 1992, Monitoring of subsidence and induced seismicity in the Larq gas field: The consequences on gas production and field operation: Engineering Geology, **32**, 123.

Maxwell, S.C. and Urbancic, T.I., 2001, The role of passive microseismic monitoring in the instrumented oil field: The Leading Edge, **20**, 636-639.

Milne, W.G. and Berry, M.J., 1976, Induced seismicity in Canada: Eng. Geol.: **10**, 219-226.

Pavlis, G. L., 2003, Imaging the earth with passive seismic arrays: The Leading Edge, **22**, 224-231.

Phillips, W.S., House, L.S., and Fehler, M.C., 1997, Detailed joint structure in a geothermal reservoir from studies of induced microearthquake clusters: J. Geophys. Res., **102**, 11745 – 11763.

Phillips, W.S., Rutledge, J.T., House, L.S., and Fehler, M.C., 2002, Induced microearthquake patterns in hydrocarbon and geothermal reservoirs, six case studies: Pure Appl. Geophys., **159**, 345 – 369.

Plumlee, C.H., 1962, Subsidence in the Wilmington oil field and the Long Beach Naval Shipyard: J. Geophys. Res., **67**, 1653.

Pratt, W.E. and Johnson, D.W., 1926, Local subsidence of the Goose Creek oil field: J. Geology, **34**, 577 – 590.

Raleigh, C.B., Healy, I.H., and Bredehoeft, J.D., 1976, An experiment in earthquake control at Rangely, Colorado: Science, **191**, 1230-1237.

Rieven, S.A., 1999, Analysis and interpretation of clustered microseismicity at geothermal and petroleum reservoirs: *PhD thesis*, MIT.

Ross, A., Foulger, G.R., and Julian, B.R., 1999, Source processes of industrially-induced earthquakes at the Geysers geothermal area, California, Geophysics, **64**, 1877-1889.

Rutledge, J.T. and Phillips, W.S., 2003, Hydraulic stimulation of natural fractures as revealed by induced microearthquakes, Carthage Cotton Valley gas field, East Texas: Geophysics, **68**, 441 – 452.

Rutledge, J.T., Phillips, W.S., and Schuessler, B.K., 1998, Reservoir characterization using oil-production-induced microseismicity, Clinton County, Kentucky: Tectonophysics, **289**, 129 – 152.

Segall, P., 1989, Earthquakes triggered by fluid extraction: Geology, **17**, 942-946.

Segall, P. and Fitzgerald, S., 1998, A note on induced stress changes in hydrocarbon and geothermal reservoirs, Tectonophysics, **289**, 117-128.

Segall, P., Grasso, J.R., and Mossop, A., 1994, Poroelastic stressing and induced seismicity near the Lacq gas field, southwestern France: J. Geophys. Res., **99**, 15423 – 15438.

Shapiro, S.A., Audigane, P., and Royer, J.-J., 1999, Large-scale in situ permeability tensor of rocks from induced microseismicity: Geophys. J. Int., **137**, 207-213.

Snider, L.C., 1927, A suggested explanation for the surface subsidence in the Goose Crek oil and gas field, Texas: Goose Creek oil field: Bulletin AAPG, **11**, 729 – 745.

Stark, M.A., 1990, Imaging injected water in the Geysers reservoir using microearthquake data, Geotherm. Resources Counc. Trans., **14**, 1697-1704.

Talebi, S. and Boone, T.J., 1998, Source parameters of injection-induced microseismicity: Pure Appl. Geophys., **153**, 113 – 130.

Teanby, N., Kendall, J.-M., Jones, R.H., and Barkved, O., 2004, Stress-induced temporal variations in seismic anisotropy observed in microseismic data: Geophys. J. Int., **156**, 459-466.

Wetmiller, R.J., 1986, Earthquakes near Rocky Mountain House, Alberta, and their relationship to gas production facilities: Can. J. Earth Sci., **23**, 172 – 181.

Chapter 2

Microearthquake Locations in the Field in Oman

2.1 Introduction

2.1.1 Structure and Production History of the Field

The Field is one of the largest oil producing fields in the Fahud Salt Basin and Oman. The main oil producing Shuaiba reservoir has a Stock Tank Oil Initially in Place (STOIIP) of 604×10^6 m^3 (Litsey et al., 1986). Oil is relatively light (40° API). The Shuaiba oil reservoir is located at a depth of 1420 m. Gas is also produced from the shallower but smaller Middle Cretaceous Natih "A" reservoir. The Field is a highly faulted, gentle anticline that is dominated by a major NE-SW trending central graben (Blaskovich et al., 1985). This divides the Field into the east and west reservoir blocks. All faults are high-angle normal faults. The dome is about 15 × 20 km in size with a northeast-southwest axial elongation. The matrix permeability is low (1 – 100 mD) with low viscosity (0.6 cp) but the faults and fractures partially connect the field together (Mijnssen et al., 2003).

The Shuaiba oil reservoir was initially produced by natural depletion but water injection was introduced in 1972 to maintain reservoir pressure. Horizontal wells were drilled in 1994 and production reached to a peak of approximately 225,000 B/D in 1997 and began to decline rapidly afterwards (Mijnssen et al., 2003). Gas production from

Natih has been extracted only by depletion drive. The Natih gas reservoir in the Field is currently a depleting gas reservoir and pressure has dropped from 10,120 KPa to 7,920 KPa since 1973 (van Driel et al., 2000).

A more detailed summary of the geology and production history of the North-Central Oman and the Fahud Salt Basin can be found in the Appendix A.

2.1.2 Seismicity in North-Central Oman

Seismicity in Oman has been historically low. Figure 2.1 illustrates the regional seismicity in the Oman region since 1960 reported by the Incorporated Research Institutions for Seismology (IRIS) and the International Seismological Centre (ISC). The four earthquakes that occurred near northern Oman are listed in Table 2.1. There were only two recorded earthquakes that occurred inside the country in more than forty years: a magnitude 5.0 earthquake on March 3, 1971 and a magnitude 4.7 earthquake on October 28, 1984. Two additional earthquakes with magnitudes 4.2 and 3.8 located in the Musandam Peninsula of United Arab Emirates. were recorded on April 12, 1984 and April 20, 1996, respectively. However, no noticeable natural earthquake activity was recorded in north-central Oman by the IRIS-ISC network, and the region is considered to be a seismically quiet area.

Staff working in the Field have reported increasing microseismic activities since 1996. Surface subsidence of up to 50 cm in the center of the field has been observed by

Synthetic Aperture Radar (InSAR) interferometric and leveling surveys (van Driel et al., 2000), mainly due to the compaction of the depleting Natih gas reservoir. There is a concern about the integrity of the Shuaiba oil wells where these penetrate the Natih reservoir layer. In highly compacting fields (i.e., those with reservoirs in 'weak' formations), shear stress may cause slip and failure of wells. Preliminary modeling results done in Petroleum Development Oman (PDO) show that Natih gas reservoir is predicted to display significant compaction upon depletion (van Driel et al., 2000). A seismic and surface subsidence monitoring program of the Field was established to provide information about the magnitude and spatial variations in Natih formation compaction that could damage well casings in the field. An additional objective of the program was the identification of seismic risk to the surface facilities from the largest microearthquakes that can be expected at the field.

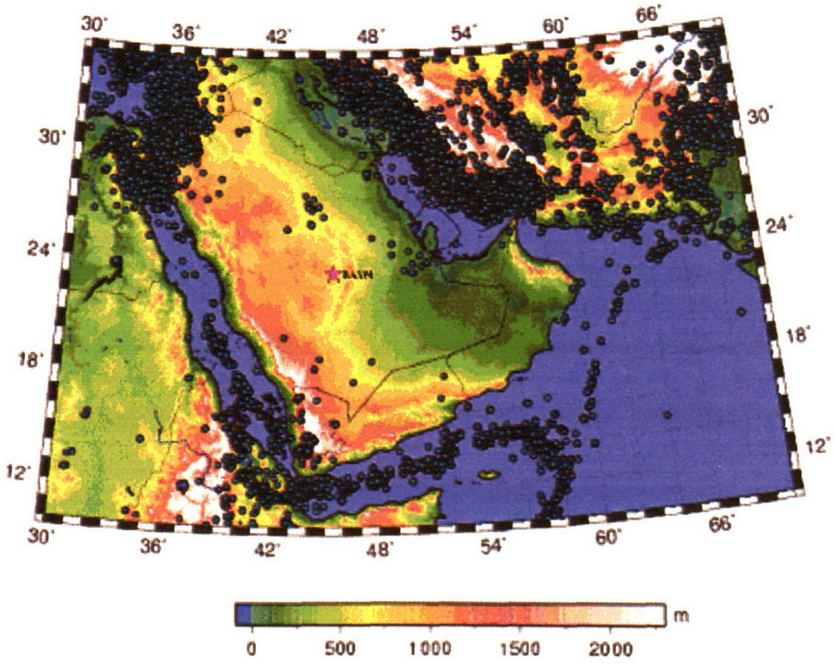

Figure 2.1. Regional seismicity around the Arabian Peninsula reported to IRIS-ISC. Earthquakes of magnitude 4 or greater for the period 1950 to 2001 are plotted. Detection capability of the global seismic network, based on regional tests, is estimated to be about magnitude 4.

Since earthquakes often are associated with structural weaknesses such as faults, locating these induced seismic events accurately is helpful in understanding the potential seismic hazard and the regional geologic structure. Ideas about the nature of earthquakes, and in particular their spatial and temporal distribution range from purely stochastic models (Kagan, 1982) to those in which earthquakes are organized in both space and time (Oppenheimer et al., 1988; Vidale et al., 1994; Nadeau et al., 1995). A major impediment to a better understanding of the processes that control earthquake occurrence and interaction is the poor spatial resolution of earthquake locations routinely determined by seismic networks. This is particularly problematic for associating the earthquakes with active faults. The use of the oil-production- or injection-induced microseismicity in reservoir characterization has become a more developed technique as more precise earthquake locations can be estimated. In this chapter, I describe seismic monitoring of the Field in northern Oman and study the microseismicity in detail. I carried out a series of tests and using different location algorithms to assess the stability of the epicentral relocations and to estimate reasonable bounds on the relocation errors. This chapter presents the results and the problems encountered with the relocation of the microearthquakes in sufficient detail that the reader can have reasonable confidence in the epicenter map, and in the spatial and temporal development of the microseismic

sequence. First, I relocated the events using the Hypoinverse2000 code (Klein, 2000). Then, a probabilistic nonlinear grid-search algorithm, NonLinLoc (Lomax et al., 2000), was applied to the relocation problem. Finally, the relative relocation algorithm, the double-difference method of Waldhauser & Ellsworth (2000), was used to determine the earthquake locations. I compare the depth determinations obtained with all the three methods for the best-located events. The improved locations of the microearthquakes revealed the spatial pattern of a fault zone / fracture networks, and this was consistent with the interpretation of 3D reflection seismic data.

Time	Latitude	Longitude	Depth (km)	Magnitude
03/03/1971	22.14°	59.37°	35.3	5.0
10/28/1984	22.33°	59.86°	33	4.7
04/12/1984	25.43°	55.97°	33	4.2
04/20/1996	24.76°	55.45°	0	3.8

Table 2.1. A list of natural earthquakes reported to IRIS near and inside Oman since 1960.

Finally, the work presented here paves the way for an interpretation of faulting in the Field during the earthquakes, which is presented in the next chapter. By combining the relocations, focal mechanisms, source sizes and the tectonic evidence observed in the field, it becomes possible to associate the induced microseismic events with specific motion on certain subsections of the fault zone.

2.2 Data Acquisition and Data Processing

The microearthquake waveform data were collected by the PDO using downhole geophones, over a period from October 29, 1999 to June 18, 2001. There were 5 monitoring stations, labeled VA1, VA2, VA3, VA4 and VA5 (Figure 2.2). Each borehole was 150 m deep. Each hole had four three-component geophones, at depths of 150 m, 145 m, 140 m and 135 m. The downhole geophones were of type Sensor SM-6B, 4.5 Hz. The Data recorders were Nanometrics Orion 24 bit systems. The three-component geophones were arranged in an orthogonal configuration with two horizontal components and one vertical component. The coordinates of the holes, the depths of the geophones, and the orientations of the horizontal components are shown in Table 2.2. The locations of the five borehole seismic stations are shown in Figure 2.2. Placing seismic sensors downhole reduces the microseismic noise and, in general, greatly improves the resolution of mapping active reservoir fractures or faults (Phillips et al., 1997; Rutledge et al., 1998a, b; Gaucher et al., 1998; Phillips, 2000).

There were two recorders next to each hole, each recording the 150 m and 145 m detectors. Data were recorded continuously, with a sampling rate of 8 ms (125 samples per second). The network recorded 802 events during the period of 20 months. An example three-component waveform of an event recorded by a geophone is shown in Figure 2.3.

High quality hypocenter estimates are dependent on the use of high quality arrival time estimates. Therefore, considerable effort has been invested in obtaining good phase arrival times. First, I rotate all data to the common backazimuth coordinates of radial, transverse and vertical motions. Next, I pick the P- and S-wave arrival times. It has to be done carefully since accurately determining the time of these arrivals is important in determining the location of a seismic event. This is not a problem when the records are clean with high signal to noise ratio and the arrivals are impulsive. However, electrical and surface noises associated with well drilling operations which took place during the recording period limited the signal quality in some of the available seismic datasets. I use two particle-motion attributes to aid the picking: polarization and three-component amplitude (Jurkevics, 1988).

				Rcvr Depth	H1 Azimuth	H2 Azimuth
Hole	Elevation	Latitude	Longitude	m	deg	deg
VA-1	101.73	22° 7'51.858"N	56° 3'15.719"E	135	71.6	161.6
				140	63.8	153.8
				145	62.7	152.7
				150	54.3	144.3
VA-2	105.19	22° 7'54.485"N	55°58'42.150"E	135	160.7	250.7
				140	157.4	247.4
				145	157.7	247.7
				150	161.1	251.1
VA-3	99.46	22°11'24.646"N	55°58'57.085"E	135	-112.7	-22.7
				140	-112.7	-22.7
				145	-120.7	-30.7
				150	-109.1	-19.1
VA-4	115.67	22°11'24.496"N	56° 3'15.915"E	135	-45.8	44.2
				140	-46.7	43.3
				145	-55.6	34.4
				150	-64	26
VA-5	114.14	22° 9'39.490"N	56° 0'33.179"E	135	94.9	184.9
				140	90.9	180.9
				145	98.4	188.4
				150	92.2	182.2

Table 2.2. Coordinates and orientation of the shallow borehole array. H1, H2 Azimuths are angles of horizontal components with North measured clockwise. Reservoir (Rcvr) depths are depths in meters below surface. Elevations are surface depths above mean sea level.

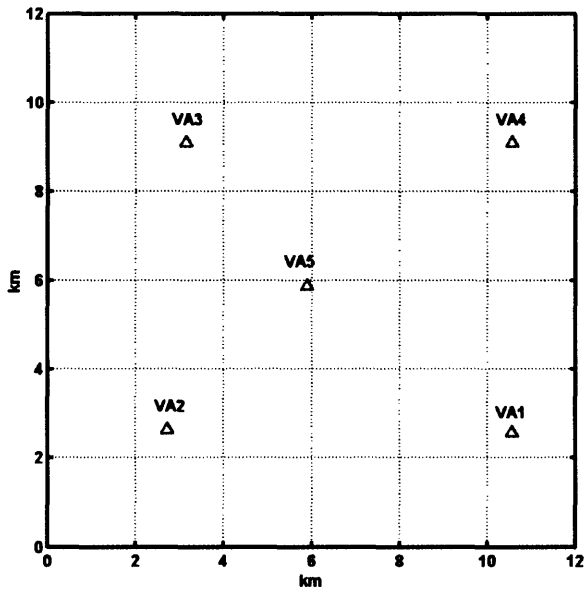

Figure 2.2. The geometry and distribution of the five borehole seismic stations in the Field.

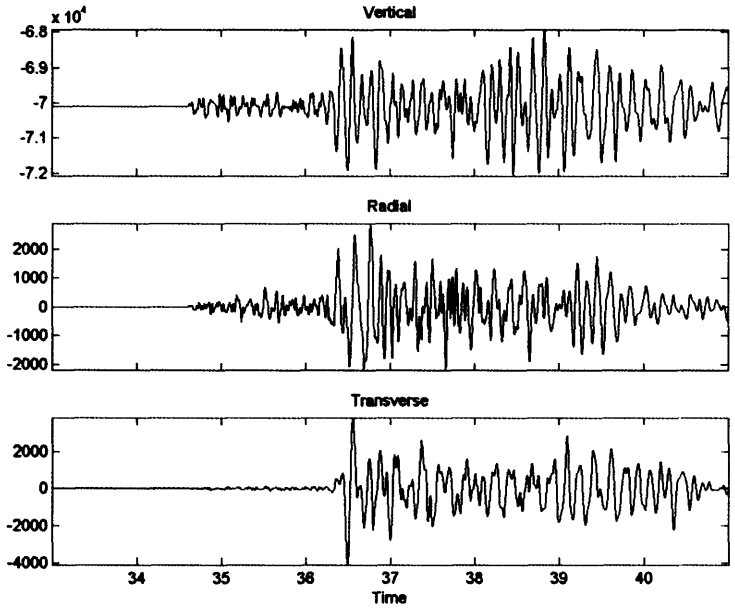

Figure 2.3. An example of the three-component waveforms of an event recorded by a geophone after rotation. From top to bottom: the vertical-, radial-, and the transverse-component of the seismogram.

Polarization analysis is a powerful tool to identify P-wave arrivals since their particle motions are linearly polarized. To compute the degree of linear polarization of a wave, I apply short sliding time windows and then calculate the polarization ellipsoid from the covariance matrix in each window:

$$\mathbf{M} = \begin{bmatrix} Var(x) & Cov(x,y) & Cov(x,z) \\ Cov(x,y) & Var(y) & Cov(y,z) \\ Cov(x,z) & Cov(y,z) & Var(z) \end{bmatrix}, \qquad (2.2.1)$$

where x, y and z are the three components of the seismic signal. The covariance of x and y is defined as

$$Cov(x,y)=\frac{1}{N}\sum_{i=1}^{N}x_i y_i \tag{2.2.2}$$

and the variance of x is defined as

$$Var(x)=Cov(x,x). \tag{2.2.3}$$

The covariance matrix, **M**, is symmetric and positive semidefinite, which means that the eigenvalues are real and non-negative. In quadratic form, **M** represents an ellipsoid whose principal axes are defined by the eigenvectors of **M**. Therefore, I calculate the eigenvalues of each polarization ellipse, and then construct the rectilinearity function, F, which is defined as

$$F=1-\frac{\lambda_2+\lambda_3}{2\lambda_1}, \tag{2.2.4}$$

where $\lambda_1 > \lambda_2 > \lambda_3$, and are the eigenvalues of the covariance matrix **M**. For P-waves, we can expect that λ_1 is much greater than λ_3 and therefore, the rectilinearity function is equal to 1 at points where the wave is perfectly linearly polarized (e.g. pure P-wave). On the other hand, the rectilinearity is equal to zero where there is no polarization.

Determination of S-wave arrivals posed considerably more difficulty. Information from the three-component seismograms helped to add constraint on the arrival time

estimates. I applied the same method to calculate the polarization of the SV-wave motion which is linearly polarized perpendicular to the propagation direction but with little success. Polarization for the S-wave is difficult to interpret because seismic records usually contain both the SH and SV components, as well as higher-mode Rayleigh and Love overtones all with similar arrival times (Ruud et al., 1988; Jepsen and Kennett, 1990). The three-component amplitude is the attribute defined as square root of the trace of the covariance matrix in a time window. It is a useful attribute to identify S-waves as it is usually high for the S-waves and low for the P-waves. After producing initial S-wave arrival time estimates by direct visual inspection and performing polarization analysis of the seismic records, the arrivals are checked against expected arrival windows calculated from the original P-wave hypocenter locations.

2.3 Earthquake Location Methods

One of the most important tasks in observational seismology is locating seismic events. That is to determine the point in space and time at which seismic energy was first initiated, which is specified by three spatial coordinates (latitude, longitude, depth) from the surface, and origin time. These four parameters represent the hypocenter for the event. The four hypocentral parameters have to be estimated from the phase information collected at a limited number of seismic stations. In reality, the distribution of these seismic stations is often sparse, and therefore, it is difficult to secure high accuracy in estimating seismic locations. In order to locate an event, the minimal information needed is four sets of arrival times for a single phase such as *P*, but arrival-time readings from

more stations and various other phases are almost always required to determine an earthquake hypocenter and origin time accurately. The use of multiple phases can reduce the number of stations required.

2.3.1 Iterative Linearized Method

Conventional travel-time location methods, such as the HYPOINVERSE-2000 algorithm (Klein, 2000) which I use here, are the most commonly used procedure to locate hypocenters for earthquakes. HYPOINVERSE-2000 is one of a long line of similar U.S.G.S. programs including HYPOLAYR (Eaton, 1969), HYPO71 (Lee & Lahr, 1972), and HYPOELLIPSE (Lahr, 1980). These methods are based on Geiger's method (Geiger, 1912) or its variants. If the event is at local distances, the two principal phases on the seismogram are P and S. For the *i*th station that records the *k*th earthquake, the seismic phase arrival time, t_k^i, can be written as (Geiger, 1912)

$$t_k^i = \tau^k + \int_i^k u dl \tag{2.3.1}$$

where τ^k is the origin time of event *k*, *u* is the slowness field and *dl* is an element of raypath length. The earthquake location problem is intrinsically non-linear because the slowness and the raypath are dependent on each other in equation (2.3.1). Using Taylor series expansion and keeping only the first-order terms, and assuming that the travel time residual, r_k^i, is small, we can linearize the problem,

$$\frac{\partial t_k^i}{\partial x^i}\Delta x^i + \frac{\partial t_k^i}{\partial y^i}\Delta y^i + \frac{\partial t_k^i}{\partial z^i}\Delta z^i + \frac{\partial t_k^i}{\partial \tau^i}\Delta \tau^i = \left(t_{obs} - t_{cal}\right)_k^i = r_k^i \qquad (2.3.2)$$

where $[\Delta x^k, \Delta y^k, \Delta z^k]$ are the perturbed hypocenter location in Cartesian coordinates, $\Delta \tau^k$ is the perturbed origin time, t_{obs} and t_{cal} are the observed and predicted travel times, respectively. Now, let **G** be the partial derivative matrix,

$$\mathbf{G} = \frac{\partial t_k}{\partial \mathbf{m}} \qquad (2.3.3)$$

where the model vector $\mathbf{m} = \left(x^k, y^k, z^k, \tau^k\right)$. The matrix **G** has a dimension of $M \times 4$ matrix (M equals the number of observations). We can write a system of linear equations that maps changes in model parameters, $\Delta\mathbf{m}$, onto perturbations to improve the fit to the data,

$$\mathbf{G}\Delta\mathbf{m} = \mathbf{d}, \qquad (2.3.4)$$

where **d** is the data vector containing the travel time residuals. Since this is often an overdetermined problem, the least squares solution which best solves equation (2.3.4) is (Menke, 1989)

$$\Delta\hat{\mathbf{m}} = \left[\mathbf{G}^{\mathrm{T}}\mathbf{G}\right]^{-1}\mathbf{G}^{\mathrm{T}}\mathbf{d}, \qquad (2.3.5)$$

where $\left[\mathbf{G}^{\mathrm{T}}\mathbf{G}\right]^{-1}\mathbf{G}^{\mathrm{T}}$ is called the generalized inverse of $\mathbf{G}$, $\Delta\hat{\mathbf{m}}$ is an estimator of the true perturbation model vector $\Delta\mathbf{m}$. As a result, this method is iterative with the updated model

$$\mathbf{m}^{k+1} = \mathbf{m}^{k} + \Delta\mathbf{m}^{k} \tag{2.3.6}$$

where $\mathbf{m}^{k}$ is the model parameter vector after k^{th}-iteration. The process of refinement of hypocenter estimates is repeated until it converges on the minimum RMS travel-time residual.

This procedure works well for the Field where most local earthquakes occur within the seismic network. It becomes more difficult to constrain focal depths for regional earthquakes occurring outside a network and hypocenter-station distances significantly larger than distances between stations.

2.3.2 Nonlinear Grid-Search Method

The conventional approach to event location presented in the previous section is to use L_2 misfit representations in iterative inversion with linearization around successive location estimates, which requires calculation of the derivatives of the times and slownesses with respect to hypocentral parameters. The calculation of such derivatives limits the class of velocity models that can be conveniently employed. However, with the advent of faster computers, it is now feasible to calculate the travel times afresh for each

postulated source location rather than relying on linearization, thus avoiding any differentiation. In absolute location studies, nonlinear global-search methods have several advantages over linearized approaches. First, nonlinear global-search methods produce more stable solutions than linearized methods because they are not strongly dependent on starting locations and other inversion parameters. Second, nonlinear global-search methods can be easily performed in three-dimensional structures, which is more difficult with linearized models. In general, the linear and nonlinear locations and uncertainties are similar for events inside of the network, but they can differ significantly outside of the network, particularly in depth. In this section, I used the NonLinLoc algorithm (Lomax et al., 2000) to locate the Oman microseismic events, which follows the probabilistic formulation of inversion approach of Tarantola and Valette (1982), Moser et al. (1992), and Wittlinger et al. (1993).

Let $\mathbf{t} = g(\mathbf{X}, \mathbf{Y}, \mathbf{Z}, \mathbf{T}) = h(\mathbf{X}, \mathbf{Y}, \mathbf{Z}) + \mathbf{T}$ be the theoretical relationship of equation (2.3.1) between arrival times and the spatial-temporal coordinates of the hypocenter, where $\mathbf{T}$ is the origin time. Assume that the arrival time data possess a Gaussian structure, then the a priori density function has a Gaussian form for all parameters (Lomax et al., 2000),

$$\rho(\mathbf{t}) = \exp\left\{-\frac{1}{2}(\mathbf{t}-\mathbf{t}_0)^T \mathbf{C}_t^{-1}(\mathbf{t}-\mathbf{t}_0)\right\}. \qquad (2.3.7)$$

where $\mathbf{t}_0$ is the vector of mean values of data and $\mathbf{C}_t$ is the data covariance matrix.

Let $\mathbf{C_T}$ be a covariance matrix which is an estimation of the errors of the calculation of the arrival times by the raytracer or finite difference scheme. If we assume that the travel time errors are also Gaussian, the theoretical relationship between data and hypocentral parameters can be written as

$$\theta(\mathbf{t} \mid \mathbf{X,Y,Z,T}) = \exp\left\{-\frac{1}{2}[\mathbf{t} - g(\mathbf{X,Y,Z,T})]^T \mathbf{C_T^{-1}} [\mathbf{t} - g(\mathbf{X,Y,Z,T})]\right\}. \qquad (2.3.8)$$

When the density functions giving the prior information on the model parameters $\rho(\mathbf{X,Y,Z,T})$ and on the observations $\rho(\mathbf{t})$ are independent, a complete and probabilistic solution can be expressed as *a posteriori* density function, $\sigma(\mathbf{X,Y,Z,T})$, according to Lomax et al. (2000),

$$\begin{aligned}\sigma(\mathbf{X,Y,Z,T}) &= \rho(\mathbf{X,Y,Z,T}) \int \frac{\rho(\mathbf{t})\theta(\mathbf{t} \mid \mathbf{X,Y,Z,T})}{\mu(\mathbf{t})} d\mathbf{t} \\ &= \rho(\mathbf{X,Y,Z,T}) \cdot \\ &\quad \cdot \exp\left\{-\frac{1}{2}[\mathbf{t}_0 - g(\mathbf{X,Y,Z,T})]^T \left(\mathbf{C_t^{-1}} + \mathbf{C_T^{-1}}\right)[\mathbf{t}_0 - g(\mathbf{X,Y,Z,T})]\right\}\end{aligned} \qquad (2.3.9)$$

To obtain the spatial location but not the temporal location of the earthquake, we can compute the marginal density function (Lomax et al., 2000),

$$\sigma(\mathbf{X,Y,Z}) = \int_{-\infty}^{\infty} \sigma(\mathbf{X,Y,Z,T}) d\mathbf{T} \qquad (2.3.10)$$

in which we integrate over the range of the origin time T. Least-squares computation of hypocenter is based on the maximization of $\sigma(\mathbf{X},\mathbf{Y},\mathbf{Z})$. Since it is generally impossible to have a priori information (independent from the data) about the origin time T, we can assume an a priori density function uniform on T (Lomax et al., 2000),

$$\rho(\mathbf{X},\mathbf{Y},\mathbf{Z},\mathbf{T}) = \rho(\mathbf{T})\rho(\mathbf{X},\mathbf{Y},\mathbf{Z}) = \rho(\mathbf{X},\mathbf{Y},\mathbf{Z}). \tag{2.3.11}$$

According to Tarantola & Valette (1982), the marginal posteriori density function reduces to

$$\sigma(\mathbf{X},\mathbf{Y},\mathbf{Z}) = K\rho(\mathbf{X},\mathbf{Y},\mathbf{Z})\cdot \cdot \exp\left\{-\frac{1}{2}\left[\tilde{\mathbf{t}}_0 - \tilde{h}(\mathbf{X},\mathbf{Y},\mathbf{Z})\right]^T (\mathbf{C}_t + \mathbf{C}_T)^{-1}\left[\tilde{\mathbf{t}}_0 - \tilde{h}(\mathbf{X},\mathbf{Y},\mathbf{Z})\right]\right\} \tag{2.3.12}$$

where

$$\begin{aligned} p_i &= \sum_j (\mathbf{C}_t + \mathbf{C}_T)^{-1}_{ij} \\ K &= \sum_{ij} (\mathbf{C}_t + \mathbf{C}_T)^{-1}_{ij} = \sum_i p_i \\ \tilde{t}_0^i &= \tilde{t}_0^i - \frac{\sum_j p_j t_0^j}{\sum_j p_j} \\ \tilde{h}^i &= h^i - \frac{\sum_j p_j h^j}{\sum_j p_j} \end{aligned} \quad , \tag{2.3.13}$$

and gives the general solution for the spatial location of an earthquake in the Gaussian case, including information on uncertainty and resolution. In equations (2.3.12) and (2.3.13), $\tilde{\mathbf{t}}_0$ is the vector of $\tilde{t}_0^i$ containing the observed arrival times minus their weighted mean, $\tilde{\mathbf{h}}$ is the vector of $\tilde{h}^i$ containing the theoretical travel times minus their weighted mean. This solution does not contain any linear approximation, and the resulting posteriori density function may be irregular and multi-modal because the forward calculation involves a non-linear relationship between hypocenter location and travel-times.

A 3-D Eikonal finite-difference approximation of Huygen's principle (Podvin and Lecomte, 1991) is employed to compute the first arriving, infinite frequency P and S travel-times at all nodes of the grid. These travel-times are then stored on disk. The errors in the arrival time picks and in the travel-time calculation are assumed to be Gaussian. This assumption allows analytic calculation of a maximum likelihood origin time given the observed arrival times and the calculated travel times between the seismic stations and the hypocenter in xyz space. This reduces the 4-D problem of earthquake location to 3-D search over the x, y, z space. The maximum likelihood origin time corresponding to a hypocenter at (x, y, z) is given by (Moser et al., 1992),

$$T_{ml}(\mathbf{X},\mathbf{Y},\mathbf{Z}) = \frac{\sum_i \sum_j (\mathbf{C}_t + \mathbf{C}_T)_{ij}^{-1} \left[t^i - h^i(\mathbf{X},\mathbf{Y},\mathbf{Z}) \right]}{\sum_i \sum_j (\mathbf{C}_t + \mathbf{C}_T)_{ij}^{-1}}. \qquad (2.3.14)$$

The grid-search algorithm systematically calculates the *posteriori* probability density function $\sigma(\mathbf{X,Y,Z})$ over a three-dimensional spatial grid. The maximum likelihood (or minimum misfit) point of the posteriori probability density function is selected as an optimal solution.

2.3.3 Relative Location Method

Relative location methods estimate event locations relative to some selected reference events. Several approaches have been used for estimation of relative location of both natural and induced seismic events (Poupinet et al., 1984; Got et al. 1994; Li et al., 1998), but all of them take advantage of the similarity of waveforms from events that are close to each other. Since the separation of the hypocenters is small compared to the source-receiver distance and scale length of the velocity heterogeneity, it is reasonable to assume that the difference between travel times is due to spatial offset between events. The estimation of this spatial offset can be significantly improved because the absolute errors are subtracted off by just working on the differential travel-time data.

Waldhauser and Ellsworth (2000) developed an efficient method, called the double-difference algorithm, to determine high-resolution hypocenter locations by incorporating absolute travel-time measurements and P-wave differential travel-time measurements. Starting with equation (2.3.2), they followed the Frechet (1985) approach

to obtain an equation for the relative change in hypocentral distance between two events *i* and *j*, by taking the difference between equation (2.3.2) for the two events,

$$\left(\frac{\partial t_k^i}{\partial x^i}\Delta x^i + \frac{\partial t_k^i}{\partial y^i}\Delta y^i + \frac{\partial t_k^i}{\partial z^i}\Delta z^i + \Delta\tau^i\right) - \left(\frac{\partial t_k^j}{\partial x^j}\Delta x^j + \frac{\partial t_k^j}{\partial y^j}\Delta y^j + \frac{\partial t_k^j}{\partial z^j}\Delta z^j + \Delta\tau^j\right) = \Delta r_k^{ij} \tag{2.3.15}$$

where

$$\Delta r_k^{ij} = r_k^i - r_k^j = \left(t^{obs} - t^{cal}\right)_k^i - \left(t^{obs} - t^{cal}\right)_k^j \tag{2.3.16}$$

and is called the "double-difference". It is the residual between the observed and calculated differential travel time between two events *i* and *j*. Equation (2.3.15) links the difference between residual times to the sought perturbations of the hypocentral parameters. The double-difference minimization of Δr_k^{ij} attempts to equalize, but not necessarily to reduce the residual times r_k^i and r_k^j at each station for closely located earthquakes. This is the fundamental difference that distinguishes double-difference locations from standard, single event location.

The double-difference relative location method takes advantage of the fact that if the hypocentral separation between two earthquakes is small compared to the event-station distance and the scale length of velocity heterogeneity, then the ray paths between

the source region and a common station are similar along almost the entire ray path. When the earthquake location problem is linearized using the double-difference equations, the common model errors cancel, principally those related to the receiver-side structure. However, Michelini and Lomax (2004) performed synthetic tests on the method and showed that the double-difference technique does not preclude the need for a good velocity model for the study region. This is because an incorrect velocity model gives erroneous values of partial derivatives in the kernel matrix for the least-squares inversion, and this leads to bias and error in the relative locations. For events with similar waveforms, accurate reading of differential travel times of closely located earthquakes can be achieved by using the waveform correlation technique (Poupinet et al., 1984; Li et al. 1998). Unfortunately, the waveform correlation technique does not perform well in this case, where waveforms are dominated by strong scattering in the carbonates and shales although the general velocity structure in the area is not complicated. Therefore, only P- and S-wave catalog travel-time differences are used.

2.4 Location Results

2.4.1 Seismic velocities and Vp/Vs ratio at the Field

Seismic velocities in the Field are relatively simple due to almost flat layers of sediments and the lack of structures with large velocity contrasts. A layered velocity model was determined from a check-shot survey conducted in the field (Figure 2.4).

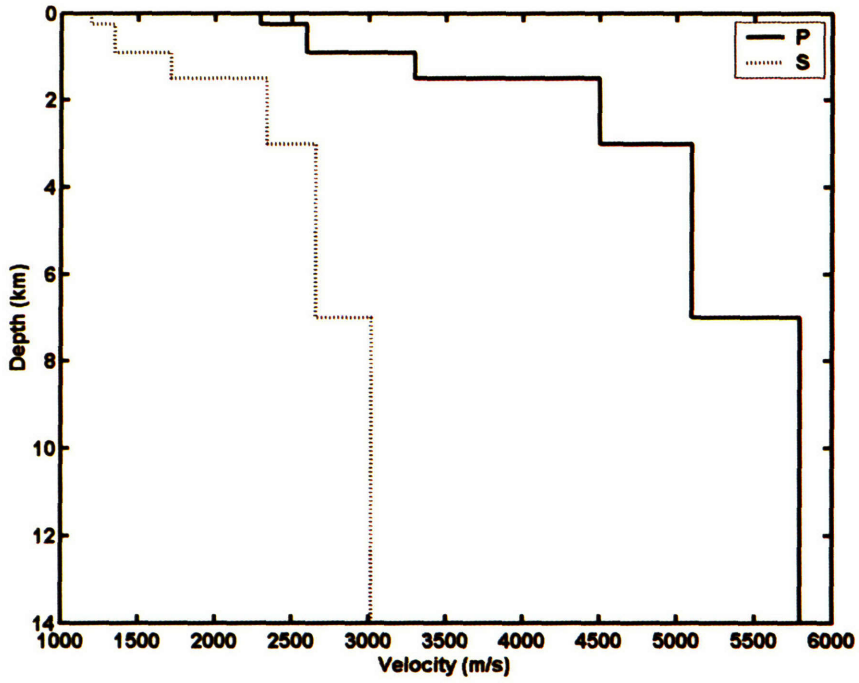

Figure 2.4. The layered velocity model used in this study.

In order to use S-wave arrivals, a Vp/Vs ratio of 1.92 was reported by the PDO (Figure 2.4). To validate this result, I estimate the Vp/Vs ratio using both the Wadati diagram and the method described by Chatelain (1978), since a change in the S-wave velocity can change the estimate of hypocentral depth significantly. Wadati diagrams are made for events of the sequence for which at least four pairs of P and S readings are available. The Wadati diagram plots the difference in time of arrival of S and P waves, (ts – tp), on a seismogram against the time of P-wave arrival time, tp (Figure 2.5). This yields the equation:

$$(t_s - t_p) = \left(\frac{V_p}{V_s} - 1\right)(t_p - t_o). \qquad (2.4.17)$$

The slope of the curve is usually near linear (Vp/Vs – 1) and gives the ratio of apparent P to S velocity ratio. The best-fit value of Vp/Vs ratios obtained with this method is 1.90 with 751 S-P travel-time differences of 405 events, which is close to the Vp/Vs ratio of 1.92 obtained from the check-shot survey.

The method described by Chatelain (1978) allows us to determine a Vp/Vs ratio which is common to the whole set of analyzed events. For each earthquake, the method requires at least one pair of stations with time readings for both P- and S-waves. At two different stations i and j for a given event, the differences between the P- and S-wave arrival times are

$$\begin{aligned} t_{Pj} - t_{Pi} &= \frac{d_j - d_i}{V_P} \\ t_{Sj} - t_{Si} &= \frac{d_j - d_i}{V_S} \end{aligned}, \qquad (2.4.18)$$

respectively, where d_i and d_j are the distances between the earthquake and stations i and j, respectively. Thus,

$$t_{Sj} - t_{Si} = \frac{(t_{Pj} - t_{Pi})V_P}{V_S} . \qquad (2.4.19)$$

For each event, the P- and S-wave arrival time differences are calculated. All the S-wave arrival time differences obtained are plotted on Figure 2.6 as a function of the P-wave

arrival time differences. The slope of the best-fitting line yields the Vp/Vs ratio of 1.91 with 2275 pairs of P- and S-arrival time differences from 405 events, which is also consistent with 1.90 obtained from the Wadati diagram.

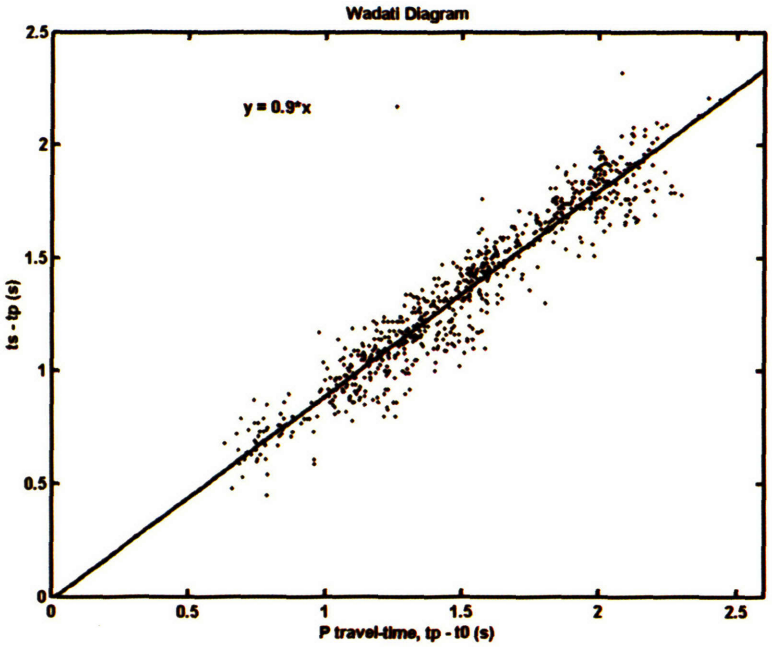

Figure 2.5. Wadati diagram. The difference in time of arrival of S and P waves (ts-tp) on a seismogram is plotted against the time of arrival of P (tp).

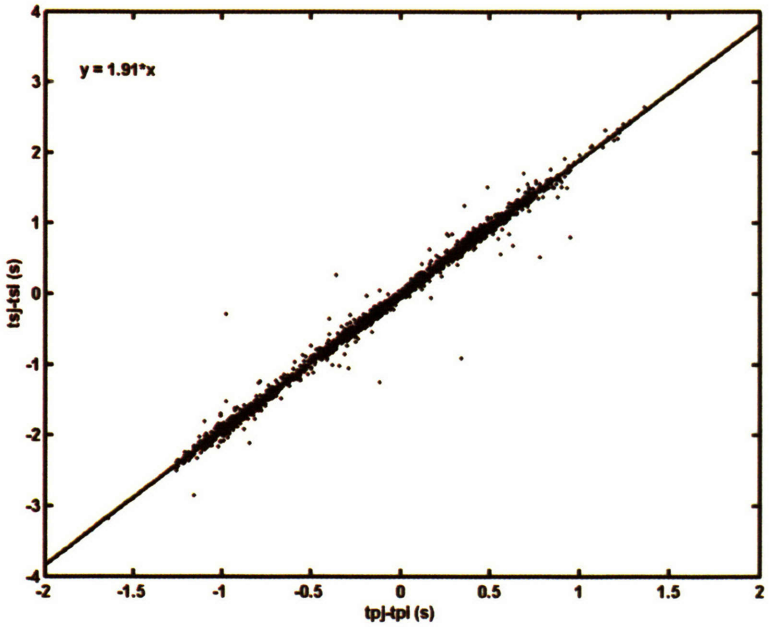

Figure 2.6. Chatelain diagram. S-wave time differences are plotted against the P-wave time differences.

2.4.2 Location Results by Iterative Linearization and Grid-Search Methods

Of the 802 events detected by the network, 405 with at least six arrival time picks are considered for mapping. The locations of the Oman microearthquakes are first determined by the iterative linearization method (Hypoinverse-2000 code) and the grid-search method (NonLinLoc code), using the flat-layered velocity model shown in Figure 2.4. The inversions are performed for all events that fall within a model volume of 12km × 12km × 4km deep. The NonLinLoc algorithm parameterizes the model by constant velocity, cubic cells of 10m × 10m × 10m.

The locations of all the events determined by both methods are summarized in Appendices A and B. The hypocenters obtained with Hypoinverse-2000 and the maximum-likelihood hypocenters of the grid-search method are shown in Figures 2.7 and 2.8, respectively. In general, the grid-search method yields smaller rms misfit error, with an average decrease of 11.5 ms. Average rms misfits for the linearized method and the grid-search method are 30.60 ms and 19.01 ms, respectively. The differences in hypocentral coordinates between the two methods are typically of the same order or smaller than the spatial uncertainty as indicated by the confidence ellipsoids, except for some events with very small confidence ellipsoids. In mapview the relocated seismicity reveals a narrow fault zone along the NE-SW trend. The overall microseismicity in the Field occurs in a 9km long NE-SW zone, no wider than 500 m throughout most of its length. This zone is not continuous throughout its length, nor at all depths within any given section, but includes highly active clusters of events and several seismic gaps. Most of the on-fault seismicity collapses into narrow streaks of epicenters that are oriented in the general direction of the trend of the seismicity. Few earthquakes are located northwest of the fault zone.

I subdivide the seismic zone into five sections and their locations are shown in Figure 2.9. The five sections A-A', B-B', C-C', D-D', E-E' in Figures 2.10 – 2.15 show each section parallel and perpendicular to the seismic zone. Fault-parallel cross-sectional views of the on-fault seismicity indicate that most of the events are located within a depth range of ~0.5 – 3.5 km. Most of the events occur in a shallower zone of a depth range of

0.5 – 1.5km and a deeper zone of 2.0 – 3.5km, with a relatively quite zone between 1.5 – 2.0km. Events of segments A-A', C-C', and D-D' are more scattered in depth, whereas events of segment B-B' are all shallow (< 1.5km). Cross-sectional views perpendicular to the fault show that the general dip of the fault at of A-A', B-B', and C-C' are steeply dipping or near-vertical. Dips of D-D', E-E', and F-F' are difficult to determine visually since there are too few events in each segment.

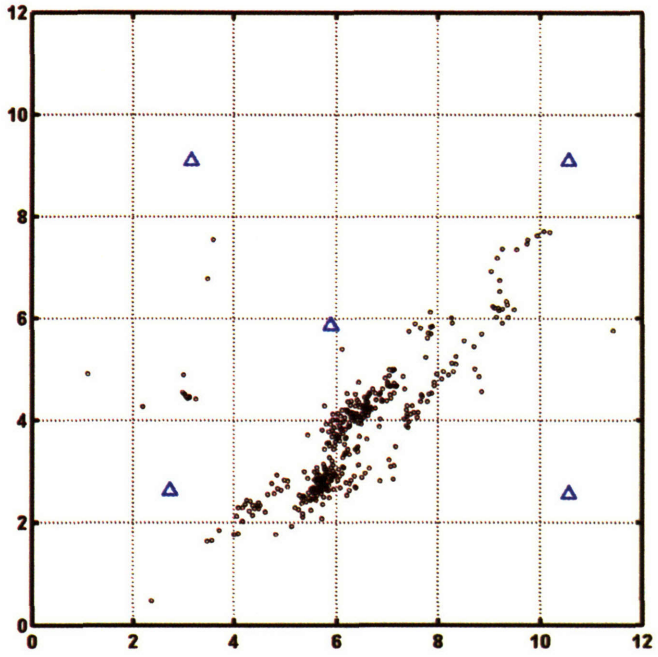

Figure 2.7. Earthquake locations determined by the Hypo-2000 shown in map-view.

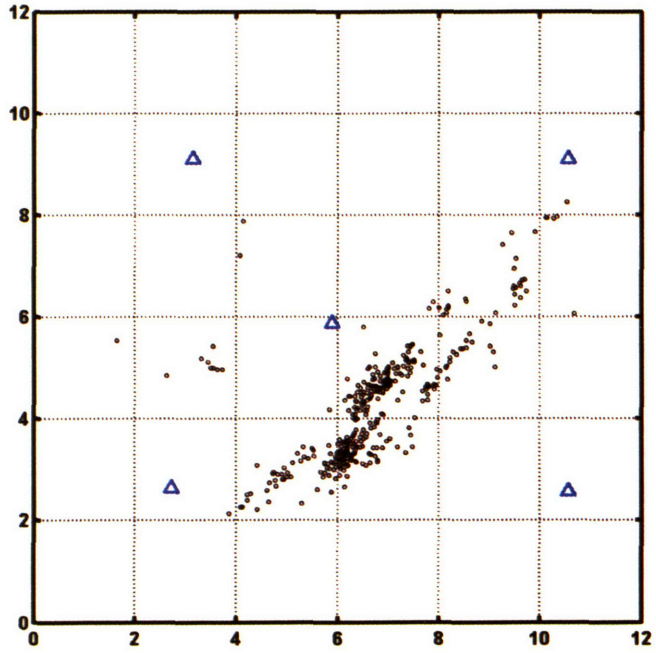

Figure 2.8. Earthquake locations determined by the NonLinLoc Grid-search method.

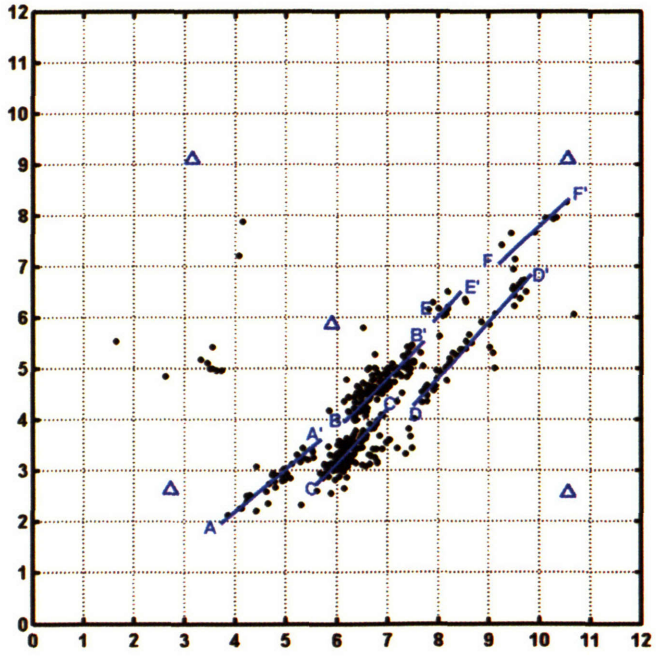

Figure 2.9. Map-view of the five cross-sections.

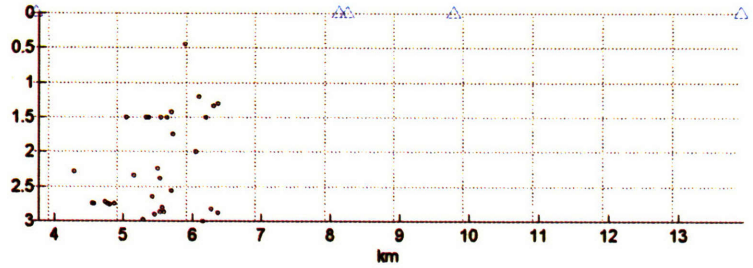

(a)

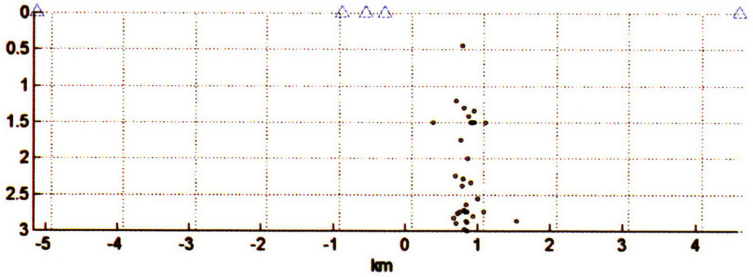

(b)

Figure 2.10. A – A' (a) fault-parallel view, (b) cross-sections perpendicular to the fault.

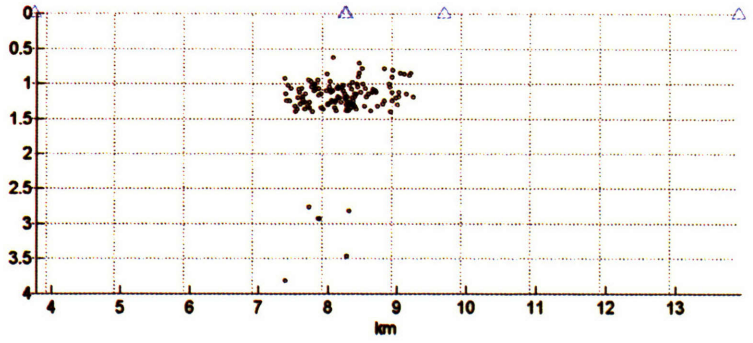

(a)

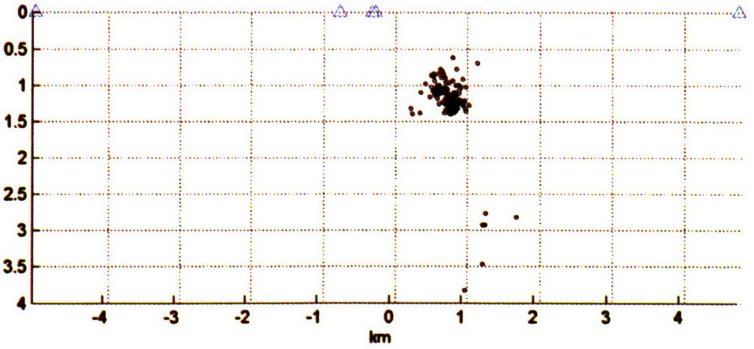

(b)

Figure 2.11. B – B' (a) fault-parallel view, (b) cross-sections perpendicular to the fault.

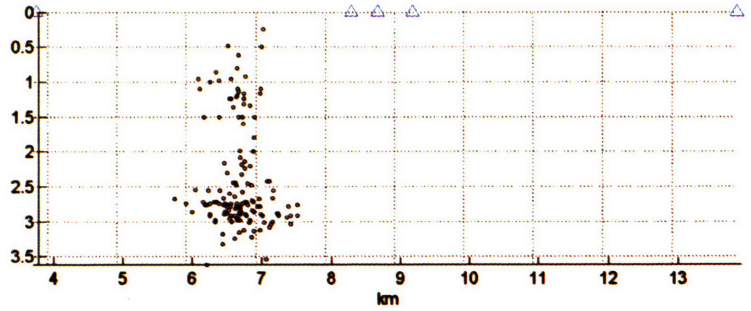

(a)

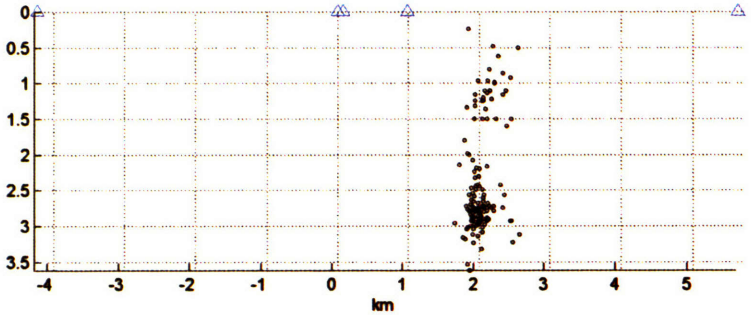

(b)

Figure 2.12. C – C' (a) fault-parallel view, (b) cross-sections perpendicular to the fault.

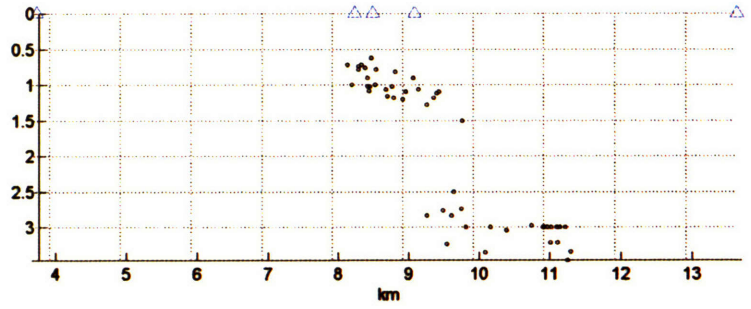

(a)

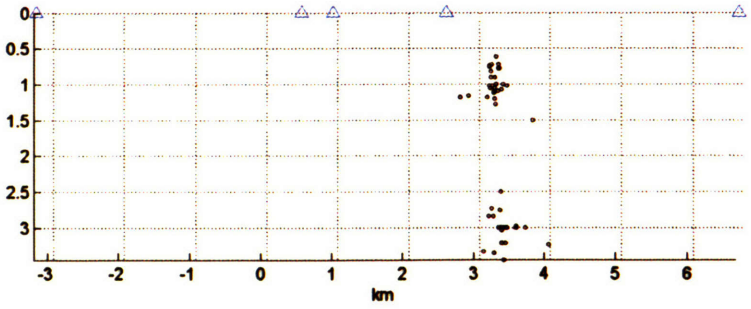

(b)

Figure 2.13. D – D' (a) fault-parallel view, (b) cross-sections perpendicular to the fault.

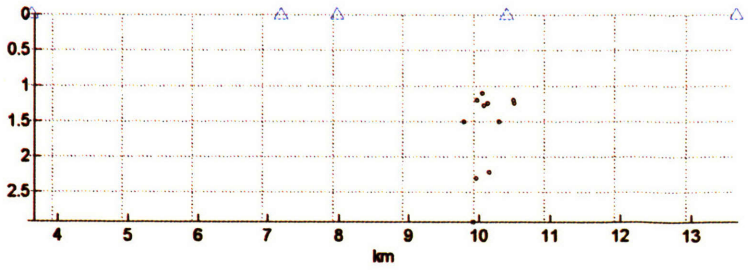

(a)

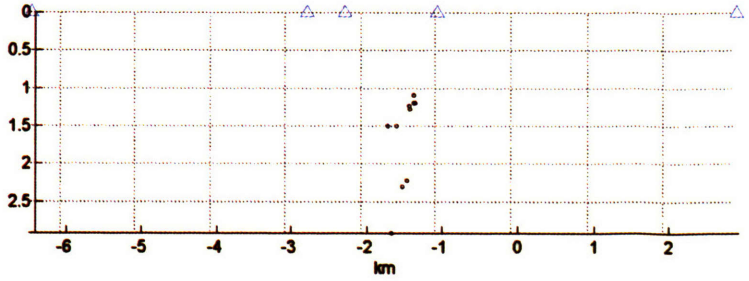

(b)

Figure 2.14. E – E' (a) fault-parallel view, (b) cross-sections perpendicular to the fault.

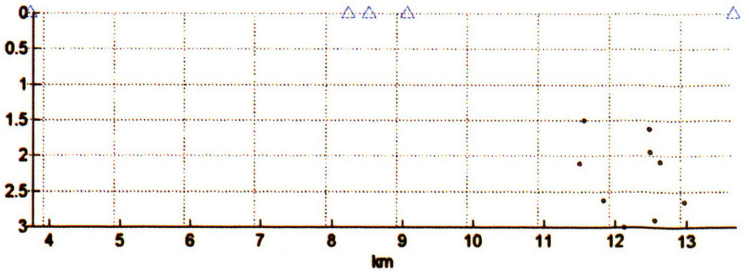

(a)

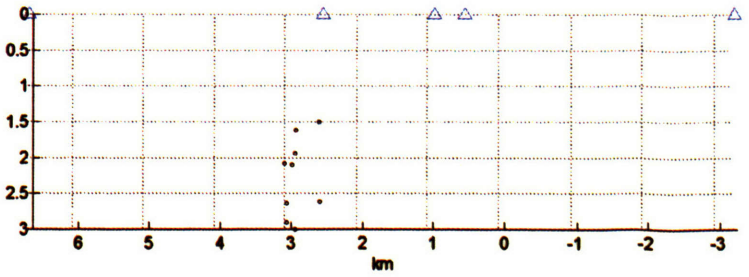

(b)

Figure 2.15. F – F' (a) fault-parallel view, (b) cross-sections perpendicular to the fault.

2.4.3 Location Results by Relative Location Method

The Double-Difference algorithm (Waldhauser and Ellsworth, 2000) is employed to obtain the relative locations for the microearthquakes in the Field. The travel-time differences are selected to build a network of pair-wise connected events in which any event is linked to a maximum of ten neighboring events by at least eight pair-wise observations, so that all events are simultaneously relocated relative to each other. Only catalog travel-time differences are used. Cross-correlation travel-time differences are not used because there are not enough records with identical waveforms. This is possibly due to heavy scattering in the Field, even though many events are separated by less than a few hundred meters. Event pairs with hypocentral separation less than 0.5 km are considered, in order to keep the effect of ray path differences outside the source region small. There are 2,080 linked event pairs with 9,232 P-phase pairs and 6,381 S-phase pairs. The average offset between linked events is about 0.23 km. Equal weights are used for P and S-wave data. Residuals are reweighed after each iteration according to the misfit and the distance between events. Closely spaced events get the highest weights and then weights drop exponentially with increasing separation distance. Residuals larger than six times the standard deviation from the mean of each data type are considered outliers and discarded. Since events get deleted during relocation when they lose linkage to neighboring events due to outlier removal, only 362 out of 405 events are eventually located by the method. The locations are summarized in Appendix C.

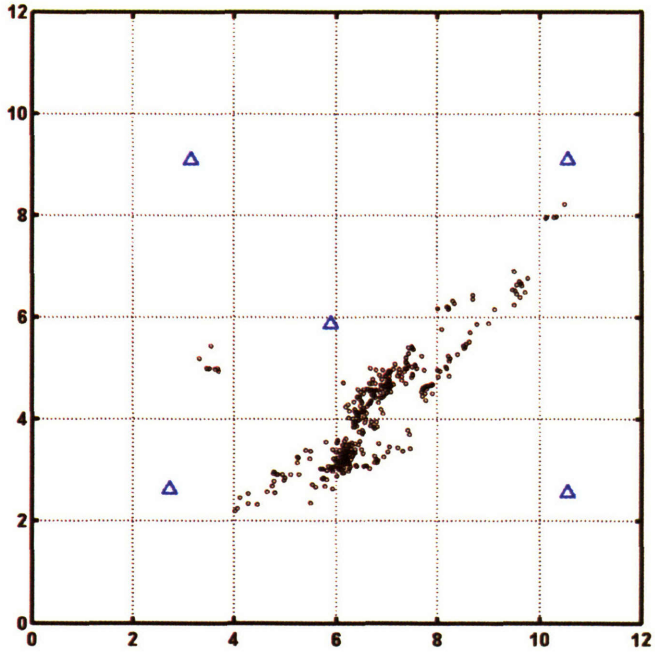

Figure 2.16. Earthquake locations determined by the Double-Difference relative method.

Comparing the double-difference results shown in Figure 2.16 to the locations estimated by grid-search method (Figure 2.8), the differences are small. Double-difference does not collapse the hypocenters further into narrower streaks or clusters in mapview (Figure 2.8) or fault-parallel and cross-sectional views (shown in Figures 2.17 to 2.20). The average rms misfit is 22.43 ms, which is surprisingly larger than the misfit obtained by the grid-search method. There are two possible reasons that the relative location method does not perform better than the grid-search method in this case. First, in spite of the strong scattering effects, the simplicity of the velocity structure in the Field is well-known from 3-D reflection seismic surveys and the check-shot survey. Therefore, the minimization of common model travel time errors related to the receiver-side structure can be quite small and may not be significant (note: this can also be

compensated by the station corrections done by the grid-search method). Secondly, the unavailability of cross-correlation travel-time differentials hampers further improvements by double-difference's use of data with higher measurement accuracy.

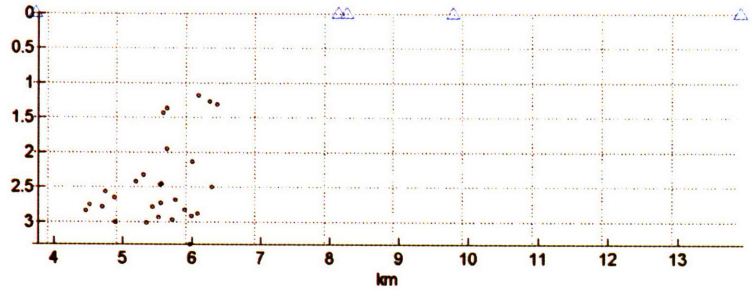

(a)

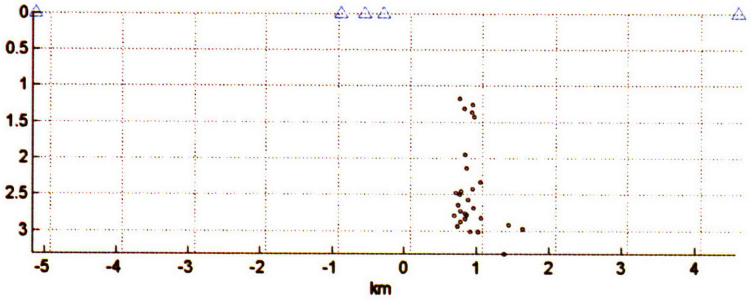

(b)

Figure 2.17. A – A' (a) fault-parallel view, (b) cross-sections perpendicular to the fault.

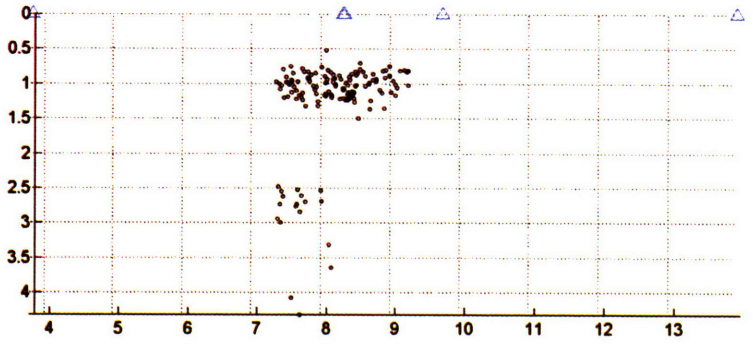

(a)

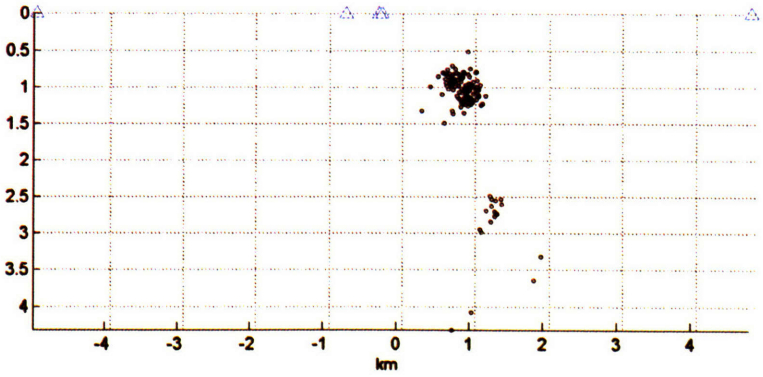

(b)

Figure 2.18. B – B' (a) fault-parallel view, (b) cross-sections perpendicular to the fault.

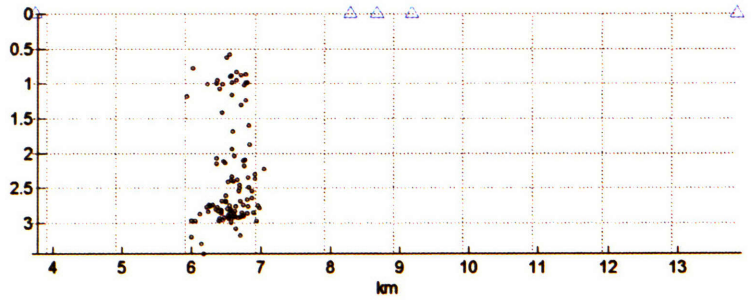

(a)

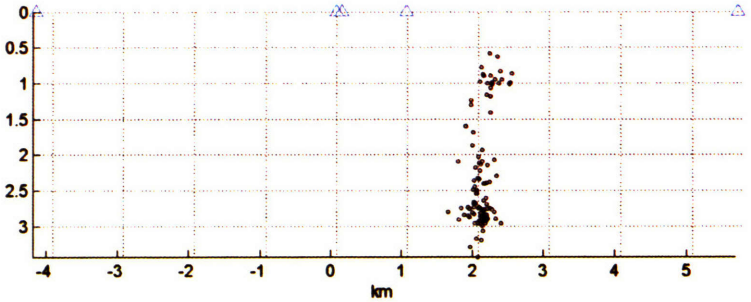

(b)

Figure 2.19. C – C' (a) fault-parallel view, (b) cross-sections perpendicular to the fault.

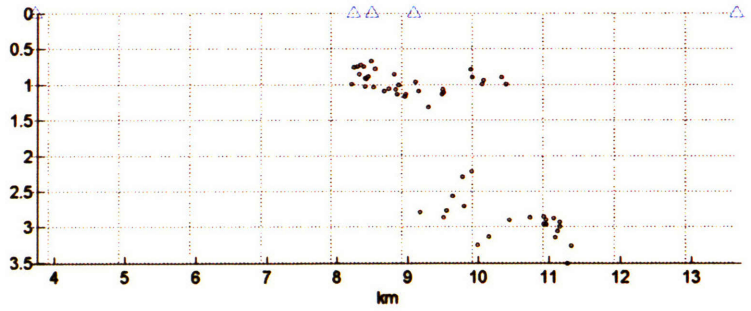

(a)

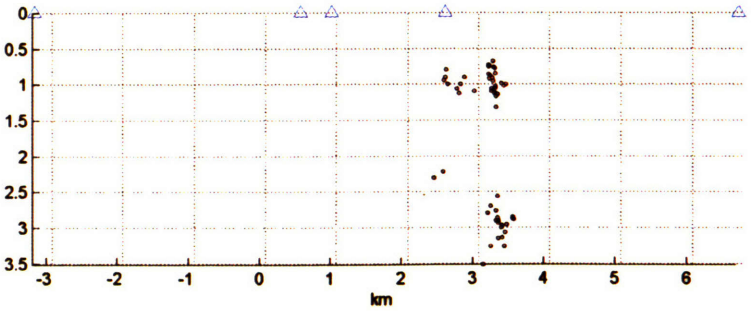

(b)

Figure 2.20. D – D' (a) fault-parallel view, (b) cross-sections perpendicular to the fault.

2.5 Location Error Estimation

The accuracy of hypocenter locations is controlled by several factors. Important sources of error affecting the location inversion results include (Pavlis, 1986; Gomberg et al., 1990):

1. inconsistency of the arrival time estimates due to human error, onset times obscured by other phase arrivals and scattered energy.
2. biases in arrival times introduced by inconsistencies in data acquisition (e.g. clock errors).
3. inadequate traveltime predictions due to poor choice of velocity model. All location schemes for seismic events depend on having a suitable model of propagation characteristics of the seismic phases which are observed. In particular, information on the depth and origin time of the seismic event cannot be extracted without invoking a model of the earth.
4. incorrect *a priori* information, such as incorrect hypocentral depth constraints
5. poor seismic array distribution with respect to the event being observed. The horizontal coordinates of the hypocenter (e.g., latitude and longitude) will be most accurate when there is good azimuthal distribution of recording stations around the source.

Error ellipsoids determined by absolute location methods (iterative linearized and grid-search methods) cannot be compared directly with those determined by relative location method because the error estimation of the double-difference method does not

take the error of the master events into account, assuming that they are accurately located. It has to be noted that the estimators $\hat{\mathbf{m}}$ are only asymptotically efficient (Hartley, 1961) and the error estimates are exact only as the number of stations becomes infinite. This can be a problem when the station distribution is sparse and limited in azimuth, as in this case. To test the robustness of the relocation results and error estimates of the relative locations due to variations in station distribution, I apply the jackknife method (Efron, 1982) to estimate the standard error in each coordinate direction. I resample the data set by deleting one station and perform the relocation at one time, and repeat this process. The standard deviation errors of each event in each coordinate direction were calculated. I obtain standard errors of 485.9m, 461.5m, and 954.2m in the east, north, and vertical direction, respectively for the Hypoinverse-2000. For the nonlinear grid-search method (NonLinLoc), I obtain 497.2m, 441.0m, and 821.2m. For the double-difference method, I obtain standard errors of 249.0m, 337.0 m, and 853.8 m in the east, north and vertical direction, respectively. This shows that the errors due to station geometry are relatively important because of the small number of stations available and non-optimal station distribution. The standard errors of double-difference method are relative location errors and cannot directly compared with those of the hypoinverse-2000 method. I apply the jackknife method to estimate the influence of one event on the locations of others. This is important when there is a bad event due to mispick or misidentification. I relocate the resampled data set with one event deleted each time and repeat this process. In general, the effect on the relative locations is negligible.

2.6 Quantitative Interpretation of the Oman Microearthquakes

Microearthquake locations have been interpreted by visual inspection in section 2.4. However, locations are subject to uncertainties as discussed in section 2.5, and are not the same for every individual earthquake. In this section, with the aid of analytical techniques, I process the location results to improve and quantify the geologic interpretation.

3.6.1 Collapsing Method for Identifying Significant Structures

A common problem in seismology is to relate a diffusive cloud of earthquake locations to geological and tectonic structures. This is usually done by visual inspection of earthquake location maps, as has been done in the previous sections. Analytical methods, however, can help identify structures within "clouds" of earthquakes, such as the principal components method (Michelini & Bolt, 1986) which identifies seismic clusters in space and time, the three-point method (Fehler et al., 1987) which determines statistically significant fracture/fault planes, and the collapsing method (Jones & Stewart, 1997) which simplifies structures by moving earthquake locations within their respective confidence ellipsoids.

In this study, I follow a similar approach to that introduced by Jones & Stewart (1997). In general, earthquake locations are subject to uncertainties and therefore,

interpretation of locations should take account of the estimates of the location uncertainties. Assuming that all errors are normally distributed, each hypocenter determined by a location algorithm, such as the grid-search method in section 2.3.2, have a spatial uncertainty ellipsoid, which is a three-dimensional probability density function. For a cloud of earthquakes, if the location uncertainties are large relative to the separation of the locations (i.e., the uncertainty ellipsoids overlap to a large degree), then the earthquake cloud can be completely collapsible to a point. This can be the simplest structural interpretation of the cloud, since the arrival time data alone cannot disprove the null hypothesis that randomly normal errors are all that is required to explain the earthquake cloud (Jones & Stewart, 1997).

Therefore, based on the reasoning above, we can assume that the actual clustering of earthquake hypocenters is obscured by the uncorrelated, random scatter of individual hypocenters determined by location algorithms. The collapsing method consists of two loops, and requires information about 3-D uncertainty ellipsoids for all earthquakes. The inner loop repeats analysis on all earthquakes and the outer loop updates the next generation of collapsed hypocenters.

In summary the inner loop consists of three steps and is repeated for each object earthquake:

a. Find all earthquakes whose locations lie within the volume of the uncertainty ellipsoid of the object earthquake;

b. All earthquake locations are given equal weighting, including the object earthquake. Calculate the center of mass of the events;

c. Move the object earthquake toward the center of mass by a fraction (0.6 in this study) of the distance between the earthquake and the center of mass. The location of the uncertainty ellipsoid remains unchanged for all iterations.

The outer loop consists of two steps:

1. Update the new locations calculated in the inner loop to create the next generation of hypocenters;
2. Calculate the distance from the original to the new locations.

The outer loop is repeated until the sum of the moving distances for all earthquakes becomes small. The only variable in the collapsing method is the level of confidence used to truncate the uncertainty ellipsoid. I used the 99.86% confidence level, or four standard deviations, in this study.

For the application of the collapsing method, I used the Oman earthquakes that are relocated by the grid-search method (Section 2.4.2). The analysis of the Oman data proceeded for 38 iterations until the hypocentral movements become negligible. The resulting locations are shown in mapview in Figure 2.21(b). The event locations are classified by depth: the red dots show events with focal depths greater than 1.5 km, and the blue dots show events with focal depths smaller than 1.5 km. The fault-parallel and cross-sectional views in Figures 2.22 to 2.27. The black lines are the faults interpreted from reflection seismic and surface geologic data. Compared to the original locations in

Figure 2.21(a), the collapsed locations line up well with known faults determined by reflection seismic data. The collapsing method also works well on the more problematic fault-parallel and cross-sectional views and has sharpened up the microseismicity. We can now clearly see that the active fault zones A–A' and C–C' are almost vertically dipping and extends from 0.5 to 3km, and fault zone B–B' has only shallow event and dips 65° towards the southeast. Figure 2.28(a) and (b) show the cross-sectional view of event locations projected onto a plane perpendicular to the general strike of the fault zone. We can see that the faults delineated by the microearthquakes agree well both in dipping angles and directions with the known faults inferred by reflection seismics (solid black lines). Therefore, it is likely that reactivation of the central graben fault system near the crest of the field generate the observed microseismicity.

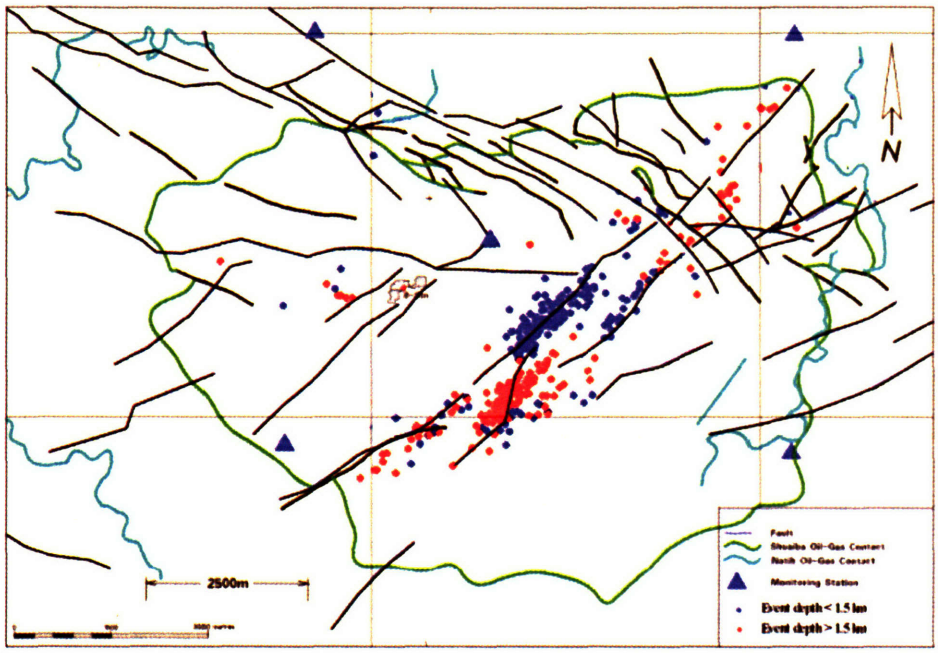

(a)

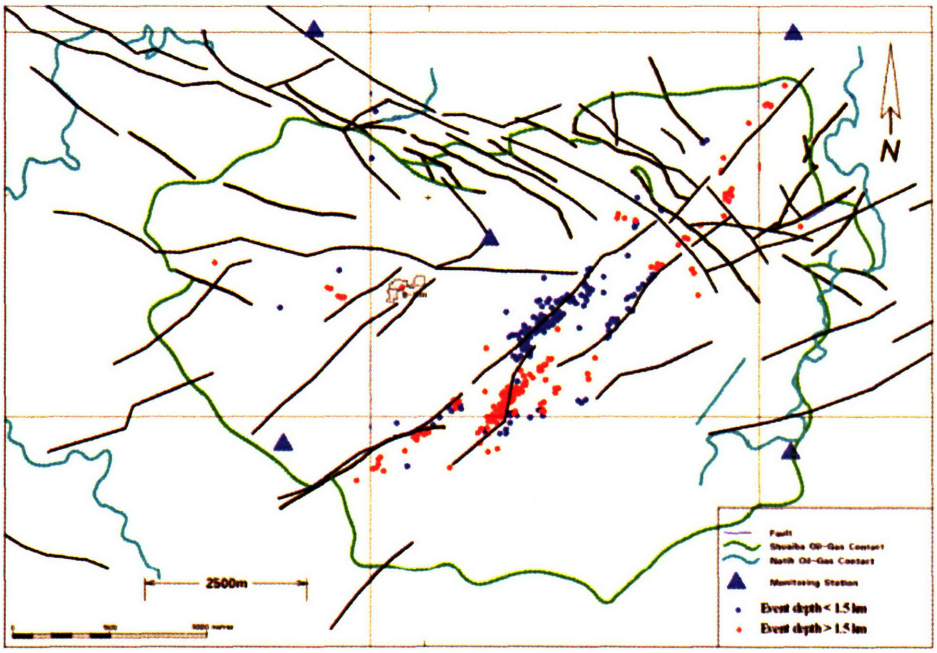

(b)

Figure 2.21. (a) Oman microearthquake locations determined by nonlinear grid-search method. (b) Oman microearthquake locations after application of the collapsing method.

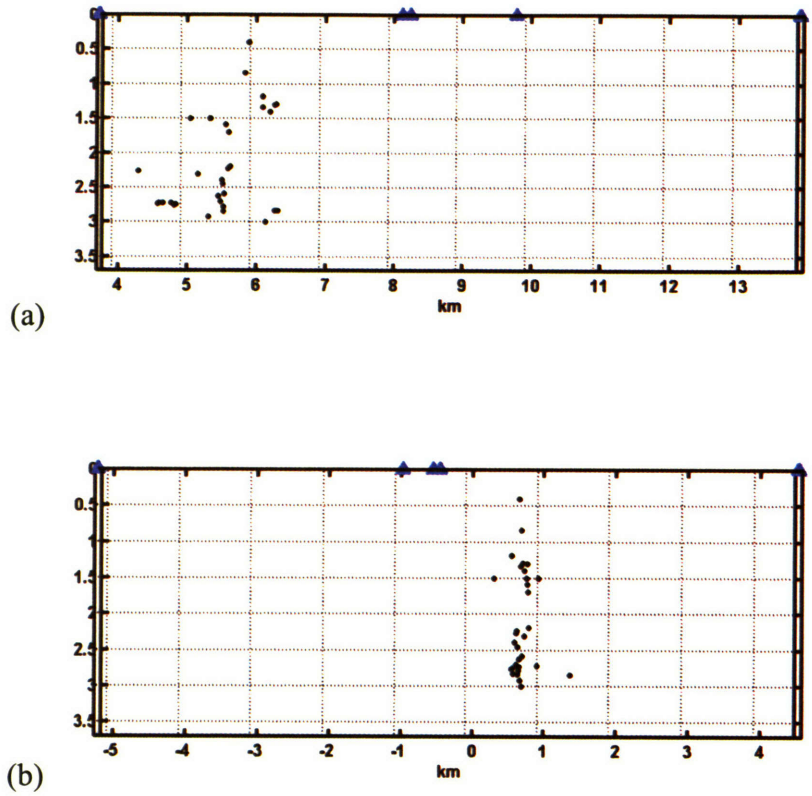

Figure 2.22. Collapsing earthquake locations determined by grid-search method: A – A' (a) fault-parallel view, (b) cross-sections perpendicular to the fault.

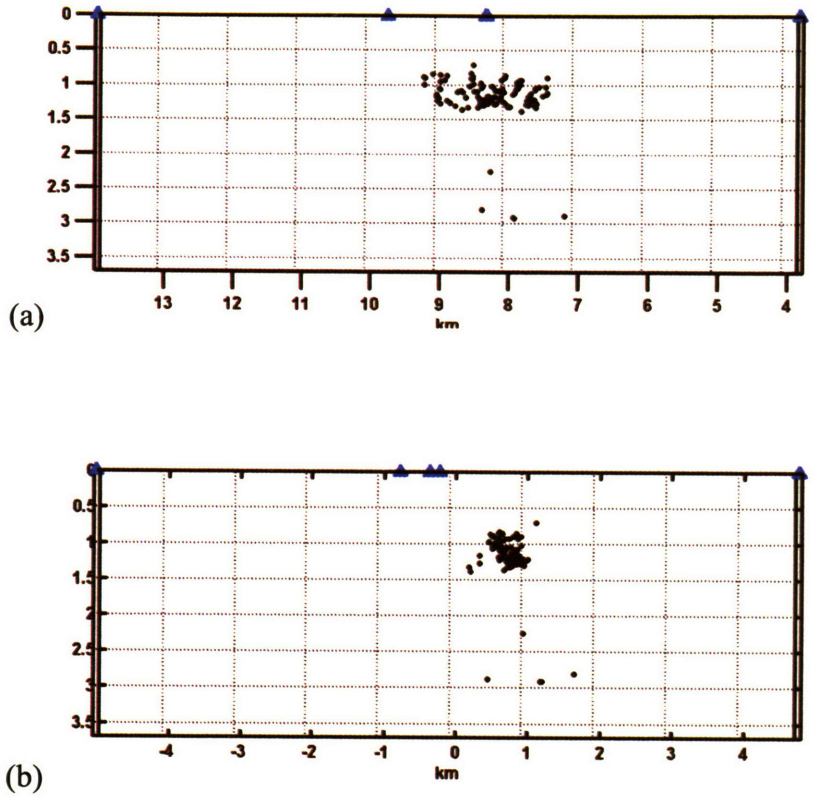

Figure 2.23. Collapsing earthquake locations determined by grid-search method: B – B'

(a) fault-parallel view, (b) cross-sections perpendicular to the fault.

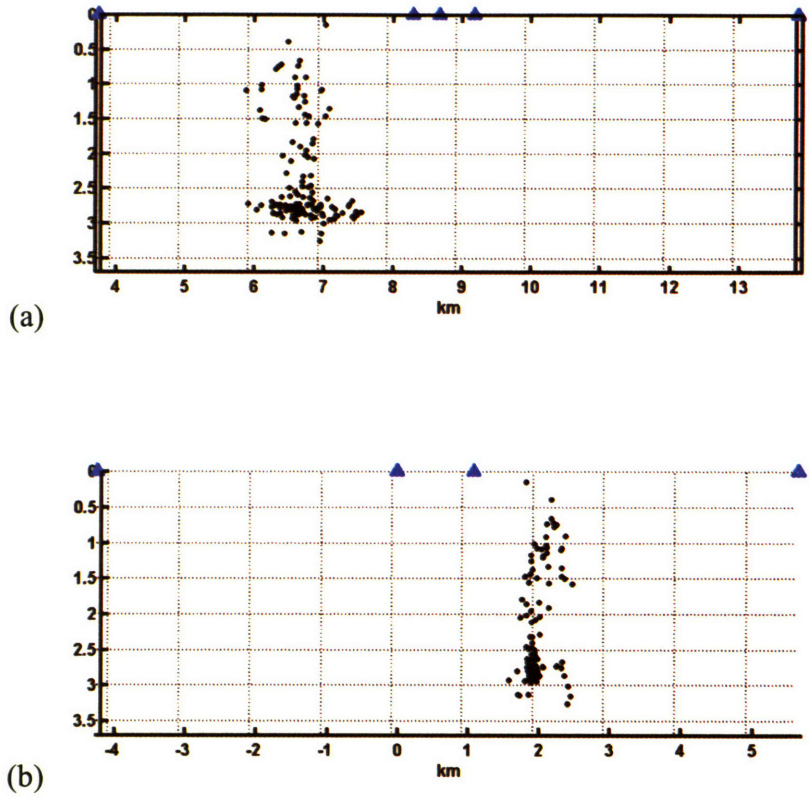

Figure 2.24. Collapsing earthquake locations determined by grid-search method: C – C'

(a) fault-parallel view, (b) cross-sections perpendicular to the fault.

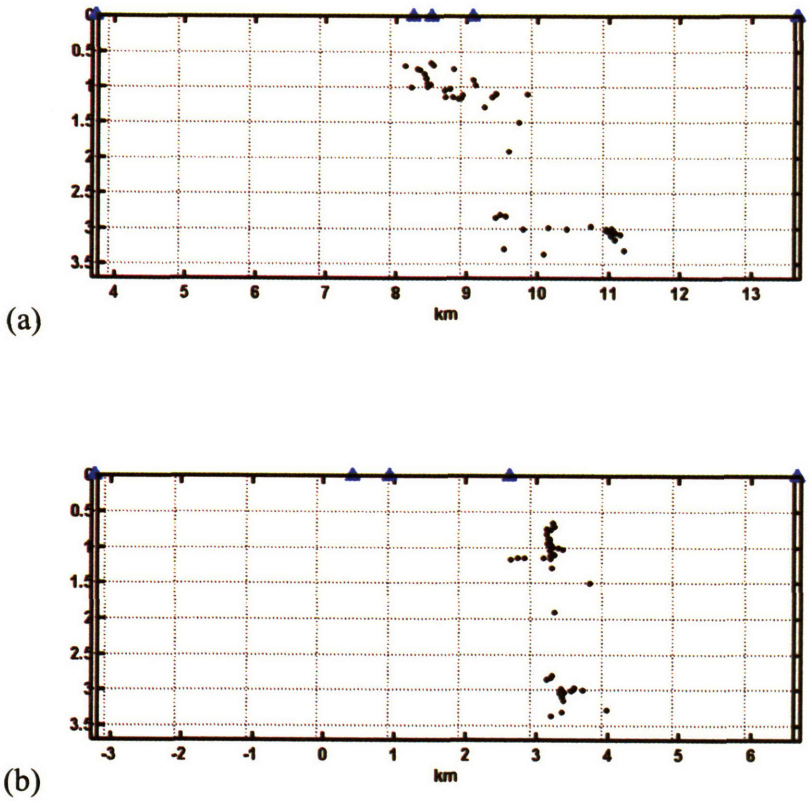

Figure 2.25. Collapsing earthquake locations determined by grid-search method: D – D'

(a) fault-parallel view, (b) cross-sections perpendicular to the fault.

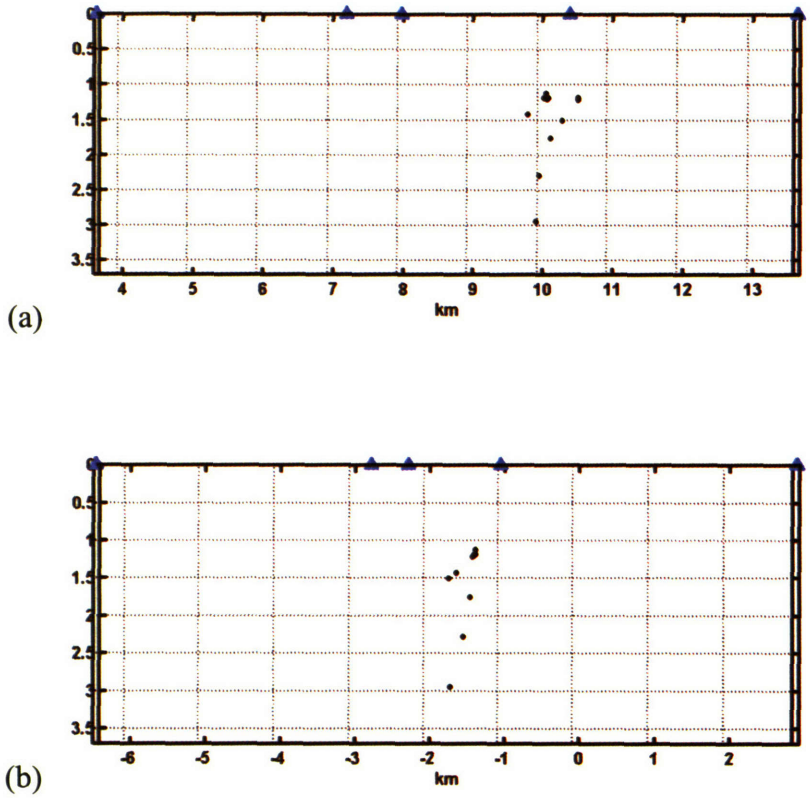

Figure 2.26. Collapsing earthquake locations determined by grid-search method: E – E' (a) fault-parallel view, (b) cross-sections perpendicular to the fault.

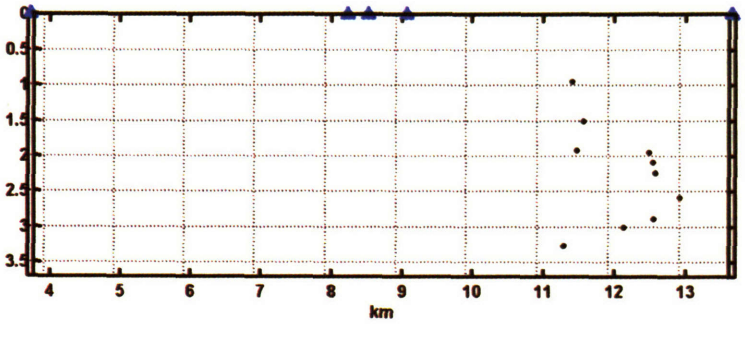

(a)

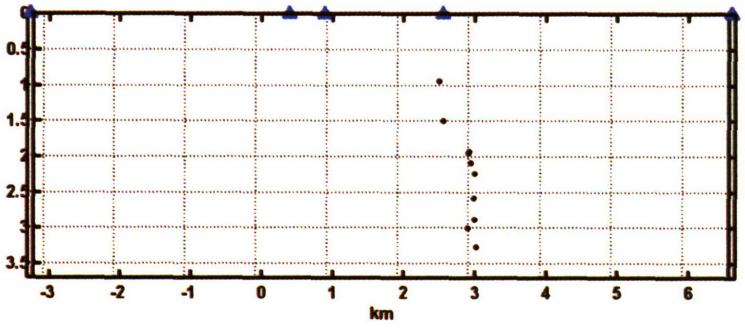

(b)

Figure 2.27. Collapsing earthquake locations determined by grid-search method: F – F'

(a) fault-parallel view, (b) cross-sections perpendicular to the fault.

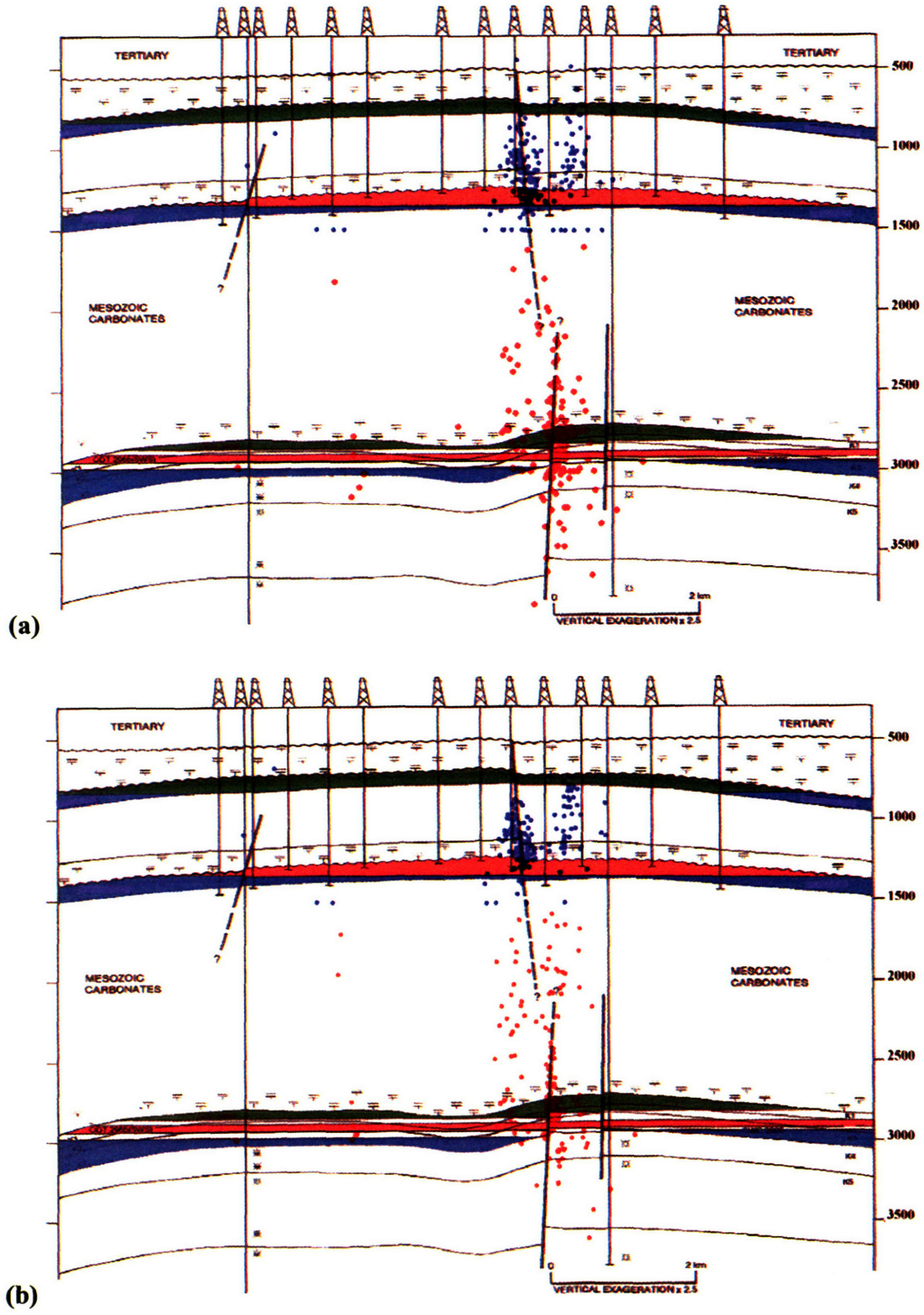

Figure 2.28. Cross-sectional view of Oman microearthquake locations projected onto a plane (320°) perpendicular to the gross strike of the fault system. (a) Locations

determined by nonlinear grid-search method, and (b) locations after application of the collapsing method. The geologic interpretation is adopted from van Driel et al. (2000).

2.6.2 Planarity Analysis

In order to assess quantitatively whether the microearthquakes delineate a fault plane or just distribute randomly, I attempt to fit a plane to each set of microearthquake clusters using least-squares. This procedure involves calculating a least-squares fit to the normal N to a plane through a set of hypocenter with coordinates (x, y, z) in the form

$$N_1 x + N_2 y + N_3 z = D \tag{2.4.20}$$

Normally, N is normalized so that $D = 1$ unless it is close to zero, i.e., a plane goes near the coordinate system origin. The measure of planarity can be quantified by the fitting errors or by the polarization analysis (Xu et al., 2004) performed on the microearthquake locations. Motivated by the theory of polarization filters, this technique was originally applied to measure rectilinearity on seismograms by Shimshoni & Smith (1964) and subsequently to shear-wave splitting (Silver & Chan, 1991). Here, the general idea of polarization analysis is to analyze the covariance matrix constructed from the event locations (x, y, z) in 3-D space, which is defined as

$$COV = \begin{bmatrix} xx & xy & xz \\ yx & yy & yz \\ zx & zy & zz \end{bmatrix}. \tag{2.4.21}$$

The covariance matrix has two non-zero eigenvalues if the event locations lie in one plane, and the eigenvector corresponding to the minimum eigenvalue gives the normal direction of the optimal fault plane. Thus, the degree of planarity, P_p, can be defined as

$$P_p = 1 - \left(\frac{2\lambda_3}{\lambda_1 + \lambda_2} \right)^n, \qquad (2.4.22)$$

where $\lambda_1 \geq \lambda_2 \geq \lambda_3$ and are the eigenvalues of the covariance matrix *COV*, and $0 < n < 1$. I use $n = 0.75$ for this study. The planarity is equal to 1 when the earthquake locations lie perfectly on a plane. On the other hand, the planarity is equal to zero when earthquakes are distributed volumetrically in space. Figure 2.29 to 2.34 show the results of polarization analysis on the five segments of the fault zone, A-A', B-B', C-C', D-D', E-E'. Tables 2.3 and 2.4 summarize the results and presents the dip, strike, and degree of planarity of the five optimal fault planes estimated from the nonlinear grid-search locations before and after applying the collapsing method, respectively. Microearthquakes on all five segments exhibit high degree of planarity (> 0.89), with NE-SW strike directions (~28° – 54°NE) and are consistent with the general trend of the general fault zone. The dips of the fault planes are all steep with angles larger than 75°. The results confirm our hypothesis that the microearthquakes in Oman are mainly associated with faults in or near the reservoir.

Section	# of Events	Dip	Strike	Planarity
A - A'	29	88.2°NW	37.4°	0.95
B - B'	119	75.0°SE	39.4°	0.89
C - C'	123	85.4°NW	41.6°	0.94
D - D'	28	83.0°SE	54.0°	0.96
E - E'	9	82.7°NW	28.4°	0.98
F - F'	9	88.1°SE	36.8°	0.93

Table 2.3. Summary of analysis of planarity on five different sections on the fault zone based on the nonlinear grid-search locations.

Section	# of Events	Dip	Strike	Planarity	Norm of residual errors
A - A'	29	89.0°NW	37.5°	0.98	0.96
B - B'	119	74.3°SE	41.7°	0.90	1.81
C - C'	123	84.9°NW	39.5°	0.96	1.93
D - D'	28	78.7°SE	58.5°	0.98	1.54
E - E'	9	79.9°NW	39.3°	0.98	0.29
F - F'	9	85.0°SE	43.1°	0.94	0.26

Table 2.4. Summary of analysis of planarity on five different sections on the fault zone based on the "collapsed" nonlinear grid-search locations.

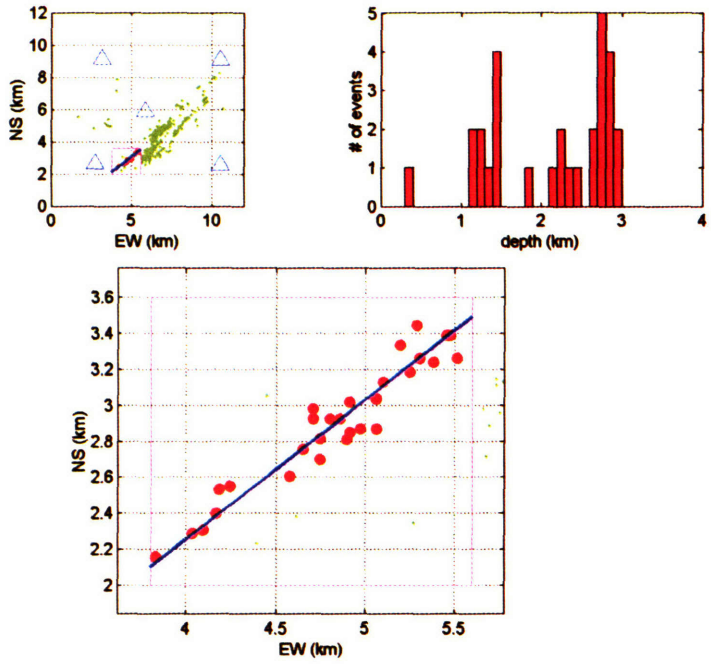

Figure 2.29. Results of polarization analysis on segment A – A'. The blue line shows the strike of the optimal fault plane determined by the selected earthquakes (red dots).

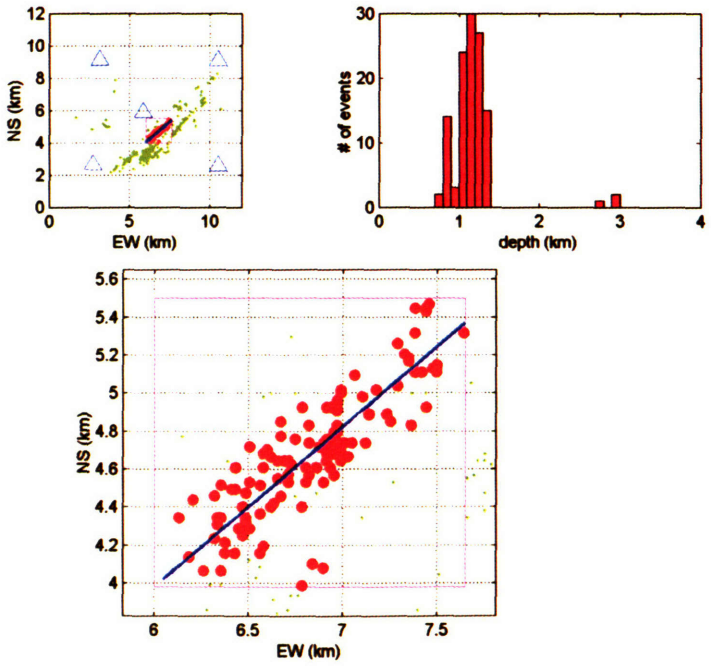

Figure 2.30. Results of polarization analysis on segment B – B'.

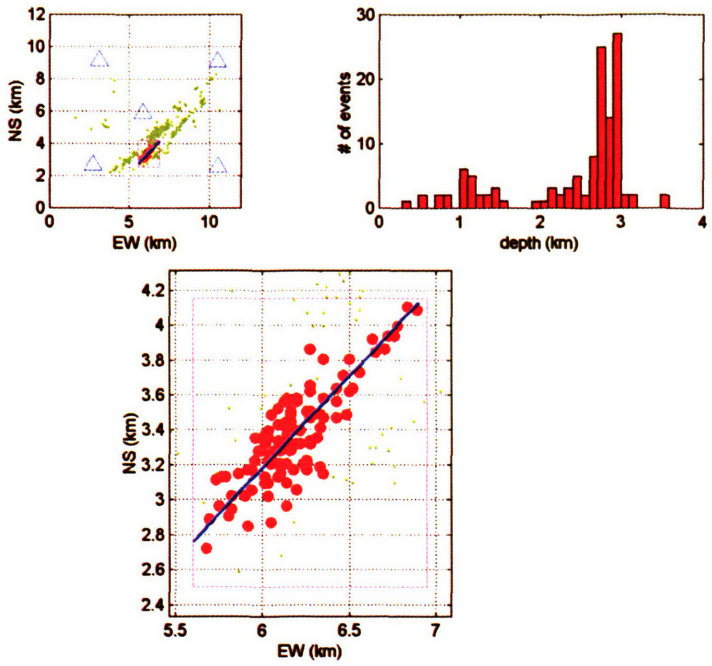

Figure 2.31. Results of polarization analysis on segment C – C'.

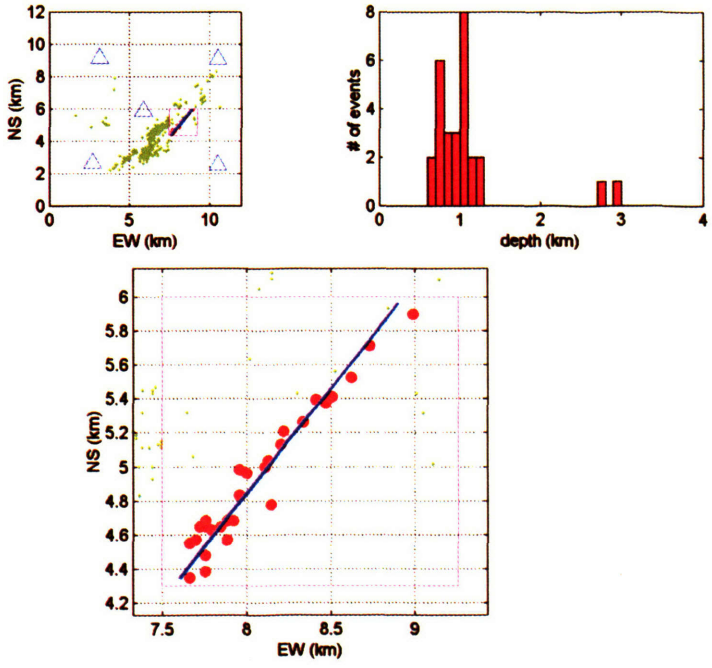

Figure 2.32. Results of polarization analysis on segment D – D'.

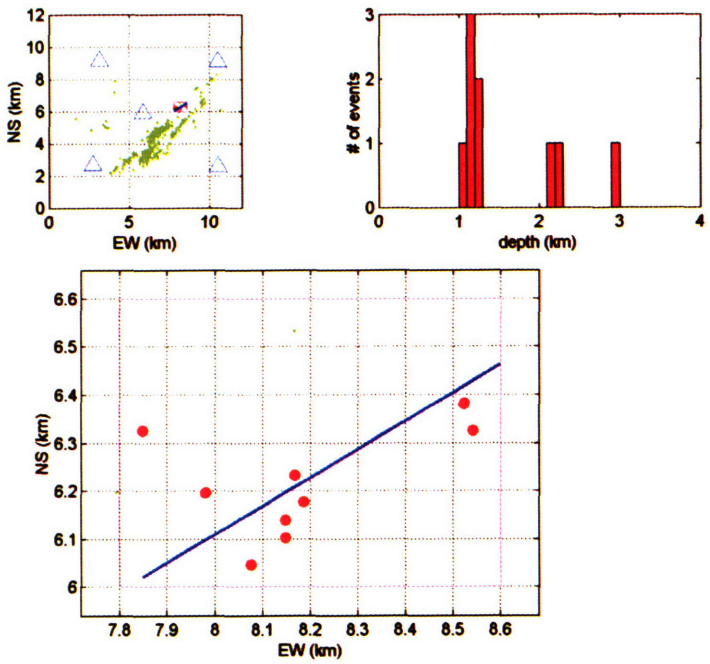

Figure 2.33. Results of polarization analysis on segment E – E'.

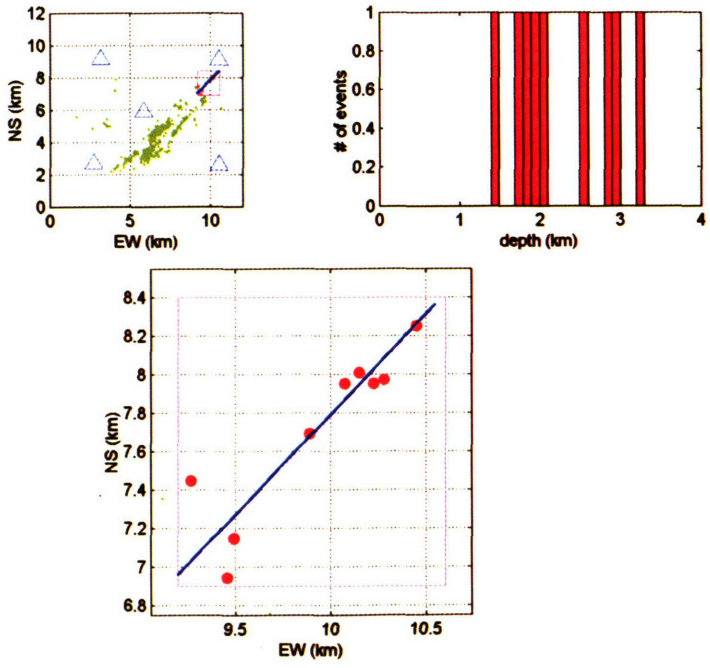

Figure 2.34. Results of polarization analysis on segment F – F'.

2.7 Conclusions

The distribution of microearthquakes provides information about the location and characterization of the fracture and fault systems of the petroleum reservoir. I repicked P- and S-wave arrival times carefully, and employed the conventional linearized method, grid-search method, and relative location method, to estimate the hypocenters of microearthquakes induced by oil and gas production in the Field, Oman. I applied the techniques on a waveform dataset with a selection of 405 high-quality events collected in a 20-month span from October 29, 1999 to June 18, 2001 by a seismic network that consisted of five shallow downhole stations. The relocated seismicity clearly delineates a complex fault zone comprised of several narrow, near-vertical faults which are subparallel to the major lineament of a gross NE-SW striking trend. The two distinct groups of event depths, the shallow (inside the reservoir) and deep (below reservoir) groups, may imply that the vertical extents of faults vary spatially, or there are spatial variations of production or injection in the Field that induce the microearthquakes. Comparing the three different location methods, the grid-search method yields the best results with the lowest rms data residuals. The conventional linearization method gives the largest rms residuals, which suggests some local minima exist in the solution space. The Oman case cannot take full advantages of the relative location method because the number of earthquakes with similar waveforms is limited. Only catalog travel-time differences can be used for the algorithm. However, the location differences between the three algorithms should not be over-interpreted because they may be caused by differences in equation weighting (Wolfe, 2002). The work presented in this chapter is

the first step toward understanding the faulting process in Oman and forms the foundation of the further detailed analyses in the subsequent chapters.

2.8 References

Blaskovich, F.T., Thurber, S.S., Echois, D.P., Al-Hinai, K.B.M., 1985, Reservoir Management of the Yibal Field in North Oman: A Simulation Approach: Middle East Oil Technical Conference and Exhibition, 11-14 March, Bahrain.

Eaton, J.P., 1969, HYPOLAYR, A computer program for determining hypocenters of local earthquakes in an earth consisting of uniform flat layers over a half space: U.S.G.S. Open-File Report.

Fehler, M., House, L., and Kaieda, H., 1987, Determining planes along which earthquakes occur: Method and application to earthquakes accompanying hydraulic fracturing: J. Geophys. Res., **92**, 9407 – 9414.

Fehler, M., 1990, Identifying the plane of slip for a fault plane solution from clustering of locations of nearby earthquakes: Geophys. Res. Lett., **17**, 969 – 972.

Geiger, L., 1912, Probability method for the determination of earthquake epicenters from the arrival time only (translated from Geiger's 1910 German article): Bull. of St. Louis University, **8**, 56-71.

Gaucher, E., Cornet, F.H., and Bernard, P., 1998, Induced seismicity analysis for structure identification and stress field determination: SPE Paper 47324, Soc. Petro. Eng./Int. Soc. Rock Mech., Proc. Eurock 98, Trondheim, Norway.

Gomberg, J.S., Shedlock, K.M., and Roecker, S.W., 1990, The effect of S-wave arrival times on the accuracy of hypocenter estimation: Bull. Seismol. Soc. Am., **80**, 1605-1628.

Got, J.L., Frechert, J., and Klein, F.W., 1994, Deep fault plane geometry inferred from multiplet relative relocation beneath the south flank of Kilauea: J. Geophys. Res., **99**, 15375 – 15386.

Jepsen, D.C. and Kennett, B.L.N., 1990, Three-component analysis of regional seismograms: Bull. Seismol. Soc. Am., **80**, 2032 – 2052.

Jones, R.H. and Stewart, R.C., 1997, A method for determining significant structures in a cloud of earthquakes: J. Geophys. Res., **102**, 8245 – 8254.

Jurkevics, A., 1988, Polarization analysis of three-component array data: Bull. Seismol. Soc. Am., **78**, 1725 – 1743.

Kagan, Y.Y., 1982, Stochastic model of earthquake fault geometry: Geophys. J. R. Astron. Soc., **71**, 659-691.

Klein, F.W., 2000, User's guide to Hypoinverse-2000, a Fortran program to solve for earthquake locations and magnitudes: U.S.G.S. Open File Report 02-171.

Lahr, J.C., 1980, Hypoellipse/Multics, a computer program for determining local earthquake hypocentral parameters, magnitude, and first motion pattern: U.S.G.S. Open-File Report, OF 80-59.

Lee, W.H.K. and Lahr, J.C., 1972, HYPO71, A computer program for determining hypocenter, magnitude, and first motion pattern of local earthquakes: U.S.G.S. Open-File Report.

Li, Y., Cheng, C.H., and Toksoz, M.N., 1998, Seismic monitoring of the growth of a hydraulic fracture zone at Fenton Hill, New Mexico: Geophysics, **63**, 120 – 131.

Litsey, L.R., MacBride Jr., W.L., Al-Hinai, K.M., and Dismukes, N.B., 1986, Shuaiba reservoir geological study, Yibal field, Oman: J. Petroleum Geology, **38**, 651-661.

Lomax, A., Virieux, J., Volant, P., and Berge, C., 2000, Probabilistic earthquake location in 3D and layered models: introduction of a Metropolis-Gibbs method and comparison with linear locations: in Advances in Seismic Event Location, Thurber, C.H., and Rabinowitz (eds.), Kluwer, Amsterdam, 101-134.

Loosveld, R.J.H., Bell, A., and Terken, J.J.M., 1996, The tectonic evolution of Oman: GeoArabia, **1**, 28–51.

Menke, W., 1989, Geophysical data analysis: discrete inverse theory: Academic Press, revised edition, 289 pp.

Michelini, A. and Bolt, B., 1986, Application of the principal parameters method to the 1983 Coalinga, California aftershock sequence: Bull. Seism. Soc. Am., **76**, 409 – 420.

Michelini, A. and Lomax, A., 2004, The effect of velocity structure errors on double-difference earthquake location: Geophys. Res. Lett., **31**, L09602, doi:10.1029/2004GL019682.

Mijnssen, F.C.J., Rayes, D.G., Ferguson, I., Al Abri, S.M., Mueller, G.F., Razali, P.H.M.A, Nieuwenhuijs, R., Henderson, G.H., 2003, Maximizing Yibal's remaining value: SPE Reservoir Evaluation & Engineering, **6**, 255 – 263.

Moser, T.J., van Eck, T., and Nolet, G., 1992, Hypocenter determination in strongly heterogeneous earth models using the shortest path method: J. Geophys. Res., **97**, 6563-6572.

Nadeau, R.M., Foxall, W., and McEvilly, T.V., 1995, Clustering and periodic recurrence of microearthquakes on the San Andreas Fault at Parkfield: Science, **267**, 503-507.

Oppenheimer, D.H., Reasenberg, R.A., and Simpson, R.W., 1988, Fault plane solutions for the 1984 Morgan Hill, California, earthquake sequence: evidence for the state of stress on the Calaveras fault: J. Geophys. Res., **93**, 9007-9026.

Pavlis, G.L., 1986, Appraising earthquake hypocenter location errors: a complete, practical approach for single-event locations: Bull. Seismol. Soc. Am., **76**, 1699-1717.

Phillips, W.S., House, L.S., and Fehler, M.C., 1997, Detailed joint structure in a geothermal reservoir from studies of induced microearthquake clusters: J. Geophys. Res., **102**, 11,745-11,763.

Phillips, W.S., 2000, Precise microearthquake locations and fluid flow in the geothermal reservoir at Soultz-ous-Forets, France: Bull. Seismol. Soc. Am., **90**, 212-228.

Podvin, P., and Lecomte, I., 1991, Finite difference computation of traveltimes in very contrasted velocity models: a massively parallel approach and its associated tools: Geophys. J. Int., **105**, 271-284.

Rutledge, J.T., Phillips, W.S., and Schuessler, B.K., 1998a, Reservoir characterization using oil-production induced microseismicity, Clinton County, Kentucky: Tectonophysics, **289**, 129-152.

Poupinet, G., Ellsworth, W.L., and Frechet, J., 1984, Monitoring velocity variations in the crust using earthquake doublets, an application to the Calaveras Fault, California: J. Geophys. Res., **89**, 5719 – 5731.

Rutledge, J.T., Phillips, W.S., House, L.S., and Zinno, R.J., 1998b, Microseismic mapping of a Cotton Valley hydraulic fracture using decimated downhole arrays: 68th Ann. Mtg., Soc. of Explor. Geophys., Expanded Abstracts, 338-341.

Ruud, B.O., Husebye, E.S., Ingate, S.F., and Christoffersson, A., 1988, Event location at any distance using seismic data from a single, three-component station: Bull. Seismol. Soc. Am., **78**, 308 – 325.

Shimshoni, M. and Smith, S.W., 1964, Seismic signal enhancement with three component detectors: Geophysics, **29**, 664 – 671.

Silver, P. and Chan, W.W., 1991, Shear wave splitting and subcontinental mantle deformation: J. Geophys. Res., **96**, 16429 – 16454.

Tarantola, A. and Valette, B., 1982, Inverse problems = quest for information: J. Geophys., **50**, 159-170.

van Driel, W.D., Hart, C., Lehr, B. and Coremans, J., 2000 Reservoir compaction, surface subsidence and fault slip in the Yibal field, Oman: Netherlands Organisation for Applied Scientific Research.

Vidale, J.E., Ellsworth, W.L., Cole, A., and Marone, C., 1994, Variations in rupture process with recurrence interval in a repeated small earthquake: Nature, 368, 624-626.

Waldauser, F. and Ellsworth, W.L., 2000, A double-difference earthquake location algorithm: method and application to the northern Hayward Fault, California: Bull. Seismol. Soc. Am., **90**, 1353 – 1368.

Wittlinger, G., Herquel, G., and Nakache, T., 1993, Earthquake location in strongly heterogeneous media: Geophys. J. Int., **115**, 759-777.

Wolfe, C.J., 2002, On the mathematics of using difference operators to relocate earthquakes, Bull. Seismol. Soc. Am., **92**, 2879-2892.

Xu, L., Kuleli, S., and Toksoz, M.N., 2004, Source characteristics of May 1, 2003 Bingol, Turkey Mw 6.4 earthquake inferred from aftershocks and seismic waveforms: Submitted to Bull. Seismol. Soc. Am.

Yerkes, R. F. and Castle, R. O., 1976, Seismicity and faulting attributable to fluid extraction, Engineering Geology, 10 (2-4), p. 151-167

Chapter 3

Wavelet-Domain Waveform Inversion For Source Parameters

3.1 Introduction

Estimation of the seismic moment tensor and source-time function using waveform inversion has been performed routinely by seismologists to study earthquake mechanisms and source-time histories. Many methods have been developed since Gilbert & Dziewonski (1975) used free oscillation data for their inversion (e.g. Langston, 1981; Kikuchi & Kanamori, 1982; Sipkin, 1982; Nabelek, 1984; Dreger & Helmberger, 1993). Different types of seismic waveforms, such as long-period surface waves (McCowan, 1976; Mendiguren, 1977) and low-frequency body wave data (Stump & Johnson, 1977; Langston, 1981), were inverted for source mechanisms. However, there has been limited success (e.g. Šílený *et al.*, 1992; Šílený & Pšenčík, 1995; Schurr & Nábělek, 1999) in applying these waveform inversion techniques to high-frequency seismograms, despite the widespread availability of broadband three-component data. All the waveform inversion methods being used are performed in either the time or frequency domain.

Geophysical inverse problems are often large-scaled and ill-posed. In earthquake mechanism waveform inversions, the most commonly used method to reduce the number

of parameters to be determined is by using boxcar functions (Langston, 1981) or overlapping triangles (Nabelek, 1984). These parameterization bases can sometimes perform poorly in approximating the model (e.g. source-time function, moment tensor rate function, etc.). If these bases fail to represent the model properly, they will also give poor estimates of the source parameters. Therefore, it is preferable to choose a basis that can construct precise approximations with a linear combination of only a small number of vectors selected inside the basis.

It is well known that wavelets have the ability to efficiently approximate signals with just a small number of coefficients. Here, I propose the use of a wavelet-based approach to the formulation of the waveform inversion problem. Wavelet analysis is becoming a popular tool for numerical studies in signal processing (Mallat, 1989; Wang *et al.*, 1995), biomedical applications (Delaney & Bresler, 1995; Zhu *et al.*, 1997), and geophysics (Deighan and Watts, 1997; Anant & Dowla, 1997; Wood, 1999; Kane & Herrmann, 2001). A complete description of geophysical applications can be found in Foufoula-Georgiou and Kumar (1995), while a theoretical treatment of wavelet analysis is given by Daubechies (1992), Strang & Nguyen (1997) and Mallat (1998). However, no previous attempt to apply wavelet analysis to earthquake source mechanism inversion has been undertaken. In the proposed method, I adopt a wavelet-based strategy to parameterize the moment tensor rate functions (MTRFs). The MTRFs allow for the time dependent source mechanism such that each moment tensor component has its own time history (Dziewonski and Gilbert, 1974; Stump & Jorhnson, 1977; Ruff & Tichelaar, 1990; Šílený *et al.*, 1992). By choosing the "best" wavelet as the basis, I can construct an

adaptive, problem dependent parameterization for the MTRFs, thereby achieving accurate approximations while significantly reducing the number of parameters that need to be estimated through inversion. Additionally, I perform the inversion in the wavelet domain instead of working in the time or frequency domain. This gives the advantage of solving the inverse problem in a multi-scale sparse matrix representation. I can then solve the problem from coarse to fine levels out to the limit of stability. At each scale level a regularized least-squares solution is obtained using the conjugate gradient method. By reducing the number of parameters that need to be estimated significantly, and solving the inverse problem from coarse to fine levels, the wavelet-based method allows us to obtain stable solutions more easily. Another advantage of transforming the inverse problem to the wavelet domain is that wavelets are powerful tools for denoising data (Donoho, 1992). Transforming the data to the wavelet domain tends to isolate signals into a few large valued coefficients, while the background noise tends to spread around equally with less energy. I can incorporate a non-linear wavelet thresholding operator to remove the small wavelet coefficients, and thus the noise is attenuated with little effect on the signals. Thus, a robust estimate of source parameters can be retrieved.

The first section of this paper reviews the theory of wavelet transform and the formulation of the least-squares solution for the seismic waveform data in the wavelet domain. The second section presents results from synthetic data. Here, I discuss the capabilities of the wavelet technique and compare it to the conventional method. Finally, the last sections of the paper demonstrate the application of the technique to three datasets: the April 20, 2002 Au Sable Fork, New York earthquake, the September 3, 2002

Yorba Linda, California earthquakes, and eleven microseismic events recorded on the Field, Oman from 1999 to 2000.

3.2 Theory and Method

Earthquakes represent the release of elastic strain energy accumulated in the Earth's crust due to the process of plate tectonics by fracturing of crustal material. The study of earthquake sources is of considerable importance because it provides information and properties about regions in the Earth which are often inaccessible physically to human investigation.

3.2.1 Forward Problem

Mathematically, a seismic source represents a temporary failure of the equations of motion in a certain part of the earth, and the source is a correction that is needed to make the equations work again. A good review can be found in Aki & Richards (1980). This correction can be introduced by boundary or initial conditions, or by virtual body forces in certain parts of the earth. The representation theorem expresses the motion due to a distribution of equivalent body force density

$$u_k(\vec{x},t) = \int_{-\infty}^{t} \int_{V} G_{ki}(\vec{x},t;\vec{\xi},\tau) F_i(\vec{\xi},\tau) dV d\tau , \qquad (3.2.1)$$

where $u_k(\vec{x},t)$ is the k-component of the ground displacement at location $\vec{x}$ and time t, $G_{ki}(\vec{x},t;\vec{\xi},\tau)$ is the Green's function, which is the k-component of the displacement at $(\vec{x},t)$ due to a unit impulse force in the i-direction at $(\vec{\xi},\tau)$, and F_i is the equivalent body force density. The integration is over a volume V containing the non-zero equivalent body forces. For a volume dislocation-type source the equivalent body force density can be expressed as

$$F_i(\vec{\xi},\tau) = -\frac{\partial}{\partial \xi_j} c_{ijpq} \varepsilon_{pq}(\vec{\xi},\tau), \tag{3.2.2}$$

where c_{ijpq} are Lame constants and ε_{pq} is the stress-free strain.

Since the net force and the net torque on the earth must vanish, an internal source can be described by a symmetric tensor quantity. The seismic moment tensor density, M_{ij}, is related to the body force density, F_i, by

$$F_i = -\frac{\partial}{\partial \xi_j} M_{ij} \tag{3.2.3}$$

Substituting (3.2.3) into (3.2.2), the seismic moment tensor density is

$$M_{ij} = c_{ijpq} \varepsilon_{pq}. \tag{3.2.4}$$

The ground displacement due to a moment tensor density distribution can be obtained by substituting (3.2.3) into (3.2.1), integrating by parts, and replacing the time integration by the convolution,

$$u_k(\bar{x},t) = \int_V G_{ki,j}(\bar{x},t;\bar{\xi},0) * M_{ij}(\bar{\xi},t)dV \,. \tag{3.2.5}$$

Assuming the wavelengths under consideration are much longer than the dimensions of the source, we can expand the Green's function around point $\bar{\xi}^0$ in V and keep only the first few terms of the Taylor series expansion,

$$\begin{aligned} G_{ki}(\bar{x},t;\bar{\xi},\tau) = G_{ki}(\bar{x},t;\bar{\xi}^0,\tau) + (\xi_l - \xi_l^0)G_{ki,jl}(\bar{x},t;\bar{\xi}^0,\tau) + \dots \\ + (\xi_l - \xi_l^0)\dots(\xi_n - \xi_n^0)G_{ki,jl\dots n}(\bar{x},t;\bar{\xi}^0,0) \end{aligned} \,. \tag{3.2.6}$$

Substitute (3.2.6) into (3.2.5) gives

$$\begin{aligned} u_k(\bar{x},t) = & \int_V G_{ki,j}(\bar{x},t;\bar{\xi}^0,0) * M_{ij}(\bar{\xi},t)dV \\ & + \int_V (\xi_l - \xi_l^0)G_{ki,jl}(\bar{x},t;\bar{\xi}^0,0) * M_{ij}(\bar{\xi},t)dV \\ & + \cdots \\ & + \int_V (\xi_l - \xi_l^0)\dots(\xi_n - \xi_n^0)G_{ki,jl\dots n}(\bar{x},t;\bar{\xi}^0,0) * M_{ij}(\bar{\xi},t)dV \end{aligned} \,. \tag{3.2.7}$$

Define

$$M_{ijl}(\vec{\xi},t)=(\xi_l-\xi_l^0)M_{ij}(\vec{\xi},t),$$
$$M_{ijl\ldots n}(\vec{\xi},t)=(\xi_l-\xi_l^0)\ldots(\xi_n-\xi_n^0)M_{ij}(\vec{\xi},t). \tag{3.2.8}$$

$M_{ij}(t)$ is called the seismic moment tensor of degree 0, and $M_{ijl\ldots}(t)$ are the higher order seismic moment tensors. The number of independent parameters grows rapidly with each additional moment. By keeping only the first term of the expansion, we have six independent parameters. Then the number of parameters increases to 24 by keeping the first two terms, and increases to 60 by keeping the first three terms. This becomes an important issue when we solve the equations as an inverse problem.

Following Aki and Richards (1980), neglecting the higher order terms of the Taylor expansion of the Green's function, the k-component of the ground displacement at location $\vec{x}$ and time t can be expressed as a linear combination of the time-dependent moment tensor $M_{ij}(t)$ convolved with the spatial derivative of Green's function $G_{ki}(\vec{x},t)$ with source location $\vec{\xi}^0$ and station location $\vec{x}$,

$$u_k(\vec{x},t)=\sum_{i,j=1}^{3}G_{ki,j}(\vec{x},t;\vec{\xi}^0,0)*M_{ij}(t). \tag{3.2.9}$$

Since all internal seismic sources can be represented by a moment tensor density, similar to the body force density, it is useful in the forward problem to provide a weighting factor for the excitation functions in the volume integration. However, from equation (3.2.3), we can see that if the moment tensor density is known, the body forces are uniquely

specified but not vice versa. Due to the non-uniqueness, its use in the inverse problem is limited to situations where earthquake can be approximated by a point source.

If we take the far-field approximation of equation (3.2.9), the Green's function operates only on the time derivative of the moment tensor (Sipkin, 1982), that is, the moment tensor rate functions (MTRFs), $\dot{M}_{ij}(t)$. Then equation (3.2.9) can be written as

$$\begin{aligned} u_k(\bar{x},t) &= \sum_{i,j=1}^{3} G_{ki,j}(\bar{x},t;\bar{\xi}^0,0) * \dot{M}_{ij}(t) \\ &= \sum_{m=1}^{6} G_{km}(\bar{x},t;\bar{\xi}^0,0) * \dot{M}_m(t) \end{aligned} \quad . \tag{3.2.10}$$

3.2.2 Inverse Problem

The relation between the MTRFs and the Green's functions in equation (3.2.10) is linear and this system of linear equations can be written in matrix form:

$$\mathbf{d} = \mathbf{A}\mathbf{m}\,, \tag{3.2.11}$$

where matrix **A** is the linear data kernel containing the Green's functions, **d** is the vector of observed seismograms, and **m** is the vector of model parameters, i.e. the MTRFs. Equation (3.2.11) represents a forward modeling relation, whereas our goal is to perform

the inverse of these calculations. Mathematically speaking, we can pose the problem as trying to minimize the misfit between the observed and predicted data,

$$\min\left\|\mathbf{Am}-\mathbf{d}\right\|^2 \tag{3.2.12}$$

where **m** is an element of the model space. A least-squares minimizing model associates with a critical point of this misfit function. Differentiating equation (3.2.10) with respect to **m** and setting the result equal to zero gives the normal equations,

$$\mathbf{A}^T\mathbf{Am}=\mathbf{A}^T\mathbf{d}\,. \tag{3.2.13}$$

Most real inverse calculations must be regularized because in practice linear least squares calculations usually involve singular matrices or matrices that are numerically singular (have very small eigenvalues). Regularization is a process by which these singularities are tamed. In the presence of a model null space it is useful to penalize the size of the solution as well as the data misfit. In other words, we replace the minimization problem with

$$\min\left(\left\|\mathbf{Am}-\mathbf{d}\right\|^2+\lambda\left\|\mathbf{Rm}\right\|^2\right) \tag{3.2.14}$$

The first term is the data misfit, and the second is the regularization term. Here, we are minimizing the norm of the data misfit and also the norm of some linear function of the model **Rx**. The factor λ controls the tradeoff between the two norms. In this case, $\mathbf{R}\equiv\partial$,

and ∂ is an 1st order discrete difference operator which penalizes the roughness of the model. Penalizing roughness is useful if we want a smooth solution. The normal equations associated with this objective function, obtained by setting the derivative of (3.2.12) equal to zero, are

$$\left(\mathbf{A}^T\mathbf{A} + \lambda\mathbf{R}^T\mathbf{R}\right)\mathbf{m} = \mathbf{A}^T\mathbf{d}\,. \qquad (3.2.15)$$

In solving inverse problems, the model needs to be properly parameterized so that the unknown parameters can be solved. Because earthquakes vary in size and complexity, a parameterization appropriate for one earthquake may not be appropriate for another. The inversion is, therefore, necessarily a step-wise trial-and-error process. After determining a set of parameters, one must look and compare the model predictions with the observed data. If the predictions agree to within the accuracy of the data and the uncertainties in the model parameters are acceptable, one's job is finished. If, however, the data are not matched acceptably one must either filter the data or increase the number of model parameters if one suspects that the discrepancies are due to particular features of the earthquake source.

If the source time function is overparameterized it may becomes unstable. We can smooth it by decreasing the number of time function elements and increasing their duration. The control of model grid spacing is an important part of any inverse problem because it saves computer time and simplifies the interpretation.

Conventionally, two types of far-field source-time function are used. First, Langston (1981) discretized the source-time function by a series of boxcar functions, $B^{\Delta\tau}(t)$, of equal durations $\Delta\tau$ and of variable amplitude A_k (Figure 3.1a),

$$M_{ij}(t) = \sum_k A_{ijk} B_{ij}^{\Delta\tau}(t - \tau_k), \tag{3.2.16}$$

where $\tau_k = \Delta\tau(k-1)$. Secondly, Nábělek (1984) introduced the use of overlapping isosceles triangles, $T^{\Delta\tau}(t)$ for the parameterization that has the form (Figure 3.1b),

$$\begin{aligned} M_{ij}(t) &= \sum_k A_{ijk} T_{ij}^{\Delta\tau}(t - \tau_k) \\ T_{ij}^{\Delta\tau}(t) &= B_{ij}^{\Delta\tau}(t) * B_{ij}^{\Delta\tau}(t) \end{aligned} . \tag{3.2.17}$$

The unknown amplitudes A_k are determined by the inversion and the number of time function elements and their durations has to be chosen a priori. Comparing the two methods, the boxcar functions usually produce synthetic seismogram that are too rich in high frequencies, and require more elements to describe the source than the triangular functions.

However, in the next section, I will show that both of the above basis functions sometimes cannot describe the source-time function adequately, and the use of wavelets for the parameterization can dramatically improve the results. If the chosen bases fail to represent the model parameters properly, they will also give poor estimates. Therefore, it

is preferable to choose a basis that can construct precise approximations with a linear combination of only a small number of vectors selected inside the basis.

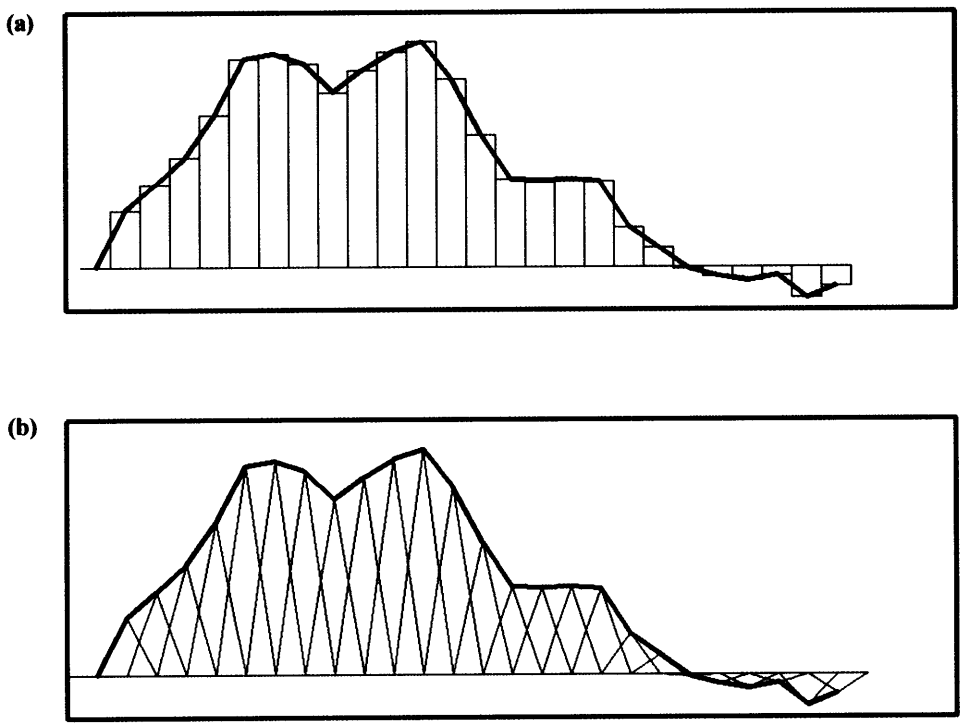

Figure 3.1. Illustration of the source-time function parameterization using (a) a series of boxcar functions and (b) overlapping isosceles triangular functions.

3.2.3 The Discrete Wavelet Transform

The success of data compression using wavelets suggests that only a fraction of wavelet coefficients may contain sufficient information to reconstruct the original signal.

Therefore, we can expect that the size of an inverse problem can be greatly reduced without sacrificing the quality of the approximation of the model if the inversion of parameters is carried out in wavelet-represented form. However, no previous attempt to apply wavelet analysis to earthquake source mechanism inversion has been undertaken.

In wavelet analysis one adopts wavelet prototype functions called the scaling function, $\varphi(t)$, and the wavelet function, $\psi(t)$. Through dilations and translations of these functions one constructs an orthonormal basis of $L^2(\mathbf{R})$ such that

$$\varphi_{j,k}(t) = 2^{j/2}\varphi(2^j t - k) \tag{3.2.18}$$

$$\psi_{j,k}(t) = 2^{j/2}\psi(2^j t - k) \tag{3.2.19}$$

where j, $k \in \mathbf{R}$. The parameter $2^{j/2}$ is known as the scale factor and k is the translation factor. The wavelet $\psi(t)$ is generated from a scaling function $\varphi(t)$ through the relationship:

$$\begin{aligned} \varphi(t) &= \sqrt{2}\sum_l h_0 \varphi(2t - l) \\ \psi(t) &= \sqrt{2}\sum_l g_0 \psi(2t - l) \end{aligned} \tag{3.2.20}$$

where h_0 and g_0 are the refinement filter and the corresponding orthogonal wavelet filter, respectively. In the Fourier domain, the refinement filter $\hat{h}(\omega)$ is given by

$$\hat{h}_0(\omega) = \sqrt{2}\frac{\hat{\varphi}(2\omega)}{\hat{\varphi}(\omega)}, \tag{3.2.21}$$

and then we can obtain the corresponding wavelet filter $\hat{g}(\omega)$ using Mallat's recipe (Mallat, 1989):

$$\hat{g}_0(\omega) = -e^{-i\omega}\hat{h}_0^*(\omega+\pi). \tag{3.2.22}$$

From a filter-bank point of view, h_0 and g_0 are a pair of quadrature-mirror lowpass and bandpass filters. The dilations and translations of the scaling function $\varphi_{j,k}(t)$ lead to the multiresolution analysis (MRA) of $L^2(\mathbf{R})$. Following Mallat (1989), any $f(t)$ can be represented as

$$f(t) = \sum_k u_{j_0,k}\varphi_{j_0,k}(t) + \sum_{j=j_0}^{J}\sum_k v_{j,k}\psi_{j,k}(t) \tag{3.2.23}$$

where $\mathbf{u} = u_{j_0,k}$, $v = v_{j,k}$ are called the wavelet coefficients. The wavelet coefficients can be obtained by the discrete wavelet transform (DWT) which is defined as the inner products of $f(t)$ with dilated and translated scaling function, ϕ (t), and dilated and translated wavelet functions, $\psi(t)$:

$$\begin{aligned} u_{j_0,k} &= \int f(t)\phi_{j_0,k}^*(t)dt \\ v_{j,k} &= \int f(t)\psi_{j,k}^*(t)dt \end{aligned} \tag{3.2.24}$$

For a discrete seismic signal with K samples, equation (3.2.24) can be written in the following matrix form:

$$\tilde{\mathbf{f}} = \begin{bmatrix} \mathbf{u} \\ \mathbf{v} \end{bmatrix} = \mathbf{W}\mathbf{f} \tag{3.2.25}$$

where $\mathbf{f} = [f(t_1), f(t_2), \ldots, f(t_K)]^T$ consists of discrete samples of the original signal, and $\mathbf{W}$ is an $K \times K$ transform matrix in which each row vector corresponds to a transform basis vector. The transform matrix $\mathbf{W}$ is an orthogonal matrix since only orthogonal wavelets are considered here.

3.2.3 Fractional Spline Wavelets

In this study, I deal exclusively with fractional spline scaling and wavelets functions. Splines are piecewise polynomial approximations of a true function. They are representable by linear combinations of spline basis functions, which are the building blocks of any arbitrary spline. By manipulating the coefficients of such basis functions one can effectively perform operations on the spline. Traditional B-splines, $\beta^{\alpha}(t)$, are restricted to have integer order of α, but Unser and Blu (2000) have relaxed this restriction. The resulting fractional spline basis functions can be causal, anti-causal, or symmetric. However, it is more appropriate to use causal functions for solving

geophysical problems. The explicit forms of fractional causal B-spline scaling and wavelet function for $\alpha > -1/2$ are

$$\phi_+^\alpha(t) = \frac{1}{\Gamma(\alpha+1)} \sum_{k=0}^{\infty} (-1)^k \binom{\alpha+1}{k} (t-k)_+^\alpha$$
$$\psi_+^\alpha(t/2) = \sum_{k \in Z} \frac{(-1)^k}{2^\alpha} \sum_{l \in Z} \binom{\alpha+1}{l} \phi_*^{2\alpha+1}(l+k-1) \phi_+^\alpha(t-k) \qquad (3.2.26)$$

where

$$\Gamma(u+1) = \int_0^\infty x^u e^{-x} dx,$$
$$\binom{u}{v} = \frac{\Gamma(u+1)}{\Gamma(v+1)\Gamma(u-v+1)},$$
$$t_+^\alpha = \begin{cases} x^\alpha, & x \geq 0 \\ 0, & \text{otherwise} \end{cases},$$

$$\phi_*^{2\alpha+1}(t) = \frac{1}{\Gamma(\alpha+1)} \sum_{k \in Z} (-1)^k \binom{\alpha+1}{k + \frac{\alpha+1}{2}} |t-k|_*^\alpha \quad \text{, and}$$

$$|t|_*^\alpha = \begin{cases} \dfrac{|x|^\alpha}{-2\sin(\pi\alpha/2)}, & \alpha \text{ not even} \\ \dfrac{x^{2n} \log x}{(-1)^{1+n} \pi}, & \alpha \text{ even} \end{cases}.$$

Examples of the fractional B-spline scaling and wavelet functions for degrees $4 \geq \alpha \geq 0$ are shown in Figure 3.2 (a) and (b), respectively. The wavelet becomes smoother as α becomes larger. By choosing the appropriate order of the wavelet, it provides a flexible way to incorporate smoothness information into the inverse problem.

The fractional spline wavelets of degree α, irrespective of their type, have $[\alpha]+1$ vanishing moments,

$$\int_{-\infty}^{\infty} x^n \psi^{\alpha}(t)dt = 0, \quad n = 0,\ldots,[\alpha] \tag{3.2.27}$$

This is a direct consequence of the polynomial reproduction properties of the fractional *B*-splines and the fact that the scaling functions and wavelets are orthogonal.

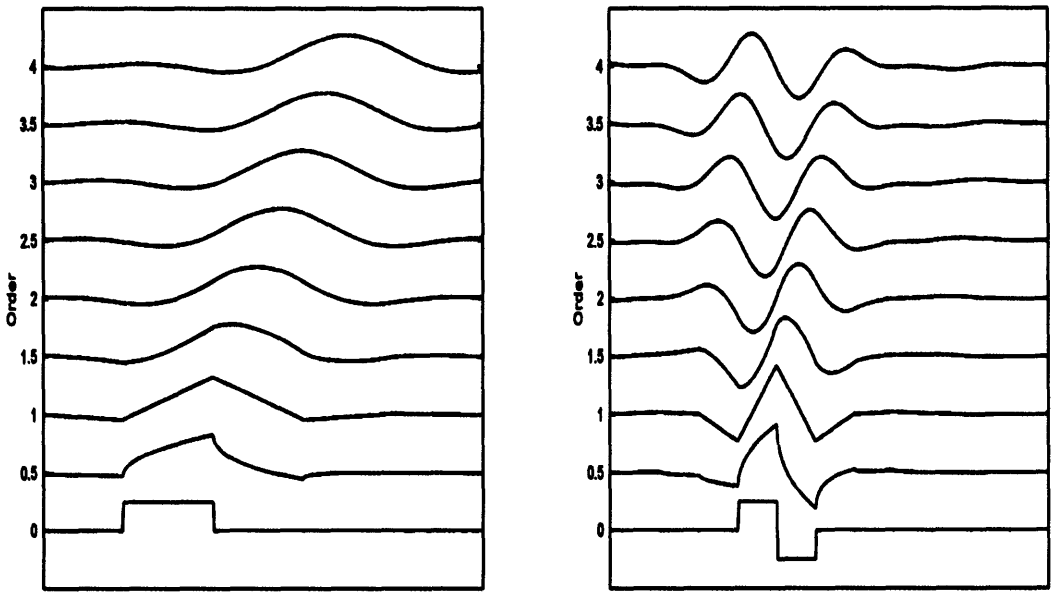

Figure 3.2. (a) The fractional B-spline scaling functions with $4 \geq \alpha \geq 0$. Note that the zero order B-spline is a boxcar function. The scaling function becomes smoother as the order increases. (b) The fractional B-spline wavelets with $4 \geq \alpha \geq 0$. Same as the scaling function, the wavelet becomes smoother as the order increases.

3.2.4 Waveform Inversion in the Wavelet-Domain

According to equation (3.2.24), I can represent each MTRF component in the wavelet domain by means of DWT on the model vector in equation (3.2.11):

$$\begin{bmatrix} \mathbf{u}_m \\ \mathbf{v}_m \end{bmatrix} = \begin{bmatrix} 2^{-J/2} \sum_t \dot{M}_m(t) \phi^*_{j_0,k}(t) dt \\ 2^{-j/2} \sum_t \dot{M}_m(t) \psi^*_{j,k}(t) dt \end{bmatrix} = \mathbf{W}_M \dot{\mathbf{M}} \tag{3.2.28}$$

where $\mathbf{W}_M$ is the transform matrix for the MTRFs and $\dot{\mathbf{M}} = \left[\dot{M}_m(t_1) \quad \cdots \quad \dot{M}_m(t_K)\right]$, m = 1, ..., 6. In addition, the linear system of equations of equation (3.2.11) can be represented in the wavelet domain and it now becomes

$$\begin{aligned} \mathbf{W}_d \mathbf{d} &= \mathbf{W}_d \mathbf{G} * \mathbf{W}_M^T \mathbf{W}_M \dot{\mathbf{M}} \\ &= \left(\mathbf{W}_d \mathbf{G} * \mathbf{W}_M^T\right) \mathbf{m} \end{aligned} \tag{3.2.29}$$

and therefore,

$$\mathbf{d}_w = \mathbf{G}_w \mathbf{m} \tag{3.2.30}$$

where $\mathbf{d}_w = \mathbf{W}_d \mathbf{d}$, $\mathbf{G}_w = \mathbf{W}_d \mathbf{G} * \mathbf{W}_M^T$, $\mathbf{m} = \mathbf{W}_M \dot{\mathbf{M}}$, and $\mathbf{m}$ is the vector of unknown wavelet coefficients that we want to solve. The regularized least-squares solution is given by

$$\hat{\mathbf{m}} = \left(\mathbf{G}_w^T \mathbf{G}_w + \lambda \mathbf{I}\right)^{-1} \mathbf{G}_w^T \Theta_T[\mathbf{d}_w] \tag{3.2.31}$$

where λ is called the regularization parameter. I incorporate a nonlinear wavelet thresholding operator $\Theta_T[\cdot]$ into the equation for denoising data. It takes advantage of characteristic differences of signal and noise in the wavelet domain. The idea is that noise will mainly map to small wavelet coefficients with its energy being distributed along all scales, while signal maps to a few large wavelet coefficients due to its coherence. Therefore, the goal of the wavelet thresholding operator is to zero out or downweight the coefficients below the computed threshold values. I employ a scale level dependent thresholding scheme (Donoho, 1992):

$$\Theta[\cdot] = 2^{(j-J)/2} \sigma \sqrt{2\log(n)}, \; j = 0, \ldots, J \tag{3.2.32}$$

where n is the total number of seismogram samples, J is the number of decomposition levels, σ is the noise standard deviation, and j is the scale level. It uses larger thresholds at higher scale levels.

Although many earthquake sources are double-couples, it is useful to use the unconstrained moment tensor as the source model. This is because it makes the problem linear and simplifies the procedures while the double-couple constraint is non-linear. In this study, I do not impose any constraint on the mechanism on the moment tensor inversion.

When the system of linear equations in equation (3.2.31) to be solved is very large, one can resort to iterative methods that solve a large set of simultaneous equations without the need to write down the matrix of coefficients. In this case, we use an iterative scheme, such as the LSQR (Paige and Saunders, 1982) or the conjugate gradient method, to obtain the regularized least-squares solutions.

The technique of principal component analysis (Vasco, 1989) is used to factor the MTRFs into a set of orthogonal source-time functions through the singular value decomposition of the time-varying moment tensor. This allows us to estimate the dimensionality of the source-time function space and find the best set of successive approximations to the source-time functions. In the analysis, it is assumed that each component of the time-varying MTRFs is a weighted sum of source-time functions plus a noise term,

$$\hat{\mathbf{m}}^T = \mathbf{A}^T \mathbf{B}^T \tag{3.2.33}$$

where $\mathbf{A}$ is a 6×6 matrix of basis function weights, $\mathbf{B}$ is an $n \times 6$ matrix of source-time basis functions, for n time sampling points. Decomposition of equation (3.2.33) is nonunique because there are $n \times 6$ knowns and $(n + 6) \times 6$ unknowns, but the singular value decomposition is a useful technique to apply in this situation,

$$\hat{\mathbf{m}}^T = \mathbf{U} \boldsymbol{\Lambda} \mathbf{V}^T = \mathbf{A}^T \mathbf{B}^T \tag{3.2.34}$$

where $\mathbf{U}$ is a 6×6 column-orthogonal matrix, $\mathbf{\Lambda}$ is a 6×6 diagonal matrix of singular values, and $\mathbf{V}^T$ is a $n \times 6$ row-orthogonal matrix. The singular values act as weighting factors for the columns of $\mathbf{B}$, and is useful in identifying the dimension of the basis set needed to explain the observations. For example, if one singular value is large relative to the other five, then only one basis function is contributing significantly to the MTRF components

3.2.5 Algorithm

The wavelet-domain least-squares algorithm that I propose for solving the MTRFs through waveform inversion can now be summarized as follows:

1. Define the wavelet basis to be used and max scale level of wavelet decomposition, j.
2. Transform both the data and data kernel to the wavelet-domain by discrete wavelet transform (DWT).
3. Perform wavelet thresholding on waveform data to enhance signal-to-noise ratio.
4. Solve the regularized least-squares solution by the conjugate gradient method.
5. If solution is stable, go back to Step 1 and solve the inverse problem at a higher scale level, j+1.
6. The final solution (moment tensor rate function) is factorized into a set of orthogonal source-time functions using the principal component analysis.

3.2.6 Confidence intervals and bias corrections for linear inversion

To construct a confidence interval from the value of an estimator, i.e., the MTRFs, we must determine the variance of the estimator. We can have an unbiased estimator that is very sensitive to data perturbations (large variance). Let $\hat{\mathbf{A}}$ be the regularized pseudo-inverse for equation (3.2.14), the regularized solution, $\hat{\mathbf{m}}$ is

$$\hat{\mathbf{m}} = \hat{\mathbf{A}}\mathbf{d} = \left(\mathbf{A}^T\mathbf{A} + \lambda\mathbf{R}^T\mathbf{R}\right)^{-1}\mathbf{A}^T\mathbf{d}. \tag{3.2.35}$$

The covariance matrix of $\hat{\mathbf{m}}$ is

$$\mathrm{cov}(\hat{\mathbf{m}}) = \hat{\mathbf{A}}\,\mathrm{cov}(\mathbf{d})\hat{\mathbf{A}}^T. \tag{3.2.36}$$

Assuming that the covariance of data is $\sigma^2\mathbf{I}$, the variance of the ith model parameter is

$$\mathrm{var}(\hat{\mathbf{m}}_i) = \sigma^2\left(\hat{\mathbf{A}}\hat{\mathbf{A}}^T\right)_{ii}. \tag{3.2.37}$$

The variance of the residual vector $\mathbf{Am} - \mathbf{d}$ is used as an estimation of σ^2. If the estimator has a Gaussian distribution, the $(1-\alpha)$ confidence intervals can be defined by

$$\hat{\mathbf{m}}_i \pm z_{\alpha/2}\sigma\sqrt{\left(\hat{\mathbf{A}}\hat{\mathbf{A}}^T\right)_{ii}} \tag{3.2.38}$$

where $z_{\alpha/2}$ is the $1-\alpha/2$ quartile of the Gaussian distribution. Therefore, as the data uncertainties increase, the uncertainty in our parameter estimates increases. Moreover, the parameters associated with the smallest singular values will be less well resolved than those associated with the largest.

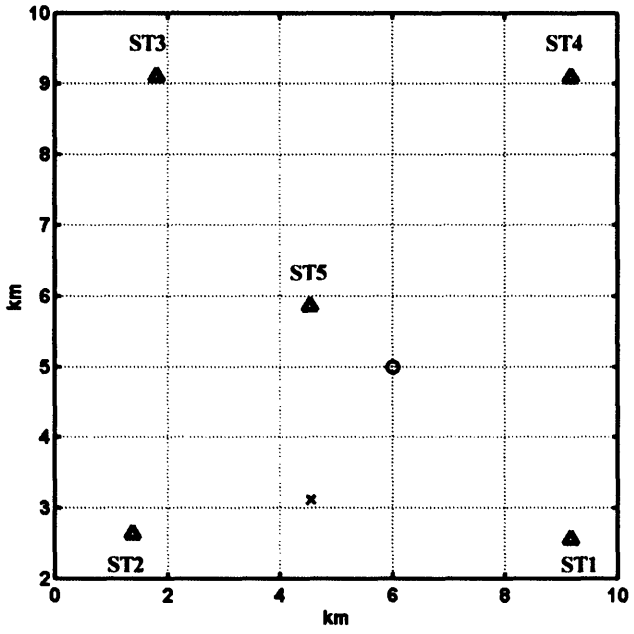

Figure 3.3. Station locations of a local seismic network operating on a petroleum reservoir. There are five stations: ST1, ST2, ST3, ST4, and ST5. The circle marks the location of the synthetic source. The estimated location of the induced seismic event for the real data test is indicated by the cross mark.

3.3 Synthetic Tests

Through synthetic data tests, I apply the method to high-frequency seismograms to retrieve the MTRFs and compare the results with those estimated by conventional time-domain method using overlapping triangular parameterization, which is one of the most commonly used technique to discretize the model space. The synthetic data and the Green's functions are generated by the 1-D modeling code based on the reflectivity method (Kennett, 1983) with a sampling rate of 125 Hz. Figure 3.3 shows the station network geometry of a local seismic network on a petroleum reservoir, and the synthetic source location is indicated by the circle with a source depth is 0.5 km. It does not have a simple double-couple mechanism and has the following moment tensor,

$$\mathbf{M} = \begin{bmatrix} 1 & 0 & 0 \\ 0 & 1 & -1 \\ -1 & 0 & 1 \end{bmatrix}.$$

The moment tensor represents a complex source that has a combination of an explosion and a vertical dip-slip mechanism. All MTRF components have the same source time history that is a cosine function: $1+\cos(t), t \leq |\pi|$, with a duration of 0.5 s. I use data collected at all stations except ST5 in the synthetic tests. There are four stations with three-component seismograms on the surface. All the stations are located within an epicentral distance of 10 km. I assume a six-layered velocity model for the area and the structure is shown in Figure 2.4. The S-wave velocity is deduced from a constant P-to-S

velocity ratio of 1.92, and density is assumed to be constant throughout the medium. Both the synthetic data and the Green's functions are generated using the same velocity model.

Using these synthetic data, I invert for the MTRFs using both the wavelet-based method that I proposed in the previous section, and the conventional time-domain method with overlapping triangular parameterization. Two sets of inversion experiments are performed: the first with noise-free data and the second with correlated white noise. In both experiments, I assume that the MTRFs have a duration of 1 s (125 samples if fully discretized). Maximum scale level of wavelet decomposition, $j = 11$, is used for the wavelet transform. Fractional spline wavelet of order 2.5 is chosen to serve as the basis function for the wavelet-domain inversions. Later in the section, I will investigate the influence on the solution caused by the choice of wavelet used.

3.3.1 Noise-free Data

For the noise-free data, I test the capability of the wavelet-based method and the conventional method to resolve the MTRFs by changing the number of model parameters used from 4 to 64 (i.e., wavelets and overlapping triangles). Figure 3.4 (a) – (g) show the inversion results. The focal mechanism and its original time history are given by the six independent functions corresponding to the six moment tensor components (M_{11}, M_{22}, M_{33}, M_{12}, M_{13} and M_{23}, from top to bottom), indicated by the black dash lines. Figures 3.4 (a) – (d) show the inversion results obtained with conventional least-squares method using overlapping triangular functions, and Figure 3.4 (e) – (h) show the results obtained

by the wavelet-based method. For the wavelet-based method, I solve the regularized least-squares solutions for the maximum scale level (j = 11), the same maximum level that I used for wavelet decomposition. The estimated MTRFs are plotted as black solid lines. At the coarsest parameterization case where only four model parameters are used (Fig 3.4a and e), both the wavelet-based and the conventional methods get the correct mechanism but fail to resolve the time histories. As I increase the number of model parameters, I start to be able to resolve the MTRFs better. The wavelet-based method needs only eight wavelet coefficients to recover the MTRFs almost perfectly, while conventional method needs to employ at least 32 overlapping triangles to obtain good results (Fig. 3.4d). However, stability and solution nonuniqueness degrades the result quality of both the wavelet-based and conventional methods, and this becomes obvious when I increase the number of model parameters to 32 (Fig. 3.4d and g). This is a problem that we often encounter in geophysical inverse problems, but the wavelet-based method offers a convenient way for us to attain stable solutions. By decreasing the maximum scale by two levels (j = 9), I find that the MTRFs can be resolved accurately again (Fig. 3.4i), due to nonexistence of the high wave number components.

Figure 3.5 plots the data misfit at log scale versus the number of model parameters. As we can expect, the misfits of both methods are largest when the model is significantly under-parameterized since a few, coarse basis functions cannot adequately approximate the model space. The misfits become smaller as the number of model parameters increase. Note the wavelet-based method has a faster misfit reduction rate

than that of conventional method. This is mainly due to the superior ability of the wavelet functions to represent the MTRFs over triangular functions.

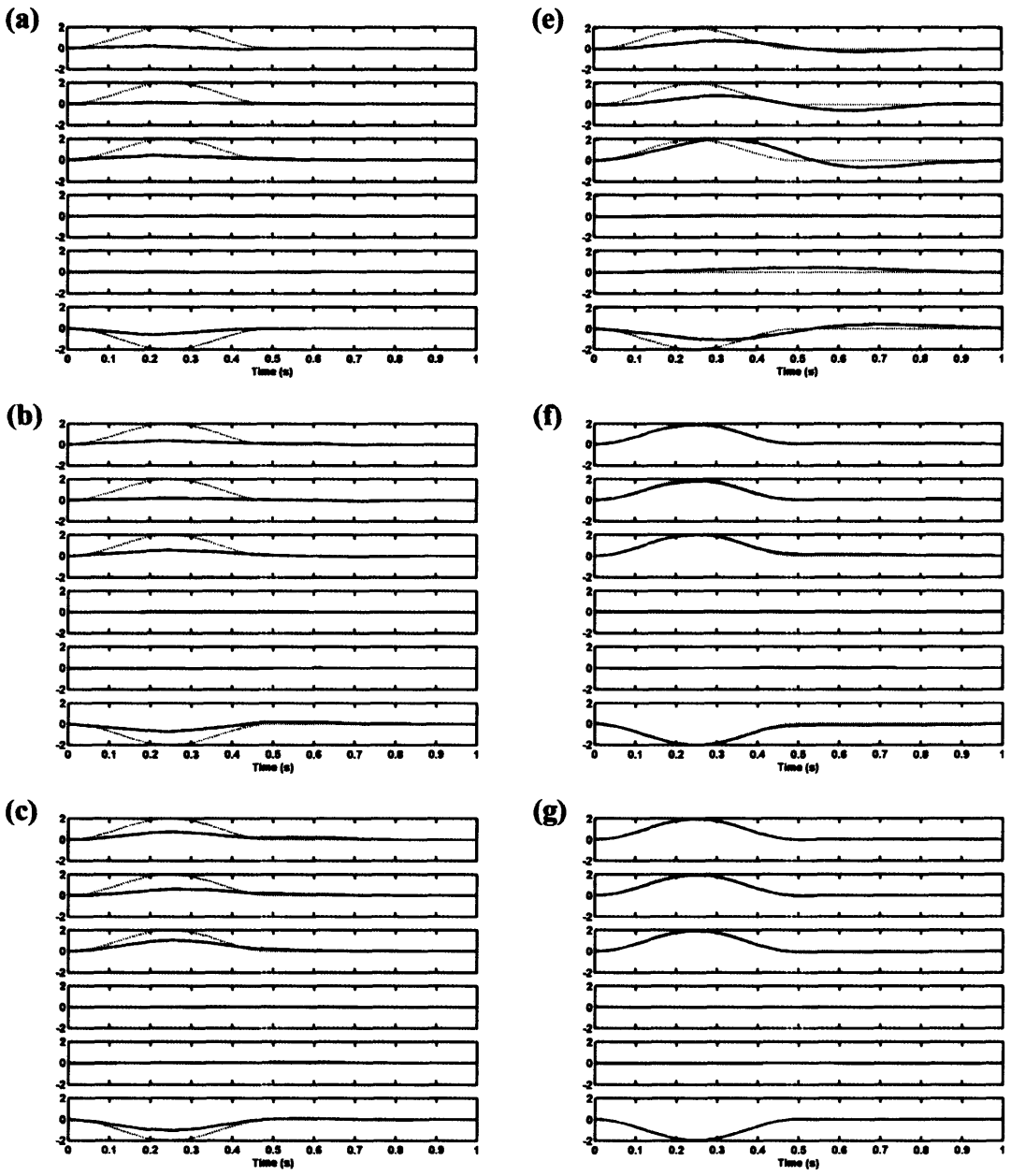

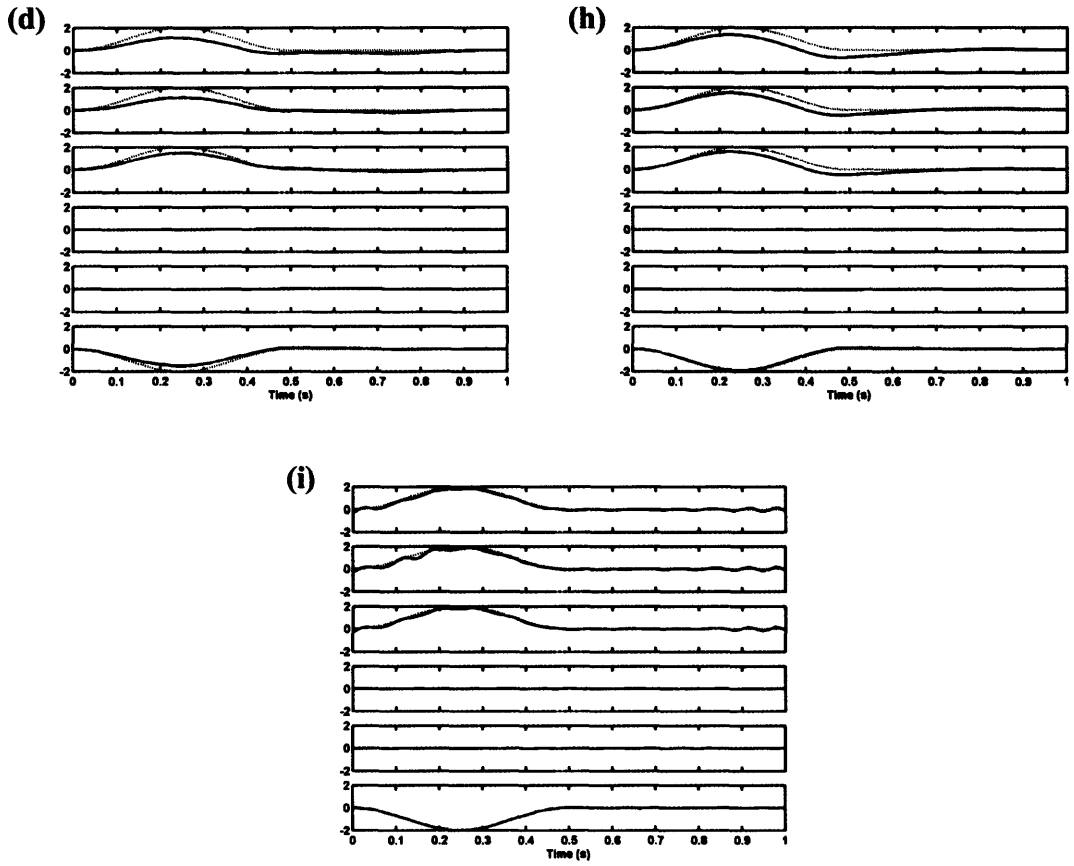

Figure 3.4. Moment tensor rate functions retrieved by conventional time-domain inversion using overlapping triangular parameterization (a – d) and wavelet-domain inversion (e – i) of noise-free synthetic data. Each figure shows the moment tensor rate function, which has six independent components, and are plotted in the order M_{11}, M_{22}, M_{33}, M_{12}, M_{13}, and M_{23}, from top to bottom. The dot lines show the synthetic source time history for each component and the solid lines show the corresponding source time retrieved by inversion. Source duration of one second is assumed for all inversion. Different numbers of overlapping triangles, n_t, are used to parameterize the MTRFs: (a) $n_t = 4$, (b) $n_t = 8$, (c) $n_t = 16$, and (d) $n_t = 32$. For the wavelet-domain inversions, all of them except (i) are solved up to the maximum scale level ($j = 11$) that is used for the wavelet decompositions. Fractional spline wavelet of order 2.5 is used in all inversions. Again,

different numbers of wavelets, n_w, are used to parameterize the MTRFs: (e) $n_w = 4$, (f) $n_w = 8$, (g) $n_w = 16$, (h) $n_w = 32$, and (i) $n_w = 32$ but the inversion is solved only up to a lower scale level, $j = 9$.

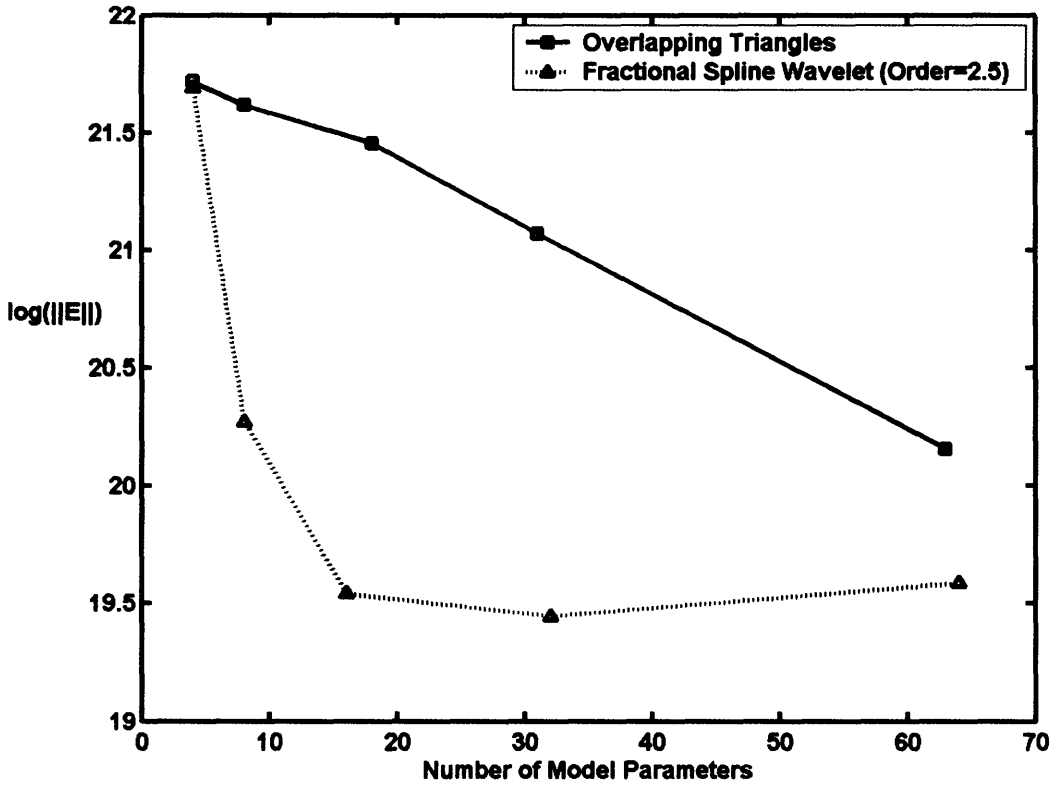

Figure 3.5. Comparison of data misfit of conventional time-domain method using overlapping triangular parameterization versus wavelet-domain method for the noise-free synthetic data. Starting with the coarsest parameterization with four model parameters, both methods give almost the same amount of misfit. However, the misfit for the wavelet-domain method decreases rapidly relative to the conventional method once the number of parameters increases.

3.3.2 Data contaminated with correlated noise

In the second experiment, I test the wavelet-based method on data contaminated with correlated noise (Figure 3.6). I solve the problem to the maximum scale level (j = 11) of wavelet decomposition. Each component of the MTRF is parameterized by eight wavelet coefficients of fractional spline wavelet of order 2.5. Correlated noise is simulated by sampling an autoregressive process of order 2. The standard deviation of the noise is about 20% of the standard deviation of the signal. Again, I plot the estimated MTRFs and the original inputs by black solid lines and black dash lines, respectively. Šílený *et al.* (1992) report that spurious correlated artifacts arises in the MTRFs when random noise is equal or more than 10% of the peak signal amplitude. My inversion results displayed in Figure 3.7 show that the MTRFs can be recovered by the wavelet-based method with no significant degradation in spite of the presence of strong correlated noise. The MTRFs are slightly underestimated but both the isotropic components and the double-couple are well-resolved. Also, I do not see any large artifacts even at the later parts of the time-histories. I believe that this improvement of the robustness is mainly due to the incorporation of the nonlinear wavelet thresholding operator that helps denoise the waveform data. Repeated tests on data corrupted with correlated noise seem to indicate that diagonal elements of the moment tensor are more sensitive to noise than the double-couple components. This finding is consistent with previous studies (e.g. Šílený & Pšenčík, 1995). Since random noise has no directivity, the inversion attributes it to the isotropic component of the source.

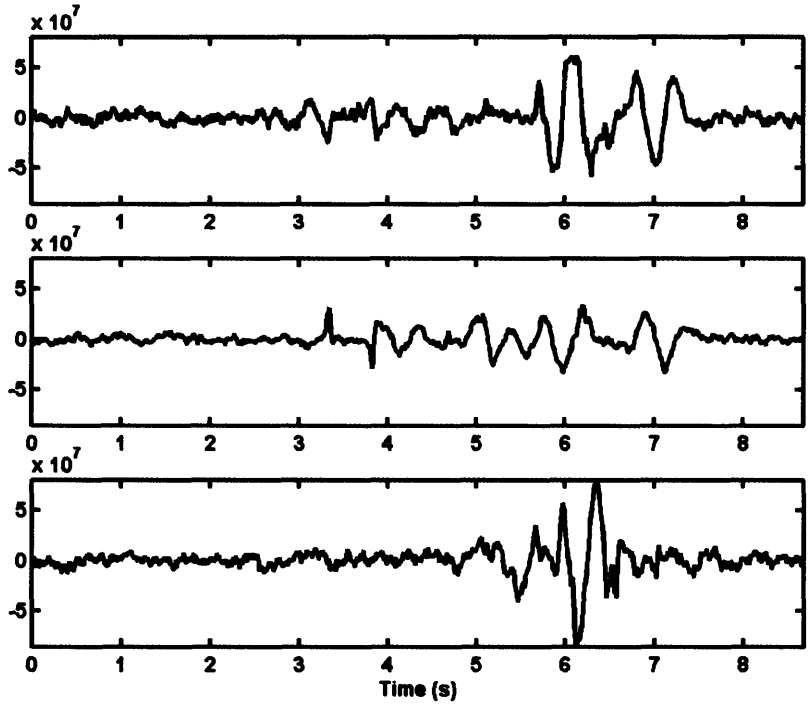

Figure 3.6. An example of the synthetic three-component waveforms contaminated by correlated random noise. The data are generated for station ST3 by the reflectivity method. From top to bottom: vertical, radial, and transverse components.

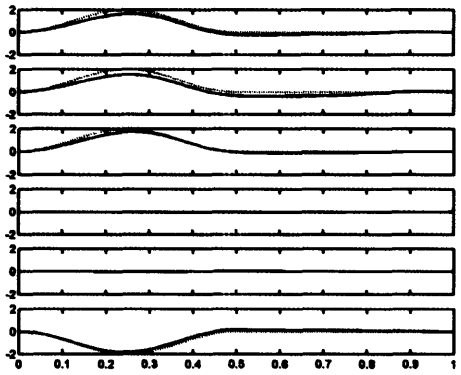

Figure 3.7. Moment tensor rate functions retrieved by wavelet-domain inversion of noisy synthetic data. The dot lines show the synthetic source time history for each component and the solid lines show the corresponding source time retrieved by inversion.

3.3.3 The Influence of choice of fractional spline wavelet

In the third experiment, I repeat the inversion on the noise-free synthetic data using wavelets for a series of different orders from –0.4 to 5.5, in order to investigate the influence of choice of wavelet on the solution. Choosing the "best" wavelet for particular applications has been an active research topic in wavelet analysis. I plot the norm of the data misfit against the order of fractional spline wavelet used for inversion in Figure 3.8. We can see that the data misfit is relatively large for low-orders compared to high-order wavelets. The magnitude of misfit reduces rapidly as the order increases from 1.0 to 2.0, and reaches a minimum at about 2.8. Thereafter, using wavelets of higher order does not improve the waveform fitting and the misfit fluctuates more or less at a constant level. This performance curve can be explained by comparing the smoothness of the fractional spline wavelet and the source-time history of the MTRFs. Low-order fractional spline wavelets are generally less smooth (Fig. 3.2b). For example, a fractional spline wavelet of order zero is the sum of two boxcar functions, while a first order fractional spline wavelet resembles closely to an isosceles triangle. It is difficult for a few of these rough functions to adequately approximate the smooth cosine source-time function. However, they can be represented easily by wavelets of smoother versions, those of order above 2.0, in this case. By systematic searching for the best data fitting, we can find the "best" wavelet for an inversion, and thus making the parameterization strategy problem adaptive.

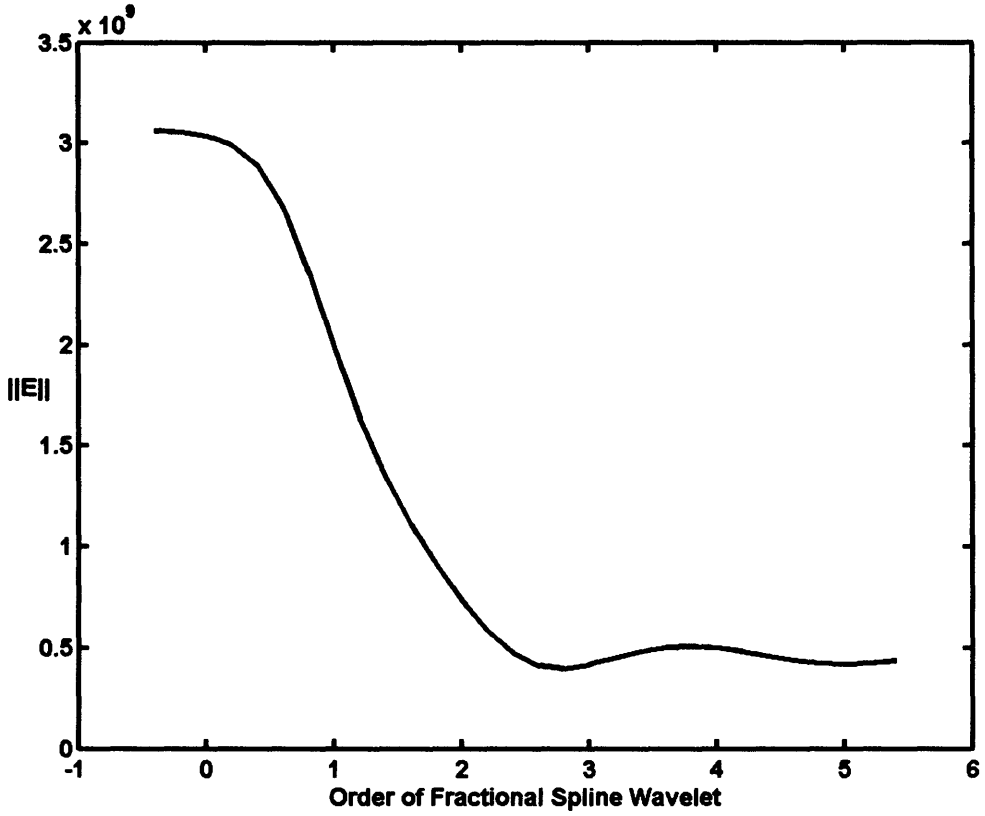

Figure 3.8. Data misfit versus order of fractional spline wavelet used for inversion. For the noise-free synthetic data case, using wavelet of order 2.8 gives the best data fitting. Searching for the "best" wavelet allow us to optimize the parameterization strategy to become problem dependent.

3.4 Application to April 20, 2002 Au Sable Forks, New York earthquake

I apply the wavelet-domain waveform inversion method to the three-component broadband seismograms of a magnitude 5.1 earthquake that occurred on April 20, 2002,

about 29 km southwest of Plattsburg, near the town of Au Sable Forks, New York. This earthquake was the largest earthquake centered in the northeastern U.S. since 1983, and was felt from New Brunswick and Maine to Ohio and Michigan and from Ontario and Quebec to Maryland. Some buildings and infrastructures were moderately damaged in the Clinton and Essex Counties. The northeastern part of New York State is an area that experiences moderate-sized but infrequent seismic activity. Earthquakes in this region occur on geologic faults but it is difficult to assign them to a particular fault because they rarely cause surface rupture. However, the location and the moment tensor solution are well-constrained (Seeber et al., 2002) and provide a good test for the inversion. The fault plane solution based on P-wave first motion polarities plotted by Professor John Ebel at Weston Observatory, is shown in Figure 3.9. The source mechanism determined by regional seismic waveform data using conventional moment tensor inversion method by Dr. Kim at Lamont-Doherty Earth Observatory is well-constrained and indicates predominantly thrust motion along 45 degree dipping fault striking due South. At least three aftershocks with magnitude greater than 3.0 followed the main event. About 70 aftershocks were detected in the following three months. The aftershock distribution clearly delineates the mainshock rupture to the westerly dipping fault plane at a depth of 11 to 12 km. The difference in the dip of fault plane suggests a complex source process of the earthquake sequence.

I obtain broadband waveform data from the IRIS database and select regional stations that have epicentral distances of less than 2.5 degrees. The locations of the earthquake and stations are displayed in Figure 3.10 and the coordinates are given in

Table 3.1. For the generation of Green's functions, I use an average 1-D velocity model based on the 2-D model derived by Hughes and Luetgert (1991) from a seismic refraction experiment. The predominant earthquake mechanism in the Adirondacks – western Quebec seismic zone is thrust faulting along medium to steeply dipping planes.

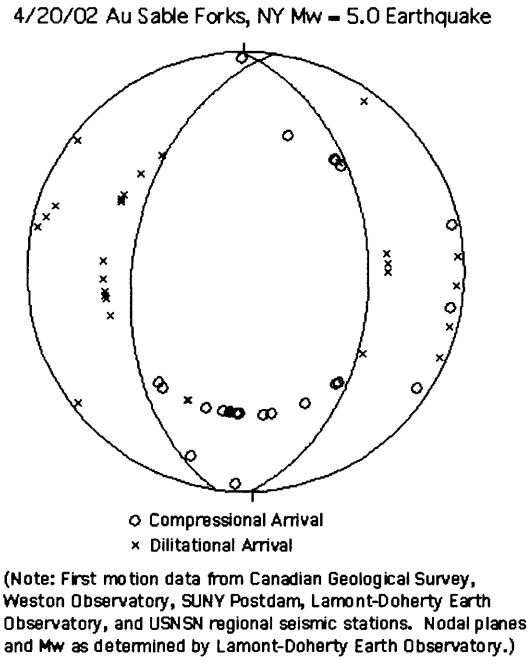

Figure 3.9. The fault plane solution based on P-wave first motion polarities plotted by Professor John Ebel at Weston Observatory

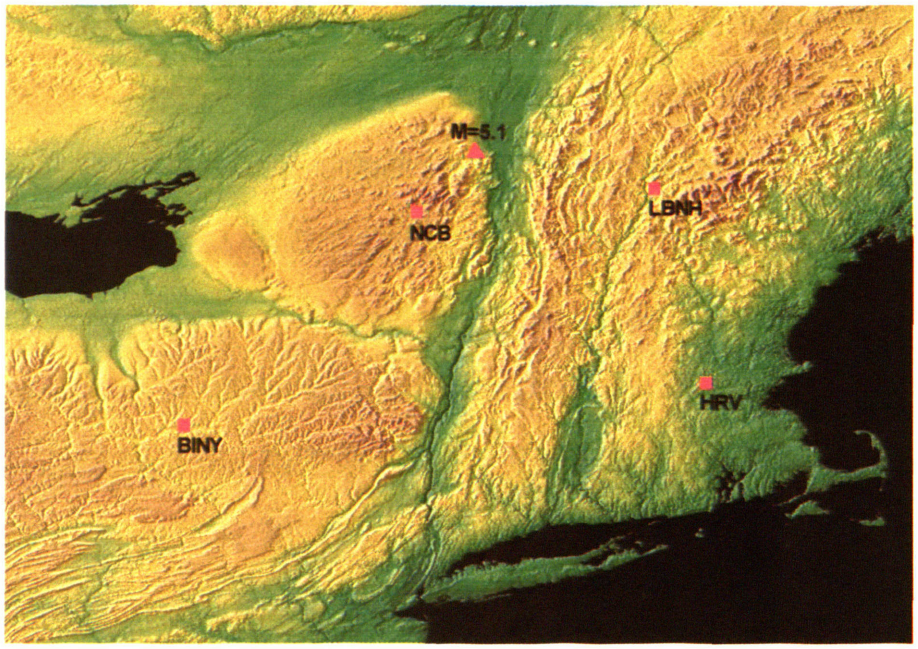

Figure 3.10. The epicenter of the Au Sable Fork earthquake and the station locations.

Station	Lat	Long	Elevation (m)	Azimuth
HRV	42.51N	71.56W	180	141°
BINY	42.20N	75.99W	498	217°
NCB	43.97N	74.22W	500	217°
LBNH	44.24N	71.93W	367	101°

Table 3.1. Summary of station locations.

The rotated three-component waveform data are displayed in Figure 3.11. Data are sampled at 100 Hz and have high signal-to-noise ratios. The waveforms are lowpass filtered at 5 Hz before the inversion. I set the maximum scale level for wavelet decomposition to be $j = 9$. The inversion requires us to set the source duration a priori. According to Beresnev (2002) the source duration can be estimated if we assume the displacement-time history at the fault radiates in the far-field with a "ω^{-2}" spectrum,

$$u(t) = u\left[1 - \left(1 + \frac{t}{\tau}\right)\exp\left(-\frac{t}{\tau}\right)\right], \tag{3.3.1}$$

where τ is the parameter controlling the rise time (the time it takes the dislocation to reach its static value *U*), and u is the static displacement. The modulus of the Fourier transform of the radiated displacement far-field is

$$\Omega(\omega) = \left|\int_{-\infty}^{\infty} \dot{u}(t)\exp(-i\omega t)dt\right| = \frac{u}{1+(\omega\tau)^2}, \tag{3.3.2}$$

where ω is the angular frequency and $\dot{u}(t)$ is the slip velocity. Equation (3.3.2) is valid provided that (1) the medium is homogeneous; (2) the source dimension can be considered small compared with the distance to the observation point; and (3) the distance is longer than the wavelength of interest. Since the far-field radiation of both P and S waves from a displacement-discontinuity source is controlled by the same displacement-time history, both waves will have the same spectral shape and the same corner frequency. In the "ω^{-2}" model, the spectral content of a seismic pulse should be flat at periods longer than the rupture time of the fault. The corner frequency is the crossover frequency between the plateau and the ω^{-2} behavior, defined by the intersection of the asymptote to the plateau and the asymptote of the ω^{-2} decay.

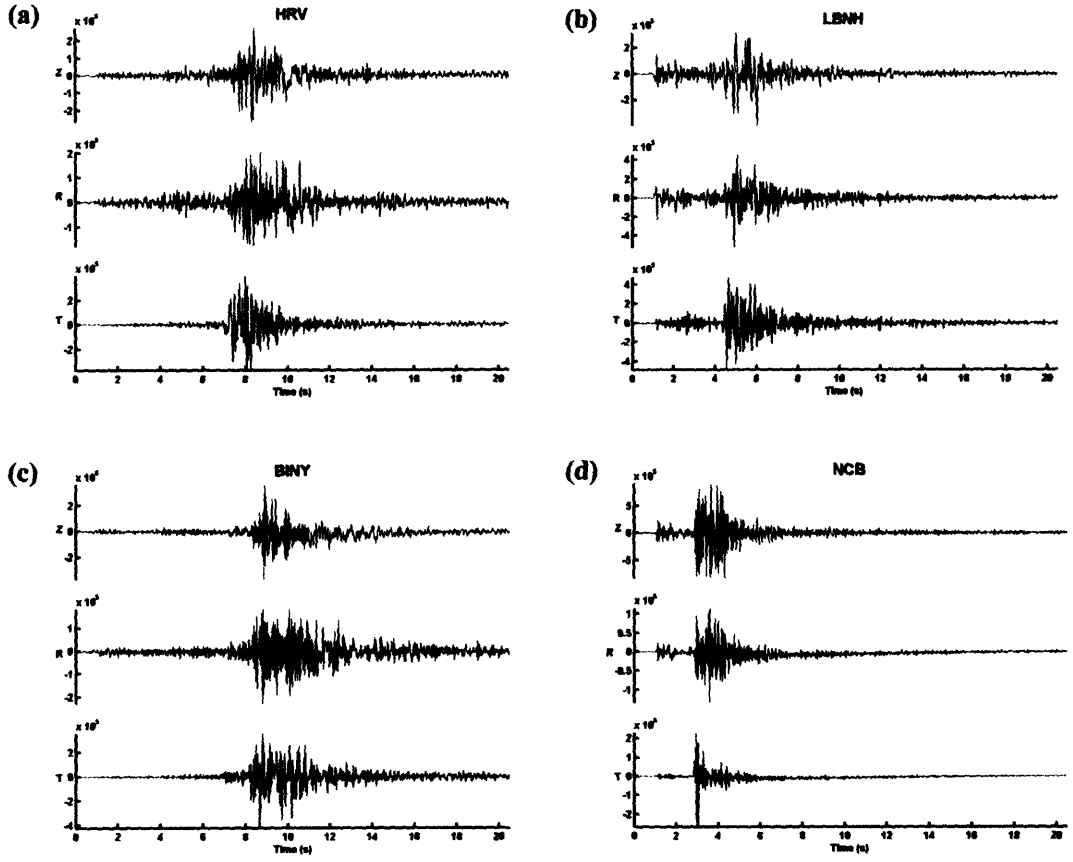

Figure 3.11. Three-component seismograms of the 2002 April 20 Au Sable Forks, New York earthquake. The data are record by (a) HRV, (b) LBNH, (c) BINY, and (d) NCB.

The source rise time is formally infinite in equation (3.3.1). However, it could be reasonably well-defined as the time T over which 90% of static displacement is reached. Then equation (3.3.1) becomes

$$\left(1+\frac{T}{\tau}\right)\exp\left(-\frac{T}{\tau}\right)=1-0.9, \tag{3.3.3}$$

Given $\omega_c \equiv 1/\tau$ is the corner frequency of the spectrum, the relation between the corner frequency and the source duration is

$$T \approx 0.6/f_c \tag{3.3.4}$$

where $f_c = \omega_c/2\pi$. Equation (3.3.4) is a good approximation for the a priori source duration required to provide for the inversion. Figure 3.12 plots the amplitude spectra of the P-wave arrivals at four different stations, and shows the corner frequency of the Au Sable Forks earthquake is about 1 Hz. This gives a source duration of about 3.5 second.

Wavelet-domain waveform inversion results showing the MTRF components in Figure 3.13 indicate that the wavelet-based method works well in this case. A stable solution can be attained by solving the linear system of equation up to scale level of $j = 9$ for 64 wavelet coefficients. I repeat the inversion with different choices of fractional spline wavelets for parameterization and find that the order $\alpha = 0.1$ fractional spline wavelet gives the best results. The fit between the observed and synthetic seismograms (Fig. 3.13) is quite satisfactory. Since full moment tensors are available, I can decompose them into the double-couple and non-double-couple components. The non-DC component is defined as the sum of the compensated linear vector dipole (CLVD) and isotropic (ISO) components. The size of the ISO, CLVD and DC can be evaluated in percent as follows:

$$\mathrm{ISO} = \frac{1}{3}\frac{\mathrm{Tr}(\mathbf{M})}{|M_{\max}|} \times 100\%, \tag{3.3.5}$$

$$\mathrm{CLVD} = -2\frac{M^*_{\min}}{|M^*_{\max}|}\left(100\% - |\mathrm{ISO}|\right), \tag{3.3.6}$$

$$\mathrm{DC} = 100\% - |\mathrm{ISO}| - |\mathrm{CLVD}|, \tag{3.3.7}$$

where Tr(**M**) is the trace of the seismic moment tensor **M**, $M_{\max}$ is the eigenvalue of **M** that has the maximum absolute value, and $M^*_{\max}$ and $M^*_{\min}$ are the eigenvalues of the

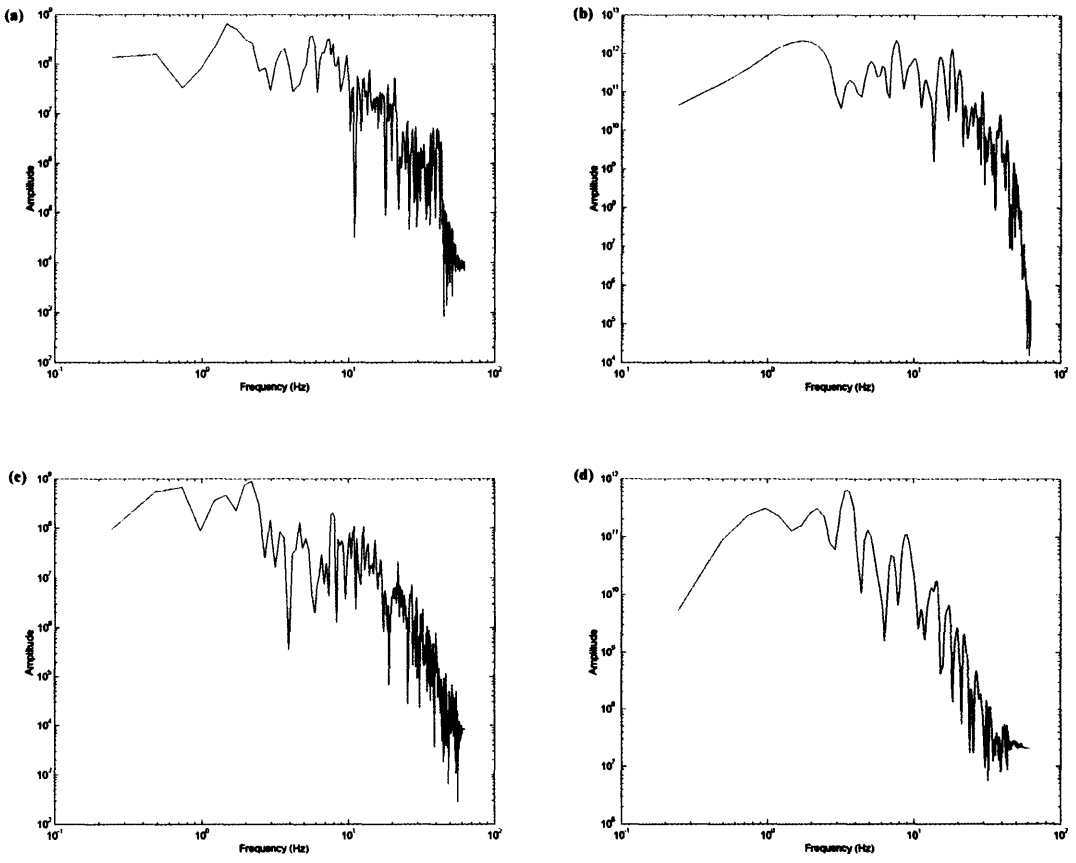

Figure 3.12. The amplitude spectra of the P-wave arrivals recorded at (a) HRV, (b) LBNH, (c) BINY, and (d) NCB.

deviatoric moment tensor with the maximum and minimum absolute values, respectively. ISO and CLVD components can be either positive or negative, and the DC component is always positive. The plus / minus signs of the ISO and CLVD components express the explosive / implosive or tensile / compressive character of the source.

Decomposition of the moment tensor yields an isotropic part (13%), a double-couple (79%), and a compensated linear vector dipole (–8%). The duration of the source function is about 3.0 s. The recovered double-couple MTRFs reveal a predominantly thrust mechanism striking north (Figure 3.13). Following Vasco (1989)'s procedure, I perform singular value decomposition of the MTRFs into 'principal components' to find the best common source-time function corresponding to the biggest singular value. The source-time function of the earthquake seems to be characterized by two main subevents. The first one lasts for about 2 s, and the smaller second subevent lasts for about 1 s. There is no significant change in mechanism with time. The 95% confidence limit error bars plotted in Figure 3.13 show that while the first subevent is statistically significant, the resolvability of the second subset is more doubtful. To double-check the validity of the results, I find that the predominantly thrust mechanism is consistent with the waveform inversion at lower frequencies (0.03–0.1 Hz) performed by Seeber et al., (2002) and also with the results from P-wave polarities (Ebel, 2002).

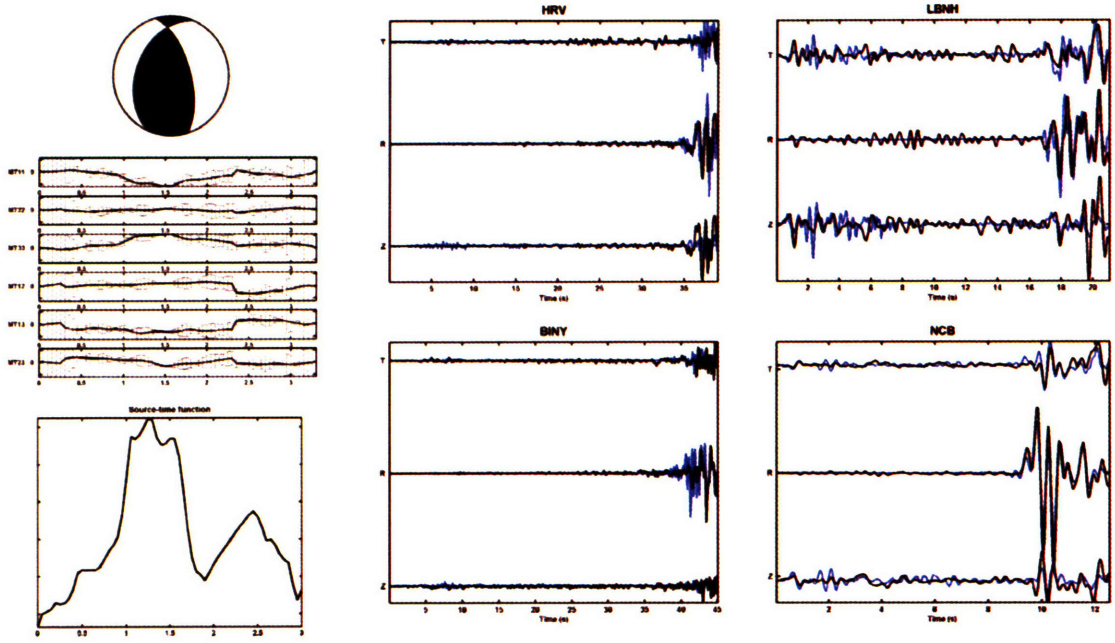

Figure 3.13. Moment tensor rate functions retrieved by wavelet-domain inversion of the 20 April 2002 Au Sable Forks, New York earthquake. Upper left part: Upper hemisphere, equal-area stereo plot of the source mechanism yielded by the MTRFs. The filled areas correspond to compressional quadrants. Middle left part: the MTRFs components, from top to bottom, M_{11}, M_{22}, M_{33}, M_{12}, M_{13}, and M_{23} are shown. Lower left part: the source-time function obtained by singular value decomposition of the MTRFs. Waveform fitting between the observed (black lines) and synthetic seismograms (blue lines) for stations HRV (upper middle part), BINY (lower middle part), LBNH (upper right part), and NCB (lower right part).

The source-time function is parameterized by fractional spline wavelets whose relative amplitudes are determined by inversion. The scale level of wavelet decomposition is dependent on the frequency content of the seismic signal. If the level is too high, the result is instability in the estimated amplitudes. On the other hand, if it is too low, the result is a poor description of the source and possibly poor estimates of the source parameters.

For most shallow earthquakes, the strongest effect that limits the resolution of the source mechanism, depth and the source-time function is the interference between direct and surface reflected phases. If the source is deep and the direct and reflected phases are well separated in time, the resolution is mainly limited by the incomplete coverage of the focal sphere. This limitation can be minimized by using both P and S waves in the analysis. Interference affects the resolution in a complicated manner.

Random background microseismic noise poses no serious problem for the inversion as long as the signal-to-noise ratio is large. The inversion techniques discussed in this study are based on a least-squares minimization of the differences between the data and the theoretical seismograms. In a linear problem, in the presence of Gaussian noise, the least-squares criterion gives an unbiased estimate of the parameters and unbiased measure of their uncertainty. Other errors, such as errors in the instrument magnification, in the receiver crustal response, or in the geometrical spreading pose more serious problems to the least-squares solution. Patton and Aki (1979) made an extensive investigation of the effects of multiplicative errors on the moment tensor estimates from surface waves. The phase incoherence between the observed and theoretical seismograms, in general, causes

an underestimation of the strength of the source. Anisotropy is frequently present in geological structures. Due to coupling of propagation and source effects in the seismic waveforms, neglect of anisotropy will lead to errors in the retrieved source, resulting in the presence of spurious isotropic and compensated linear-vector dipole components in the moment tensor (Šílený and Vavryèuk, 2002).

3.5 Application to September 3, 2002 Yorba Linda, California earthquake

A M4.8 mainshock occurred at 00:08 am on 3 September 2002 northeast of Yorba Linda in Orange County at a depth of 10 km. It was preceded by two foreshocks at 09:50pm (ML2.6) and 10:23pm (ML1.5) on Sept 2nd. It was also followed by 23 aftershocks during the next 9 hours, with the two largest aftershocks of ML2.8 at 00:15am and 04:28am.

Earthquakes in California are studied extensively and so, the Yorba Linda earthquake provides a good test for the wavelet-domain waveform inversion technique. The results presented by the U.S.G.S. exhibited strike-slip faulting on a vertical plane striking N30°W. This mechanism is consistent with the mainshock being near the Whittier fault. The Whittier fault is one of the fastest moving faults in the Los Angeles basin. A right-lateral Late-Quaternary slip rate of about 2.8 mm/year was obtained for the Whittier fault during recent investigations by Gath et al. (1992). The fault extends from

Corona, northwest of Lake Elsinore, into the Los Angeles basin to the northwest. The approximately 25 mile long Whittier fault is the west-northwest continuation of the Elsinore fault. The Whittier is a right-lateral strike-slip fault that transfers a substantial portion of the dextral slip on the Elsinore into the Los Angeles basin creating north-south compressional faults.

Preliminary locations of the aftershocks appeared to form a northeast trend, suggesting that this sequence occurred on a small conjugate fault, adjacent to the Whittier fault. Alternatively, this sequence might occur near a jog in the Whittier fault itself. This sequence is located along the eastern part of the Los Angeles basin where the Whittier fault and the buried thrust faults to the west from a complex zone of deformation. The 1987 ML5.9 Whittier Narrows earthquake occurred near the north end of this zone. The last previous M4 earthquake to occur in the greater Los Angeles area was located near Compton on 28 October 2001. The Yorba Linda M4.6 event is the largest in the Los Angeles metropolitan area since a M5.1 Northridge aftershock in April 1997.

I inverted seismic waveforms that were recorded by six seismic stations (Figure 3.14) with epicentral distances not greater than 1.5 degrees. Using the reflectivity method, Green's functions were calculated for smooth 1-D seismic velocity model of each station derived from the 3D Vp/Vs models (Hauksson, 2000) that were determined for Southern California using P and S-P travel times from local earthquakes and controlled sources. The duration of the source-time function estimated from the corner

frequency is about 2 seconds. Figure 3.14 shows that the observed and best-fit theoretical seismograms are generally well matched for the Yorba Linda event. Figure 3.15 shows the fault-plane solution of the earthquake, and the mechanism is strike-slip faulting on a almost vertical plane with a N40°W strike, which is consistent with the U.S.G.S solution.

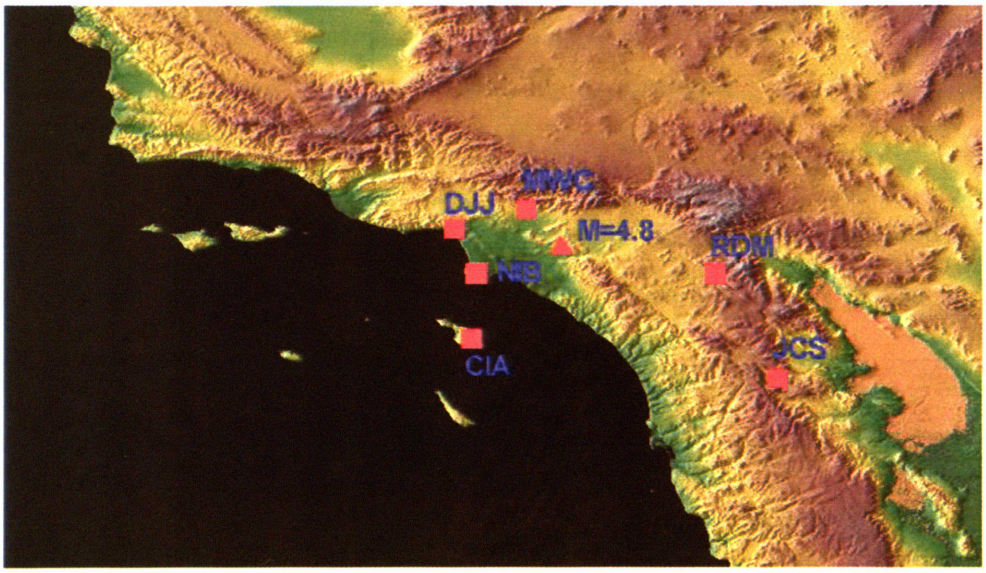

Figure 3.14. The epicenter of the Yorba Linda earthquake and the station locations.

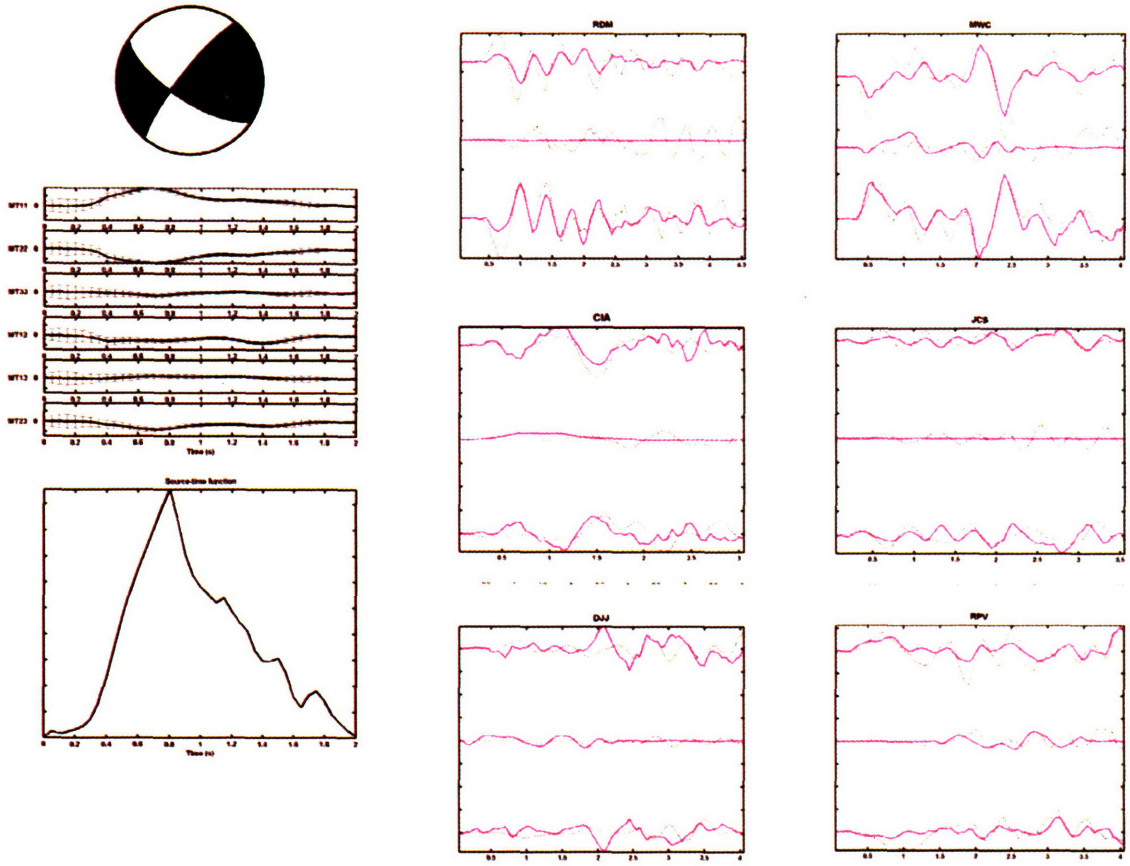

Figure 3.15. Moment tensor rate functions retrieved by wavelet-domain inversion of the 3 September 2002 Yorba Linda, California earthquake. Upper left part: Upper hemisphere, equal-area stereo plot of the source mechanism yielded by the MTRFs. The filled areas correspond to compressional quadrants. Middle left part: the MTRFs components, from top to bottom, M_{11}, M_{22}, M_{33}, M_{12}, M_{13}, and M_{23} are shown. Lower left part: the source-time function obtained by singular value decomposition of the MTRFs. Waveform fitting between the observed (black lines) and synthetic seismograms (red lines) for stations RDM, MWC, CIA, JCS, DJJ, and RPV.

3.6 Application to the Oman Microseismic Events

I estimated the seismic moment tensor using wavelet-domain waveform inversion to study the microearthquake mechanisms. Most microearthquakes in the Field were too small to generate waveforms and P-wave polarities that can be read reliably. Therefore, only larger events with local magnitudes greater than one were selected for analysis. The waveforms of these selected events have substantial signal-to-noise ratio. P-wave first motions are also read from the five borehole stations.

The source parameters, the linear data kernel, and the waveform data were represented by wavelet expansions, leading to a multiscale sparse matrix representation. The regularized least-squares solution was solved by the conjugated gradient method. The theoretical seismograms, or the Green's functions, were computed by the discrete wavenumber method (Bouchon & Coutant, 1994). The seismograms were dominated by strong scattering and very little similarity in waveforms between events was observed. The waveform inversion technique requires a correct identification of various wavetrains but the strong scattering makes this almost impossible. The presence of strong shear wave splittings also makes the observed S-waves in the seismograms difficult to use for inversion. Therefore, I applied the waveform inversion method only on P-waves but not on the P-wave codas and S-waves. Vertical and radial components of the seismograms from the five borehole stations and five P-wave polarities were used for each event. The waveforms of the selected events recorded at one of the five stations are displayed in Figure 3.16.

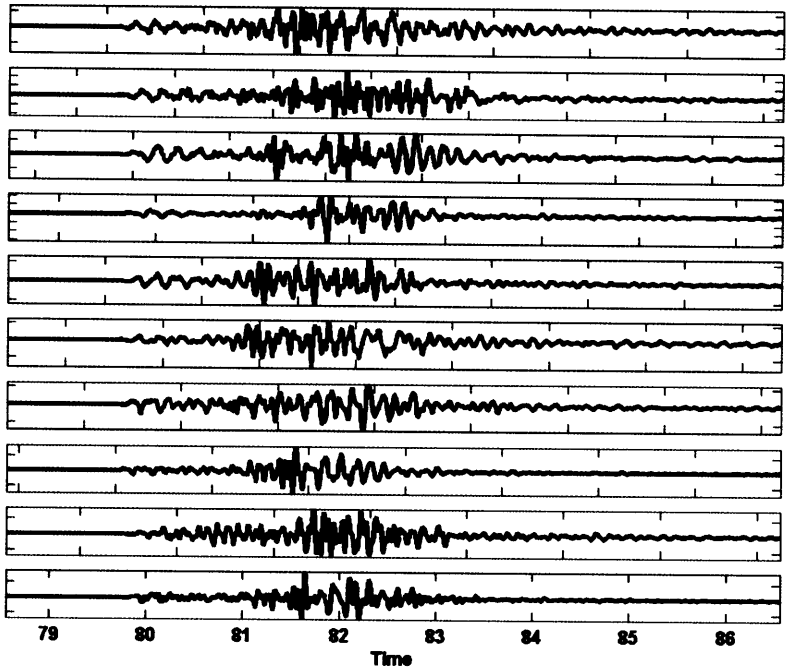

(a)

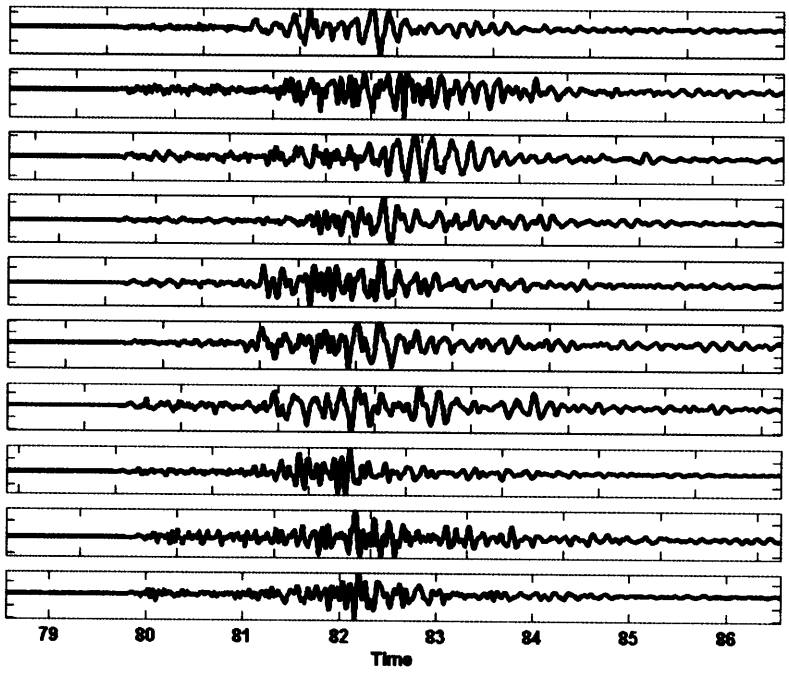

(b)

Figure 3.16. Waveforms of selected events with magnitude > 1.0 recorded by station VA1.

Summaries of all inversion results are given in Figure 3.17. The focal mechanisms displayed in Figure 3.17 show that the dominant style of faulting is left-lateral strike-slip in the shallow depths less than 1.5 km. Dip-slip along an obliquely trending fault predominates for deeper events (greater than 2.0km). All waveform inversion results are in good agreement with the P-wave polarities. The nearly vertical planes generally have a strike of NE-SW. The strikes of the inferred fault planes are consistent with the trend of the seismicity and the faults observed both in the field and reflection seismics. It also matches the orientation of the subvertical fractures that are parallel to the major faults in the Field. The obtained focal mechanisms consist of mostly double-couples (> 80%) and only a minor share of volumetric and CLVD parts. I also confirm the results by comparing the observed data and synthetic waveforms reconstructed by using the double-couple component only. Both shallow strike-slip and deep dip-slip events infer a maximum extensional stress regime in the WNW-ESE direction.

Some of the shallow strike-slip events have focal plane orientation that deviate from the fault trace by as much as 20 to 30 degrees. Given that the strike uncertainties are smaller (less than 20 degrees for 90% confidence) than the observed deviation, it is possible that this observed deviation is statistically significant. This can be explained by the en echelon structures that are commonly observed with strikes that deviate from the main fault system. Generally, Faults are more complex than an idealized rectiplanar structure. Traces of many normal faults form an array of closely overlapping distinct segments rather than a single slip plane (Peacock & Sanderson, 1991, 1994). From the mapview of the Field (Figure 3.17), we can see that the central graben fault system in the

Field comprises segmented normal and strike-slip faults, similar in appearance to those observed in rift systems and regions of crustal extensions worldwide. These overlapping segments that can either be unconnected or link vertically or laterally into a single continuous fault surface. This segmented, discontinuous character of faults is observable both in nature and experiments. The fault segements are commonly organized en echelon (Jackson & McKenzie, 1983), zigzag (Freund and Merzer, 1976), or sinusoidal pattern (Wu & Bruhn, 1994). Slip on overlapping, segmented normal faults perturbs the local stress field and can promote failure across the ramp (Crider & Pollard, 1998). In some cases, the fault may be continuous but exhibit one or more jogs or bends. Such jogs may represent breached relay structures between originally discontinuous segments.

In loose and granular materials, it is common that a fault appears as a zone of en echelon faults. Along left-lateral fault ruptures, these faults are predominantly right-stepping that allows a small component of tensile opening (Yeats et al., 1997). If two echelon faults are not connected across the ramp by a continuous fault surface or a zone comparable to the segments themselves, the pair is soft-linked, leaving an active ramp (Davies et al., 1997). Active ramps may allow fluid communication from the footwall to the hanging wall of the composite structure. If the two segments are connected by a comparable fault across the ramp, the pair is hard-linked, and the ramp is mechanically breached. This creates a composite fault. For sealing faults, such a breach would prevent fluid communication across the composite structure (Crider & Pollard, 1998).

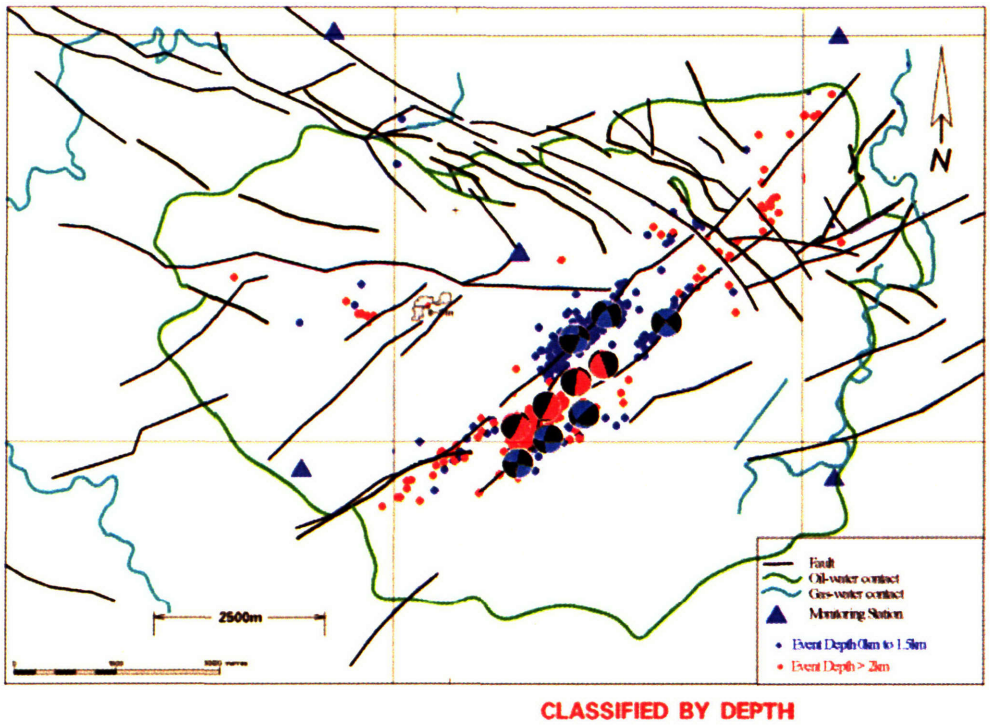

Figure 3.17. Focal mechanisms of the selected 10 events in the Field. The blue beach-balls denote events with focal depth less than 2km, and the red ones denote events with focal depth greater than 2 km.

3.7 Conclusions

I have described a wavelet-based approach to linear waveform inversion to estimate the point source mechanism and source-time history. The source parameters, the linear data kernel, and the waveform data are represented by wavelet expansions, leading to a multiscale sparse matrix representation. The regularized least-squares solution is computed by an iterative solver, such as the conjugated gradient method. I have tested the method on three-component synthetic data generated for a configuration of a local seismic network, and have demonstrated the success for applying the algorithm to small seismic events. Unlike previous methods, I discretize the MTRFs by wavelets and perform the inversion in the wavelet domain. The formulation of the inverse problem is linear and so, there is no dependence on the initial guess of the solution. Solving a linear inverse problem in the wavelet domain leads to a multiscale representation, and this provides a flexible way to explore and attain stability by solving the problem from coarse to fine scale levels.

Experiments of inversion on noise-free synthetic data show good resolution of all components of the MTRF. Compared to the conventional time-domain method with overlapping triangular parameterization scheme, I have shown that the proposed method can recover the MTRFs with comparable or improved quality and accuracy. The high compressibility of wavelets is shown to be a desirable feature, which allows us to determine the source parameters satisfactorily while decreasing the number of parameters to be estimated by several times.

Tests on records corrupted by correlated random noise demonstrate that robust estimates of the source parameters can also be achieved even if the noise level reaches about 20% of the standard deviation of the signal amplitude. Implementation of a wavelet thresholding technique improves the robustness of the method because it denoises the data before they are inverted. Strong random noise mainly limits the ability to estimate the isotropic components of the moment tensor, with little effect on the double-couple components. I have investigated the influence on the choice of wavelet on the solution. By repeating the inversion using different orders of fraction spline wavelets, I have found that improvement on data misfit is possible if the "right" choice of wavelet is used, and this leads to a data adaptive parameterization strategy.

I apply the method to three cases in different geological settings: (1) the April 20, 2002 Au Sable Forks, New York earthquake, (2) the September 3, 2002 Yorba Linda, California earthquake, and (3) eleven microseismic events in the Field, Oman. In all three cases, the source parameters are retrieved satisfactorily with good fitting between the observed and synthetic seismograms. The Au Sable Forks earthquake source has a large double-couple component (79%) with a predominantly thrust mechanism striking north and a source duration of 3 s. The results are consistent with other estimates using waveform inversion at lower frequencies and P-wave polarities. The waveform inversion of the Yorba Linda, California earthquake yielded a mechanism of strike-slip faulting on an almost vertical plane with a N40°W strike, which is consistent with the U.S.G.S solution. For the inversion of the microseismic events in the Field, Oman, I limited the

dataset to only the direct P-waves because no adequate model of the medium was available for modeling the later phases. The solutions revealed NE-SW trending left-lateral strike-slip and dip-slip to be the dominant styles of faulting in the field. All waveform inversion results are in good agreement with the P-wave polarities.

Despite the various improvements offered by the wavelet-based method, several other factors will continue to play important roles in the success of applying waveform inversion to estimate earthquake source parameters. One of the foremost challenges is to construct an accurate velocity model. Analysis of the source parameters of small earthquakes is often complicated by their spectral properties at high frequencies, where path and site effects are not easily distinguished from the source characteristics. This also makes calculating realistic Green's functions difficult. Commonly, we need to simplify the seismogram in such cases. This can be done by low-pass filtering of the data (e.g., Schurr & Nábèlek, 1999). Alternatively, with the wavelet approach, we can solve the inverse problem at a lower scale level. Both methods help us alleviate the problem of fitting high-frequency seismic signals that are poorly modeled due to limited knowledge of the medium.

3.8 References

Aki, K. and Richards, P.G., 1980, Quantitative Seismology, Theory and Methods, vol I,: W.H. Freeman & Co., CA., 557 pp.

Anant, K.S. and Dowla, F.U., 1997, Wavelet transform methods for phase identification in three-component seismograms: Bull. Seism. Soc. Am., **87**, 1598 – 1612.

Beresnev, I..A., 2002, Source parameters observable from the corner frequency of earthquake spectra: Bull. Seis. Soc. Am., **92**, 2047-2048.

Bouchon, M. and Coutant, O., 1994, Calculation of synthetic seismograms in a laterally varying medium by the boundary element-discrete wavenumber method: Bull Seismol. Soc. of Am., **84**, 1869 – 1881.

Crampin, S. and Lovell, J.H., 1991, A decade shear-wave splitting in the Earth's crust: what does it mean? What use can we make of it? And what should we do next?: Geophys. J. Int., 107, 387-407.

Crider, J.G. and Pollard, D.D., 1998, Fault linkage: three-dimensional mechanical interaction between echelon normal faults: J. Geophys. Res., **103**, 24,373 – 24,391.

Daubechies, I, 1992, Ten lectures on wavelets: SIAM, 357 pp.

Davies, R.K., Crawford, M., Dula, W.F., Cole, M.J., and Dorn, G.A., 1997, Outcrop interpretation of seimic-scale normal faults in south Oregon: description of structural styles and evaluation of subsurface interpretation methods: Leading Edge, **16**, 1135 – 1141.

Deighan, A.J. and Watts, D.R., 1997, Ground-roll suppression using the wavelet transform: Geophysics, **62**, 1896 – 1903.

Delaney, A.H. and Bresler, Y., 1995, Multiresolution tomographic reconstruction using wavelets: IEEE Trans Image Processing, **4**, 799 – 813.

Donoho, D.L., 1992, Wavelet thresholding and W.V.D.: A 10-minute tour: Int. Conf. On Wavelets and Applications, Toulouse, France.

Dreger, D.S. and Helmberger, D.V., 1993, Determination of source parameters at regional distances with three-component sparse network data: J. Geophy. Res., **98**, 8107 – 8125.

Dziewonski, A.M. and Gilbert, F., 1974, Temporal variation of the seismic moment tensor and evidence of precursive compression for two deep earthquakes: Nature, **247**, 185 – 188.

Finkbeiner, T., Zoback, M., Flemings, P., and Stump, B., 2001, Stress, pore pressure, and dynamically constrained hydrocarbon columns in the South Eugene Island 330 field, northern Gulf of Mexico: AAPG Bull., **85**, 1007-1031.

Foufoula-Georgiou, E., and Kumar, P. (ed.), 1995, Wavelets in Geophysics: Academic Press, 373 pp.

Freund, R. and Merzer, A.M., 1976, The formation of rift valleys and their zigzag fault patterns: Geol. Mag., **113**, 561 –568.

Gaarenstroom, L., Tromp, R.A.J., Jong, M.C.D., and Brandenburg, A.M., 1993, Overpressures in the Central North Sea: implications for trap integrity and drilling safety: in Parker, J.R. (eds.), Petroleum Geology of Northwest Europe: Proceedings of the 4th Conference: 2. Geological Society, London, 1305-1313.

Gath, E. M., Gonzalez, T., and Rockwell, T. K., 1992, Evaluation of the Late-Quaternary rate of slip, Whittier Fault, Southern California: U.S. Geological Survey, Final

Technical Report, National Earthquake Hazards Reduction Program, September 3, 22 pp.

Gilbert, F. and Dziewonski, A.M., 1975, An application of normal mode theory to the retrieval of structural parameters and source mechanisms from seismic spectra: Philos. Trans. R. Soc. London, Ser. A, **278**, 187 – 269.

Hauksson, E., 2000, Crustal structure and seismicity distribution adjacent to the Pacific and North America plate boundary in southern California: J. Geophys. Res., **105**, 13875-13903.

Hughes, S. and Luetgert, J.H., Crustal structure of the western New England Appalachians and the Adirondack Mountains: J. Geophys. Res., **96**, 16471 – 16494.

Jackson, J. and McKenzie, D., 1983, The geometrical evolution of normal fault systems: J. Struct. Geol., **5**, 471 – 482.

Kane, J.A. and Herrmann, F.J., 2001, Wavelet domain inversion with application to well logging: 71st Ann. Int. Mtg. Soc. Expl. Geophys., Expanded Abstracts, 694 – 697.

Kennett, B.L.N., 1983, Seismic wave propagation in stratified media: Cambridge University Press, Cambridge, 339 pp.

Langston, C.A., 1981, Source inversion of seismic waveforms: the Koyna, India earthquake of 13 September 1967: Bull. Seis. Soc. Am., **71**, 1-24.

Mallat, S.G., 1989, A theory for multiresolution signal decomposition: the wavelet representation: IEEE Trans. Pattern Analysis Machine Intel., **11**, 674 – 693.

Mallat, S., 1998, A wavelet tour of signal processing: Academic Press, 577 pp.

McCowan, D.W., 1976, Moment tensor representation of surface wave sources: Geophys. J. R. Astr. Soc., **44**, 595 – 599.

Mendiguren, J.A., 1977, Inversion of surface wave data in source mechanism studies: J. Geophys. Res., **82**, 889 – 894.

Mildren, S.D., Hillis, R.R., and Kaldi, J., 2002, Calibrating predictions of fault seal reactivation in the Timor Sea: APPEA J., **42**, 187-202.

Nábělek, J., 1984. Determination of earthquake source parameters from inversion of body waves: *PhD thesis*, MIT.

Patton, H., and Aki, K., 1979, Bias in the estimate of seismic moment tensor by the linear inversion method: Geophys. J. R. Astr. Soc., **59**, 479-495.

Peacock, D.C.P, and Sanderson, D.J., 1991, Displacements, segment linkage and relay ramps in normal fault zones: J. Struct. Geol., **13**, 721 – 733.

Peacock, D.C.P, and Sanderson, D.J., 1994, Geometry and development of relay ramps in normal fault systems: AAPG Bull., **78**, 147 – 165.

Reynolds, S., Hillis, R..R., and Paraschivoiu, E., 2003, In situ stress field, fault reactivation and seal integrity in the Bight Basin, South Australia, Exploration Geophysics, **34**, 174-181.

Ruff, L.I. and Tichelaar, B.W., 1990, Moment tensor rate functions for the 1989 Loma Prieta Earthquake: Geophys. Res. Lett., **17**, 1187 – 1190.

Schurr, B. and Nábèlek, J., 1999, New techniques for the analysis of earthquake sources from local array data with an application to the 1993 Scotts Mills, Oregon, aftershock sequence: Geophys. J. Int., **137**, 585 – 600.

Seeber, L., Kim, W.-Y., Armbruster, J.G., Du, W.-X., Lerner-Lam, A., and Friberg, P., 2002, The 20 April 2002 Mw 5.0 earthquake near Au Sable Forks, Adirondacks, New York: a first glance at a new sequence, Seism. Res. Lett., **73**, 480-489.

Šílený, J., Panza, G.F., and Campus, P., 1992, Waveform inversion for point source moment tensor retrieval with variable hypocentral depth and structural model: Geophys. J. Int., **109**, 259 – 274.

Šílený, J. and Pšenčík, I., 1995, Mechanisms of local earthquakes in 3-D inhomogeneous media determined by waveform inversion, Geophys. J. Int., **121**, 459 – 474.

Šílený, J., and Vavryèuk, V., 2002, Can unbiased source be retrieved from anisotropic waveforms by using an isotropic model of the medium?: Tectonophysics, **356**, 125-138.

Sipkin, S.A., 1982, Estimation of earthquake source parameters by the inversion of waveform data: Phy. Earth Planet. Interiors, **30**, 242 – 259.

Strang, G. and Nguyen, T., 1997, Wavelets and filter banks: Wellesley-Cambridge Press, 520 pp.

Stump, B.W. and Johnson, L.R., 1977, The determination of source properties by the linear inversion of seismograms: Bull. Seismol. Soc. Am., **67**, 1489 – 1502.

Unser, M. and Blu, T., 2000, Fractional splines and wavelets: SIAM Review, **42**, 43 – 67.

Vasco, D.W., 1989, Deriving source-time functions using principal component analysis: Bull. Seismol. Soc. Am., **79**, 711 – 730.

Wang. G., Zhang, J. and Pan G., 1995, Solution of inverse problems in image processing by wavelet expansion: IEEE Trans. Image Processing, **4**, 579 – 593.

Willemse, E.J.M., 1997, Segmented normal faults: correspondence between three-dimensional mechanical models and field data: J. Geophys. Res., **102**, 675 – 692.

Wood, W., 1999, Simultaneous deconvolution and wavelet inversion as a global optimization: Geophysics, **64**, 1108 – 1115.

Wu, D. and Bruhn, R.L., 1994, Geometry and kinematics of active normal faults, South Oquirrh Mountains, Utah: implications for fault growth: J. Struct. Geol., **16**, 1061 – 1975.

Yeats, R.S., Sieh, K., and Allen, C.R., 1997, The geology of earthquakes: Oxford Unviersity Press, 518 pp.

Zhu, W., Wang, Y., Deng, Y, Yao, Y. and Barbour, R., 1997, A wavelet-based multiresolution regularized least squares reconstruction approach for optical tomography, IEEE Trans. Medical Imaging: **16**, 210 – 217.

Chapter 4

Characterization of reservoir fracture pattern using shear-wave splitting analysis

4.1 Introduction

Shear-wave splitting was first identified in the crust above small earthquakes in Turkey by Crampin et al. (1980), and has been observed widely in a variety of tectonic settings from earthquake recordings to exploration seismic data, independent of source orientation. It has become well-known that crack-induced stress-aligned shear wave splitting, with azimuthal anisotropy, is an inherent characteristic of almost all rocks in the upper crust (Crampin and Lovell, 1991). Such splitting writes easily recognizable signatures into the three-component particle motion of shear wave arrivals (visible in particle motion diagrams or hodograms), so that shear wave splitting is the key diagnostic phenomenon for investigating seismic anisotropy.

When a shear wave enters an anisotropic region it usually splits into two approximately orthogonal polarizations which propagate with different velocities so that a time delay develops between the two shear waves (Figure 1). Fast shear-wave polarizations are independent of the initial polarization of shear-wave at the source and are produced by the anisotropic properties of the medium. The common observation of aligned first split shear-wave polarizations perpendicular to the local minimum principal stress supports the hypothesis that stress-aligned fluid-filled microcracks, cracks and

porespace exists in most rocks of the upper crust. The differential time delay between the arrival of the fast and the slow shear-wave is proportional to the crack density (number of cracks per unit volume) within the rock body and the length of the raypath.

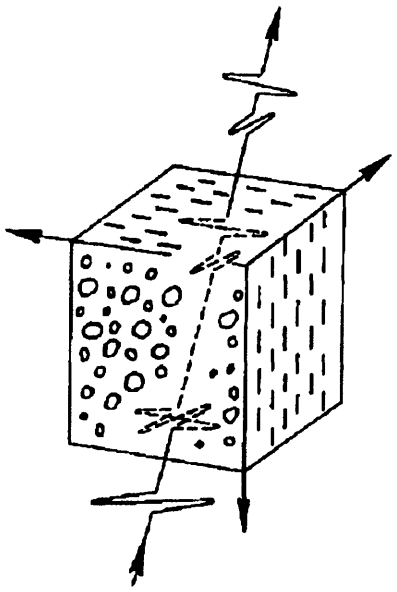

Figure 4.1. Schematic illustration of stress-aligned cracks and shear-wave splitting. The vertical stress in the crust is usually greater than the minimum horizontal compression, so that racks are aligned nearly vertically and perpendicular to the direction of minimum compression. A near vertically traveling shear wave splits into two nearly orthogonal components with different arrival times. The polarization of the faster component is usually parallel to the strike of the cracks.

Typically, below a critical depth of 500 – 1000m, the polarizations of the faster split shear wave are approximately parallel (within 20°) to the direction of maximum horizontal stress (Crampin, 1993; Crampin and Chastin, 2000). Note that in general, the

vertical stress, σ_v, is zero at the free surface but increases with depth, and a critical depth is reached when σ_v equals the minimum horizontal stress, σ_h. Below this depth, cracks open normal to the minimum stress, which is typically horizontal so that the cracks are usually vertical striking approximately parallel to the maximum horizontal stress, σ_H (Crampin, 1990) and gives the characteristic stress-parallel shear wave polarizations. Above this depth, crack distributions are controlled by stress-release and lithologic phenomena, and may be very disturbed. This means that the orientations of hydraulic fractures, directions of water floods and other hydrocarbon production strategies can be optimized by analyzing shear wave splitting.

Shear waves are much more sensitive than compressional waves to the presence of fractures or microfractures and the fluid content within the fracture network. S-wave splitting and velocities are extremely sensitive to the local stress field because all rocks, especially carbonates, contain incipient networks of microfractures at a state of near-criticality.

The monitoring of shear-wave splitting is an important tool for determining the direction and evaluating the bulk density of reservoir fractures. In azimuthally anisotropic media, the split shear-wave properties, fast shear-wave polarization directions (φ) and differential time delays (δt) constitute valuable data to invert for subsurface fracture geometry and to estimate crack density and permeability anisotropy within hydrocarbon and geothermal fractured reservoirs.

This chapter presents the results of analysis of shear waves from induced microearthquakes recorded in the Field. The shear waves show splitting, with the polarizations of most of the leading shear waves approximately parallel to the regional maximum compressional stress. Only four out of five stations have sufficient time-delay observations for temporal variations to be assessed; the variations at theses stations 6 km apart show different patterns but no clear trend is visible in the 19 months of data analyzed.

4.2 Methodology

4.2.1 Covariance Matrix Method

Shear wave splitting is controlled by small differences in the velocities of the two polarized shear waves. One commonly seeks a coordinate rotation or by plotting hodograms that separates the particle motion into distinct "fast" and "slow" waves, each of identical shape and linearly polarized in mutually-perpendicular directions. On the other hand, Xu and I (Xu et al., 2004) developed a new method, the covariance matrix method, to estimate splitting parameters from three-component seismograms. The method was motivated by the theory of polarization filter, which was first introduced by Montalbetti and Kanasewich (1970). The idea was applied on shear-wave splitting analysis to extract the upper mantle anisotropy (Silver and Chan, 1991), but only the horizontal components of the seismogram were used. Here, we extended the method to deal with three-component data.

Given a seismic signal with three components of **u**, **v**, **w**, the polarization can be determined by forming the covariance matrix, *COV*,

$$COV = \begin{bmatrix} uu & uv & uw \\ vu & vv & vw \\ wu & wv & ww \end{bmatrix}. \tag{4.1}$$

If the polarization of the signal is linear, *COV* has only one non-zero eigenvalue, and the corresponding eigenvector is the polarization of the signal. On the other hand, if the polarization of the signal is planar, there are two non-zero eigenvalues, and the corresponding eigenvectors define this plane. With these relationships, the linearity, P_l, and planarity, P_p, can be defined as

$$\begin{aligned} P_l &= 1 - \frac{\lambda_2 + \lambda_3}{\lambda_1} \\ P_p &= 1 - \frac{2\lambda_3}{\lambda_1 + \lambda_2} \end{aligned}, \tag{4.2}$$

where $[\lambda_1, \lambda_2, \lambda_3]$ are eigenvalues of *COV* with $\lambda_1 \geq \lambda_2 \geq \lambda_3$.

Our approach for applying this method to S-wave splitting analysis is to find a solution that satisfies the following condition: if the assigned time delay and fast wave polarization are correct, then the output of the processed signal should be mostly linear. Two steps of processing will be performed. Suppose the incident wave splits into fast and slow wave with orthogonal polarization directions, the particle motion of the signal will

be confined to the plane defined by those polarizations. Since the minimum eigenvalue of the covariance matrix of (4.1) corresponds to the direction perpendicular to this signal plane, the first step is to find the direction perpendicular to this plane, V_{signal}. Then the signals are projected onto the plane V_{signal}. The second step involves searching for the amount of time delay over a specified range, such that the covariance matrix of the two rotated and time-shifted components gives the minimum eigenvalue and thus the highest degree of linearity. These two steps will give us estimates of the two shear-wave splitting parameters, fast shear-wave polarization directions (φ) and differential time delays (δt).

Synthetic tests are conducted to check the method's sensitivity to noise interference and the time window size in which the signal is processed. Synthetic seismic signal with specified polarization and time differences is constructed to test the method. For the case of a linearly polarized incident wave, the synthetic signal shown in Figures 4.2 and 4.3 is constructed by projecting a linear incident signal onto two orthogonal directions with certain time differences. To achieve statistically meaningful results each test was simulated with 60 realizations at each noise level. The test results are summarized in Tables 4.1 and 4.2. Figure 4.3 shows the particle motions for input and recovered signals. In Table 4.1, $(\theta_{inc}, \phi_{inc})$ is the polarization direction of incident waves, $(\theta_{slow}, \phi_{slow})$ is the polarization of slow wave, $(\theta_{non}, \phi_{non})$ is the direction of the eigenvector corresponding to the minimum eigenvalue of covariance matrix constructed from the three-component data, and T_{diff} is the time delay between fast and slow split shear-wave. The random noise level is measured relative to the maximum amplitude of

the input three-component signals. The sampling rate of the synthetic signal is 0.01 second.

Table 1 shows that even with 100% noise level (S/N = 1), the estimated polarizations and time delays are good. The errors only increase slowly with noise. From 0% to 100% noise levels, the polarization errors are generally less than 10 degrees. Table 2 shows the results for difference time window sizes, which is a free parameter in this method. We can see that as long as the window size (NT2 – NT1)*dt is larger than two times the delay time ($2*T_{diff}$), the results are reasonable.

Comparing the performance of our method with traditional analysis which processes only the horizontal components, the test results are shown in Table 4.3. We can see that traditional approach can also provide reasonable estimates of polarization azimuth, but it gives poor estimates of the time difference.

For the case of a planar incident wave, we computed a single simulation for three different noise levels: 0%, 5%, and 20%. Figure 4.4 shows an example of the analysis from particle motions of input and recovered signals. Table 4.4 shows the results, where $(\theta_{inc\_norm}, \phi_{inc\_norm})$ is the direction perpendicular to the particle motion plane defined by the incident wave. The results show that this method is also useful in cases when the polarization of shear-wave is not perfectly linear.

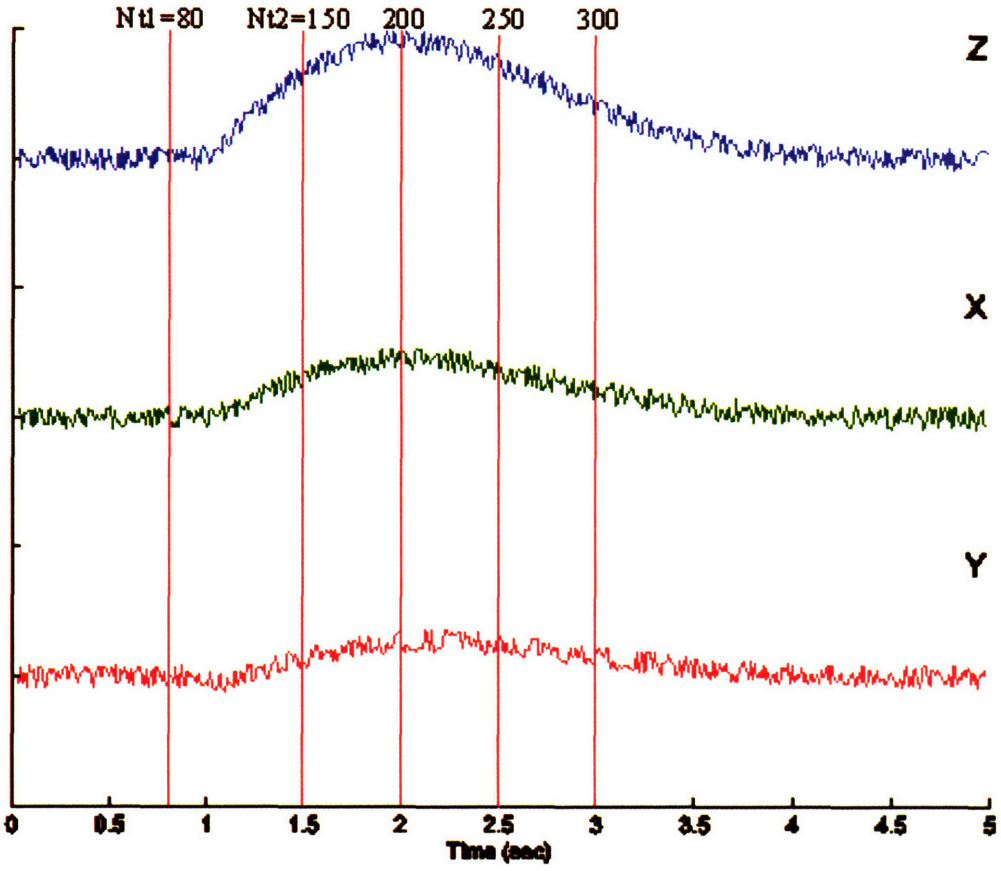

Figure 4.2. The 3-component synthetic signals with fast and slow wave polarization parameters given in Tables 4.1 and 4.2. The noise level shown here is 20%, Nt1 and Nt2 are the boundaries of time window in which data are processed to extract the polarization information.

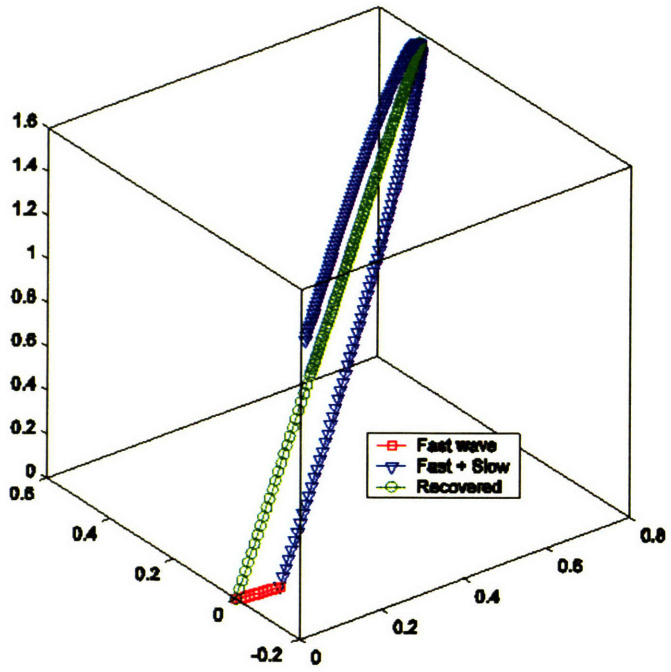

Figure 4.3. Particle motions of synthetic signal and recovered signal for linear polarization of incident wave. The red curve shows the particle motion before slow wave arrives, the blue curve shows the motion when both the fast and slow waves are present, and the green curve shows the recovered particle motion after shifting back the time delay along the slow wave direction. We can see that the recovered signal shows perfectly linear polarization, identical to the model given in Table 4.1.

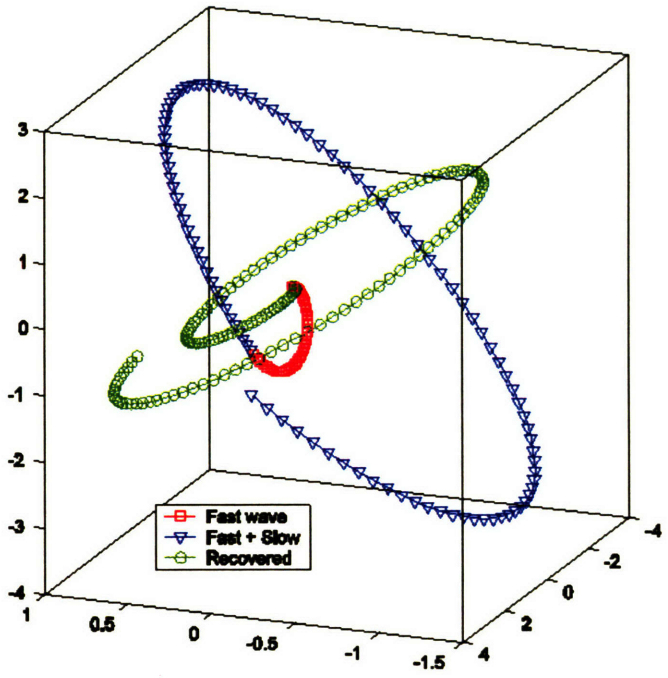

Figure 4.4. Particle motions of synthetic signal and recovered signal for planar polarization of incident shear-wave. The red curve shows the particle motion before slow wave arrives, the blue curve shows the motion when both the fast and slow waves are present, and the green curve shows the recovered particle motion after shifting back the time delay along the slow wave direction. We can see that the recovered particle motion is confined in one plane which the geometry parameters are given in Table 4.4.

Noise Level	θ_{inc} (°)	ϕ_{inc} (°)	θ_{slow} (°)	ϕ_{slow} (°)	θ_{non} (°)	ϕ_{non} (°)	T_{diff} (s)	P_l	P_p
Original Model	30	30	60	60	68.54	343.19	0.4		
0%	29.98± 0.00	29.95± 0.00	59.75± 0.00	59.86± 0.00	68.44± 0.00	343.19 ±0.00	0.40± 0.00	1.000± 0.000	1.000± 0.000
20%	29.99± 0.35	29.93± 0.64	59.86± 2.35	59.57± 1.35	68.59± 0.46	342.77 ±1.21	0.40± 0.02	0.995± 0.000	0.996± 0.000
40%	30.02± 0.66	30.36± 1.52	61.29± 4.71	60.39± 3.59	68.72± 1.12	342.82 ±2.67	0.40± 0.04	0.982± 0.001	0.985± 0.001
60%	30.44± 1.01	30.50± 2.49	63.42± 8.44	60.40± 5.74	68.92± 2.02	341.79 ±4.82	0.42± 0.07	0.961± 0.002	0.967± 0.002
80%	30.19± 1.47	30.42± 2.70	65.44± 9.88	60.98± 7.00	69.44± 2.88	343.20 ±7.78	0.41± 0.08	0.932± 0.004	0.943± 0.004
100%	30.08± 1.61	30.68± 3.30	64.70± 10.30	62.16± 8.78	69.15± 3.92	342.32 ±10.15	0.40± 0.09	0.899± 0.008	0.915± 0.007

Table 4.1. Synthetic test results for different noise levels for a fixed time window (Nt1 = 70, Nt2 = 300).

NT2	θ_{inc} (°)	ϕ_{inc} (°)	θ_{slow} (°)	ϕ_{slow} (°)	θ_{non} (°)	ϕ_{non} (°)	T_{diff} (s)	P_l	P_p
Original Model	30	30	60	60	68.54	343.19	0.4		
150	35.24± 19.90	38.51± 23.72	72.62± 19.34	67.79± 16.55	69.80± 4.66	341.71 ±24.41	0.50± 0.16	0.936± 0.021	0.954± 0.014
200	31.11± 2.44	31.27± 4.16	66.41± 9.96	62.36± 6.85	68.54± 1.50	342.56 ±6.64	0.42± 0.09	0.972± 0.004	0.978± 0.003
250	30.40± 1.42	30.38± 2.49	64.89± 10.85	61.44± 5.80	68.70± 1.77	342.40 ±4.79	0.41± 0.08	0.975± 0.003	0.980± 0.002
300	30.22± 0.88	30.21± 1.84	61.86± 6.00	61.13± 4.39	68.24± 1.56	343.69 ±4.39	0.41± 0.04	0.972± 0.002	0.977± 0.001
350	30.04± 0.90	30.23± 1.83	62.53± 6.63	61.60± 3.54	68.34± 1.53	343.78 ±3.27	0.40± 0.05	0.967± 0.002	0.972± 0.001
400	30.07± 0.89	30.37± 1.91	62.31± 7.77	61.41± 4.54	68.41± 1.68	343.74 ±4.12	0.41± 0.06	0.961± 0.002	0.967± 0.002

Table 4.2. Synthetic test results for different time windows (NT1 = 70) with fixed noise level of 50%.

Noise Level	ϕ_{inc} (°)	ϕ_{slow} (°)	T_{diff} (s)
0%	31.32±0.00	57.00±0.00	0.60±0.00
20%	31.61±1.21	57.52±2.50	0.60±0.04
40%	31.72±3.22	58.62±5.78	0.60±0.06
60%	34.21±5.93	67.98±16.12	0.56±0.09
80%	36.38±6.75	73.60±16.01	0.53±0.11
100%	34.49±8.92	71.20±19.22	0.55±0.12

Table 4.3. Synthetic test results of traditional two-component (horizontal) analysis with fixed window size (Nt1 = 70, Nt2 = 300).

Noise Level	θ_{inc_norm} (°)	ϕ_{inc_norm} (°)	θ_{slow} (°)	ϕ_{slow} (°)	T_{diff} (s)
Original Model	30	30	60	60	0.4
0%	30	60	60	60	0.4
5%	32.55	35.04	59	68	0.41
20%	24.51	42.7	55	72	0.42

Table 4.4. Synthetic test results for planar polarization of incident wave with different noise levels.

4.2.1 Internal Shear Wave Window

The shear wave window is the cone of raypaths with angles of incidence to the free surface typically less than 35°-45°. The actual angle depends on details of near-surface structure. The particle motion of shear waves can be severely perturbed by interaction with the free surface and with internal interfaces (Evans, 1984; Booth and Crampin, 1985; Liu and Crampin, 1990) due to contamination by S-to-P conversions. Liu and Crampin (1990) examine the effect of incidence angle on the polarization of shear

waves through plane boundaries. According to their study, there are usually three critical angles for low-to-high velocity interface ($V_{P1} < V_{P2}$, $V_{S1} < V_{S2}$),

$$\begin{aligned} \alpha_1 &= \sin^{-1}(V_{S1}/V_{P2}) \\ \alpha_2 &= \sin^{-1}(V_{S1}/V_{P1}) \\ \alpha_3 &= \sin^{-1}(V_{S1}/V_{S2}) \end{aligned} , \qquad (4.3)$$

and two critical angles for high-to-low velocity interfaces ($V_{P1} > V_{P2}$, $V_{S1} > V_{S2}$, $V_{P1} < V_{S2}$),

$$\begin{aligned} \alpha_4 &= \sin^{-1}(V_{S2}/V_{P2}) \\ \alpha_5 &= \sin^{-1}(V_{S2}/V_{P1}) \end{aligned} , \qquad (4.4)$$

where [V_{P1}, V_{S1}] are the P- and S-wave velocities for the 1st (shallow) layer and [V_{S1}, V_{S2}] are the P- and S-wave velocities for the 2nd (deep) layer.

The result is a series of critical angles for the interfaces, beyond which the polarizations deviate from the incident polarization and the particle motions become distorted. When a linearly polarized plane shear wave is transmitted through an isotropic-to-isotropic interface, the phase and the linear motion of the incident wave are preserved within the innermost window which the incidence less than the smallest critical angle, α_1. The particle motion becomes elliptical for angles of incidence greater than the smallest critical angle. As the angle of incidence exceeds the smallest critical angle, the coefficients of the previously real transmitted wave become complex, and the resultant

inhomogeneous interface waves become elliptically polarized, carrying energy parallel to the interface at the phase velocity of the incident shear wave. Of the two cases of high-to-low and low-to-high velocity interfaces, the latter has greater potential for significant polarization deviations (greater than ±5°) and increased ellipticity, especially beyond the widest critical angle. Only within the window can the waveforms of the incident shear wave be directly observed at a free surface (Booth & Crampin, 1985).

Suppose an earthquake occurs at a depth of 3.5 km, which is the deepest kind detected in the Field. A shear wave propagating upwards from the 3.5 km, the 5th layer in the layered velocity model (Table 4.5), encounters five high-to-low velocity interfaces. By examining SH and SV relative amplitudes (for plane waves in an isotropic structure) calculated by the Zoeppritz equations (Aki and Richards, 1980), it is possible to identify which critical angles form limits on the raypath. The Zoeppritz equations describe the reflection and transmission coefficients of plane-waves as a function of incident angle and elastic media properties (density, P-wave velocity, and S-wave velocity), but do not include wavelet interferences due to layering. Figure 4.5 (a) to (d) show these relationships for an incident shear wave propagating upward with equal SH and SV components for the four uppermost internal interfaces. The polarization angle of the transmitted shear wave, ψ, in the plane of constant phase is related to the amplitude and transmission coefficients (Douma and Helbig, 1987) by

$$\psi = \tan^{-1}\left(\frac{A_{SH}}{A_{SV}} \cdot \frac{T_{SH}}{T_{SV}}\right), \qquad (4.5)$$

where A_{SH} and A_{SV} are the relative SH and SV amplitudes, respectively, and T_{SH} and T_{SV} are the transmission coefficients of SH and SV waves, respectively. As expected, the high-to-low velocity interfaces only create minor deviation in the relative amplitudes of the transmitted SH- and SV-waves. Since the relative amplitudes of the transmitted SH- and SV-waves are essentially the same even beyond the largest critical angle (α_3), the polarization deviations are very small (less than two degrees in this case) and do not place much restriction on the raypaths. It must be noted that these angles are approximations and their validity is limited by the uncertainty in the velocity model, the earthquake locations, the effect of curved wavefronts and anisotropy. In particular, the effect of a curved wavefront is to spread out the distorted effect of the critical angle over a range of angles and thus widen the acceptable range of raypaths by a small amount.

Depth (km)	Vp	Vs	C1	C2	C3
0.00	2.300	1.198	27.44	31.39	62.23
0.25	2.600	1.354	24.22	31.38	51.97
0.90	3.300	1.719	22.46	31.39	47.17
1.50	4.500	2.344	27.36	31.39	61.95
3.00	5.100	2.656	27.25	31.38	61.54
7.00	5.800	3.021			

Table 4.5. Velocity model of the Field and the critical angles.

In summary, the analysis method used in this study involves selecting events within the shear-wave window, rotating the horizontal seismograms into radial and transverse components, identifying the onset of the first arriving shear wave, and measuring the polarization direction and delay-time using the covariance-matrix method.

Seismograms are rotated into the frame of the ray (radial and transverse components) to improve the clarity of the S-wave and maximize the energy used in the analysis to provide more accurate measurements. To confirm the particle motion interpretation, the horizontal traces are rotated into the direction of polarization of the fast split shear-wave and the traces are inspected for similarity of pulse shape (Gledhill, 1991). If the pulse shapes are dissimilar then the time delay and polarization measurements are rejected. The split shear waves are not expected to be identical in amplitude or frequency content because they will have sampled different properties of the anisotropic mass.

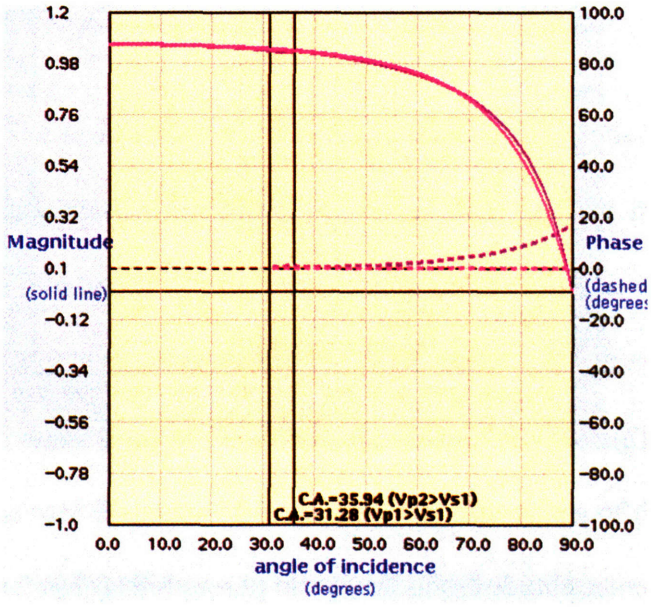

(a)

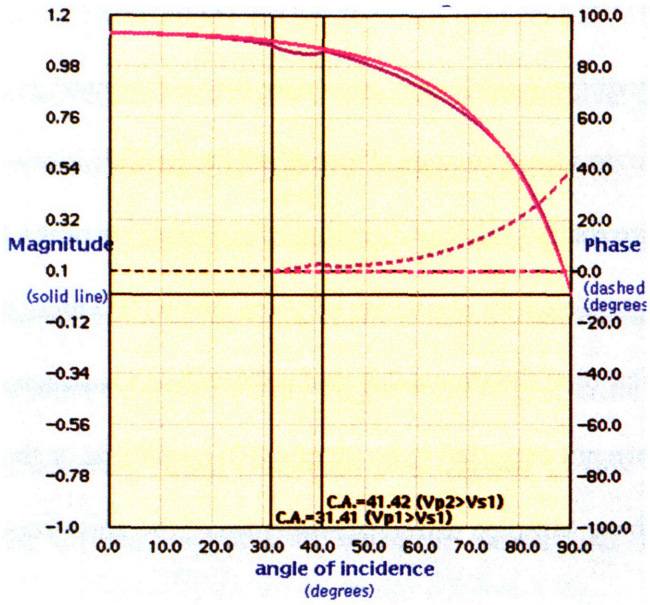

(b)

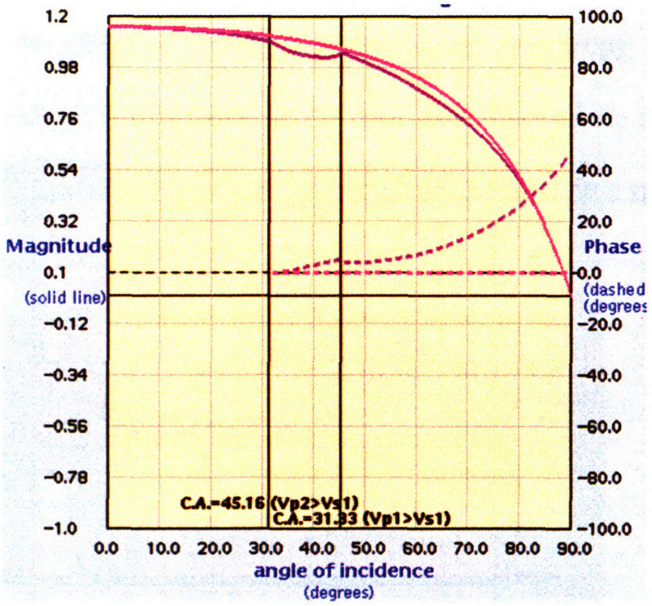

(c)

Figure 4.5. Relative amplitude (solid lines) and phase shifts (dash lines) of upgoing SH-wave (pink) and SV-wave (purple) transmitted across the (a) first (uppermost) interface at 250m , (b) second interface at 900m , (c) third interface at 1.5 km, and (d) fourth interface at 3.0 km.

4.3 Shear-wave splitting analysis

4.3.1 Fracture Orientations

Of the 405 events in Figure 3.8, 125 events that pass the criterion described in the previous section are interpreted. Only events that show good signal-to-noise ratio and identifiable splitting are interpreted. The locations of these 125 events, divided into three different groups based on their locations are plotted in Figures 4.15 to 4.17.

Figures 4.7 to 4.14 show some examples of rotated traces and particle motion diagrams, clearly demonstrating the presence of shear-wave splitting in which the two split shear-waves show dominant orthogonal polarization directions.

To determine the local strike of fractures in the Field, I plotted rose diagrams of the fast shear-wave polarization directions (ϕ) versus their relative frequency for three groups of events. The number of shear-wave splitting observations at each station for the three event groups is summarized in Table 4.6. Note that the ϕ values are corrected for the actual geographic orientation of the downhole seismic receivers (Table 4.7). Figures 4.15 to 4.17 shows the rose diagrams of the polarization directions of the fast shear-wave at the five stations for each event group. Results for stations with too few observations are not shown. Every station shows a preferred orientation of NE-SW polarizations as commonly observed in shear-wave splitting studies. The predominant orientations ϕ are

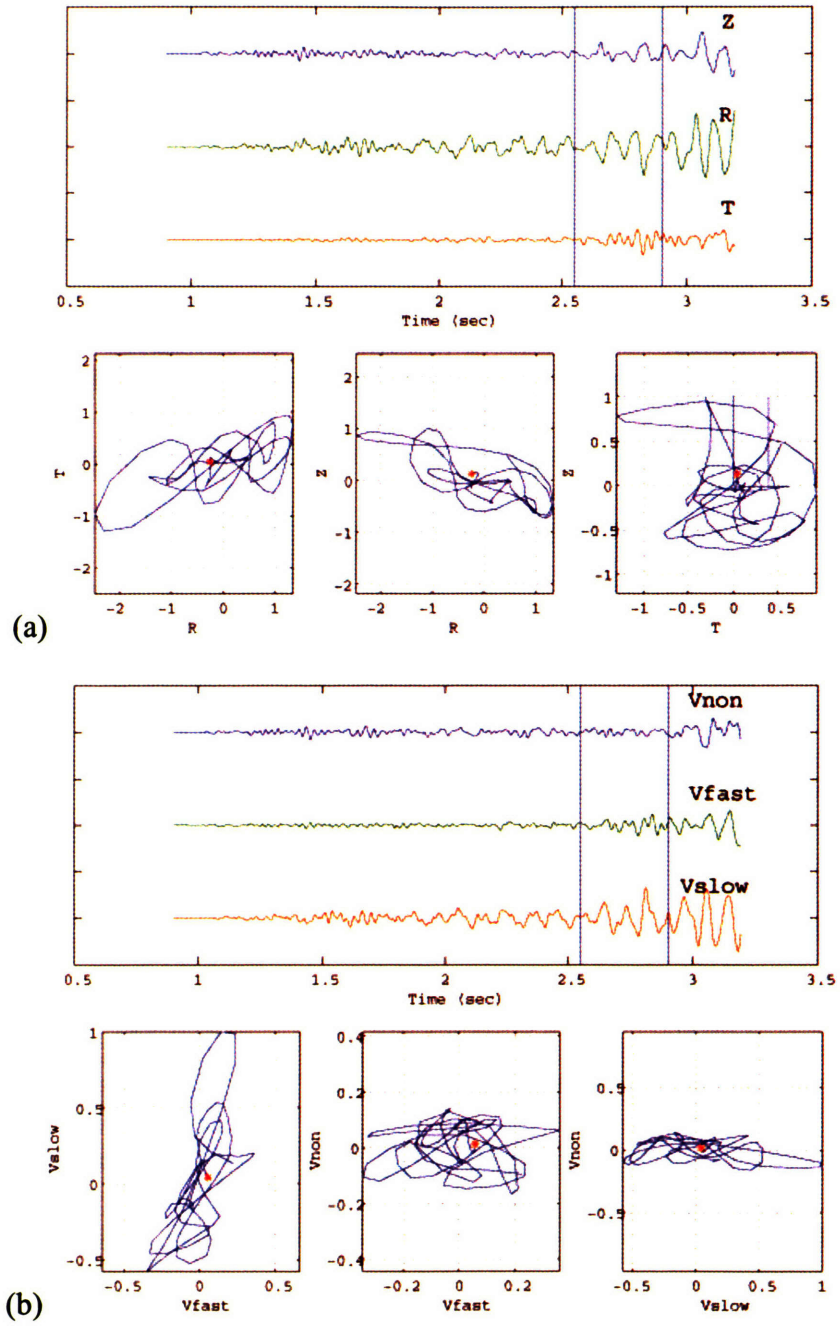

Figure 4.7. Example of a microearthquake recordings on November 15, 1999 and shear-wave splitting in the Field. The traces are about three seconds long. The vertical bars mark the time intervals of the hodograms: (a) Rotated seismograms before splitting analysis, and (b) after splitting analysis with seismograms rotated to the fast-wave polarization direction and time-shifted by the amount of time-delay.

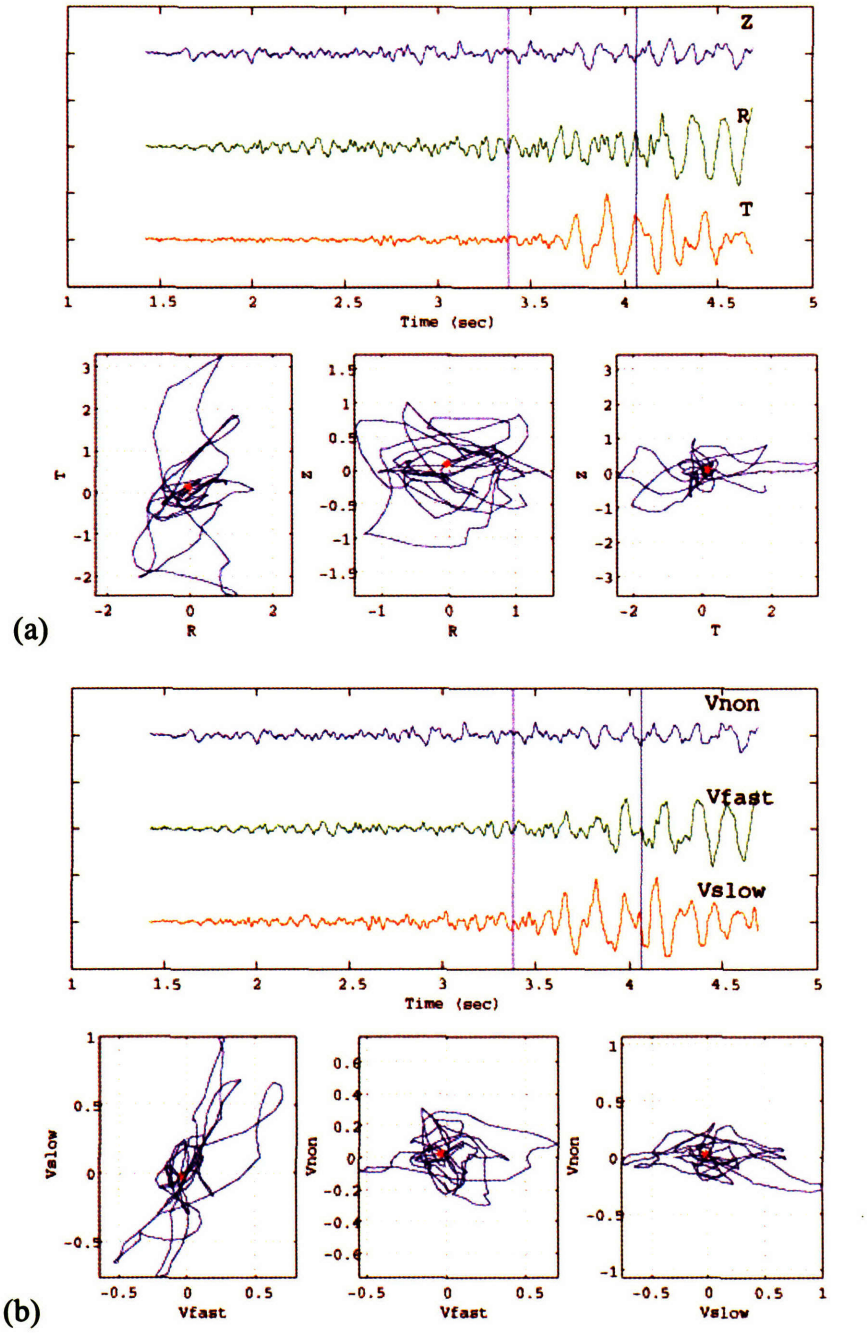

Figure 4.8. Another example of a microearthquake recordings on November 15, 1999 and shear-wave splitting in the Field.

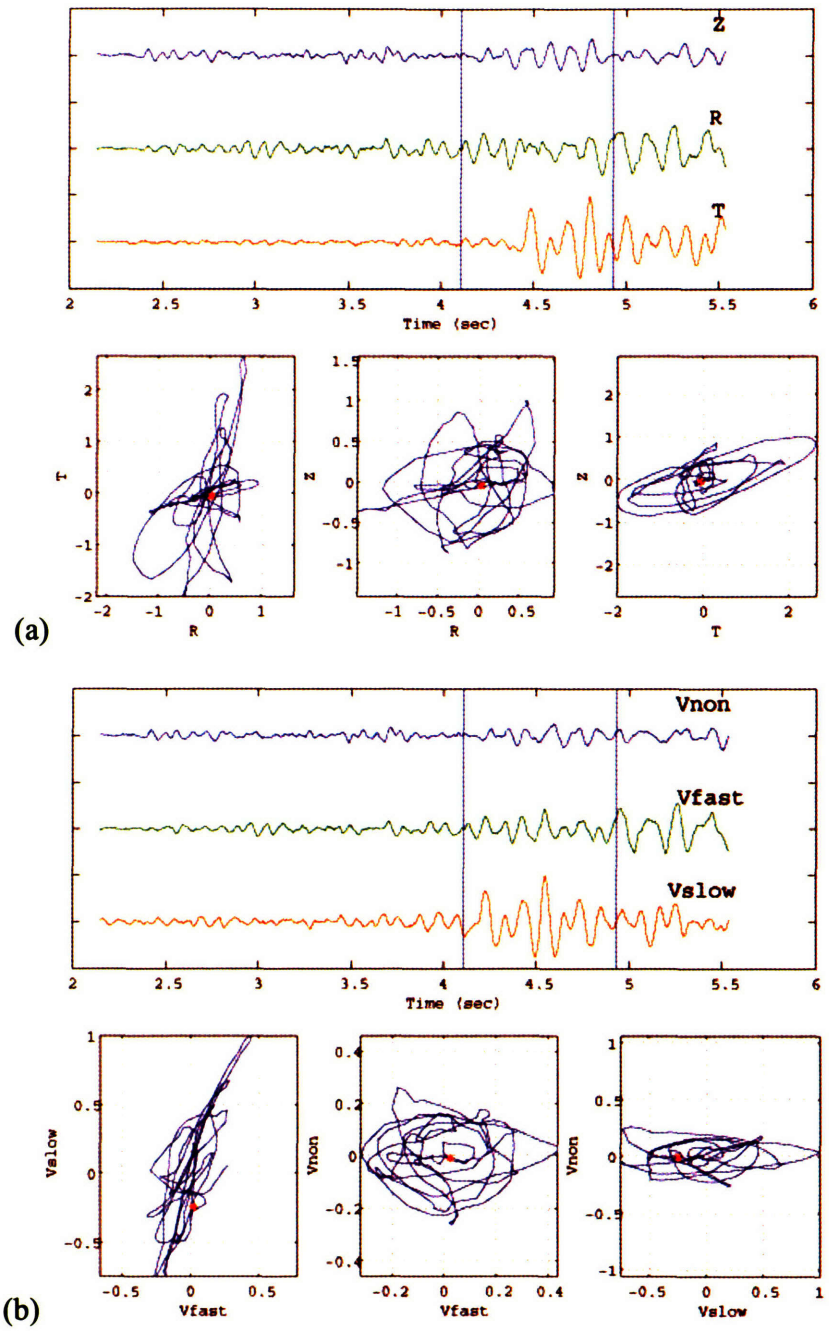

Figure 4.9. Another example of a microearthquake recordings on November 15, 1999 and shear-wave splitting in the Field.

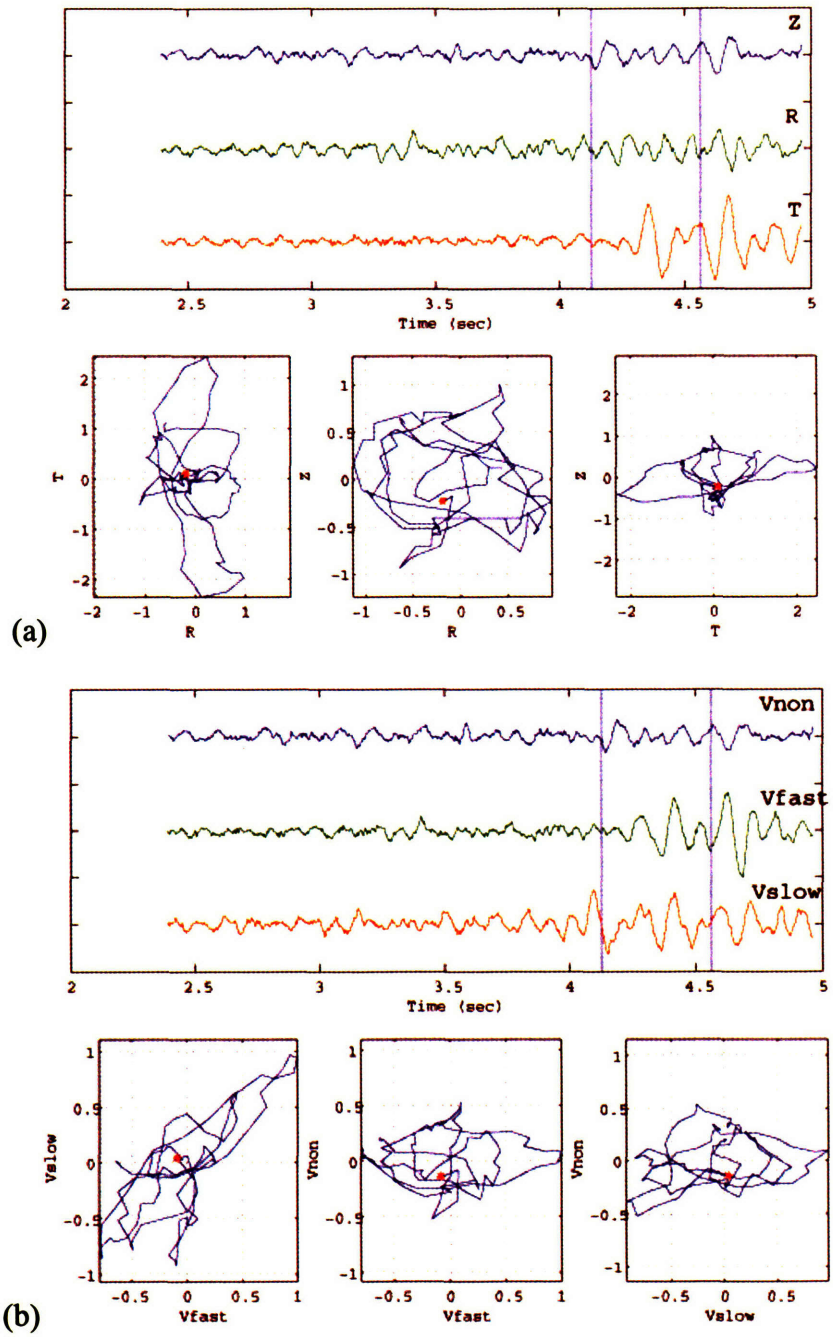

Figure 4.10. Another example of a microearthquake recordings on November 21, 1999 and shear-wave splitting in the Field.

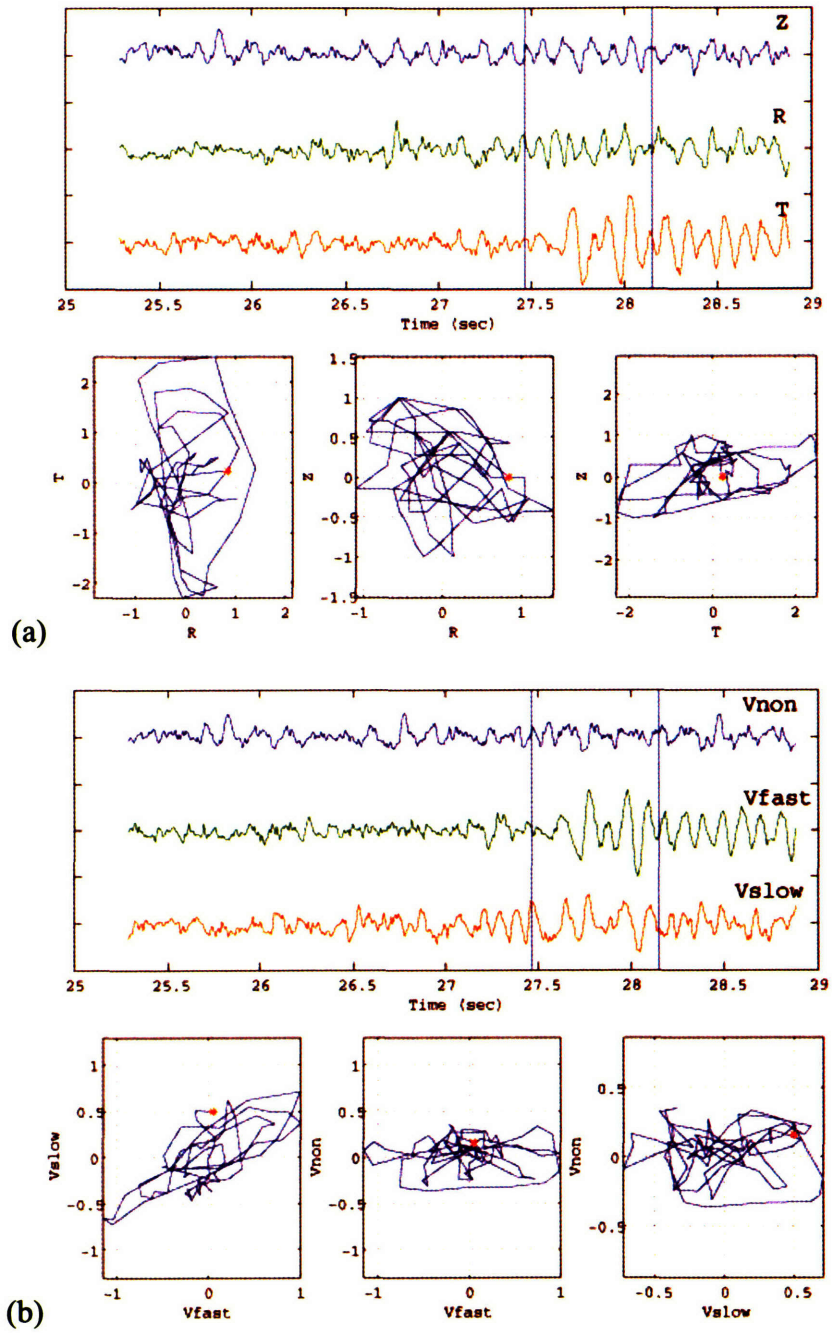

Figure 4.11. Another example of a microearthquake recordings on February 4, 2000 and shear-wave splitting in the Field.

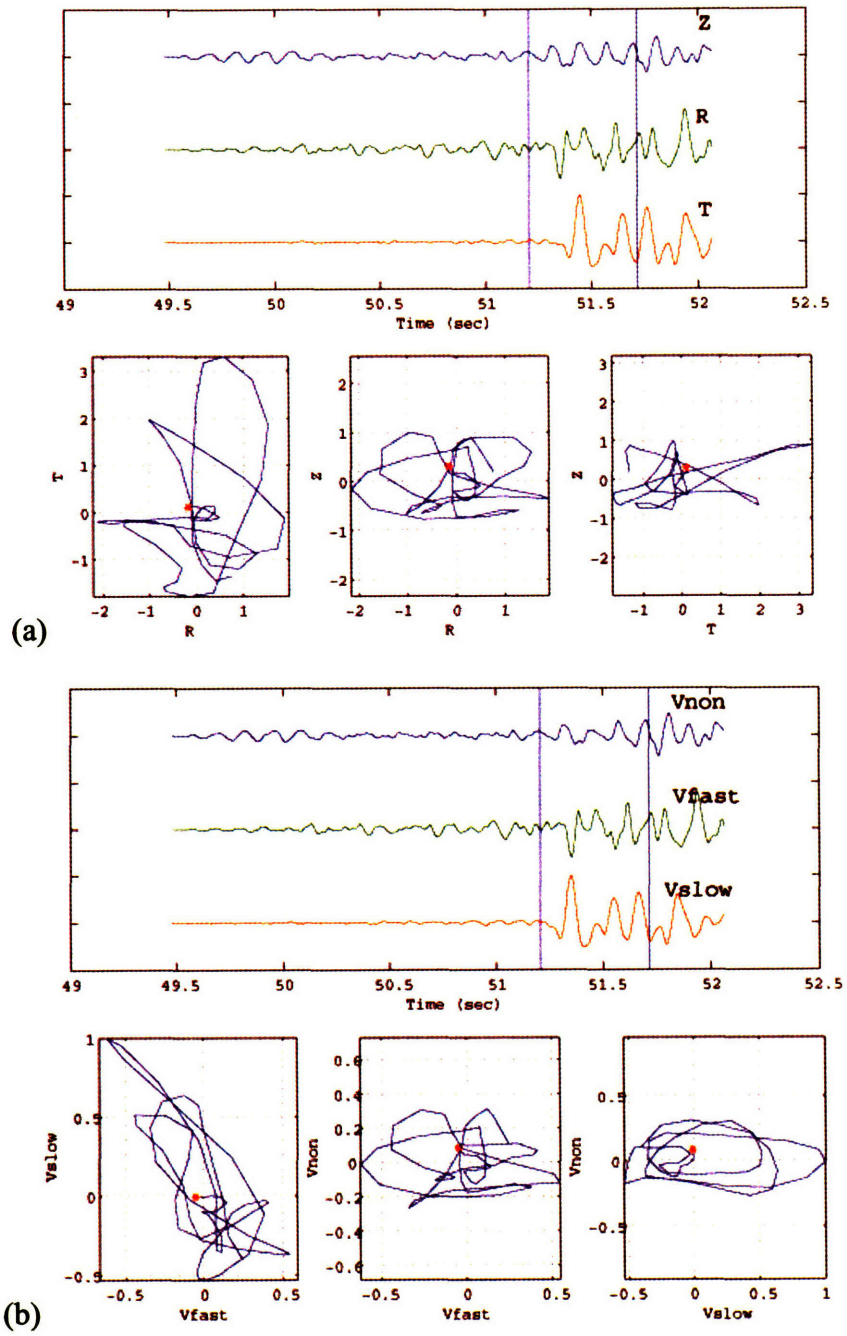

Figure 4.12. Another example of a microearthquake recordings on February 5, 2000 and shear-wave splitting in the Field.

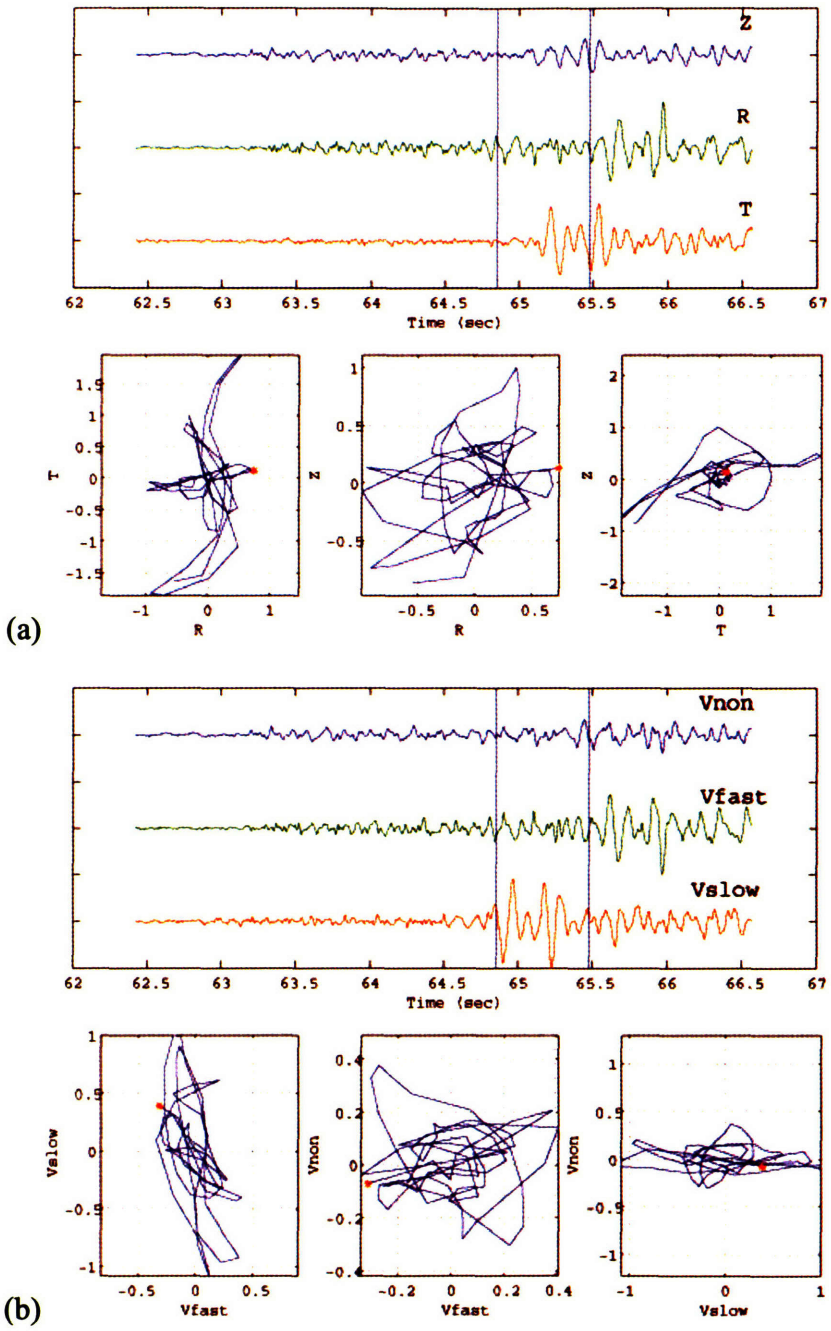

Figure 4.13. Another example of a microearthquake recordings on February 24, 2000 and shear-wave splitting in the Field.

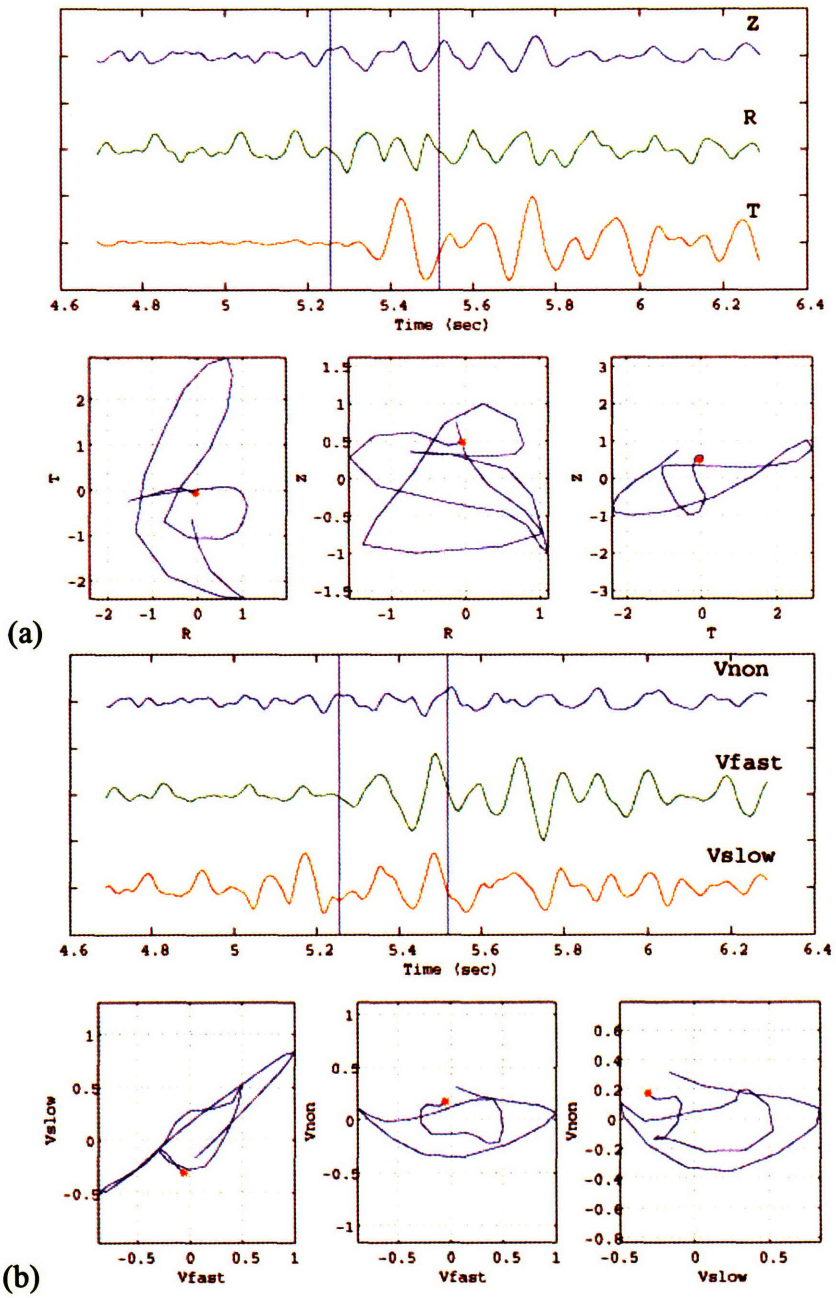

Figure 4.14. Another example of a microearthquake recordings on March 20, 2000 and shear-wave splitting in the Field.

interpreted as the strike of subsurface local fracturing system or direction of the maximum horizontal stress in the neighborhood of the recording seismic station (Crampin, 1981; Saltzer et al., 2000). These NE-SW orientations are consistent with the strike of local faults determined from independent geologic study and 3-D reflection seismics conducted in the Field (Figure 4.18). The dips of the fracture system are shown in Figure 4.19. The results shown in Table 4.8 confirm the earlier assumption of vertical fractures in the Field with most of the fractures dip steeply (greater than 75°).

In addition to the main polarization orientation, most stations show another distinct subset of polarization directions or secondary polarizations that superimpose on the main polarization orientation in rose diagrams. The secondary polarizations strike NW almost perpendicularly to the main polarization set. Secondary polarization directions provide important information on the geometry of subsurface fractures and should not be regarded as scattering noise, especially if they show azimuthally dependent patterns. Measurements of fast shear-wave polarizations are highly sensitive to deviations from horizontal transverse isotropy (vertical fracture systems). These patterns may indicate the existence of two sets of intersecting fractures, or the presence of a single set of non-vertically dipping fractures. The latter is unlikely to be the cause in the Field since the shear-wave splitting analysis of the three-component seismograms indicates almost all the fractures are close to vertical. Also, intersecting sets of fractures are possible especially for station VA4 since similar intersecting sets of conjugated fault system are observed from the interpretation of reflection seismic data (Figure 4.18). However, the exact cause cannot be confirmed confidently by inversion at this stage due to relatively limited ray coverage azimuthally at the five stations.

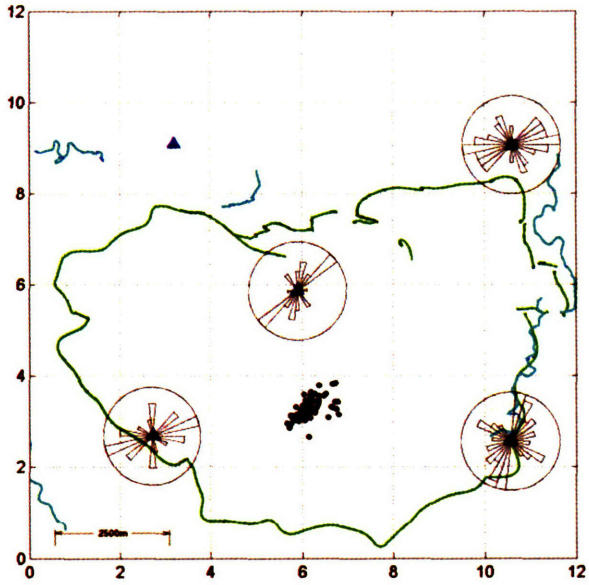

Figure 4.15. Rose diagrams showing fast shear-wave polarization directions at stations that recorded waveforms of microearthquake plotted as black dots.

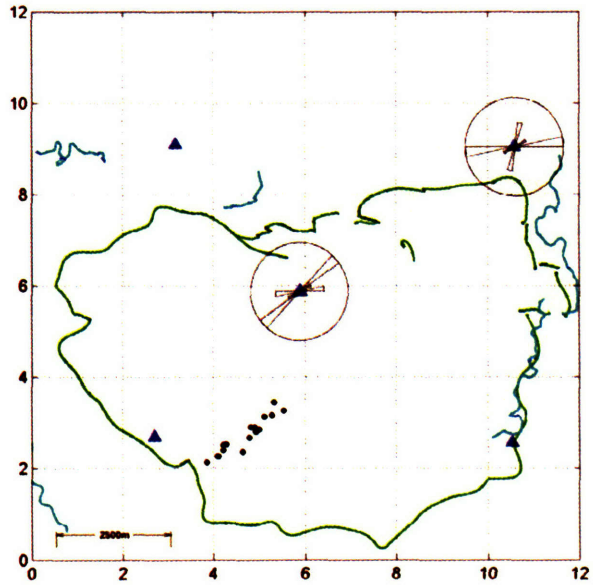

Figure 4.16. Rose diagrams showing fast shear-wave polarization directions at stations that recorded waveforms of microearthquake plotted as black dots.

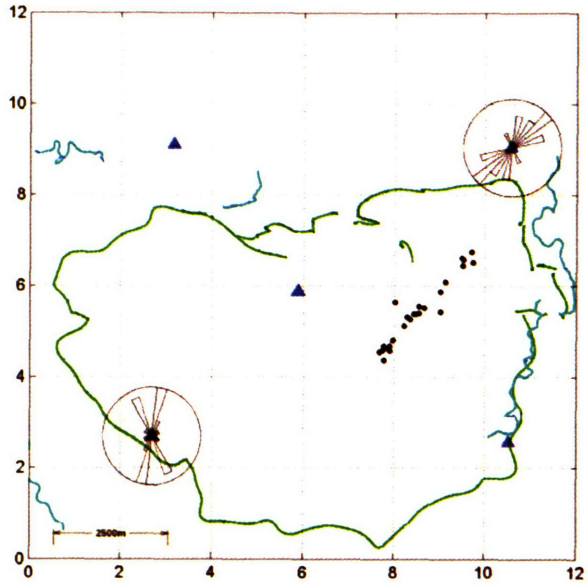

Figure 5.17. Rose diagrams showing fast shear-wave polarization directions at stations that recorded waveforms of microearthquake plotted as black dots.

	VA1	VA2	VA3	VA4	VA5
Cluster Group 1	11	47	7	51	15
Cluster Group 2	9	2	2	6	5
Cluster Group 3	0	17	2	10	2

Table 4.6. Summary of number of shear-wave splitting observations at each station for three different microearthquake clusters in the Field

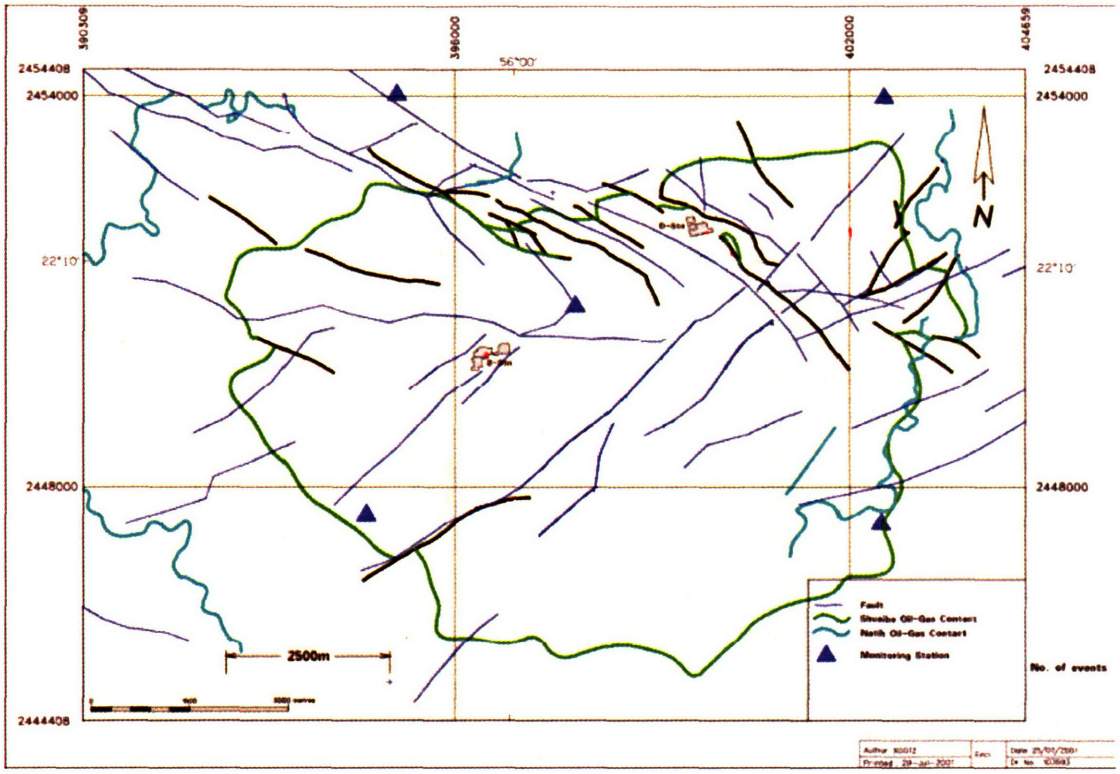

Figure 4.18. The black and blue lines indicate the locations of faults in the Field interpreted from reflection seismic data.

Station	depth (m)	deg
VA-1	135	71.6
	140	63.8
	145	62.7
	150	54.3
VA-2	135	160.7
	140	157.4
	145	157.7
	150	161.1
VA-3	135	-112.7
	140	-112.7
	145	-120.7
	150	-109.1
VA-4	135	-45.8
	140	-46.7
	145	-55.6
	150	-64
VA-5	135	94.9
	140	90.9
	145	98.4
	150	92.2

Table 4.7. Orientation correction (counterclockwise degrees of rotation) needed to align the instrument's horizontal component with geographic directions.

4.3.2 Fracture Densities

Time delays between split shear-waves depend on the degree of anisotropy of the medium, length of the propagation path within the anisotropic medium, and the direction of the propagation with respect to the orientation of the anisotropy. According to Hudson (1981), the intensity of fracture-induced anisotropy in the medium can be calculated by

$$C_D = \frac{Na^3}{V}, \tag{4.6}$$

where N is the number of fractures of average radius a in volume V. Anisotropy is assumed to be caused by aligned water-filled fractures contained in an isotropic homogeneous medium. The time delay τ of split shear-wave is related to the velocities of the fast shear-wave (β_1) and slow shear-wave (β_2) by

$$\tau = L \cdot \left| \frac{1}{\beta_1} - \frac{1}{\beta_2} \right|, \tag{4.7}$$

where L is the propagation distance between source and receiver. The velocities of the split shear waves in a symmetric plane can be written as (Hudson, 1981)

$$\beta_1^2 = \beta_0^2 \left\{ 1 - \frac{8}{7} C_D [\cos(4\theta) + 1] \right\} \tag{4.8}$$

$$\beta_2^2 = \beta_0^2 \left\{ 1 - \frac{8}{7} C_D [\cos(2\theta) + 1] \right\}, \tag{4.9}$$

where θ is the angle of the propagation measured from the strike of aligned fractures, and α_0 and β_0 are compressional and shear-wave velocities in the isotropic rock matrix, respectively. Substituting equations (4.8) and (4.9) into (4.7), we have a 4^{th} order equation for C_D,

$$JC_D^4 + KC_D^3 + MC_D^2 + QC_D + R = 0 \tag{4.10}$$

where

$$J = \frac{4096}{2401} A^2 B^2 C^4 \beta_0^8$$
$$K = \frac{1024}{343} AB(A+B)\left(C^2\beta_0^6 - C^4\beta_0^8\right)$$
$$M = \frac{64}{49}\left\{\left(A^2 + 4AB + B^2\right)\left(C^4\beta_0^8 - 2C^2\beta_0^6\right) + \beta_0^4 (A-B)^2\right\}$$

$$Q = \frac{16}{7}(A+B)\left(3C^2\beta_0^6 - C^4\beta_0^8\right)$$
$$R = C^4\beta_0^8 - 4C^2\beta_0^6$$
$$A = \cos(2\theta)+1 \qquad . \qquad (4.11)$$
$$B = \cos(4\theta)+1$$
$$C = \frac{\tau}{L}$$

If we assume the fracture density $C_D << 1$, we can take the first term of the Taylor series expansion of equation (4.10) and get an approximate solution for C_D,

$$\tau = \frac{4C_D}{7\beta_0}[\cos(4\theta) - \cos(2\theta)]L \,. \qquad (4.12)$$

Equation (4.12) shows that the shear-wave splitting delay time τ is proportional to the propagation distance L and fracture density C_D when C_D is small.

For the first event group (Figure 4.15), normalized time delays range typically between 1.0 and 4.0 ms/km for VA1, 0.6 and 5.2 ms/km for VA2, 1.0 and 4.3 ms/km for

VA4, and 0.6 and 2.5 ms/km for VA5. For the second event group (Figure 4.16), normalized time delays range between 0.8 and 3.6 ms/km for VA4, and 0.9 and 2.5 ms/km for VA5. For the third event group (Figure 4.17), normalized time delays range between 0.5 to 2.2 ms/km for VA2, and 0.4 to 5.8 ms/km for VA4. Table 4.8 summarizes all the normalized delay time obtained by the covariance method. Estimates of splitting delay time from many shear waves at a given station have been averaged or the median is taken to estimate anisotropic strength for the crust beneath that station. Station means can be quite misleading, however, in cases where both the delay time and the fast direction vary significantly with the propagation direction. Such variation can occur when an anisotropy tensor is inclined from the vertical, or has a more complicated symmetry, or both.

Event Group	Station	Delay time Range (ms/km)	Mean (ms/km)	Median (ms/km)	Average Dip (°)
1	VA1	1.0 - 4.0	2.0	1.6	79
	VA2	0.6 - 5.2	2.4	2.1	75
	VA4	1.0 - 4.3	2.6	2.6	78
	VA5	0.6 - 2.5	1.4	1.0	73
2	VA4	0.8 - 3.6	1.7	1.5	79
	VA5	0.9 - 2.5	1.5	1.4	75
3	VA2	0.5 - 2.2	2.0	1.4	80
	VA4	0.4 - 5.8	2.1	1.2	84

Table 4.8. Summary of normalized time delays and fracture dips measured by the covariance-matrix method of three-component seismograms.

Three-dimensional tomographic inversion of fracture density can be done using equation (4.12). However, given the uneven distribution of microearthquake source

locations, low number of data points, and lack of crossing rays sampling the region, the tomographic inversion results will be severely limited. Therefore, a simple inversion using equation (4.12) rather than a full 3-D inversion is done. Due to the lack of crossing rays, I assume that the orientations of the vertical crack plane detected at the stations are the same throughout the sampled raypath. Each measured delay time is inverted for fracture density. The inversion results are summarized in Table 4.9. In general, the results show that regions close to the fault zone sampled by rays traveling along the NE-SW direction (parallel to the fault) to stations VA2 and VA4 have higher fracture densities than those regions sampled by rays traveling perpendicular to the fault zone to VA1 and VA5. One possible model that fits the inversion results is that fractures in the field also have a gross NE-SW orientation parallel to the strike of the faults. Their density is also highest in regions close to the fault zone and decreases as the distance from the fault increases. Similar fracture system has also been observed in the nearby Natih field in the same Fahud Salt Basin in Oman (Hake et al., 1998; Potters et al., 1999), where the largest, open, and nearly vertical fractures are detected along the NE-SW extensional faults, and the fracture density increases in areas where deformation is largest (i.e., areas close to faults).

Station	Fracture density range	Mean	Median
VA1	0.02 - 0.08	0.039	0.032
VA2	0.05 - 0.30	0.083	0.070
VA4	0.04 - 0.14	0.078	0.083
VA5	0.02 - 0.16	0.048	0.038

Table 4.9. Summary of fracture densities inverted from time-delay measurements.

4.4 Conclusions

A new method of shear-wave splitting analysis has been developed to process three-component seismic signals. This method is based on the calculation of the covariance matrix of the three-component seismograms and is tested to be stable even for large random noise levels. It is able to retrieve the fracture dip information, which has been ignored by other commonly used methods that analyze only horizontal seismograms.

A collection of high signal-to-noise ratio seismograms from 125 microearthquakes that are recorded by shallow borehole seismic network in the Field, Oman, shows strong evidence of azimuthally dependent shear-wave splitting. It is necessary to consider both the surface and internal shear wave windows for shear-wave splitting studies. Although 405 events have been recorded, the effect of the shear-wave windows has restricted the number of events suitable for analysis.

The reservoir rocks in the study area are largely composed by carbonates, which commonly lacks anisotropy. It is thus our general assumption that shear-wave splitting is induced by crack-anisotropy in an otherwise isotropic medium. Inversion results indicate that the majority of observed shear-wave splitting parameters (strikes, dips, and delay times) agree with models of transverse isotropy that represent vertical to steeply dipping fractures striking generally parallel to the NE-SW direction. These main polarization orientations observed are in good agreement with the gross strike of the microseismicity,

locally mapped fractures, and the regional tectonic setting. Most stations show major polarization directions that are generally NE-SW (N30°E for VA1, N30°–50°E for VA2, N50°–70°E for VA4, and N45°E for VA5), and are almost parallel to the strikes of the faults revealed by the microseismicity. The average fracture dips are greater than 70° for all stations. The average normalized time delays are 2.0 ms/km for VA1, 2.0–2.4 ms/km for VA2, 1.7–2.4 ms/km for VA4, and 1.4–1.5 ms/km for VA5. From the delay time of split shear-waves, I have estimated the fracture density for the limited areas sampled by the rays. The fracture density in reservoir ranges between 0.02 and 0.30. Based on results from stations VA2 and VA4, raypaths traveling parallel to the seismic fault zone show a significantly larger shear-wave anisotropy than raypaths traveling perpendicular or across the fault zone. This indicates that a volume of increase fracture density and rock permeability in the immediate vicinity of the fault zone may be of interest to hydrocarbon production. No clear evidence of a temporal change in time delay is observed. All the above features revealed by shear-wave splitting suggest fracture arrays in the Field may be normal and strike-slip fault-hosted that are commonly characterized by steeply dipping extension fractures (Bruhn et al., 1994).

4.5 References

Aki, K. and Richards, P.G., 1980, Quantitative seismology: theory and methods, volume I: W.H. Freeman and Company, San Francisco.

Booth, D.C. and Crampin, S., 1985, Shear-wave polarizations on a curved wavefront at an isotropic free surface: Geophys. J. R. astr. Soc., **83**, 31 – 45.

Bruhn, R.L., Parry, W.T., Yonkee, W.A., and Thompson, T., 1994, Fracturing and hydrothermal alteration in normal fault zones: Pure Appl. Geophys., **142**, 609 – 644.

Crampin, S., 1981, A review of wave motion in anisotropic and cracked elastic media: Wave Motion, **3**, 343 – 391.

Crampin, S., 1990, Overview of current research in seismic anisotropy: Geophys. J. Int, **101**, 18 – 20.

Crampin, S., 1993, Arguments for EDA. Can. J. expl. Drill., **1**, 21-26.

Crampin, S., Evans, R., Ucer, B., Doyle, M., Davis, P.J., Yegorkina, G.V., Miller, A., 1980, Observations of dilatancy-induced polarization anomalies and earthquake prediction: Nature, **286**, 874 – 877.

Crampin, S. and Lovell, J.H., 1991, A decade of shear-wave splitting in the Earth's crust: what does it mean? What use can we make of it? And what should we do next?: Geophys. J. Int., **107**, 387 – 407.

Crampin S. and S. Chastin, 2000. Shear-wave splitting in a critical crust: II-compliant, calculable, controllable, fluid-rock interactions. in Anisotropy 2000: Fractures, converted waves and case studies, published by The Society of Exploration Geophysicists. pp 21-28.

Douma, J. and Helbig, K., 1987, What can the polarization of shear-waves tell us?: First Break, **5**, 95 – 104.

Evans, J.R., 1984, Effects of the free surface on shear waves: Geophys. J. R. astr. Soc., **76**, 165 – 172.

Gledhill, K.R., 1991, Evidence for shallow and pervasive seismic anisotropy in the Wellington region New Zealand: J. Geophys. Res., **96**, 21,503 – 21,516.

Hake, J.H., Gevers, E.C.A., van der Kolk, C.M., and Tichelaar, B.W., 1998, A shear experiment over the Natih field in Oman: pilot seismic and borehole data: Geophys. Prosp., **46**, 617 – 646.

Hudson, J.A., 1981, Wave speeds and attenuation of elastic waves in material containing cracks: Geophys. J. Roy. Astr. Soc., **64**, 133 – 150.

Liu E. and Crampin, S., 1990, Effects of the internal shear wave window: comparison with anisotropy induced splitting: J. Geophys. Res., **95**, 11,275 – 11,281.

Montalbetti, J.R. and Kanasewich, E.R., 1970, Enhancement of teleseismic body phases with a polarization filter: Geophy. J. R. astr. Soc., **21**, 119 – 129.

Potters, J.H.H.M., Groenendaal, H.J.J., Oates, S.J., Hake, J.H., and Kalden, A.B., 1999, The 3D shear experiment over the Natih field in Oman: reservoir geology, data acquisition and anisotropy analysis: Geophys. Prosp., **47**, 637 – 662.

Saltzer, R.L., Gaherty, J., Jordan, T.H., 2000, How are shear wave splitting measurements affected by variations in anisotropy with depth?: Geophys. J. Int., **141**, 374 – 390.

Sato, M., Matsumoto, N., and Niitsuma, H., 1991, Evaluation of geothermal reservoir cracks by shear-wave splitting of acoustic emission: Geothermics, **20**, 197 – 206.

Silver, P. and Chan, W.W., 1991, Shear wave splitting and subcontinental mantle deformation: J. Geophys. Res., **96**, 16,429 – 16,454.

Xu, L., Sze, E.K.M., Burns, D., Toksoz, M.N., 2004, S-wave splitting analysis: covariance matrix method and preliminary application: 73rd Ann. Internat. Mtg.: Soc. of Expl. Geophys.

Chapter 5

Relationship Between Production / Injection and Microseismicity in a Producing Field in Oman

5.1 Introduction

Seismicity patterns have attracted the attention of researchers as means to investigate the stress behavior of a region through the years. Changes in the rate of earthquake production are believed to be closely related to changes in stress in a particular volume (Dieterich, 1994; Rutledge et al., 2002). Following the introduction of the injection technologies, determining the underlying causes of anomalous seismicity at reservoirs became more difficult because both extraction and injection were possible causes. Segall (1989) described the poroelastic behavior of reservoir rocks undergoing fluid extraction and illustrated how a reduction of reservoir pore pressure produces contraction near the extraction point and zones of high stress in the surrounding rock mass.

Recognition of the role of faults as fluid conduits extends far back into mining history in the 18th century. While fluid overpressures are common in compressional thrust regimes, overpressures in shale-rich sediments along the Gulf Coast of North America demonstrate that this may also happen in normal faulting regimes. Direct evidence of the effect of fluid pressure on fault stability has come from earthquakes induced in intraplate

regions either through direct injection of fluids down boreholes, as in Denver and Rangely in Colorado (Healy et al., 1968; Raleigh et al., 1976) and in Cornwall in SW England (Pine & Batchelor, 1984).

In this chapter, I examine the distribution of microseismic activity in the Field with respect to time, space, and magnitude, in order to evaluate trends in seismicity. Finally, I also present aspects of earthquake occurrence which are suggestive of a dynamic role for fluids in the earthquake process.

5.2 Spatio-temporal characteristics of the microseismicity

Hypocenters determined using NonLinLoc grid-search method (Lomax et al., 2000) are shown in Figure 3.8, and show the areas where seismicity was active or inactive during the monitoring period. seven groups of microseismicity (Figure 5.3) are defined according to the spatial concentration of the events in order to distinguish between the various active zones (also see Chapter 3.4). The microseismic events on the main NE-SW seismic zone can be classified as six different groups (Groups A to F). Most of the events in the Field belongs to Group A (137 events / 33.8%) and Group B (144 events / 35.6%). Another small swarm (Group G) is located northwest of the main seismic zone.

On the chronological histograms in Figure 5.1(a) and the cumulative event count plot in Figure 5.2, we can observed that the daily rate of events ranges from 0 to 8 events with more or less continuous microseismic activity. Pronounced swarms of events clustered in time and space are not observed. The mean rate of events for the 20-month monitoring period is 0.68 event/day. Generally, the activity rate increases starting from the beginning to the end of the monitoring period. The mean rate of events for the first 10 months is 0.33 event/day, and is 1.02 events/day for the last 10-month monitoring period.

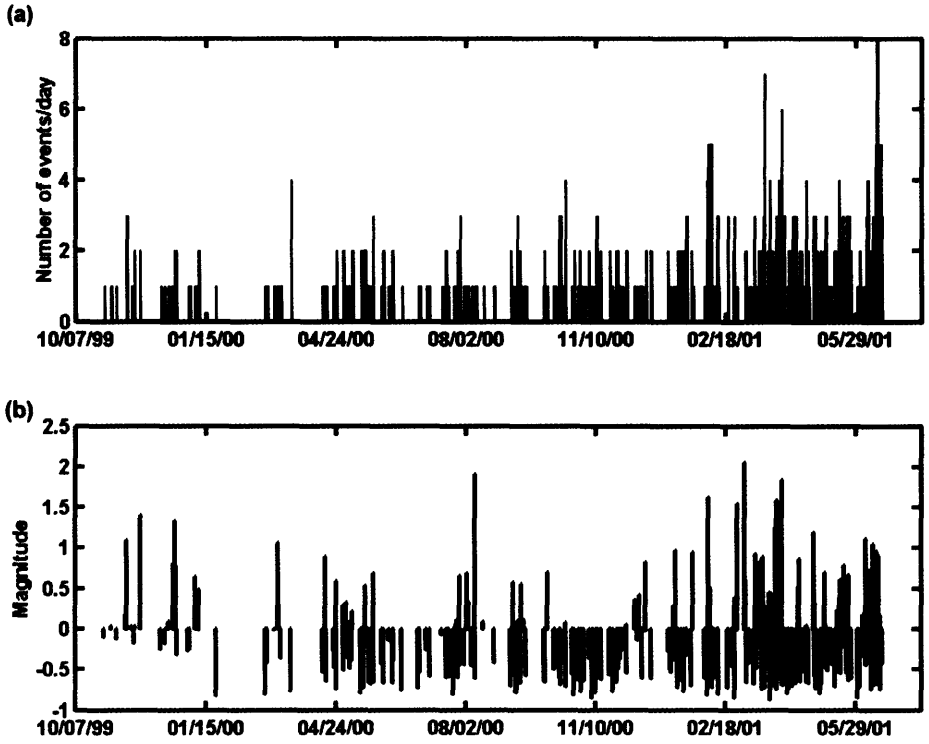

Figure 5.1.(a) Chronological histograms of Oman microseismicity (all 405 events). (b) Chronogram of magnitudes of Oman microseismicity (all 405 events).

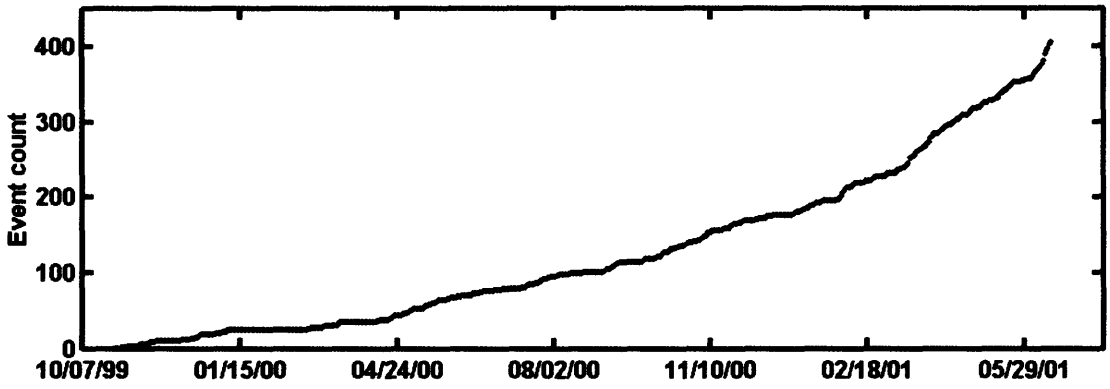

Figure 5.2. Cumulative event count from October 29, 1999 to June18, 2001.

To determine a consistent earthquake magnitude scale with the local magnitudes that PDO reported on certain events, I use the magnitude formula according to Langston et al. (1998) to solve the linear system of equations for the station-correction and attenuation terms. Consider a set of P earthquakes recorded by a network with N stations, and let A_{ij} be the largest amplitude of some wave corresponding to the jth event recorded by the ith station. If M_j is the local magnitude of the event and r_{ij} is the hypocentral distance, then,

$$\log A_{ij} + 3 = -n \log \frac{r_{ij}}{100} - k(r_{ij} - 100) + M_j - s_i, \quad i = 1, N \quad j = 1, P \tag{5.1}$$

where $N = 5$, $J = 405$ for the Oman case, n and k are empirically determined parameters related to the geometric spreading and attenuation of the waves, and s_i is a station-dependent correction term. The values of these parameters used in this study are

summarized in Table 5.1. Equation (1) incorporates the definition of local magnitude (Richter, 1935) and the expression of Hutton and Boore (1987) for the distance correction in Richter's formula.

Parameter	Numerical Value
n	-0.17115460
k	0.04955792
s_{VA1}	1.77274785
s_{VA2}	1.71767917
s_{VA3}	1.73838271
s_{VA4}	1.51918514
s_{VA5}	1.98515814

Table 5.1. Summary of empirically determined parameters for the calculation of local magnitudes of microearthquake in the Field, Oman.

The highest magnitudes recorded are M = 2.05 on March 4, 2001. Figure 5.1(b) shows the chronograms of local magnitudes for the monitoring period, highlighting the low and continuous level of the microseismic activity.

Most of the microearthquakes are located along the NE-SW trending fault zone in the central part of the Field. There is another small swarm located northwest of the main seismic fault zone. Here, I define six "groups" of microseismicity depending on their spatial locations (see Chapter 3.4), in order to distinguish between the various active zones. The locations of event groups are shown in Figure 5.3. Consequently, it is possible

to analyze the spatial distribution of chronological event rates (Figures 5.4 to 5.9) and magnitudes (Figures 5.10a – f) in the Field.

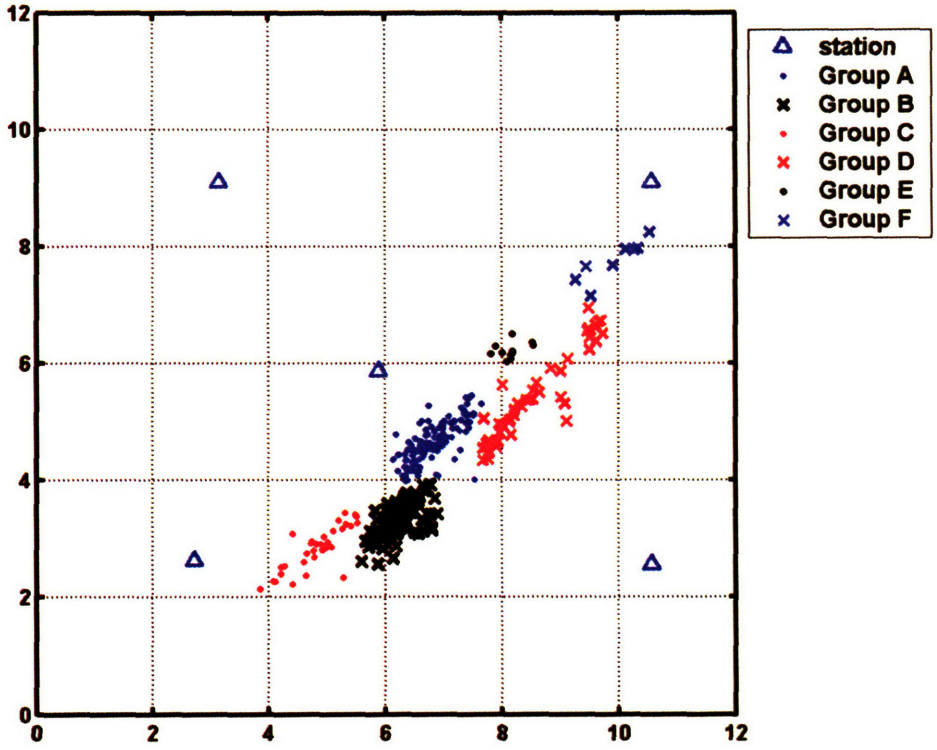

Figure 5.3. Clusters of microearthquakes define the six groups: Groups A – F.

Group A and Group C show similar trends consists of two periods having different levels of seismic activity (Figures 5.4 and 5.6). The activity in the first period (November 25, 1999 to February 4, 2001 for Group A; December 17, 2000 to January 16, 2001 for Group C) is characterized by episodic events. Subsequently, sudden increases in event rate are evident for both groups in the remaining monitoring period. Activity rate in Group B is quite continuous and constant (Figure 5.5), and is predominated by many low magnitude events (Figure 5.10b). Unlike other event groups, Group D has two periods

with significant increase in activity from April 15 to December 4 in 2000, and March 18 to June 14 in 2001, separated by a relatively long quiet period with no activity for 103 days (Figure 5.7). Microearthquake activities in Groups E and F are low compared to others (Figures 5.8 and 5.9), and activity in Group E did not start until July 17, 2000. Figure 5.10 shows the chronograms of magnitudes for all event groups.

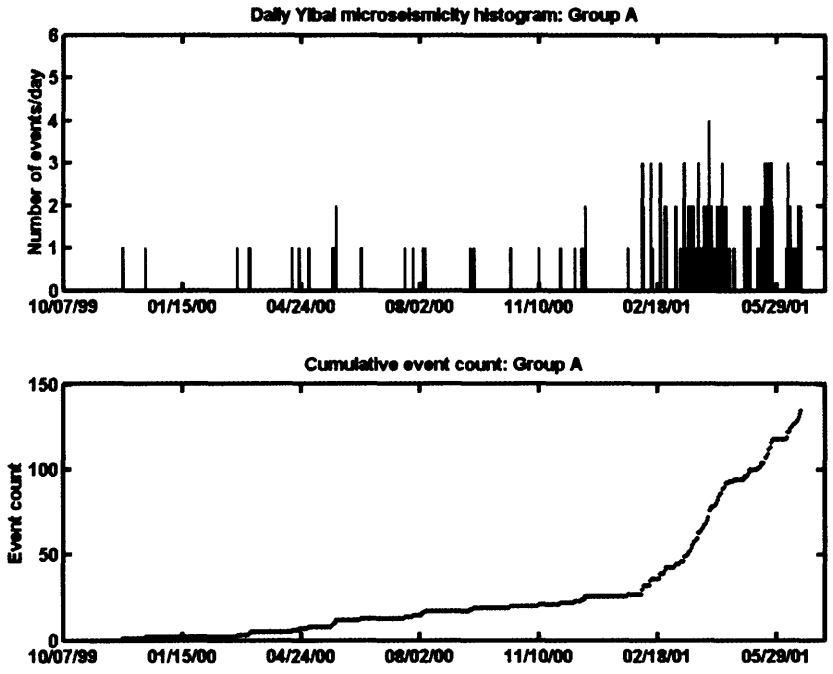

Figure 5.4. (a) Chronological histograms of Group A microseismicity. (b) Cumulative event count of Group A from October 29, 1999 to June18, 2001.

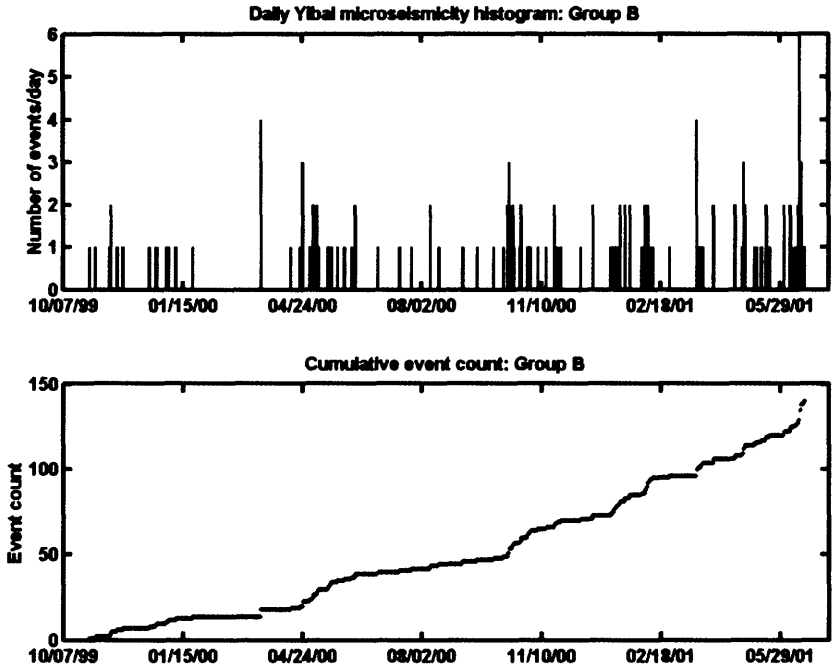

Figure 5.5. (a) Chronological histograms of Group B microseismicity. (b) Cumulative event count of Group B from October 29, 1999 to June18, 2001.

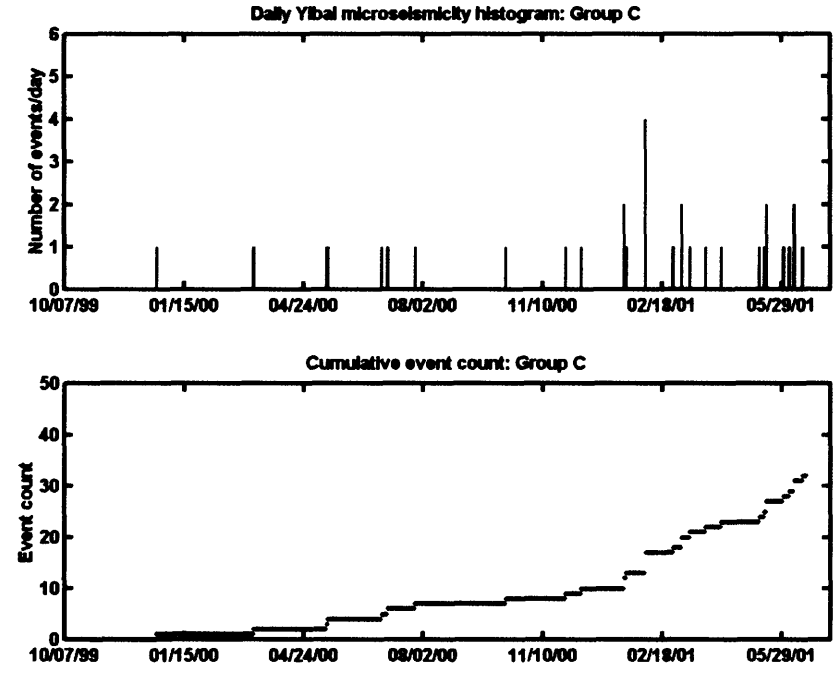

Figure 5.6. (a) Chronological histograms of Group C microseismicity. (b) Cumulative event count of Group C from October 29, 1999 to June18, 2001.

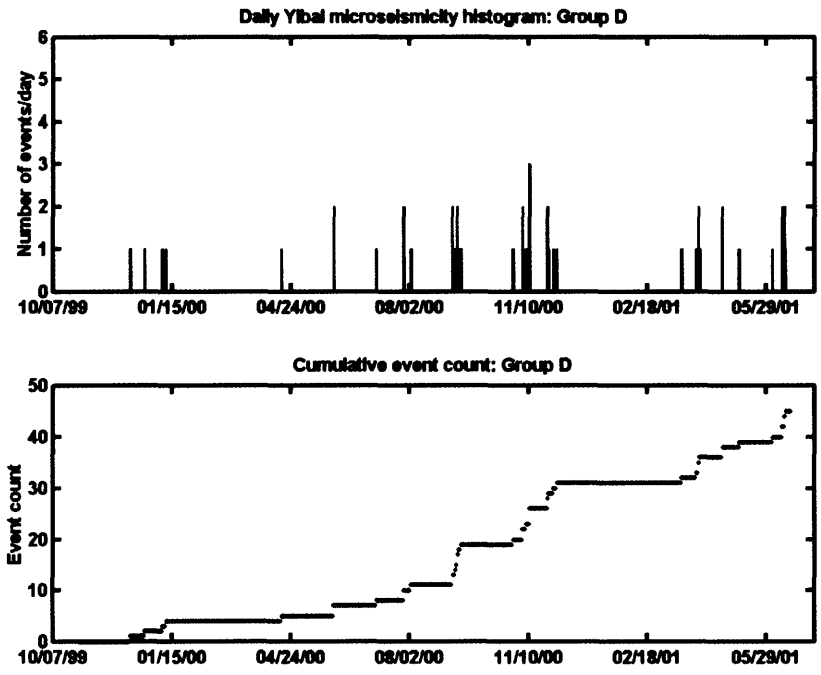

Figure 5.7. (a) Chronological histograms of Group D microseismicity. (b) Cumulative event count of Group D from October 29, 1999 to June18, 2001.

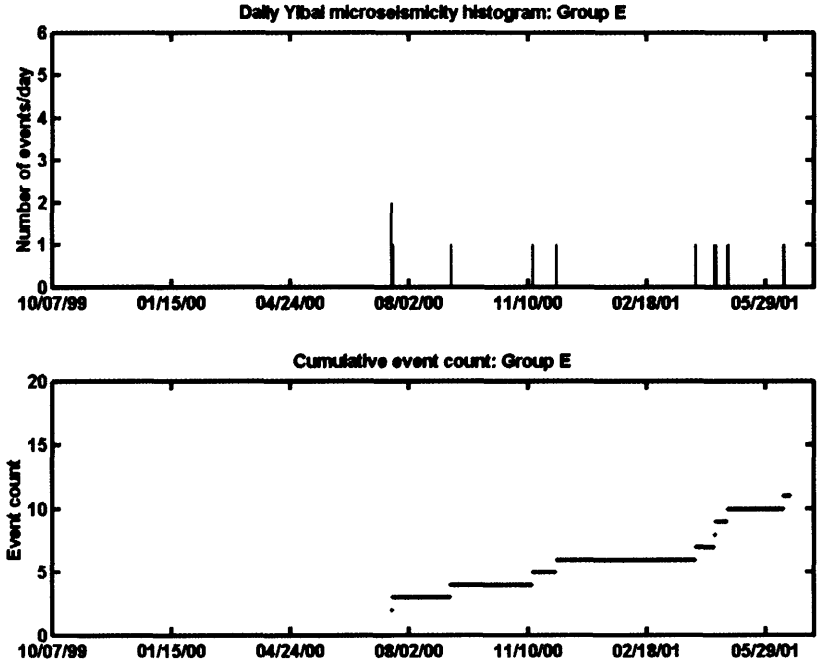

Figure 5.8. (a) Chronological histograms of Group E microseismicity. (b) Cumulative event count of Group E from October 29, 1999 to June18, 2001.

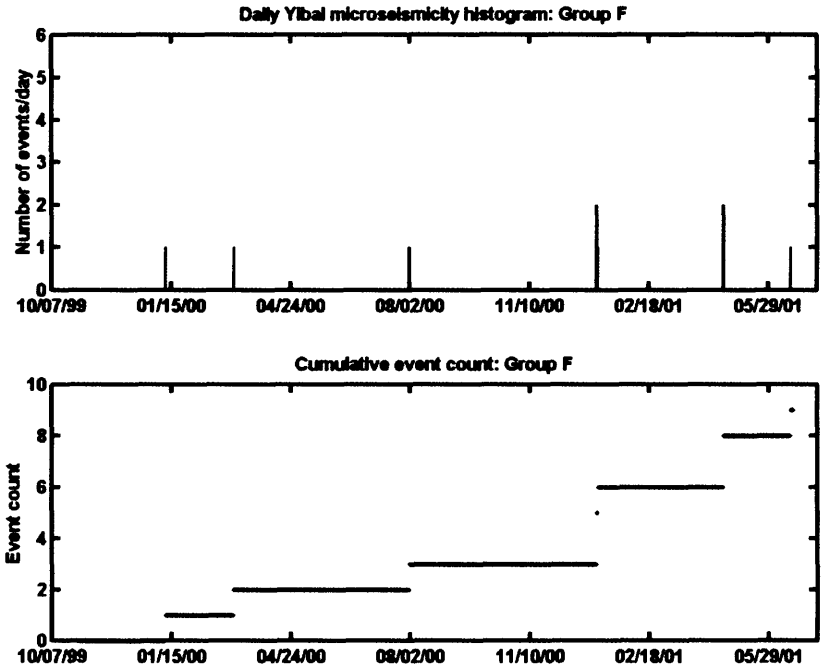

Figure 5.9. (a) Chronological histograms of Group F microseismicity. (b) Cumulative event count of Group F from October 29, 1999 to June18, 2001.

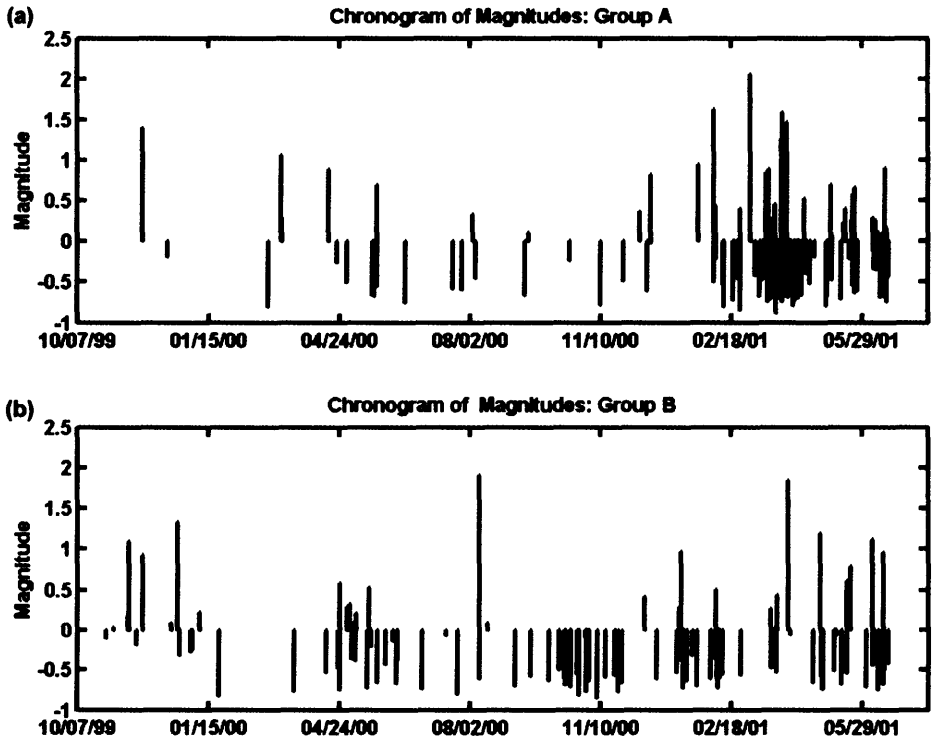

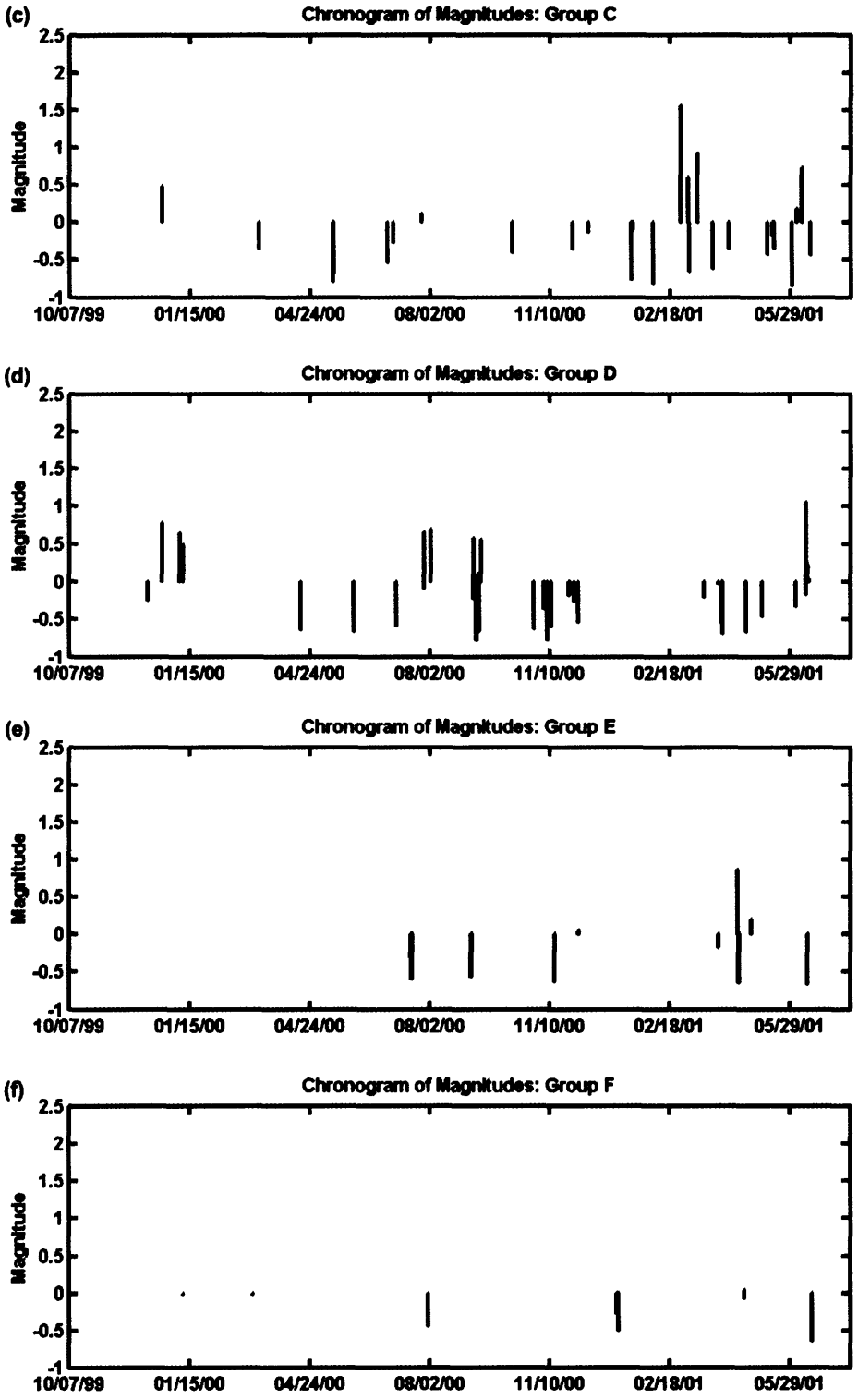

Figure 5.10. Chronograms of microearthquake magnitude of (a) Group A, (b) Group B, (c) Group C, (d) Group D, (e) Group E, and (f) Group F.

5.3 Spatio-temporal variation of *b*-value

The frequency-magnitude distribution (Gutenberg & Richter 1944) describes the power-law relationship between the frequency of occurrence and magnitude of earthquakes:

$$\log_{10}(N) = a - bM\,, \tag{5.2}$$

where N is the cumulative number of earthquakes having magnitudes larger than M, and a and b are constants. The original formulation by Gutenberg & Richter (1944) used the absolute rather than the cumulative frequency of earthquakes. However, from a practical and statistical standpoint it is preferable to use the cumulative frequency-magnitude distribution. The estimate of the b-value is calculated by using the maximum likelihood method (Aki, 1965) through the formula

$$\hat{b} = \frac{N \log_{10} e}{\sum_{i=1}^{N} (M_i - M_0)}\,. \tag{5.3}$$

It is a common procedure to group events into classes with equal magnitude increments. If the events are grouped in magnitude intervals of ΔM and the central value for the smallest class is M', then $M_0 = M' - \Delta M/2$. A magnitude bin unit $\Delta M = 0.1$ is used in this study. Ogata and Yamashina (1986) pointed out that equation (5.3) gives a biased

estimate of b because the expectation of $\hat{b}$ to be the true value b_0 is $E(\hat{b}) = Nb_0/N-1$. This suggests that the bias may be large when the number of events, N, is small. In order to obtain an unbiased estimator of b for a sample of N events, equation (5.3) is multiplied by $(N-1)/N$ to correct for asymmetric distribution about the population value,

$$\tilde{b} = \frac{(N-1)\log_{10} e}{\sum_{i=1}^{N}(M_i - M_0)}. \qquad (5.4)$$

The b-value is a measure of the relative representation of large and small earthquakes. The worldwide average for b-value is 1 and nearly all empirical values fall within the interval between 0.5 and 1.5. Since potential damage at a site is dominated by the occurrence of larger earthquakes, knowledge of the b-value is of great importance in seismic hazard analysis.

The overall frequency-magnitude distributions for the whole Field are shown in Figure 5.11. The cumulative number of microearthquakes of magnitude higher or equal to a given magnitude is plotted against magnitude. Using all 405 events, the overall b-value is equal to 0.85 for the 20-month monitoring period. This leads to an estimate of the maximum credible earthquake M $\approx$ 2.5 of the region. For the spatio-temporal variation analysis, only b-values calculated from event groups with at least 25 events have been considered. All of the volumes show low values (b_A = 0.69, b_B = 0.81, b_C = 0.66, b_D = 0.75). Because the absolute value of b depends on the magnitude scale used (Zuniga & Wyss, 1995), the b-values determined here are regarded as relative values and are used

only for comparison purposes at the Field. Figures 5.14 to 5.17 compare the frequency-magnitude distribution for four selected volumes (Groups A, B, C, and D) that are marked in the mapview of Figure 5.3. The highest *b*-values can be found in the event groups A and D where the focal depths range between less than 0.5 km and 3.5 km. The lowest *b*-value occurs in Group A where all the microearthquakes have shallow focal depths of less than 1.5 km. Low *b*-values are also observed in event group C located in the southernmost area of the fault zone. As a function of depth, I find that the $b = 0.79$, is lower at the shallow depths (0.0 – 1.5 km) than $b = 0.94$ at greater depths (1.5 – 3.5 km).

As we can see in Figures 5.4 and 5.5, Groups A and B are both very active seismicity zones but are characterized by different *b*-values. Earthquake activity in Group A is characterized by a low *b*-value of 0.69 where activity tends to be more episodic but more likely to consist of larger earthquakes of $M > 0.5$ as shown in Figure 5.11(a). The largest event ($M = 2.05$) occurred in this area on March 4, 2001. Group B is a region with higher *b*-value of 0.81. This area has more continuous earthquake activity characterized by many relatively weak events (Figure 5.11b).

The *b*-value has been considered as a kind of tectonic parameter, and a number of factors can cause variations of the *b*-value. Increased material heterogeneity often results in high *b*-values (Mogi, 1962; Sanchez et al., 2004). An increase in applied shear stress or an increase in effective stress decreases the *b*-value since *b* has been observed to be inversely proportional to stress (Scholz, 1968; Wyss 1973, Urbancic et al., 1992). For example, high pore pressures or low effective stress on the upper surface of the Wadati-

Benioff Zone (WBZ) and directly below the volcanic fronts are thought to be the causes of high anomalies in the b-value detected in the Alaska and New Zealand subduction zones (Wiemer & Benoit, 1996). In addition, an increase in the thermal gradient causes an increase in *b* (Warren & Latham, 1970). Successful applications to characterize the *b*-value have provided valuable tools to trace vesiculation and locate active magma chambers (Wiemer & McNutt, 1997), and to measure temporal changes of stress prior to major earthquakes in Japan (Imoto, 1991). Sometimes, it may not be clear which of these factors causes an observed *b*-value anomaly, unless other pieces of evidence are available. However, such variations can be expected in areas of inhomogeneous crustal structure or different earthquake generating processes.

The cause for the anomalously high *b*-value in deeper regions in the Field cannot be resolved with certainty at this point. However, it is possible to speculate that induced stresses due to production and injection are responsible for the increase in the *b*-value, since there is no indication of increased crack density and material heterogeneity beneath Shuaiba. It is also highly unlikely that an anomalous thermal gradient exists in the region. We know that the existence of water conductive faults that link the Shuaiba and Khuff reservoirs can lead to increase in pore pressure in deeper regions due to water injection into the Shuaiba aquifer. This in turn leads to a decrease in the effective stress and an increase in *b*, and may explain why Group B tends to emit more numerous smaller events.

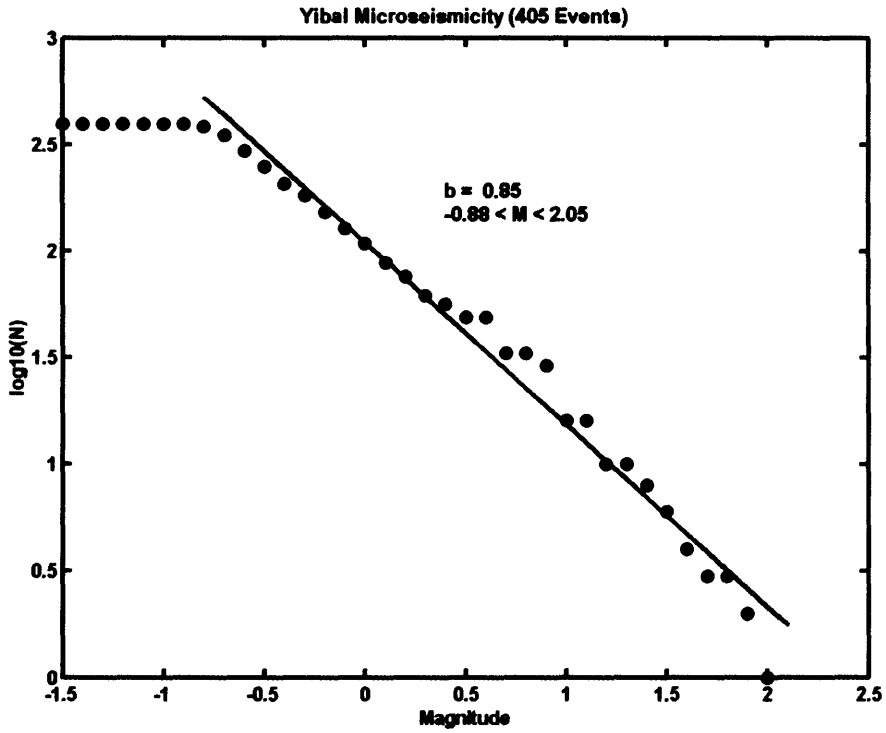

Figure 5.11. Frequency-magnitude diagram for all the 405 microearthquakes recorded in the Field, Oman.

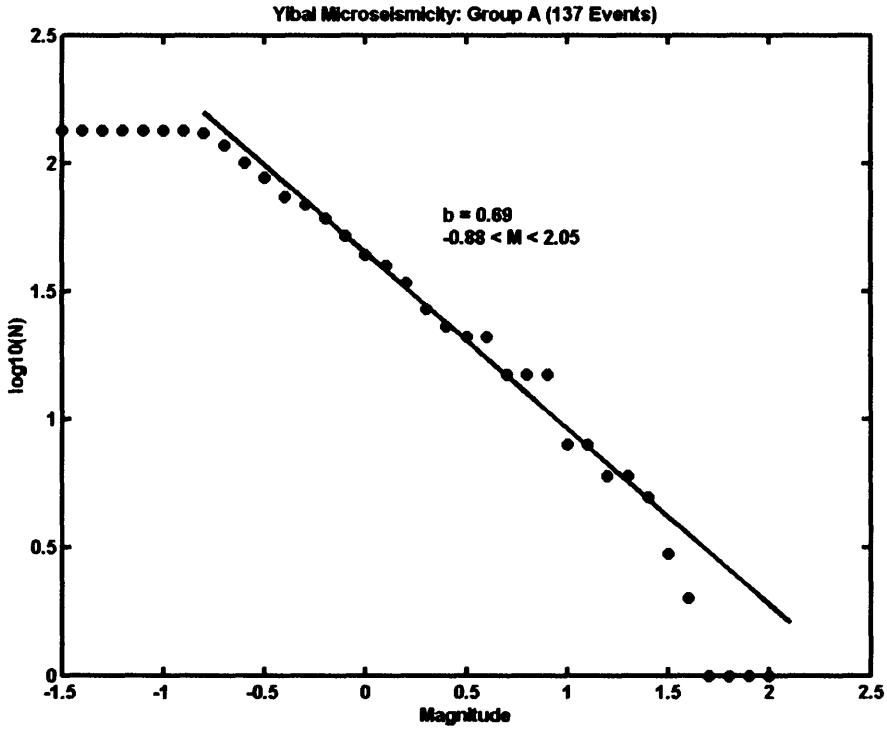

Figure 5.12. Frequency-magnitude diagram for Group A (137 events).

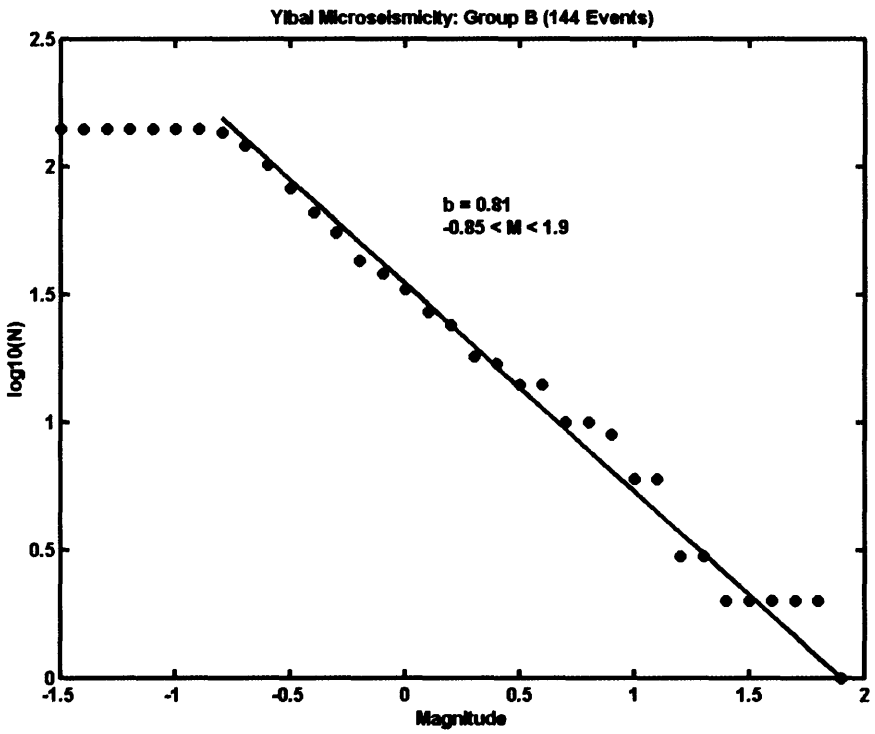

Figure 5.13. Frequency-magnitude diagram for Group B (144 events).

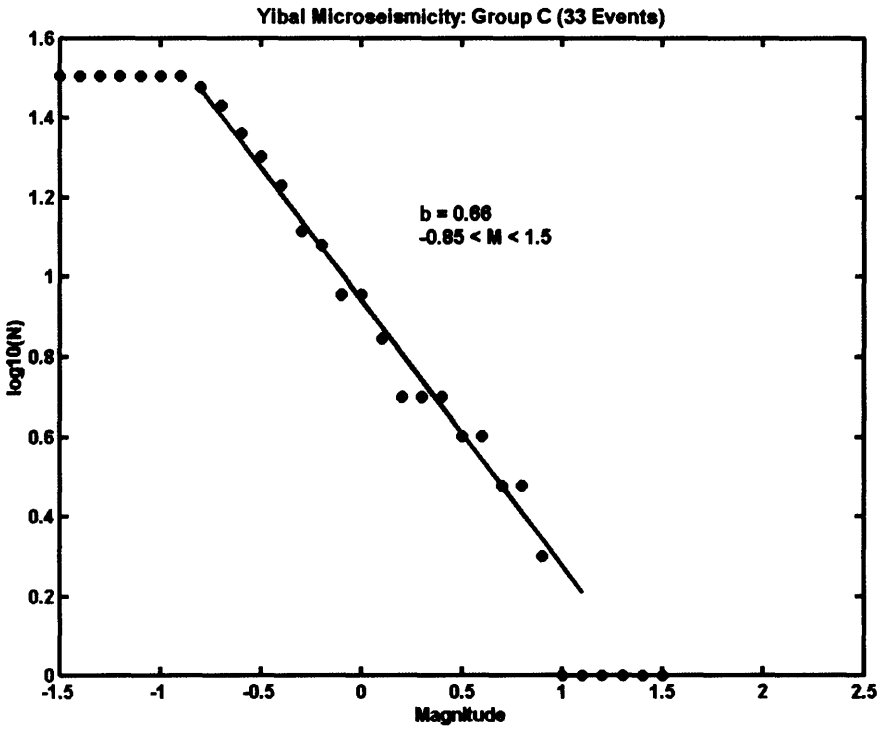

Figure 5.14. Frequency-magnitude diagram for Group C (33 events).

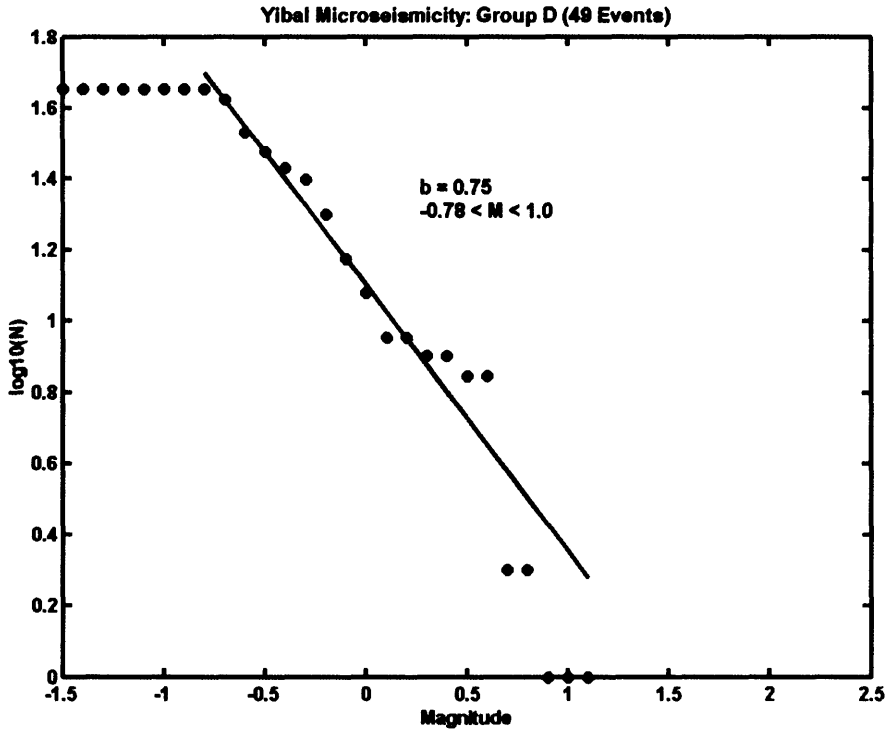

Figure 5.15. Frequency-magnitude diagram for Group D (49 events).

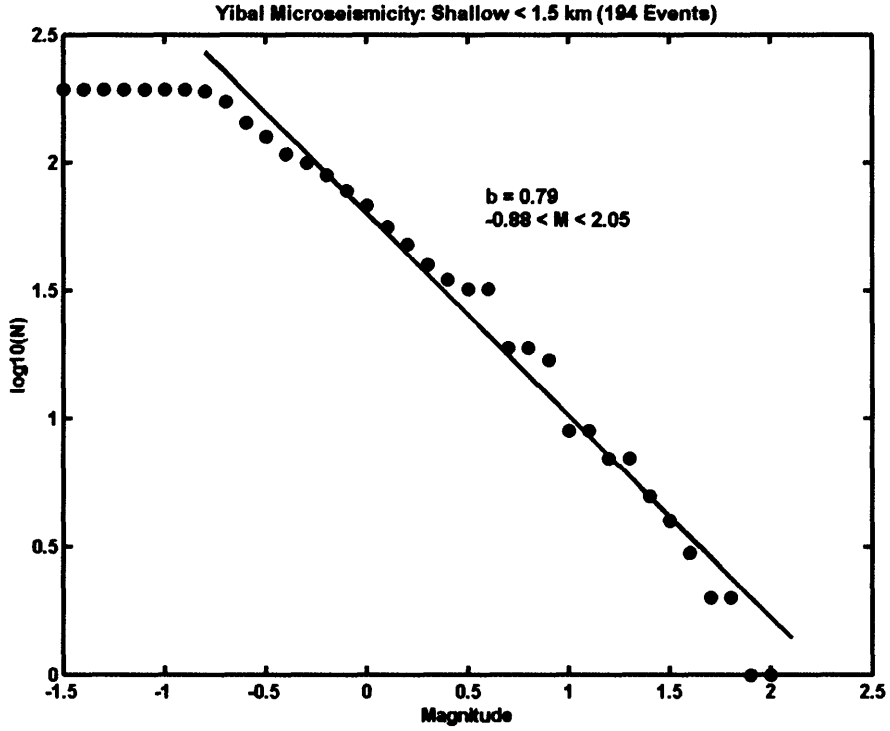

Figure 5.16. Frequency-magnitude diagram for shallow events (< 1.5 km, 194 events).

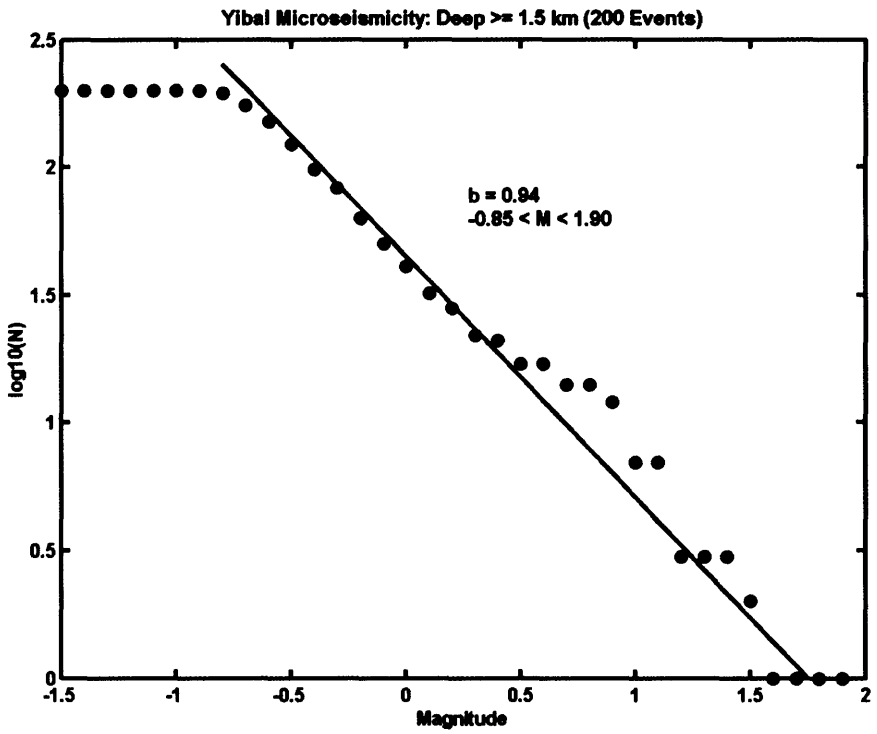

Figure 5.17. Frequency-magnitude diagram for shallow events (≥ 1.5 km, 200 events).

To investigate the temporal variations of *b*-value, I assume that stresses change before and after an earthquake, and examine the *b*-values within epicentral areas of relatively large microearthquakes with magnitudes greater than 0.8 for Groups A and B. Each of the two groups is scanned for time changes of *b* by applying a sliding time window. The number of earthquake within the time window is kept constant at 25 events and the window is moved by one earthquake at a time. This procedure establishes a constant statistical uncertainty but a variable length time window.

Results are presented in Figures 5.18 and 5.19 for Group A and Group B events, respectively. The *b*-values are plotted at the time the last event enters the time window. The *b*-value of earthquakes of Group A starts at $b = 0.7$ on December 18, 2000 and

reaches to a minimum value of b = 0.5 on April 1, 2001. Then it increases to b = 1.07 on May 5, 2001, and decreases again to b = 0.7 on June 18, 2001. The b-value of earthquake of Group B starts at b = 0.5 on May 1, 2000, increases to 0.85 on June 26, 2000 and then decreases to 0.60 on August 9, 2000. After that, it increases steadily to a maximum of b = 1.37 on November 26, 2000 and decreases slowly to b = 0.8 on June 17, 2001.

Here we can only emphasize tendencies for changes but not the details due to the large statistical uncertainties of the b-values. Large time variations in the b-value are evident for both for Group A and Group B area. It is important to emphasize that the deduced changes of b are statistically significant according to the F-distribution test. For example, consider the change in b-values from 0.85 on June 26, 2000 to 0.60 on August 9, 2000 after the occurrence of a magnitude 1.90 earthquake (Event #1 on Figure 5.19). Compare 0.85/0.60 = 1.42 with the F-value for 2×25 degrees of freedom in the numerator and 2×25 degrees of freedom in the denominator. Since $F_{0.05}(50,50)$ = 1.5995 is larger than 1.42, the change in b is significant at the 95 percent confidence level. There is a clear tendency of increasing b some years before the event and a sudden drop just before the occurrence of the earthquake. Since the time window is moved only by one earthquake at a time, neighboring b-values displayed in Figures 5.18 and 5.19 are strongly dependent on each other. Therefore, the larger the time span covered by an individual window, the stronger is the smoothing effect and the smaller is the chance to detect variations in b.

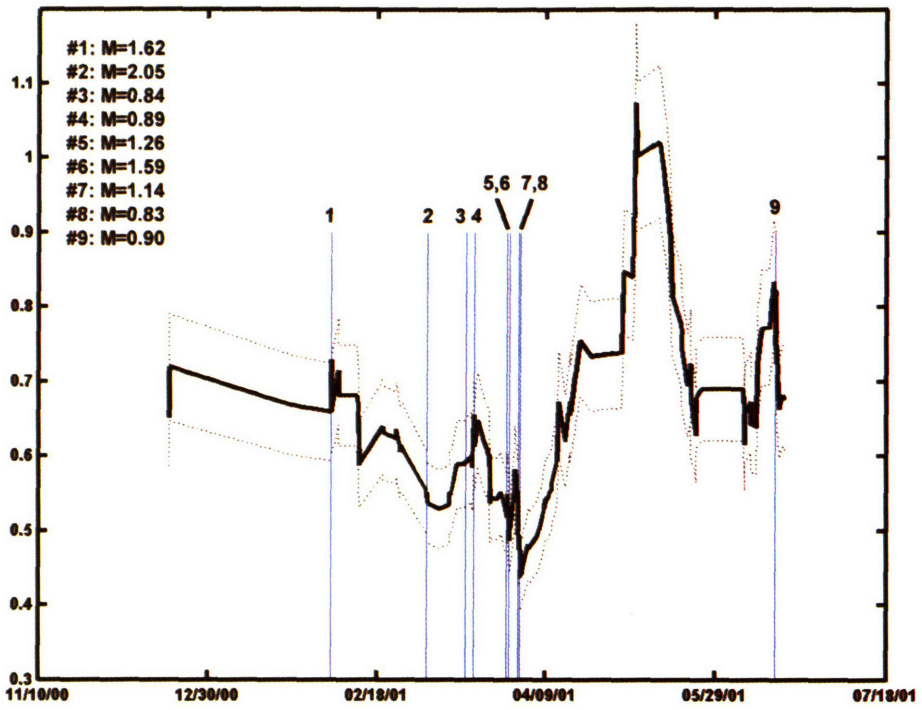

Figure 5.18. Time variation of b-value around the biggest events of Group A with magnitudes > 0.65. Blue lines indicate the time of occurrence of respective earthquakes. Dotted lines show the standard deviation, $\sigma = b/\sqrt{n}$, for each of the calculated b-values.

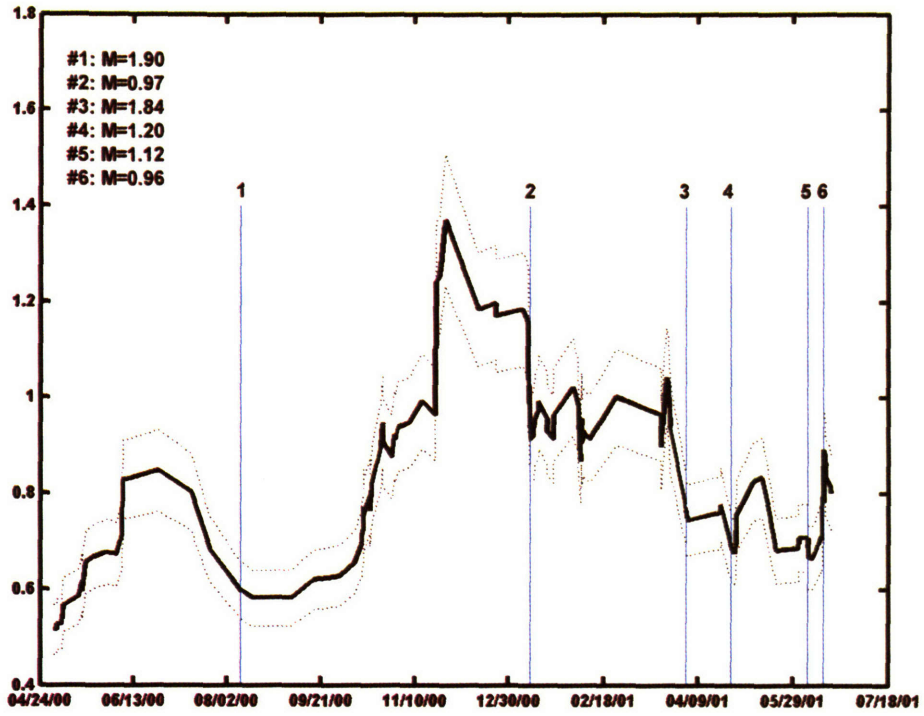

Figure 5.19. Time variation of b-value around the biggest events of Group B with magnitudes > 0.8. Blue lines indicate the time of occurrence of respective earthquakes. Dotted lines show the standard deviation, $\sigma = b/\sqrt{n}$, for each of the calculated b-values.

5.4 Hydrocarbon exploitation and microseismicity

One of the primary objectives of this work is to examine the seismicity and the changes in seismicity due to a large influx of fluid. Many natural and man-induced processes result in injection and withdrawal of fluids in the Earth. Examples include migration of magmatic fluids at depth (Murru et al., 1999), oil and gas recovery (House & Flores, 2002; Zoback & Zinke, 2002), liquid waste disposal (Healy et al., 1968), and

geothermal energy production (Rutledge et al., 2002). These processes are commonly accompanied by deformation of the host rocks. The hypothesis being that the increased microearthquake activity is due to a diverse set of mechanisms. That is, there is not one "triggering" mechanism but a variety of mechanisms in operation that may work independently, together, or superimpose to enhance or possibly reduce seismicity. Fault reactivation has been observed to be closely linked to subsurface fluid flow and hence the re-migration of hydrocarbons. There is abundant evidence that active faults and fractures provide high permeability conduits for fluid flow during deformation. Reactivation can breach fault-bound traps. Faulting and fracturing associated with the in situ stress field has been shown to control trap breaching in the North Sea (Gaarenstroom et al., 1993) and the Gulf of Mexico (Finkbeiner et al., 2001). Reactivation of faults also poses significant risk to surface buildings and wells in the oil field.

The Natih formation is a main reservoir in the Fahud Salt Basin. Like Natih Field and Fahud Field, production from Natih was initially by depletion drive. Production of the Natih gas commenced in 1971 to supply lift gas for the Shuaiba oil. Gas supply to the government gas grid was initiated in 1978. The Natih gas reservoir in the Field is a depleting gas reservoir and pressure has dropped from 10,120 KPa to 7,920 KPa since 1973 (van Driel et al., 2000). Currently, there are 14 dedicated wells producing gas from the Natih.

There is oil production from the Shuaiba reservoir with the main oil accumulation in the Upper Shuaiba. The Shuaiba reservoir was initially produced by natural depletion,

but water injection based on a five spot pattern development was introduced in 1972 to maintain reservoir pressure. It was subsequently expanded to an inverted nine spot pattern. Water was initially injected into the oil column but was later injected into the water aquifer. In 1989, quarter pattern in-fill drilling commenced on the crest of the field to increase production and improve sweep. From 1994 to 2000, further field development consisted of high density in-fill drilling by horizontally sidetracking existing watered-out wells (Mijnssen et al., 2003).

A method to identify the cause of induced seismicity is to compare the seismicity with the exploitation schedule of the oilfield. The relevant production data are the values of the monthly volume rates and cumulative volume of fluid extracted and injected for all the wells that has operated in the Field. With these values, a table can be constructed to tabulate the monthly extracted and injected volumes and the volume imbalance, or the difference between the volumes of injected and extracted fluids. However, the exploitation schedule of the Field has been very complicated with more than 480 active producing / injection wells during the period between 1999 and 2003. Therefore, I divided the Field into 2km × 2km area grids in order to analyze spatial variations of the exploitation schedule and microseismicity. The yellow shaded regions shown in Figures 5.20, 5.25, and 5.30 are selected for the spatial analysis. All the gas production, oil production, water injection, and seismic event counts that occurred within the grid are summed and compared.

5.4.1 Injection and Microseismicity

In the Field, water has been injected into the Shuaiba reservoir in attempt to maintain the pressure in the oil reservoir. Cumulative net water injection volume (blue dash lines) and cumulative seismic event counts (black solid lines) at the Field are plotted on the upper right corners of Figures 5.20 to 5.29 and Figures 5.31 to 5.33. Also, net water injection rate per month (blue dash lines) and seismic event rate per month (black solid lines) are plotted on the lower right corner of Figures 5.20 to 5.29 and Figures 5.31 to 5.33. Except in Area 5.20(a), there is no clear evidence that shows strong temporal and spatial correlations between net injection and event count. In fact, the net injection and event counts show negative correlations in Figures 5.25, 5.26, 5.27, and 5.28 on both the cumulative and rate plots. The net water injection rate for all of the Field is generally low with roughly the small amounts of liquid produced and injected. Based on these observations, the microseismicity is appears to be unlikely to be induced by water injection into the Shuaiba reservoir.

5.4.2 Gas Production and Microseismicity

The monthly gas production rates (red dash lines) and monthly event rates (solid black lines) for selected areas denoted in Figures 5.20, 5.25, and 5.30 are graphed in the lower left corners of Figures 5.21 to 5.24, Figures 5.26 to 5.29, and Figures 5.31 to 5.33. The cumulative volume of gas produced (red dash lines) is also plotted on the upper left corners. The highest rates of seismicity and the strongest correlation of seismic activity

with gas production are associated with areas with major gas production, primarily in Areas 5.20a (36% event count) and 5.20b (34% event count), followed by Areas 5.20c (8% event count), 5.20d (15% event count), and 5.25a (8% event count). The gross rate of seismicity tracks right along with changes in the gas production in these areas, and cumulative-event count curves increase in slope with increased cumulative gas production. Areas 5.25(b), 5.25(c), and 5.25(d) have only relatively minor gas production (Figures 5.26 to 5.29) and they only account for 5% of total event count. The spatial and temporal correlation of the event rates with the high gas-producing areas but not with water injection suggest that the microseismicity is mainly triggered by the gas-production induced stress changes.

The deep microseismicity in Area 5.20a seems to be more complicated than others. It is the only area where gas production and net water injection have similar patterns, and their effects cannot be separated. Similar patterns remain even when the events are categorized into shallow and deep groups. Many events in Area 5.20a occurred more than 1 km below the gas reservoir and so, the possibility that events were induced by injection cannot be ruled out. Moreover, there was only modest gas production in Areas 5.30a, 5.30b, and 5.30c, and relatively high gas production in Area 5.30d but no seismicity was observed in those areas during the monitoring period (Figures 5.31 to 5.33). There are no known faults in Areas 5.30c and 5.30d, and all faults in Area 5.30a have NW-SE strikes conjugate to the active fault zones. Microseismicity in the Field mainly reactivated pre-existed zone of weakness in the reservoir and was controlled by the regional normal stress regime rather than opening up new faults. Although minor gas

production occurs in areas with no microseismicity observed, induced stress changes due to gas production in those areas are not large enough either to reactivate old faults or to open up new ones. In addition, strong spatial correlations can be observed between shallow earthquakes and cumulative gas production in Figure 5.36(a), and deep microearthquakes and positive net fluid injection in Figure 5.36(b).

We have to be careful with comparing the event rate and corresponding production/injection rates especially when the sub-region has a low rate of microseismicity. It is because the apparent surge in event rate (i.e. spikes) may not be related to the fluid projection/injection but due to mainshock-aftershock sequences. The aftershocks are the smaller earthquakes that occur after the mainshock. They decrease in both magnitude and frequency of occurrence as times goes on. In Figure 5.35, the magnitudes are plotted against time for the sub-regions where the event occurrences are sparse. Many events cluster both in time and magnitude. Events of similar magnitudes clustered in time show that there is no apparent mainshock and aftershock relationship in the Field.

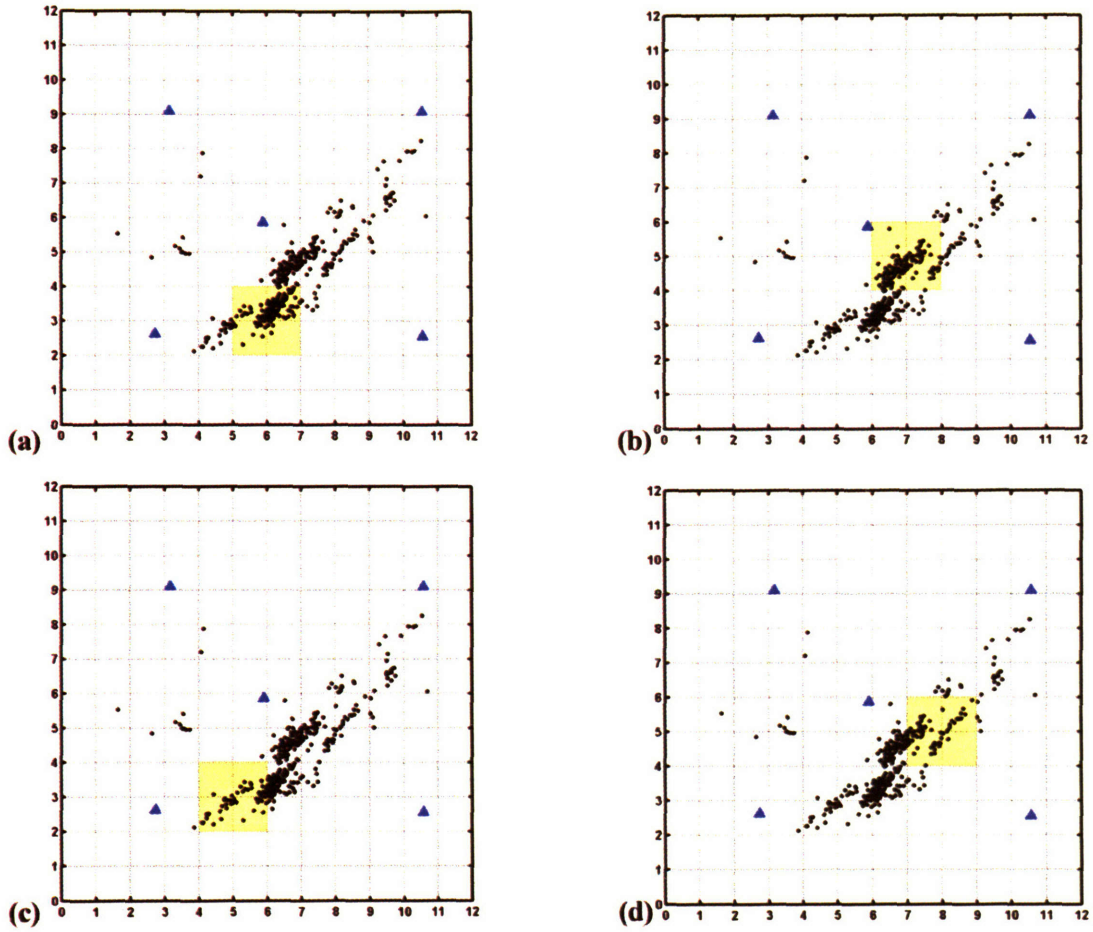

Figure 5.20. The Field is divided into 2km × 2km grids. The yellow shaded areas are the selected areas for temporal analysis of seismicity and production/injection.

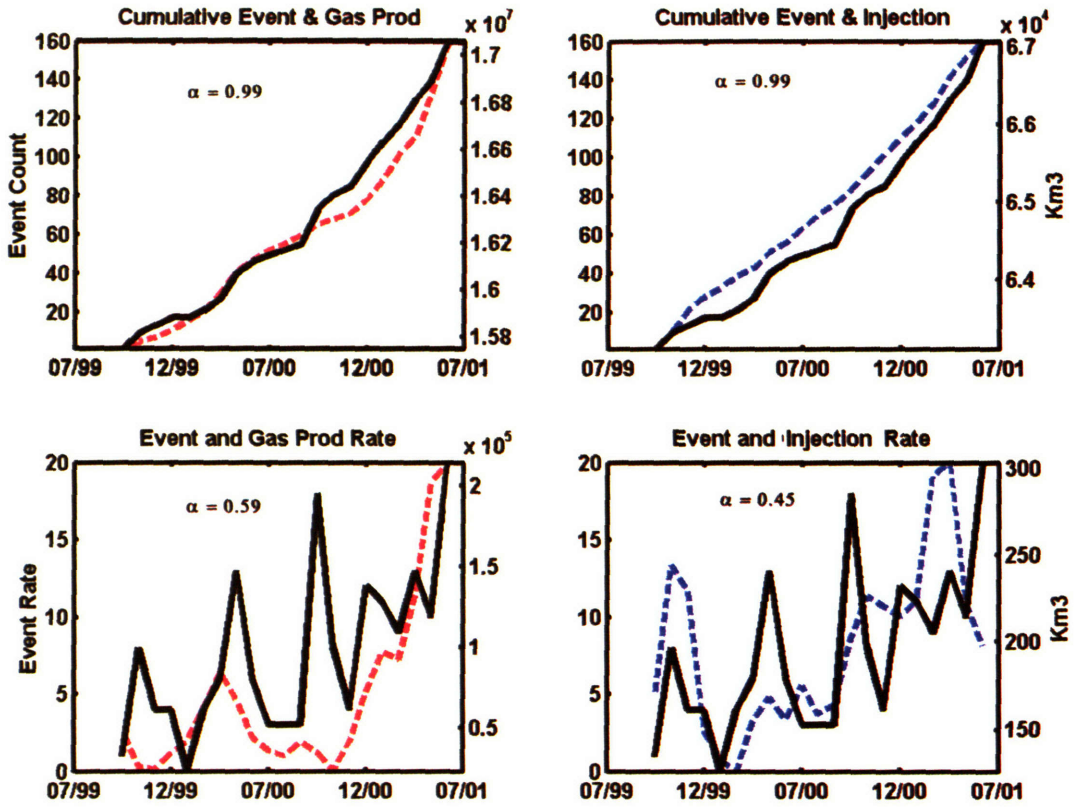

Figure 5.21. Upper left: Cumulative gas production volume (red dash line) and the cumulative event counts (black line) in the study area in figure 5.20a (Area 5.20a). Upper right: Cumulative net water injection (blue dash line) and the cumulative event counts (black line) in Area 5.20a. Lower left: Monthly gas production rate (red dash line) and monthly event count (black line) in Area 5.20a. Lower right: Monthly net water injection rate (blue dash line) and monthly event count (black line) in Area 5.20a.

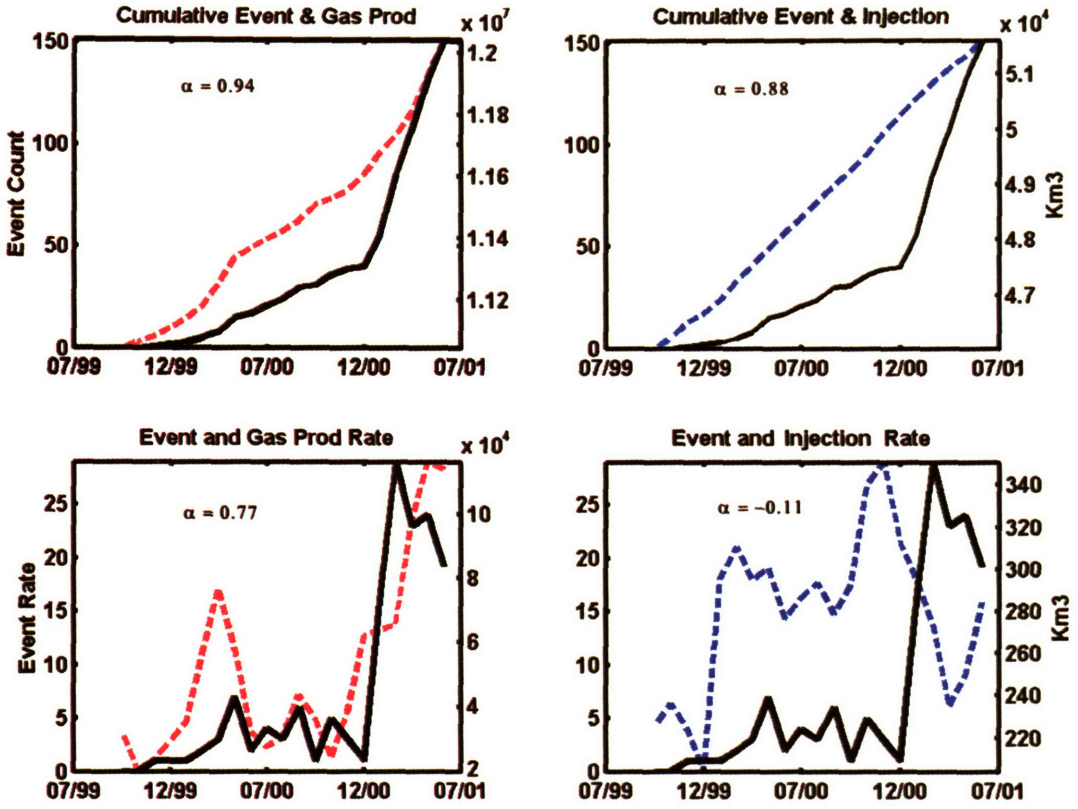

Figure 5.22. Upper left: Cumulative gas production volume (red dash line) and the cumulative event counts (black line) in the study area in figure 5.20b (Area 5.20b). Upper right: Cumulative net water injection (blue dash line) and the cumulative event counts (black line) in Area 5.20b. Lower left: Monthly gas production rate (red dash line) and monthly event count (black line) in Area 5.20b. Lower right: Monthly net water injection rate (blue dash line) and monthly event count (black line) in Area 5.20b.

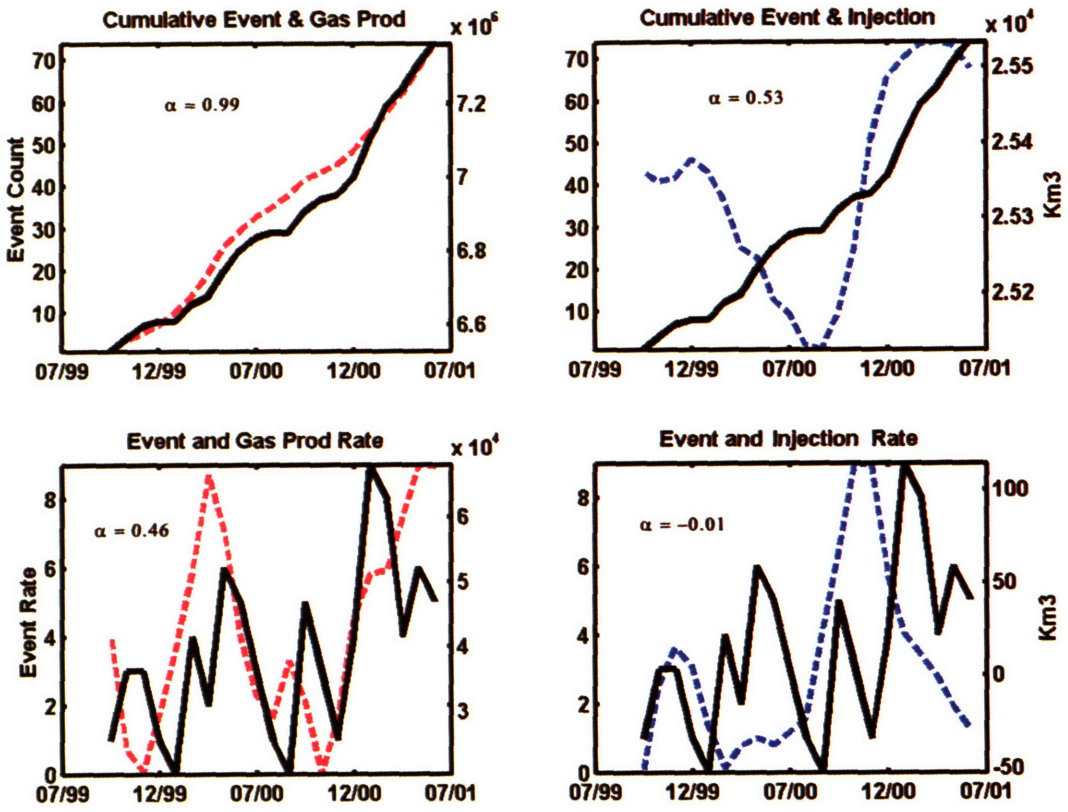

Figure 5.23. Upper left: Cumulative gas production volume (red dash line) and the cumulative event counts (black line) in the study area in figure 5.20c (Area 5.20c). Upper right: Cumulative net water injection (blue dash line) and the cumulative event counts (black line) in Area 5.20c. Lower left: Monthly gas production rate (red dash line) and monthly event count (black line) in Area 5.20c. Lower right: Monthly net water injection rate (blue dash line) and monthly event count (black line) in Area 5.20c.

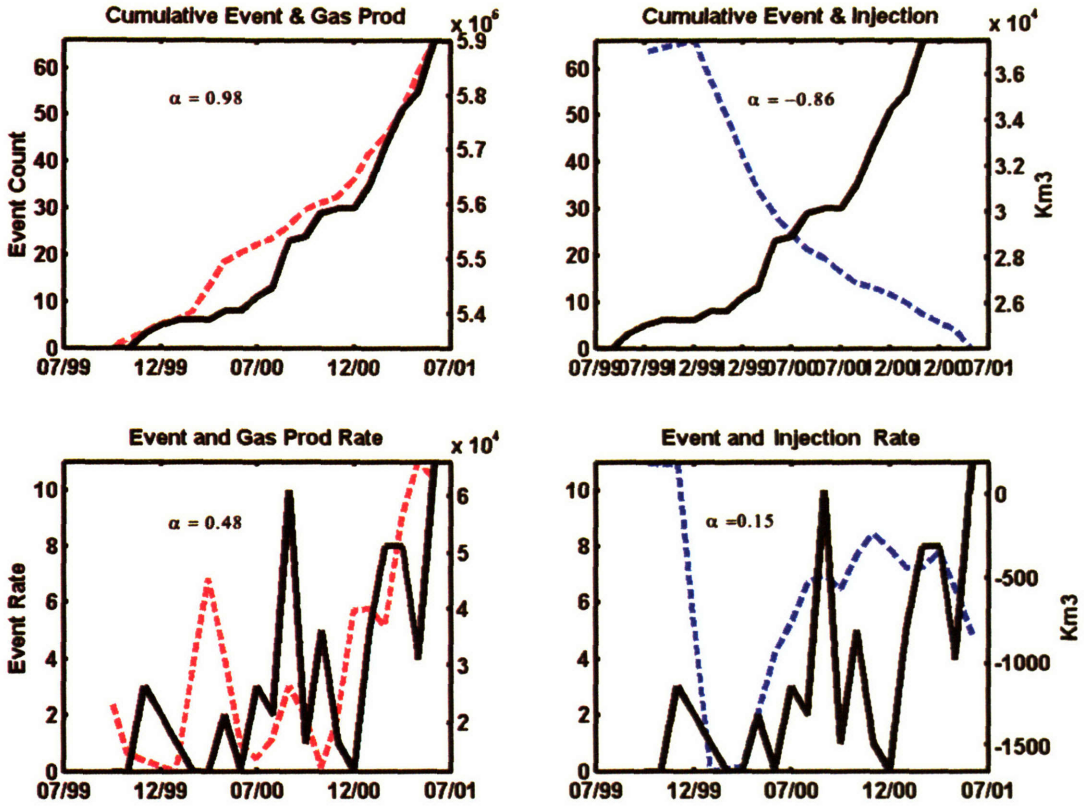

Figure 5.24. Upper left: Cumulative gas production volume (red dash line) and the cumulative event counts (black line) in the study area in figure 5.20d (Area 5.20d). Upper right: Cumulative net water injection (blue dash line) and the cumulative event counts (black line) in Area 5.20d. Lower left: Monthly gas production rate (red dash line) and monthly event count (black line) in Area 5.20d. Lower right: Monthly net water injection rate (blue dash line) and monthly event count (black line) in Area 5.20d.

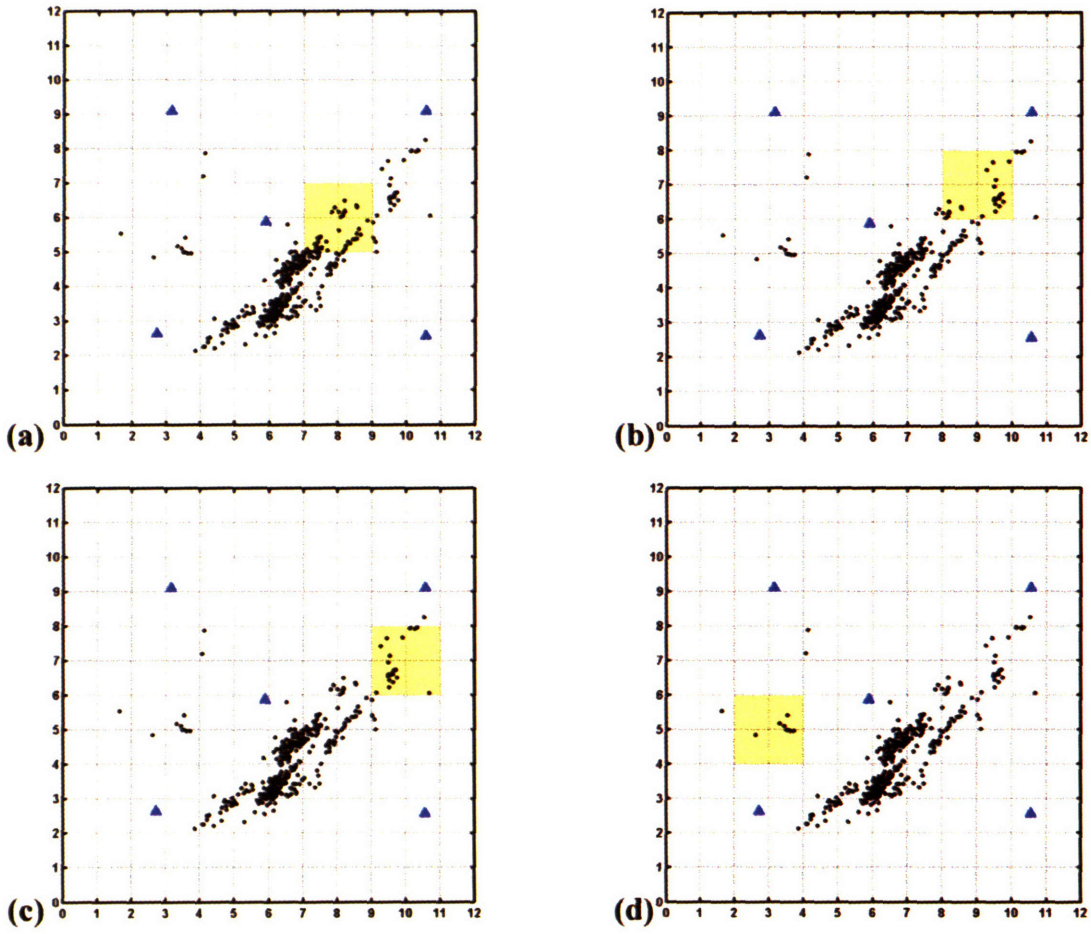

Figure 5.25. The Field is divided into 2km × 2km grids. The yellow shaded areas are the selected areas for temporal analysis of seismicity and production/injection.

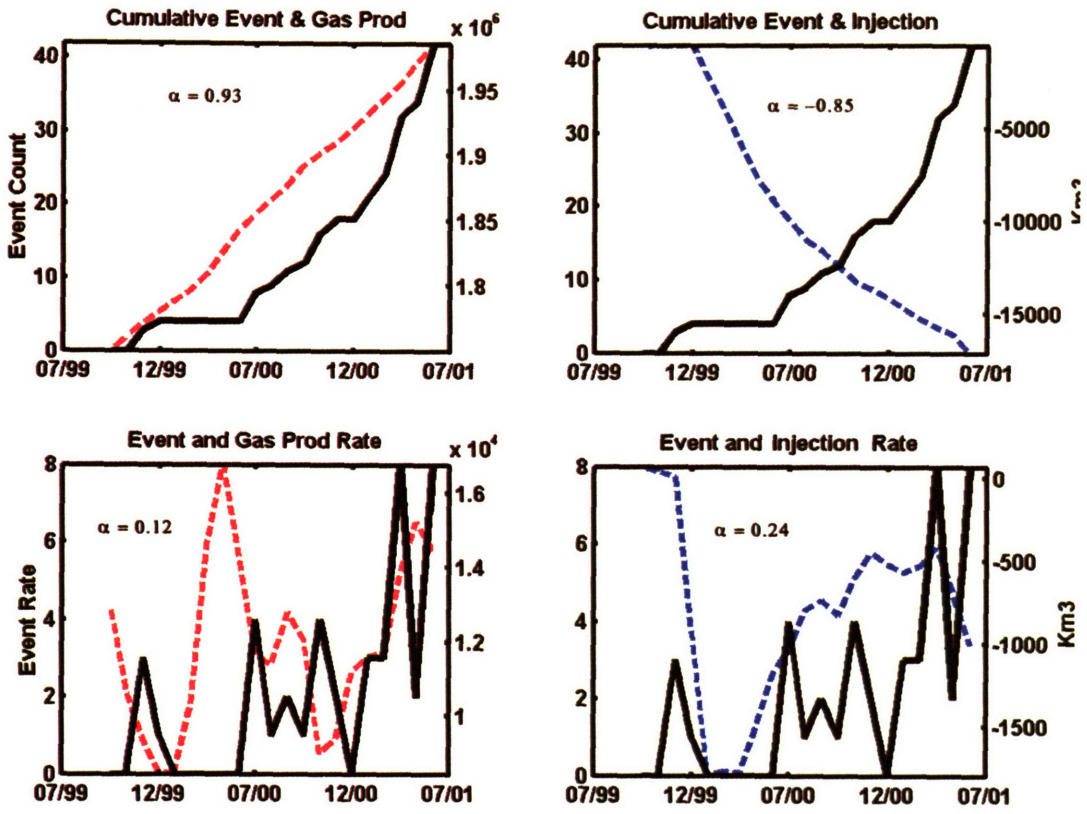

Figure 5.26. Upper left: Cumulative gas production volume (red dash line) and the cumulative event counts (black line) in the study area in figure 5.25a (Area 5.25a). Upper right: Cumulative net water injection (blue dash line) and the cumulative event counts (black line) in Area 5.25a. Lower left: Monthly gas production rate (red dash line) and monthly event count (black line) in Area 5.25a. Lower right: Monthly net water injection rate (blue dash line) and monthly event count (black line) in Area 5.25a.

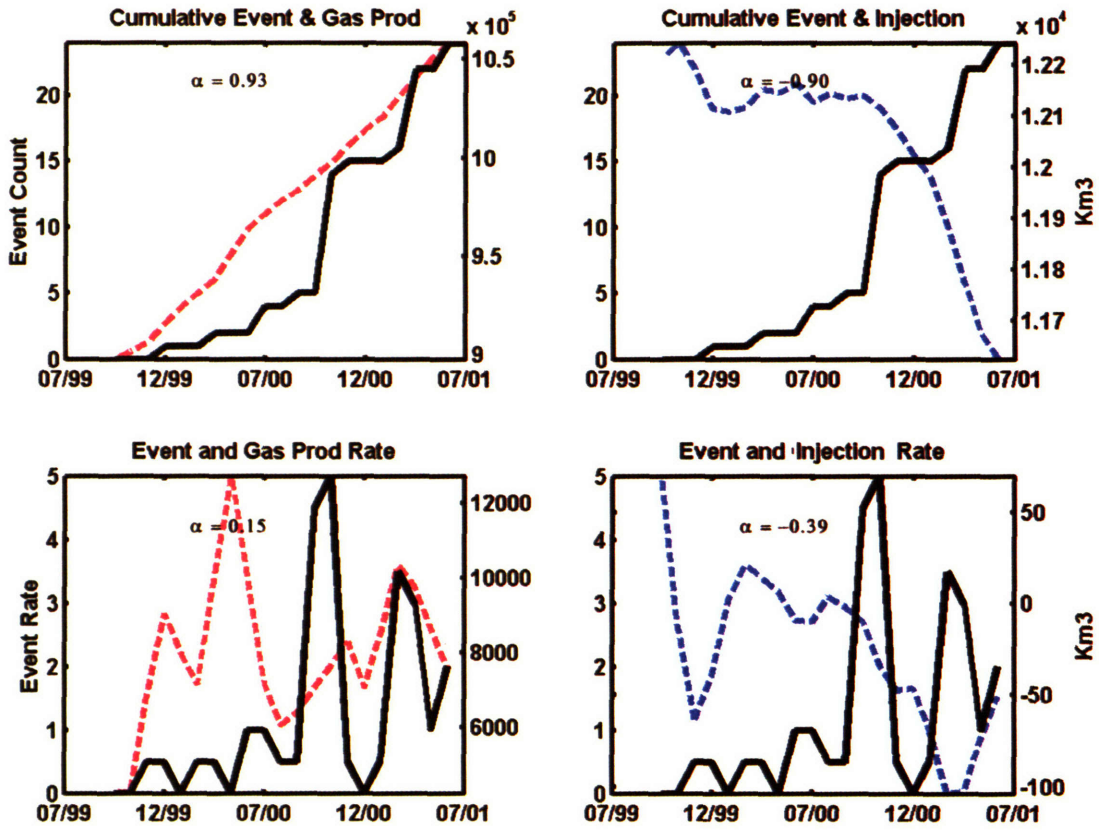

Figure 5.27. Upper left: Cumulative gas production volume (red dash line) and the cumulative event counts (black line) in the study area in figure 5.25b (Area 5.25b). Upper right: Cumulative net water injection (blue dash line) and the cumulative event counts (black line) in Area 5.25b. Lower left: Monthly gas production rate (red dash line) and monthly event count (black line) in Area 5.25b. Lower right: Monthly net water injection rate (blue dash line) and monthly event count (black line) in Area 5.25b.

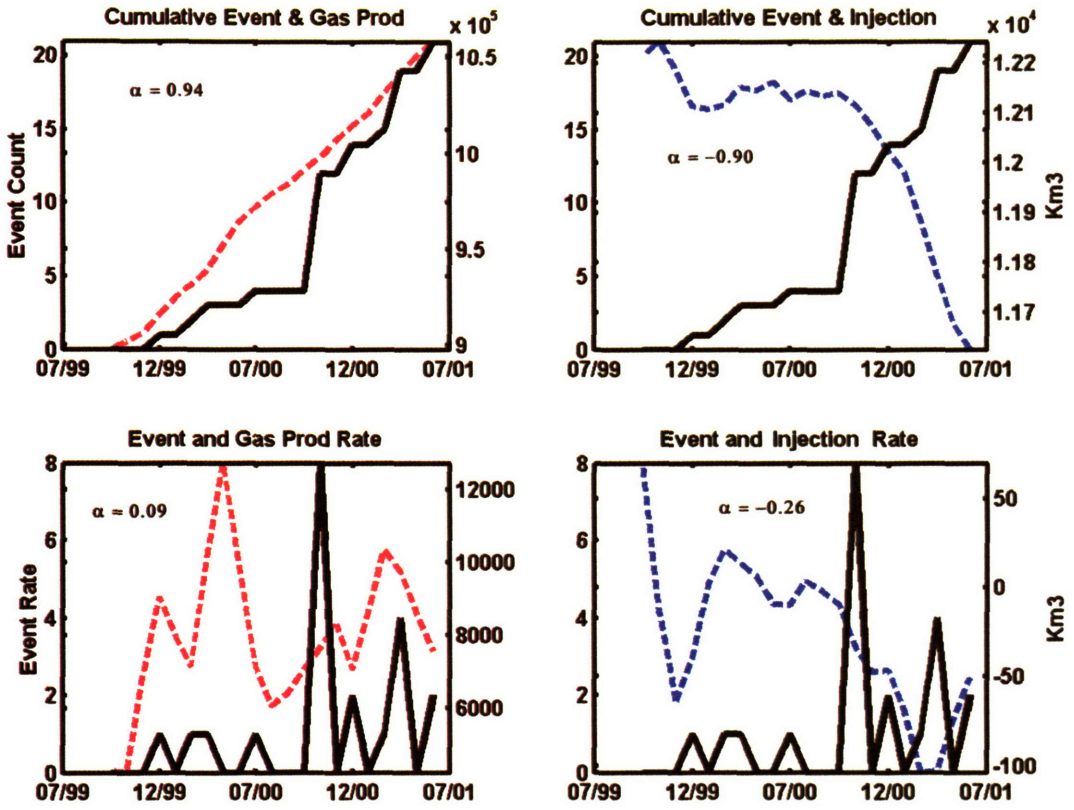

Figure 5.28. Upper left: Cumulative gas production volume (red dash line) and the cumulative event counts (black line) in the study area in figure 5.25c (Area 5.25c). Upper right: Cumulative net water injection (blue dash line) and the cumulative event counts (black line) in Area 5.25c. Lower left: Monthly gas production rate (red dash line) and monthly event count (black line) in Area 5.25c. Lower right: Monthly net water injection rate (blue dash line) and monthly event count (black line) in Area 5.25c.

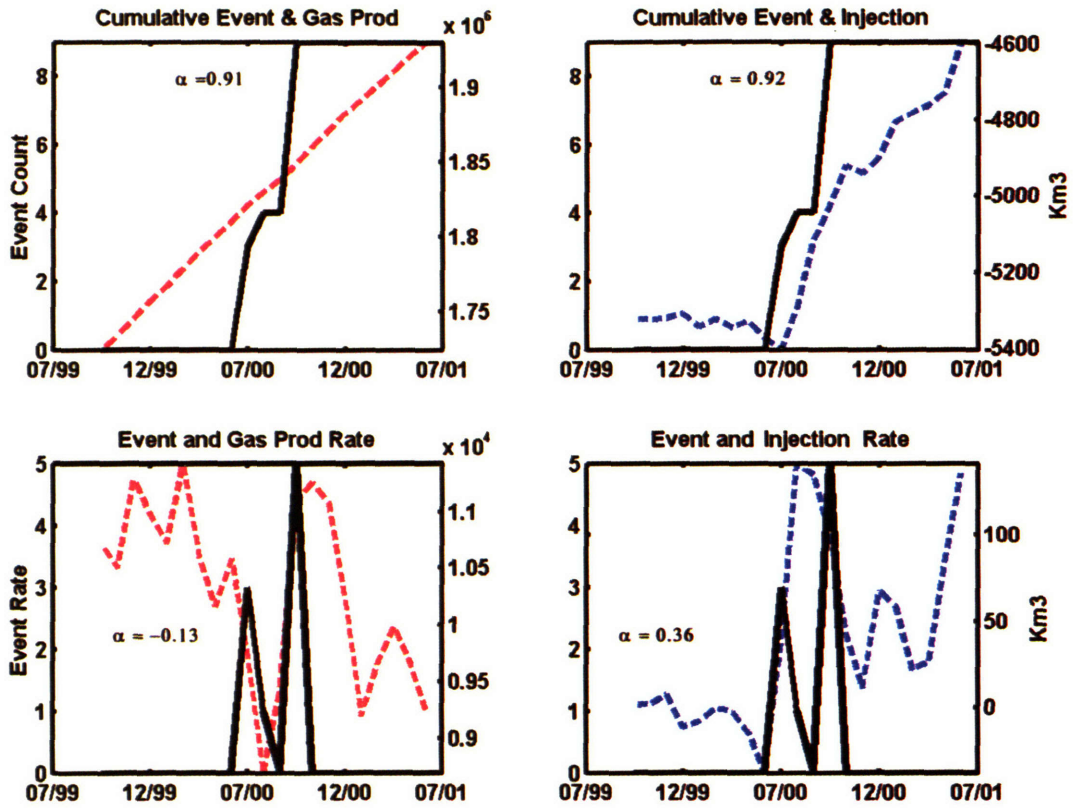

Figure 5.29. Upper left: Cumulative gas production volume (red dash line) and the cumulative event counts (black line) in the study area in figure 5.25d (Area 5.25d). Upper right: Cumulative net water injection (blue dash line) and the cumulative event counts (black line) in Area 5.25d. Lower left: Monthly gas production rate (red dash line) and monthly event count (black line) in Area 5.25d. Lower right: Monthly net water injection rate (blue dash line) and monthly event count (black line) in Area 5.25d.

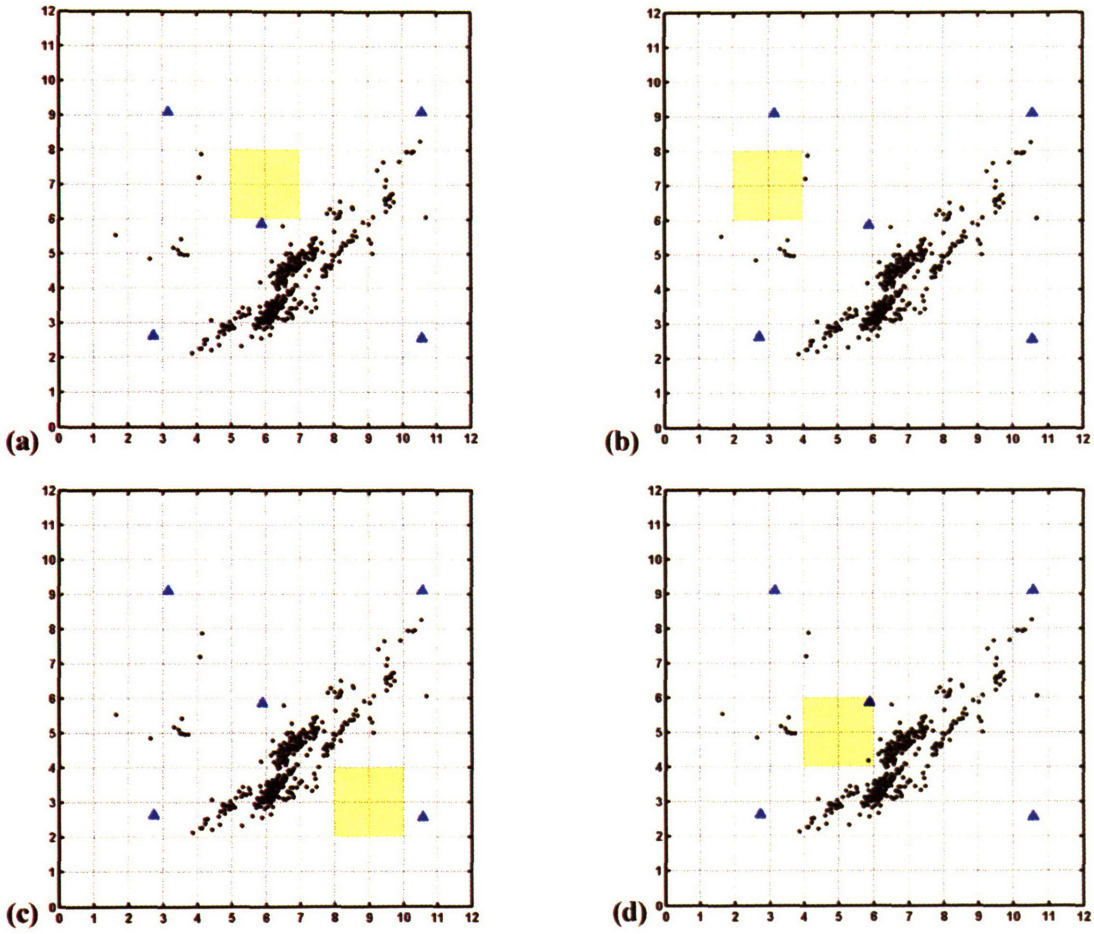

Figure 5.30. The Field is divided into 2km × 2km grids. The yellow shaded areas are the selected areas for temporal analysis of seismicity and production/injection.

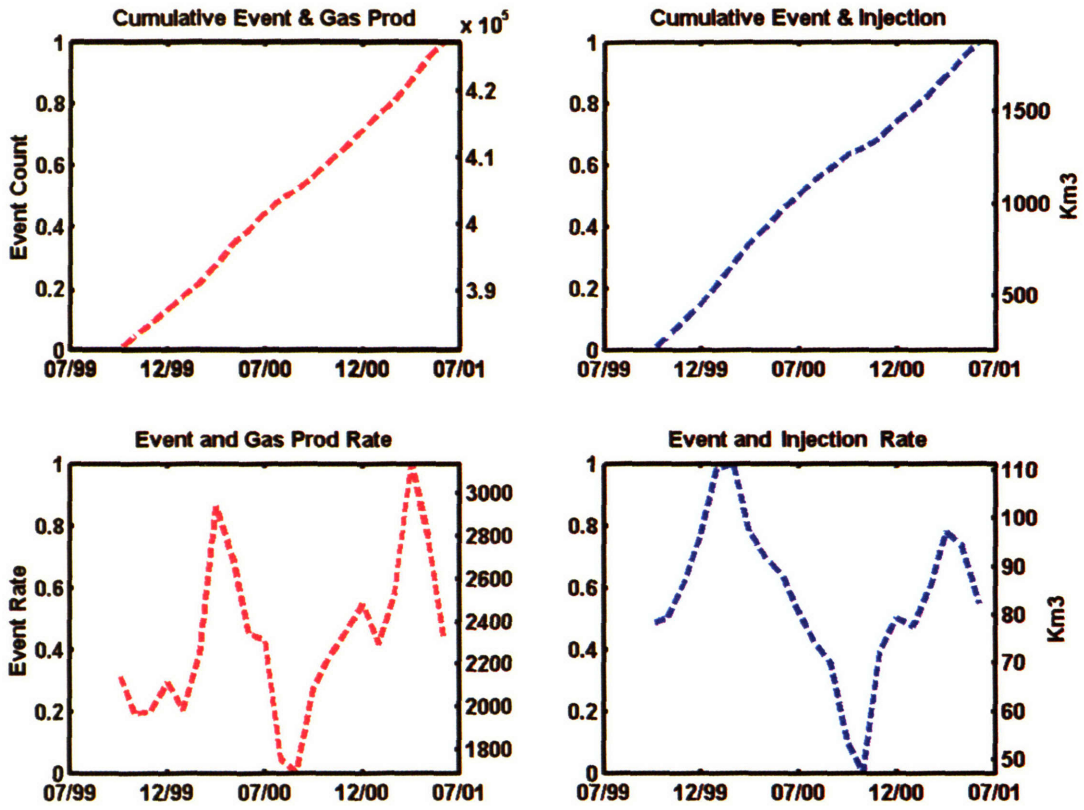

Figure 5.31. Upper left: Cumulative gas production volume (red dash line) and the cumulative event counts (black line) in the study area in figure 5.30a (Area 5.30a). Upper right: Cumulative net water injection (blue dash line) and the cumulative event counts (black line) in Area 5.30a. Lower left: Monthly gas production rate (red dash line) and monthly event count (black line) in Area 5.30a. Lower right: Monthly net water injection rate (blue dash line) and monthly event count (black line) in Area 5.30a.

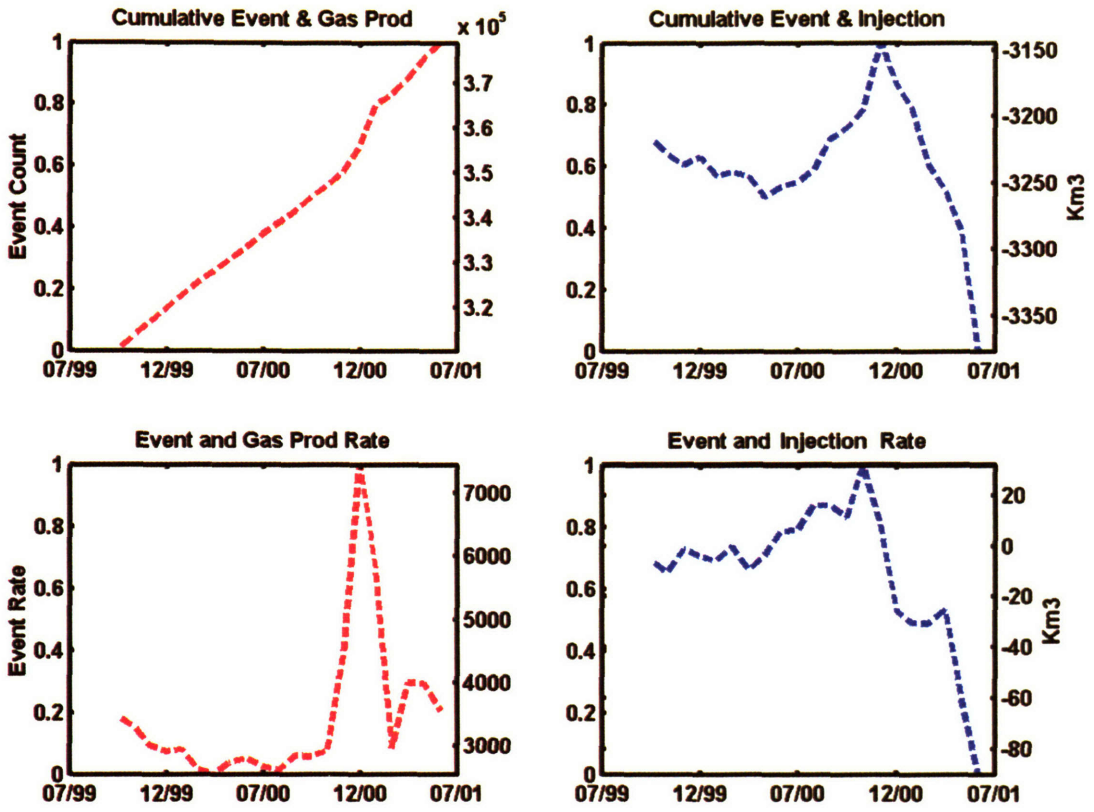

Figure 5.32. Upper left: Cumulative gas production volume (red dash line) and the cumulative event counts (black line) in the study area in figure 5.30b (Area 5.30b). Upper right: Cumulative net water injection (blue dash line) and the cumulative event counts (black line) in Area 5.30b. Lower left: Monthly gas production rate (red dash line) and monthly event count (black line) in Area 5.30b. Lower right: Monthly net water injection rate (blue dash line) and monthly event count (black line) in Area 5.30b.

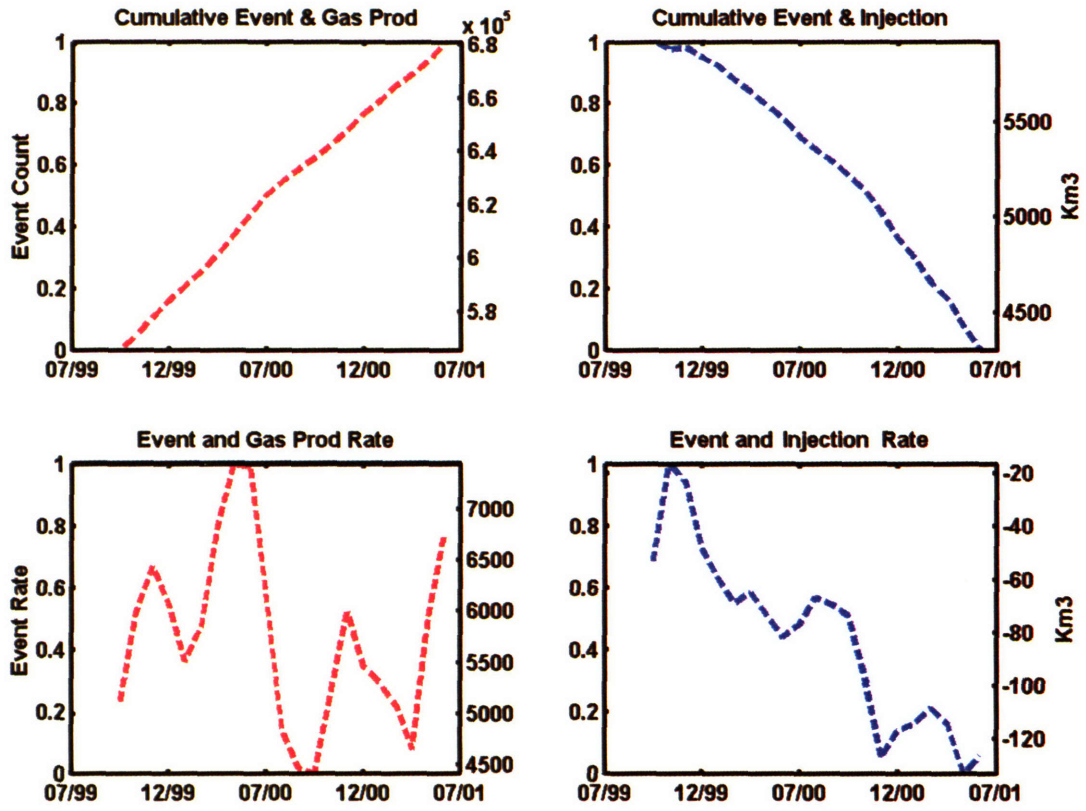

Figure 5.33. Upper left: Cumulative gas production volume (red dash line) and the cumulative event counts (black line) in the study area in figure 5.30c (Area 5.30c). Upper right: Cumulative net water injection (blue dash line) and the cumulative event counts (black line) in Area 5.30c. Lower left: Monthly gas production rate (red dash line) and monthly event count (black line) in Area 5.30c. Lower right: Monthly net water injection rate (blue dash line) and monthly event count (black line) in Area 5.30c.

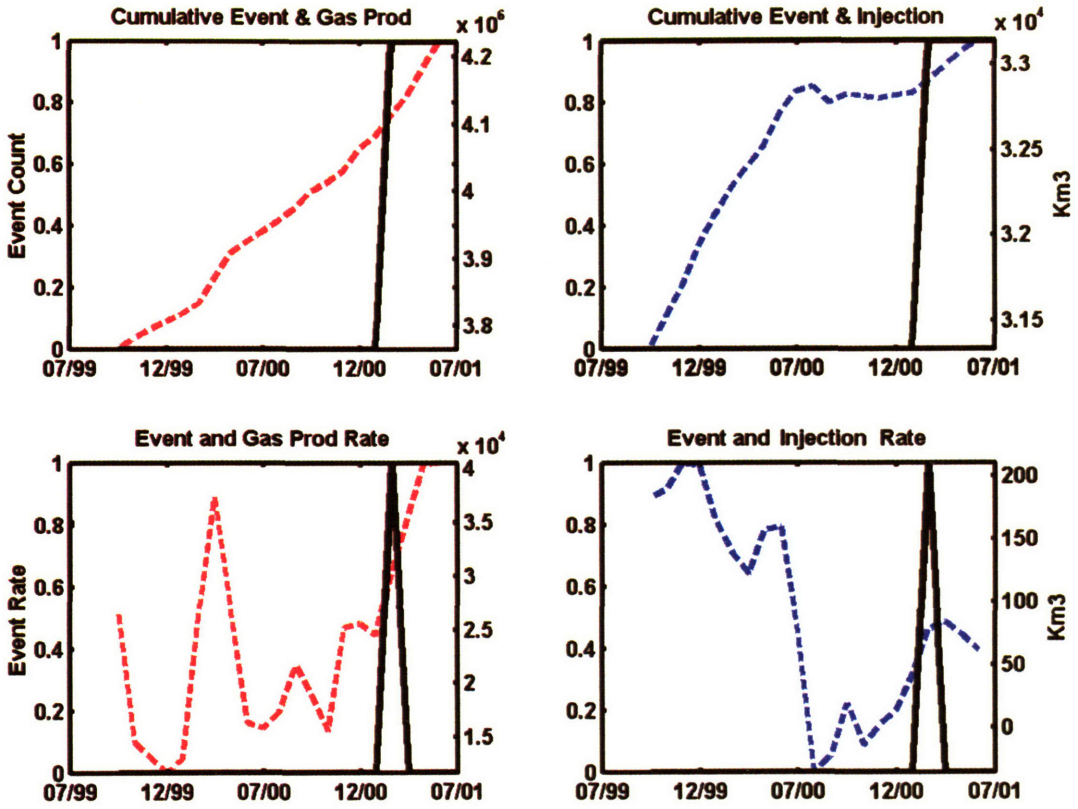

Figure 5.34. Upper left: Cumulative gas production volume (red dash line) and the cumulative event counts (black line) in the study area in figure 5.30d (Area 5.30d). Upper right: Cumulative net water injection (blue dash line) and the cumulative event counts (black line) in Area 5.30d. Lower left: Monthly gas production rate (red dash line) and monthly event count (black line) in Area 5.30d. Lower right: Monthly net water injection rate (blue dash line) and monthly event count (black line) in Area 5.30d.

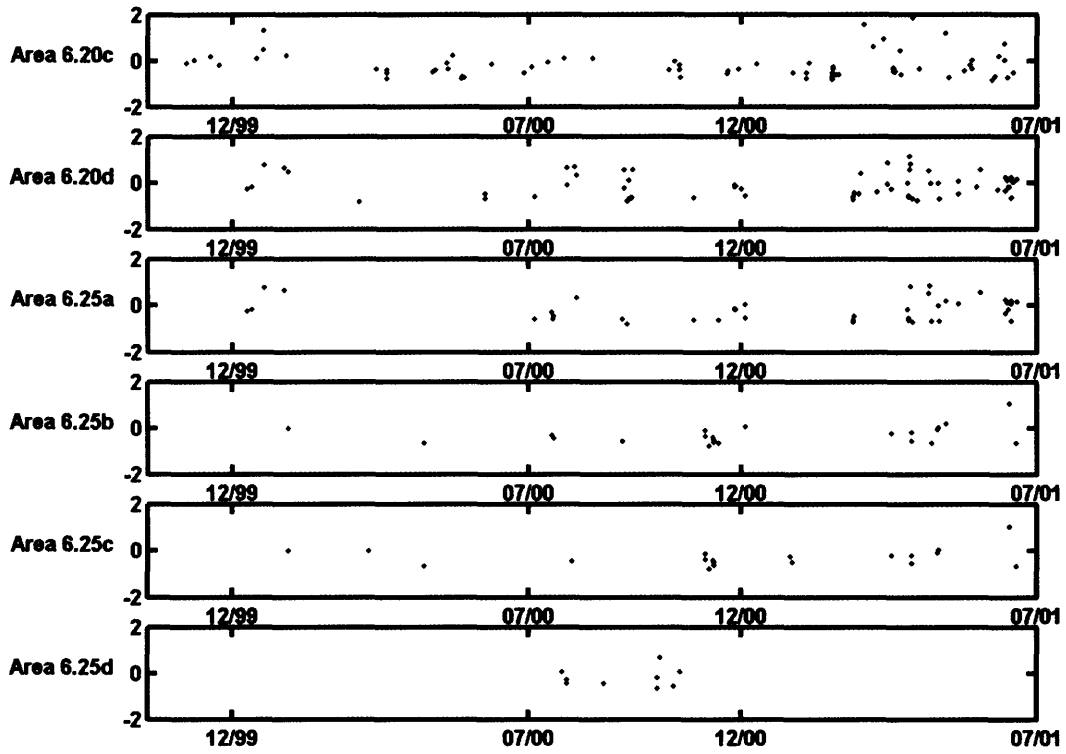

Figure 5.35. The magnitudes are plotted against time for the sub-regions where the event occurrences are sparse. Many events cluster both in time and magnitude. Events of similar magnitudes clustered in time show that there is no apparent mainshock and aftershock relationship.

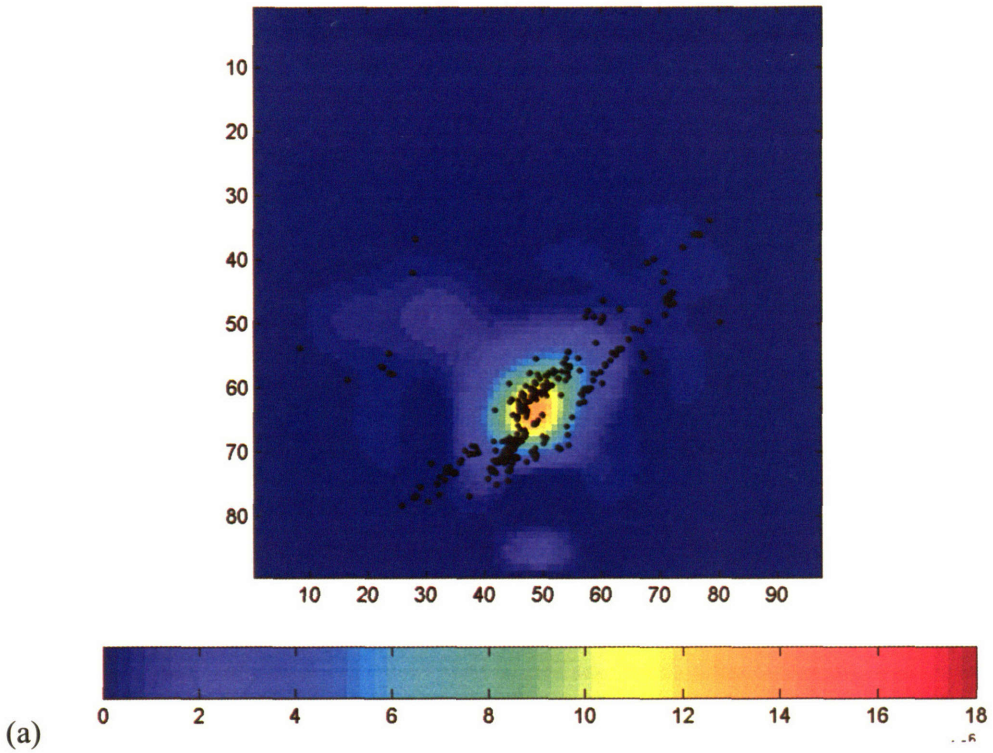

(a)

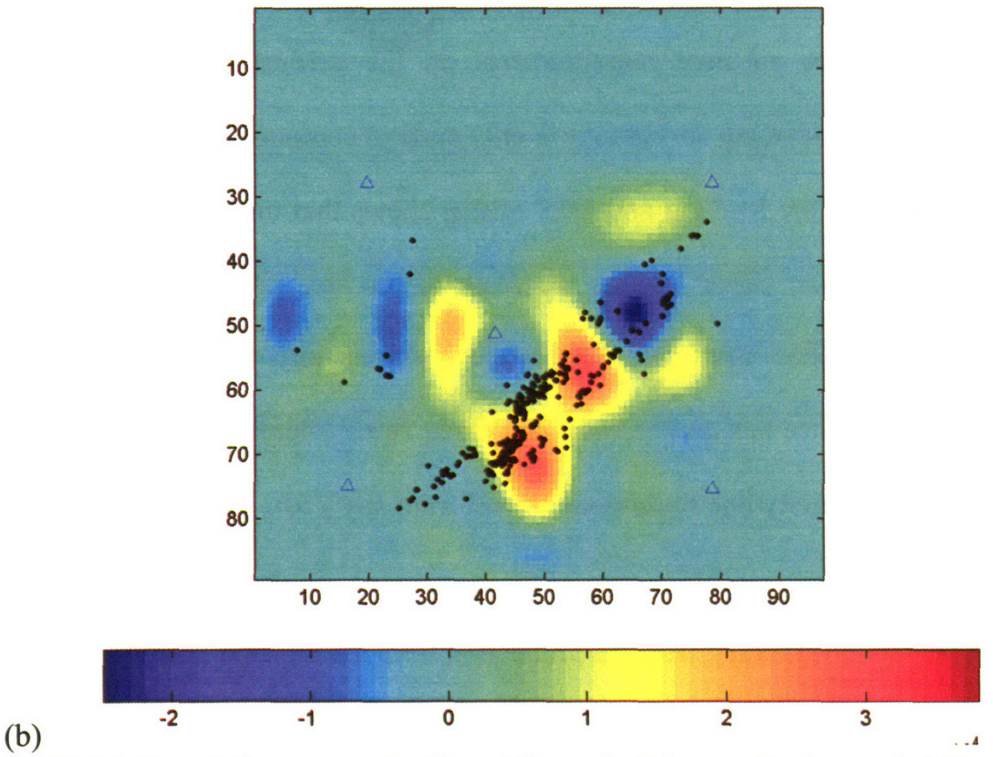

(b)

Figure 5.36. (a) Cumulative gas production at the end of the monitoring period (June, 2001). (b) Cumulative net fluid injection at the end of the monitoring period (June, 2001).

5.5 Comparisons with Surface Subsidence

In 1999, total surface subsidence detected over the center of Field since the start of oil and gas production was 50 cm (van Driel, 2000). Since then, surface subsidence in the Field has been monitored by annual precise leveling surveys. Maximum subsiding rates of up to 6 cm/year have been observed and the results are confirmed by analysis of Interferometric Synthetic Aperture Radar (InSAR) data (Bosman et al., 2001). GPS measurements of the deformation in the Field have been conducted since 2003 (Herring, personal communication). The leveling results (Herring, 2005, personal communication) in Figure 5.37 shows the subsidence of the Field between 1999 and 2001. The subsidence base on the analysis of the continuous and rover GPS data collected between July 2003 to July, 2004 provides accurate measurements on the vertical and horizontal surface velocities, whereas leveling surveys gives only vertical component. Microseismicity map superimposed onto the leveling and GPS results shows that the majority of the seismic activity occurs in the center and on the flank of the area with maximum subsidence (vertical motion). The GPS and leveling observations also show that the center of subsequent subsidence has moved westward since 2001. There is little subsidence to the southeast of a seismicity line running northwest from site YR02 to site YR25.

Compaction resulting from oil production from the Shuaiba Formation should be small because the reservoir pressure has been maintained by water injection. Therefore, the surface subsidence is likely due to compaction of the Naith gas reservoir and dislocations on faults. The fault-bounding graben acts as a barrier with less gas extracted from the reservoir to the southeast of this structure than to the northwest.

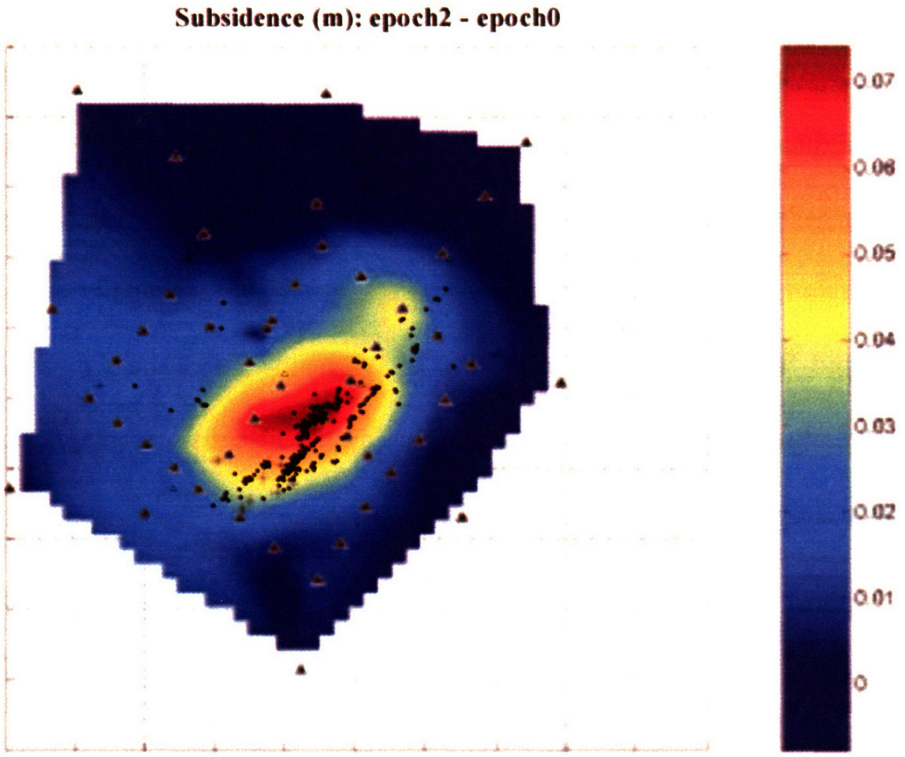

Figure 5.37. Figure adopted from Herring (personal communication). Vertical motions (interpolated) in the Field based on the analysis of leveling data collected between 1999 and 2001. The black dots denote the locations of the Oman microearthquakes.

5.6 Discussions and Conclusions

There have been a number of studies in which both fluid extraction and injection appear to have induced active faulting in hydrocarbon reservoirs. The classic study of injection-induced microearthquakes in the Rangely oil field in Colorado (Raleigh et al., 1972) concludes that induced faulting is associated with pore pressure increases due to water injection. Injected fluid propagates into cracks and causes increase of fluid pressure in pores and fractures, serving as a kind of lubricant in fractured zones. Pore pressure causes slip along pre-existing faults by reducing the effective normal stress on the fault plane according to the Coulomb criterion:

$$\sigma_s = C + \mu(\sigma_n - P), \tag{5.6.1}$$

where σ_s and σ_n are shear and normal stresses required for failure, respectively, C is cohesion, μ is coefficient of internal friction, and P is pore pressure. The effective normal stress ($\sigma_n - P$) controls the resistance to shear failure, and it can be reduced by raising the pore pressure while may induce failure. However, this mechanism may not be important in the case of Oman, where water injection is more or less balanced by oil production.

Secondly, hydrocarbon production can also cause poroelastic stress changes in the medium surrounding a compacting reservoir (Majer & McEvilly, 1979; Segall, 1989; Segall & Fitzgerald, 1998; Hillis, 2000; Zoback & Zinke, 2002). Faulting is triggered by poroelastic stresses associated with volumetric contraction of the reservoir and pore pressure/stress coupling. Declining pore pressure causes reservoir rocks to contract. Since

the reservoir is elastically coupled to the surrounding rocks, this contraction stresses the neighboring crust and results in subsidence. With the reservoir rocks shrinking more than the surroundings, this strain mismatch generates stress, and finally, earthquakes near the reservoir.

The theory of poroelasticity relates the elastic dilation of a porous rock to changes in pore pressure and stress (Biot, 1941; Engelder & Fischer, 1994). Poroelastic theory allows the total minimum horizontal stress, σ_h, to be expressed in terms of the total vertical stress, σ_v, if there is no lateral strain:

$$\sigma_h = k(\sigma_v - P) + P, \qquad (5.6.2)$$

where $k = \upsilon/1-\upsilon$, and υ is the Poisson's ratio. According to the equation above, given that $0 < k < 1$, σ_h increases with pore pressure but σ_v is unchanged since it is determined by the weight of the overburden. In normal fault regime ($\sigma_v > \sigma_H > \sigma_h$) where depletion occurs, effective vertical stress ($\sigma_v - P$) increases at the rate that pore pressure decreases. Since the total horizontal stress (σ_h) decreases with decreasing pore pressure (P), the differential stress ($\sigma_v - \sigma_h$) increases with decreasing pore pressure. Such a depletion-related increase in differential stress can lead to fault failure within the reservoir. This prediction was confirmed by hydraulic fracturing measurements (Teufel et al., 1991) in the Ekofisk field where the ratio of change in horizontal stress to reservoir pore pressure

is $\Delta\sigma_h/\Delta P \approx 0.8$. In another study, Engelder & Fishcher (1994) reported a $\Delta\sigma_h/\Delta P \approx 0.5$ for the McAllen Ranch field in Texas.

In a normal fault regime, the theory of poroelasticity also predicts normal faulting where there is a steep gradient in pore-pressure reduction (Segall & Fitzgerald, 1998), as in our case in the Field. This usually occurs at the depleting reservoir boundary or barrier fault in the Field, where the pore pressure outside the reservoir does not decrease due to production and pore pressure becomes discontinuous or its gradient becomes steep. Since the horizontal stress must be continuous at these boundaries, this suggests that normal faulting can be more pronounced and be induced in the surroundings perpendicular to the least horizontal stress.

The evidence for induced seismicity at the Field is the temporal and spatial distribution of microearthquakes in the vicinity of gas-producing wells. In order to perform spatio-temporal analysis of the exploitation schedule and its relationship with microseismicity, I discretize the field in 2 km × 2 km grids and all production/injection from wells within a particular grid are summed. I observed that during the 20-month monitoring period from October 29, 1999 to June 18, 2001, microearthquakes followed the gas extraction patterns in major producing areas. It is in Area 5.20a that we cannot exclude the presence of the first mechanism (reduction of effective normal stress) since the gas extraction and water injection patterns are very similar and they both correlate with microseismic activity. Since the faults in the Shuaiba reservoir are known to be highly permeable and water conductive, they can channel flow to the deeper formations

or the sites of deep microearthquakes. The fact that Shuaiba is in pressure communication (van Driel, 2000) with the underlying Khuff Formation at around 3km supports this view. Therefore, it is possible that the deep microseismicity in Area 5.20a was induced by the pore pressure increase associated with the Shuaiba water injection. In other areas, however, the patterns of microseismicity more or less follow the patterns of gas production of their corresponding areas. There is no clear evidence showing temporal correlation between injection and events. In fact, the voidage rates in many areas are positive (e.g., Areas 5.20d, 5.25a, 5.25b, 5.25c, 5.30b, 5.30c). Based on these observations, I hypothesize that the gas production induced stress changes in the Natih reservoir while cause the observed microseismicity. Microearthquakes induced by similar mechanisms due to pore-pressure decline has also been report in other petroleum (Teufel et al., 1991; Bou-Rabee, 1994, Zoback & Zinke, 2002) and geothermal (Oppenheimer, 1986) reservoirs.

In summary, integrating the results of passive microseismic monitoring and GPS analysis suggests that the NE-SW trending graben fault may be a fault-bounded flow boundary. The NW-SE crossing fault / fracture system does not seem to prohibit fluid flow across the faults due to the lack of microseismicity and smooth surface subsidence lateral profile. The NE-SW graben system breaks the Natih reservoir into east and west compartments, and controls the structure of pore-pressure decrease. The gas production is responsible for the observed surface subsidence. The associated poroelastic stresses reactivate the previous zones of weakness and induce normal faulting.

5.7 References

Aki, K., 1965, Maximum likelihood estimate of b in the formula $\log N = a - bM$ and its confidence limits: Bull. Earthq. Res. Inst., **43**, 237 – 239.

Biot, M. A., 1941, General theory of three dimensional consolidation: J. Appl.Phys., **12**, 155-164.

Bosman, G., Hanssen, R., and Tuttle, M., 2001, Advances in deformation measurements from spaceborne radar interferometry: Shell EPNL, **7025**, 34 – 36.

Bou-Rabee, F., 1994, Earthquake recurrence in Kuwait induced by oil and gas extraction: J. Petroleum Geology, **17**, 473 – 480.

Dieterich, J.H., 1994, A constitutive law for rate of earthquake production and its application to earthquake clustering: J. Geophys. Res., **99**, 2601 – 2618.

Engelder, T. and Fischer, M.P., 1994, Influence of poroelastic behavior on the magnitude of minimum horizontal stress in overpressured parts of sedimentary basins: Geology, **22**, 949 – 952.

Fabriol, H. and Beauce, A., 1997, Temporal and spatial distribution of local seismicity in the Chipilapa-Ahuachapan geothermal area, El Salvador: Geothermics, **26**, 681 – 699.

Finkbeiner, T., Zoback, M., Flemings, P., and Stump, B., 2001, Stress, pore pressure, and dynamically constrained hydrocarbon columns in the South Eugene Island 330 Field, northern Gulf of Mexico: AAPG Bulletin, **85**, 1007 – 1031.

Gutenberg R. and Richter C.F.,1944, Frequency of earthquakes in California: Bull. Seism. Soc. Am., **34**, 185 – 188.

Healy, J.H., Rubey, W.W., Griggs, D.T., and Raleigh, C.B., 1968, The Denver earthquakes: Science, **161**, 1301 – 1310.

Hillis, R., 2000, Pore pressure/stress coupling and its implications for seismicity: Exploration Geophys., **31**, 448 – 454.

House, L.S. and Flores, R., 2002, Seismological studies of a fluid injection in sedimentary rocks, East Texas: Pure Appl. Geophys., **159**, 371 – 401.

Hutton, K. and Boore, D., 1987, The M_L scale in southern California: Bull. Seism. Soc. Am., **77**, 2074 – 2094.

Imoto, M., 1991, Changes in the magnitude-frequency *b*-value prior ot large ($M \geq 6.0$) earthquakes in Japan: Tectonophysics, **269**, 279 – 297.

Langston, C.R., Brazier, A., Nyblade, A., and Owens, T., 1998, Local magnitude scale and seismicity rate for Tanzania, East Africa: Bull. Seism. Soc. Am., **88**, 712 – 721.

Lomax, A., Virieux, J., Volant, P., and Berge, C., 2000, Probabilistic earthquake location in 3D and layered models: introduction of a Metropolis-Gibbs method and comparison with linear locations: in Advances in Seismic Event Location, Thurber, C.H., and Rabinowitz (eds.), Kluwer, Amsterdam, 101-134.

Majer, E.L. and McEvilly, T.V., 1979, Seismological investigations at the Geysers geothermal field: Geophysics, **44**, 246 – 269.

Mijnssen, F.C.J., Rayes, D.G., Ferguson, I., Al Abri, S.M., Mueller, G.F., Razali, P.H.M.A, Nieuwenhuijs, R., Henderson, G.H., 2003, Maximizing Yibal's remaining value, **6**, 255 – 263.

Mogi K., 1962, Fracture of rocks: Bull. Volcanological Soc. Japan, **7**, 89 – 101.

Murru, M., Montuori, C., Wyss, M., and Privitera, E., 1999, The locations of magma chambers at Mt. Etna, Italy, mapped by b-values: Geophys. Res. Lett., **26**, 2553 – 2556.

Ogata, Y. and Yamashina, K., 1986, Unbiased estimate for *b*-value of magnitude frequency: J. Phys. Earth, **34**, 187 – 194.

Okada, Y., 1985, Surface deformation due to shear and tensile faults in a half-space: Bull. Seism. Soc. Am., **75**, 1135 – 1154.

Oppenheimer, D.H., 1986, Extensional tectonics at the Geysers geothermal area, California: J. Geophy. Res., **91**, 11463 – 11476.

Pine, R.J. and Batchelor, A.S., 1984, Downward migration of shearing in jointed rock during hydraulic injections: International Journal of Rock Mechanics and Mining Sciences & Geomechanics Abstracts, 21, 249 – 263.

Richter, C., 1935, An instrumental magnitude scale: Bull. Seism. Soc. Am., **25**, 1 – 32.

Rutledge, J.T., Stark, M.A., Fairbanks, T.D., and Anderson, T.D., 2002, Near-surface microearthquakes at the Geysers geothermal field, California: Pure Appl. Geophys., **159**, 473 – 487.

Sanchez, J.J., McNutt, S.R., Power, J.A., and Wyss, M., 2004, Spatial variations in the frequency-magnitude distribution: Bull. Seism. Soc. Am., **94**, 430 – 438.

Scholz C.H., 1968, The frequency-magnitude relation of microfracturing in rock and its relation to earthquakes: Bull. Seism. Soc. Am., **58**, 399 – 415.

Segall, P., 1989, Earthquakes triggered by fluid extraction: Geology, **17**, 942 – 946.

Segall, P. and Fitzgerald, S., 1998, A note on induced stress changes in hydrocarbon and geothermal reservoirs: Tectonophysics, **289**, 117 – 128.

Teufel, L.W., Rhett, D.W. and Farrell, H.E., 1991, Effect of reservoir depletion and pore pressure drawdown on in situ stress and deformation in the Ekofisk field, North Sea: Rock Mechanics as a Multidisciplinary Science, Roegier, Sj.C., Ed., Rotterdam, Balkema, 63 – 72.

Urbancic, T.I., Trifu, C.I., Long, J.M., and Young, R.P., 1992, Space-time correlations of b values with stress release: PAGEOPH, **139**, 449 – 462.

van Driel, W.D., Hart, C., Lehr, B. and Coremans, J., 2000 Reservoir compaction, surface subidence and fault slip in the Yibal field, Oman: Netherlands Organisation for Applied Scientific Research.

Warren, N.W. and Latham, G.V., 1970, An experimental study of thermally induced microfracturing and its relation to volcanic seismicity: J. Geophys. Res., **75**, 4455 – 4464.

Wiemer, S. and Benoit, J.P., 1996, Mapping the b-value anomaly at 100 km depth in the Alaska and New Zealand subduction zones: Geophys. Res. Lett., **23**, 1557-1560.

Wiemer, S. and McNutt, S.R., 1997, Variations in the frequency-magnitude distribution with depth in two volcanic areas: Mount St. Helens, Washington, and Mt. Spurr, Alaska: Geophys. Res. Lett., **24**, 189 – 192.

Wyss M., 1973, Towards a physical understanding of the earthquake frequency distribution. Geophys. J. R astr. Soc., **31**, 341 – 359.

Zoback, M.D. and Zinke, J.C., 2002, Production-induced normal faulting in the Valhall and Ekofisk oil fields: Pure Appl. Geophys., **159**, 403 – 420.

Zuniga, R. and Wyss, M., 1995, Inadvertent changes in magnitude reported in earthquake catalogs: influence on *b*-value estimates: Bull. Seism. Soc. Am., **85**, 1858 – 1866.

Appendix A

The Geology and Hydrocarbon Production in North-Central Oman

The material in this appendix is taken from various reports and papers as referenced. The purpose of the appendix is to provide a concise background geological information to the reader without the burden of searching for some hard-to-find references.

A.1 The Geology of North-Central Oman

The Sultanate of Oman is located on the southeastern side of the Arabian plate and is close to the boundaries of the Indian plate to the east, Eurasian plate to the north, and African plate to the south (Figure A.1). Consequently, plate movements have resulted in complex structural, sedimentation, and burial histories. Oman is tectonically bounded on the south by the Gulf of Aden spreading zone, to the east by the Masirah Transform Fault and the Owen Fracture Zone Trough, and to the north by the complex Zagros-Makran convergent plate margin, compression along which produced the Oman Mountains (Loosveld et al., 1996). The sedimentary section (Figure A.2) in the hydrocarbon producing provinces of Oman is made up of rocks ranging from Proterozoic to Recent (Hughes-Clarke, 1988).

The general stratigraphy of Oman is illustrated in Figure A.2. Earliest sediments of Oman are a Precambrian clastic-carbonate-evaporite sequence of the Huqf Supergroup (Droste, 1997), which form the basis of the primary petroleum systems for hydrocarbons produced throughout Oman. It is the oldest known sedimentary sequence overlying the

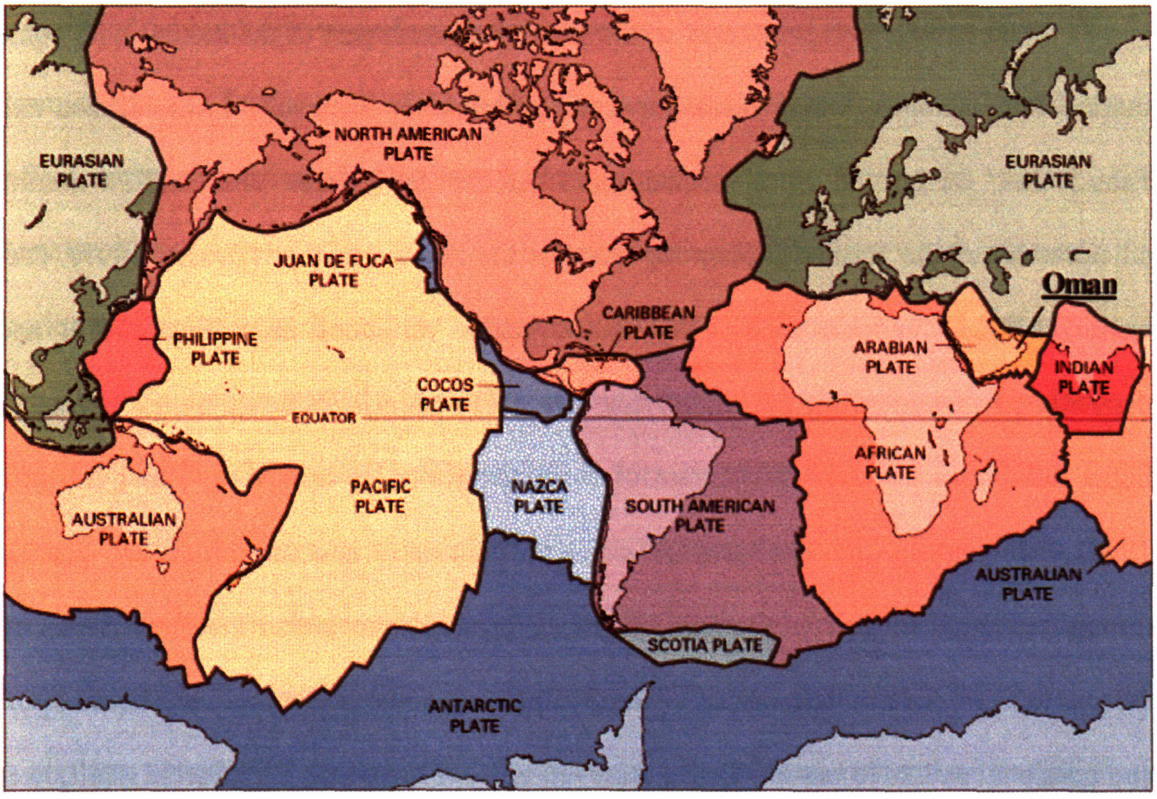

Figure A.1. Oman is located on the southeastern Arabian plate. (adapted from U.S.G.S.)

crystalline basement in Oman, and lies within the age span of late Precambrian to Early-Middle Cambrian. The Huqf Group is divided into five formations corresponding to an alternating sequence of clastics (Abu Mahara and Shuram Formations) and carbonates (Khufai and Buah Formations), terminated by the salt deposit (Ara Formation) with thickness up to 1000 m. The thick evaporites and organic-rich sediments were deposited in geographically-restricted basins during periods of low relative sea level where stratified, anoxic conditions periodically prevailed (Mattes and Conway-Morris, 1990; Edgell, 1991).

Clastic rocks comprise most of the lower Paleozoic part of the section with some marine intercalations, which form important hydrocarbon reservoirs in the Ghaba and Fahud Salt Basins. A thick sequence of rift-fill terrigenous and shallow-marine siliciclastics of the Haima Supergroup overlies the Ara Formation (Droste, 1997). Pre-existing, highly variable topography caused major variations in sediment infill and depositional movement of the underlying salt. Differential subsidence across basement highs influenced thickness and extent of these clastics (Aley and Nash, 1985; Heward, 1990). Moving up the stratigraphic column, numerous unconformities are present throughout the Paleozoic in Oman. Ordovician glaciation separated transgressive open-marine to regressive deltaic cycles of the Safiq Group. Two major and very broad uplift and erosional events in eastern Oman removed most of the overlying Silurian and Lower Devonian sediments and the interval between mid-Devonian and Upper Carboniferous (Pollastro, 1999). These erosional events are recognized in deep wells from the main producing fields in the Ghaba and Fahud Salt Basins.

In the Late Carboniferous, Oman was at the northern edge of Gondwana and on the southern side of Tethys (Scotese et al., 1979). This indicates a paleolatitude of about 50°S. After the end of the glaciation in the Late Carboniferous, Oman was covered by the deposition of the Haushi Group (Levell et al., 1988; Hughes-Clark, 1988), which comprises the glacial clastics of the Al Khlata Formation and the shallow marine and fluvial clastics of the Gharif Formation. They are important hydrocarbon reservoirs throughout Oman.

The Gondwana breakup was achieved during the Permian, thus inducing the creation of the northeastern and southeastern passive margins of the Arabian plate. The Permian through Tertiary part of the section are predominantly carbonate rocks and reflect climatic variations due to Oman's changing paleolatitude. During the Middle Permian, Oman developed into a regional shallow carbonate platform which allowed marine transgression to deposit the widespread lower Khuff Formation (Sharief, 1982). The Khuff Formation formed a regional seal above the fluvial, clastic reservoirs of the Gharif Formation. Subsequent transgressions in Jurassic to Cretaceous resulted in a sequence of blanket deposits of mainly cyclic shelf carbonates over northern Oman, including the Jurassic Sahtan and the Cretaceous Kahmah and Wasia Groups (Pollastro, 1999). Regional changes in sedimentation during the Jurassic and most of the Cretaceous in northern Oman were controlled mostly by eustatic fluctuations rather than tectonics (Harris & Frost, 1984).

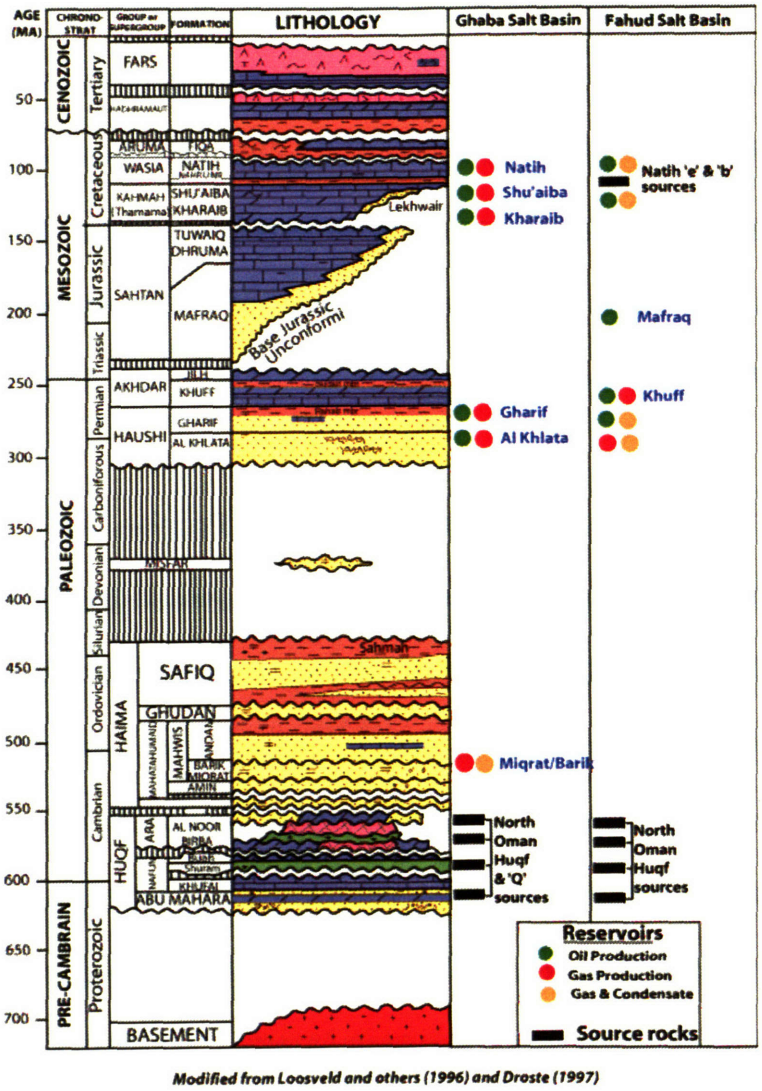

Figure A.2. Stratigraphic section of Oman showing source rocks and producing reservoirs for Ghaba and Fahud Salt Basins. Modified from Loosveld and others (1996) and Droste (1997).

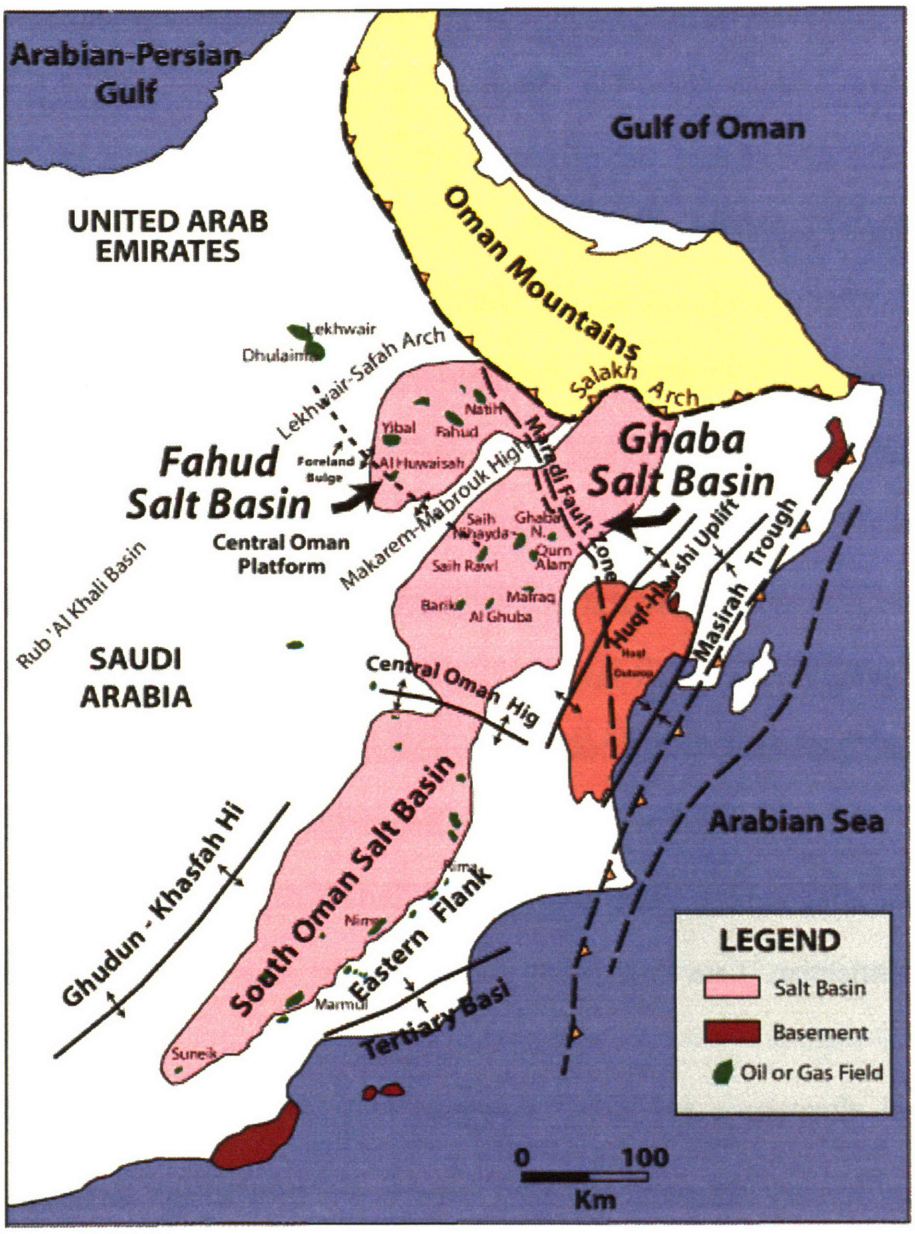

Figure A.3. Map showing salt basins, structural elements, and major oil and gas fields of Oman. Yibal field is located in the Fahud salt basin (adapted from Pollastro, 1999).

A major change in tectonic style and depositional setting took place in Late Cretaceous (Cenomanian-Turonian boundary) because of collision and partial subduction of the eastern Arabian plate. The Oman Mountains are the product of two distinct orogenies. The first of these occurred during the Late Cretaceous (Senonian) when the formerly passive, northeastern margin of the Tethys Ocean became compressive. These compressional tectonic events formed the Omani foredeep, including the Fahud Salt Basin, by thrusting, fore-buldge and downwarping. Crustal extension from downwarping initiated and / or reactivated normal faulting along a northwest-southeast trend from the northern flank for the Ghaba basin into eastern Abu Dhabi, such as those associated with Natih and Fahud fields (Figure A.3). Late Cretaceous is also a period of pronounced salt movement in the Ghaba, Fahud Salt Basins, and a large number of producing oil fields in South Oman, coincident with a worldwide eustatic sea-level rise (Vail et al., 1991). Combined, these events resulted in a change from a shallow, stable platform to a deep-water marine environment. Then, shallow-water carbonate deposition was re-established during Maastrichtian (Late Cretaceous) and formed the Aruma Group (Hughes-Clarke, 1988).

Early Tertiary sediments, including carbonates of the Hadhramaut Group and arid continental clastics and marine rocks of Fars Group, overlie the Aruma Group. The second orogeny that formed the Oman Mountains, began in the Miocene and continued to the present day, was related to the Zagros collision in Iran (Searle, 1988).

A.2 Hydrocarbon Production in North-Central Oman

A.2.1 The Fahud Salt Basin

Most of Oman's 5.5 billion barrels in proven oil reserves are located in the country's northern and central regions. In the North, the Yibal, Natih, Fahud, Al-Huwaisah and Lekhwair fields combined account for almost half of total Omani oil production. Crude oil found in this region is mainly medium or light, and is mostly found along with natural gas. Heavier oil is found in southern Oman, particularly in the Nimr and Amal fields, and normally not associated with natural gas. Hydrocarbon is produced chiefly from carbonate reservoirs of Cretaceous age in the northern Oman because of their proximity to excellent overlying seals. Major oil fields in the area were discovered in the 1960s and early 1970s and had been put on stream shortly after their discoveries. Oil-bearing reservoirs occur in two carbonate formations in north Oman, the Natih and the Shuaiba.

Through extensive exploration programs, Oman has consistently increased its natural gas reserves in recent years. As of January 1, 2002, Oman's estimated proven natural gas reserves were approximately 29.3 trillion cubic feet (TCF), up from only 12.3 TCF in 1992, largely of associated gas. Most of the associated gas comes from the Yibal field. Smaller volumes come from the Natih and Sayh Nuhayah fields in northern Oman

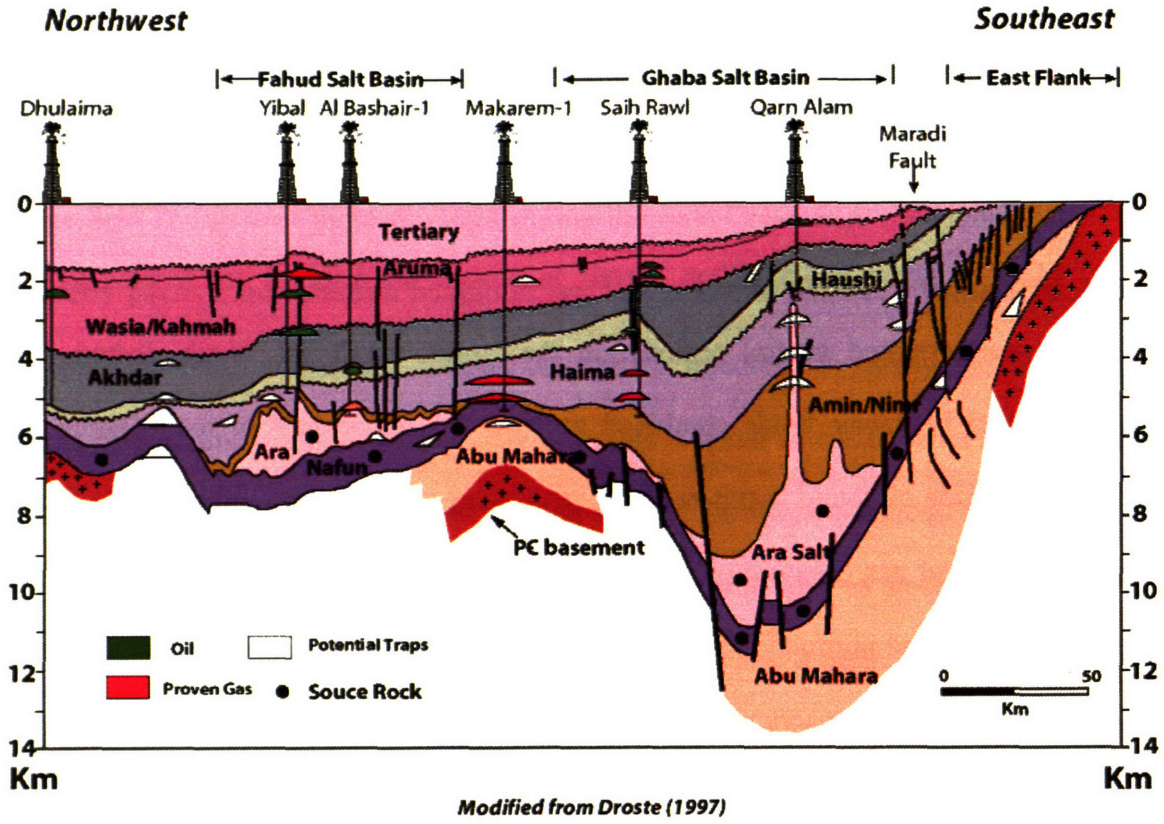

Figure A.4. Generalized northwest-southeast cross-section across northern Oman and the Ghaba Salt Basin, Central Oman Platform (Makarem High), and Fahud Salt Basin showing major oil and gas fields, proven occurrences, and potential traps (adapted from Pollastro, 1999)

and the Birba field in the south. More than 10 TCF of Oman's non-associated natural gas is located in deep geological structures, many of which are beneath active oil fields.

The Fahud Salt Basin is part of a series of subsiding rift basins stretching from India and Pakistan across the Arabian Shield to central Iran that formed during the Infracambrian and lower Cambrian (about 600 to 540 Ma) (Gorin et al., 1982; Husseini &

Husseini, 1990; Mattes & Conway-Morris, 1990). These rift basins were formed by extension from left-lateral, strike-slip (rifting and wrenching) movement of the Najd transform fault system, which ultimately dislocated the Arabian plate some 300km to the east (Schmidt et al., 1979). Generalized cross-section across the Ghaba and Fahud Salt Basins is shown in Figure A.4.

Over 90 percent of the fields in the Fahud Salt Basin, half of which are gas fields, produce from the high porosity, commonly fractured, grainstones and chalky carbonates of the Lower Cretaceous Shuaiba Formation and Middle Cretaceous Natih Formation. About 50 percent of the basin's production comes from the porous, fractured Shuaiba limestones in Yibal field. Although some fields producing from Natih reservoirs are sourced by the organic-rich facies of the Natih Formation, a large volume of oil and gas in Natih reservoirs is sourced from the Huqf. Natih oil initially migrated towards the foreland bulge and Ghaba Salt Basin but was interrupted by the formation of the Fahud fault during early development of the foreland basin. This fault created a shadow zone preventing migration of Natih oil to reach the foreland bulge and into Yibal and Al Huwaisah fields (Terken & Frewin, 1999). Deep gas is also produced from Middle Cambrian to Lower Ordovician clastics of the Haima Supergroup. Most of the fields of the Fahud Salt Basin are structurally complex, salt-induced anticlines and domes that have been broken up into several fault blocks by crestal collapse features (Nederlof et al., 1985). Primary regional seals are shales of the Cretaceous Nahr Umr and Fiqa Formations, and Ordovician Mabrouk shale and Permian Khuff carbonates. Common trap styles are faulted closures, dip closures, and faulted-dip closures (Lake, 1996).

The Shuaiba is overlain by the Nahr Umr Formation of the Wasia Group (age equivalents of the Mauddud and Mishrif Formations in the United Arab Emirates), a widespread transgressive shale, which forms a regional seal for these reservoirs. The integrity of this seal is excellent as hydrocarbons produced from the Shuaiba are commonly different from those produced in Middle Cretaceous Natih reservoirs overlying the Nahr Umr shales (Brennan, 1985). The Natih Formation in the Fahud Salt Basin is contained mostly within the basin. It is a small (about 20,000 km^2) but highly efficient petroleum system with an estimated in place resource volume of 9 billion barrels of oil equivalent (BBOE). The 400 m-thick carbonate sequence of the Natih Formation is comprised of several lithologic subdivisions designated A through G. The Natih "B" and "E" units have sourced the hydrocarbons of the reservoir. A thick shale sequence of the overlying Fiqa Formation forms a major regional seal for the Natih Formation. In both the Shuaiba and Natih Formations, shallow-water, shelf-margin carbonate build-ups (mainly rudistid reefs) and associated grainstones (debris shoals) formed on and around low relief structural highs (mostly formed by salt pillows and tilted, upthrown fault blocks) comprise the best reservoirs (Harris & Frost, 1984). Uplift from both tectonic and halokinetic movements produced secondary (mostly moldic and vuggy) porosity from subaerial erosion and meteoric diagenesis. Porosities ranging from 30 to 40 percent have been recorded in the Shuaiba at Yibal, Al Hawaisah, Natih, Fahud, and Daleel fields.

A.2.2 The Natih Field

Natih Field is an oil-producing field in the Fahud Salt Basin. It was discovered in 1963 and was estimated to contain approximately stock-tank oil initially in place (STOIIP) of 500×10^6 m^3 at 32° API. (van Dijkum & Walker, 1991). The Natih field is a dome-shaped fracture reservoir, measuring 10 km × 6 km and bounded by a reverse fault with a throw of about 1,000 m (Eikmans & Hitchings, 1999). Natih Formation forms the main reservoir in the field, a carbonate oil reservoir with a thickness of 380 m with no, or possibly a small, primary gas cap. It is again sealed by a shale cap rock, the Fiqa Formation. Minor oil production also comes from the underlying Shuaiba reservoir capped by the Nahr Umr shale Formation.

Natih Field was brought on stream in 1967, and like Fahud Field, production was initially depletion driven. As a result, reservoir pressure fell, and then water injection was installed and was later supplemented by gas injection. The permeability of the matrix is generally in the range of 1 to 10 mD, and typical porosities are 20% - 30% (Eikmans & Hitchings, 1999). After the Natih Formation was deposited, extension created NW-trending faults across the field. This was followed by compressional regimes in the Late Cretaceous which reactivated the extensional faults as reverse faults. The uplift of the Oman mountains during the Pliocene produced minor strike-slip movement along the northern segment of the Maradi fault zone, the creation of the dominating NE-trending fault and fracture set by NE-SW compression. Three types of extensional fractures, NE-trending fractures, folding related fractures, and fault-related fractures, have been identified by formation microimager (FMI) and azimuthal resitivity image (ARI). Production from the reservoir matrix is almost entirely dependent on these fracture

networks (Hitchings & Potters, 2000). The pervasive nature of the fracture network is one of the key elements determining the development strategy of the Natih field. The effective permeability of the fracture network is in the range of 1 – 10 Darcy, almost three orders of magnitude higher than the matrix permeability. Overall relative fracture volume is estimated to be 0.1 – 0.2% of rock volume. The fracture spacing is in the order of 1–10m for most of the field, but it can be as small as 0.1m in highly faulted regions (Hitchings & Potters, 2000).

A.2.3 The Fahud Field

The Fahud field was discovered in 1964 and production started 1967. It has original oil in place of 1000×10^6 stock-tank m^3 and has a density of 31° API. The Fahud field is a 16km × 2 km, northeast-dipping monocline at 15° uniformly (Nicholls et al., 1999). It is bounded in the southwest by a fault plane with a major normal fault with a throw in excess of 1000m. The northeast flank of the field is dip-closed with an oil-water contact. The chalky carbonate of the Natih Formation is subdivided into seven major reservoir units, Natih-A to Natih- G, which has a total thickness of about 440 m and overlain by the sealing Fiqa shales (O'Neil, 1988). The field is divided by a permeability barrier into two accumulations, Fahud North-West and South-East (Harris & Frost, 1984; O'Neill, 1988). Fractures identification logs, tracer tests, and outcrop studies indicate a the fracture system has a northeast-southwest directional trend, with fracture spacings of about 10 m and fracture widths of up to 2 mm.

The Fahud field was initially produced under natural depletion from 1967 to 1971, supplemented by gas injection in 1968. This led to rapid displacement of the gas/oil contact and gassing out of a number of relatively downdip completions. Subsequently, water injection was implemented in 1972 but the scheme failed to maintain the reservoir pressure and to reverse the trend of declining oil production (Al-Khodhori, 2001). During the period of 1981 to 1983, a number of thermal decay time logs and tracer tests were conducted to review the poor performance of the waterflooding (O'Neill, 1988). It was concluded that the recovery factors from waterflooding were low because the reservoir rocks were fractured and oil-wet. Recovery factors could be substantially improved, however, by reverting to full-scale gas/oil gravity drainage. The Fahud field has been produced by gas- oil gravity drainage (GOGD) process since 1984. Under this process, oil-filled rock is surrounded by gas bearing fractures. The density difference between the oil and the gas allows the oil to slowly drain by gravity from the low permeability matrix into the fracture system.

A total number of 80 horizontal wells was drilled in the Fahud field from 1984 to 2001 (Al-Khodhori, 2001). These wells are distributed across the field and completed over various reservoirs in the field. Horizontal wells are contributing more than 80% of the total field production. The field once thought to be completely covered with fractured reservoir. However, horizontal drilling in the field has gradually revealed the characteristics of a highly heterogeneous fracture system. From the analysis of well performance, mud losses and borehole image data supported by structural geological data, several areas and units within the Natih reservoir are now recognized as sparsely

fractured and hence are inefficiently drained under the GOGD recovery mechanism. Therefore, two different recovery mechanisms, GOGD and waterflood, are now being used concurrently to optimize recovery.

A.2.4 The Al Huwaisah Field

The Al Huwaisah field is located at about 350 km WSW of Muscat. It was discovered in 1969 and has been on-steam since 1971. The current STOIIP is 249×10^6 m^3 with the oil density is 38° API and 1.2 cP viscosity. It is a low relief, 22 km × 10 km, probably salt-induced dome structure (Al-Mugheiry et al., 2003). It produces from rudistid Upper Shuaiba Formation which is located at a depth of about 1450 m and unconformably sealed by shales of Nahr Umr Formation. The Shuaiba in Al Huwaisah is laterally and vertically heterogeneous. It can be subdivided into the Shuaiba A and the Shuaiba B. Shuaiba A consists of different rudistid reservoir rock types, which overlies a sequence of chalky, low permeability non-reservoir Shuaiba B (Baumann, 1983). The average permeability is 20 mD and the average porosity is about 20%. It is the most complex field within the Shuaiba of Oman in terms of facies distribution, stratal geometry and flow unit architecture.

Production peaked at 44,000 bb/d in 1973 and declined to 19,000 bb/d. Recently, increased understanding of the fracture distribution has led production rates to increase to 28,000 bb/d. Field-wide recovery factor is only 18% (Mijnssen et al., 2003). It has strong acquifer drive along the NW flanks, and poor pressure support in the SW and SE

direction. The initial reservoir pressure was 17,000 KPa with a bubble-point pressure of 6,000 KPa. The current average reservoir pressure is about 14,500 KPa in the high-pressure zones and 10,000 KPa in the low-pressure zones. The field is divided into four areas based on seismic interpretation.

A.2.5 The Lekhwair Field

The Lekhwair field lies approximately 140 km northwest of Fahud field. The field was discovered in 1968 and brought on stream in 1976. Light (38 degrees API), low viscosity (0.8 cP) oil is produced from two low-permeability (1 to 10 mD) chalky carbonate reservoirs, the Lower Shuaiba and the Kharaib (Willetts & Hogarth, 1987). The two reservoirs are separated by a 6- to 8-m layer of tight argillaceous limestone that appears to act as an effective seal. Although evidence of fractures is not very common in core material, production and injection rates seem to be controlled more by local small-scale faults.

Structurally, the field consists of two almost circular, anticlines both with a diameter of about 10 km. The main or "A" dome contains about 120×10^6 stock-tank m^3, which is 80% of the STOIIP. To the northwest the structurally lower "B" dome which contains STOIIP of 50×10^6 m^3, has poorer reservoir characteristics and contains significant oil volumes only in the Lower Shuaiba (Willetts & Hogarth, 1987). The anticlinal structures are low relief with only 84 m between the crest and the oil/water contact in the main structure and 43 m in the subsidiary structure.

The initial reservoir pressure in the A area of 13,700 KPa was some 500 KPa above the bubble point pressure. Production during the period 1976-1979 at rates building up to 4,500 m^3/d (28,300 bbl/d) resulted in the reservoir pressure declining by some 1100 KPa below bubble point with an accompanying sharp rise in producing gas-oil ratio. Consequently, production from the Lower Shuaiba was shut in order to conserve reservoir pressure while the Kharaib reservoir was allowed to produce at 500 m^3/d (3,150 bbl/day) net, and the voidage (volume of fluid extracted minus that injected) being balanced by a modest aquifer influx.

In 1992, a $300-million water injection project was completed at Lekhwair oil field. Production at the field subsequently increased from 26,000 bbl/d in 1992 to the current rate of 100,000 bbl/d. In addition to new production and injection facilities, the Lekhwair project involved drilling over 115 wells, including 21 horizontal ones, and the construction of four gas pipelines. The lines connect Lekhwair to the Yibal gas plant and will be needed as production of associated gas increases.

A.2.6 The Yibal Field

The Yibal field is located in the North Oman group of fields on the plain between the Oman Mountains and the Rub Al Khali, about 300 km southwest of the city of Muscat. It lies midway between the Persian Gulf coast of Sharjah and Abu Dhabi to the north and the Arabian Sea coast of Oman to the south. The Yibal field was discovered in

November, 1962 and was put on production in July, 1969 as productive reservoirs such as the Fahud and Natih fields were discovered in the Fahud Salt Basin. Yibal is the largest oil producing field of the Fahud Salt Basin, and in Oman in general, contributing about 15% of the country's production. The main oil producing Shuaiba reservoir has a STOIIP of 604×10^6 m^3. Moreover, Yibal accounts for about 25 percent of Oman's developed reserves. The maximum oil column is 112.8 m and the productive area is about 7×10 km (Mijnssen et al., 2003). Oil is relatively light (40° API). Yibal also produces gas from the shallower but smaller Middle Cretaceous Natih "A" reservoir. The discovery of non-associated gas in Oman dates back to 1962 when a well drilled on the Yibal crestal structure indicated non-associated gas in the Natih formation at an average depth of 750m.

Structurally, the Yibal field is a large anticline created by deep-seated salt movement (Blaskovich et al., 1985). The dome is about 15×20 km in size with a northeast-southwest axial elongation that is probably a result of regional deformation. Vertical closure is about 305 m. Dips along the flanks are 4 to 5 degrees. The structure is dominated by a major central graben and two major systems of extensive tensional faulting with two preferred directions (southeast-northwest and northeast-southwest) that affects the trapping mechanism in the oil reservoir. All faults are high-angle normal faults. Most of the faults in Shuaiba Formation and younger beds were developed as tensional release features as the dome developed. Defined by the two major fault systems, the Yibal field is divided into three areas: the north, east, and west blocks (Figure A.5). The northern block is bounded on the south by the southwest trending crossfault with

down-to-the-south displacement ranges from 30.5 to 84 m and decreases towards the west. This fault appears to provide an effective seal for the Shuaiba hydrocarbons trapped in the northern upthrown block. The northeast-trending graben divides the rest of Yibal field into two reservoir areas, referred to as the east and west reservoir blocks. Displacement along the bounding faults of the graben varies from 6 to 40 m. (Litsey et al., 1986). This major network of faults and fractures partially connects all parts of the fields together. Porosities range from 30 to 35 percent. The matrix permeability is low (1 – 100 mD) with low viscosity (0.6 cp). Permeabilities in fault and fracture zones are believed to be orders of magnitude higher than the average matrix permeability. The main oil production is from the Lower Cretaceous Shuaiba chalk overlain disconformably by Nahr Umr shale, while gas is produced from the shallower Natih Formation overlain by the Fiqa shale Formation. Structural faults in the Shuaiba reservoir are known to be very permeable and water conductive. The Shuaiba reservoir is in pressure communication with the underlying Khuff formation.

The Yibal Shuaiba reservoir is located at a depth of 1300 m. The oil column has a maximum thickness of 100 m with no primary gascap present. The Shuaiba chalk is a soft, fine-textured limestone of marine origin, consisting almost wholly of calcite formed by the moderately shallow-water accumulation of skeletal debris. At the time of deposition of the Shuaiba, it is believed that a wide carbonate shelf existed, building out into the Tethys Ocean to the east during a humid climatic period. The Aptian was a period of renewed basin-wide inundation followed by a regression that, by mid-Albian time, resulted in the spread of a clastic regime across the Middle East platform, the Nahr

Umr Formation. The Natih Formation is part of the Mesozoic platform carbonate succession deposited on the southeastern Arabian peninsula. The age of Natih is middle Cretaceous (late Albian to Cenomanian / early Turonian), and its deposition was terminated by early Turonian uplift (Hitchings & Potters, 2000). As a result of eustatic sea level changes, the Natih Formation is cyclic with a succession of coarsening-upward cycles of deeper marine shales and mudstones grading to shallow marine rudistid packstones and grainstones, each terminated by an emergence surface.

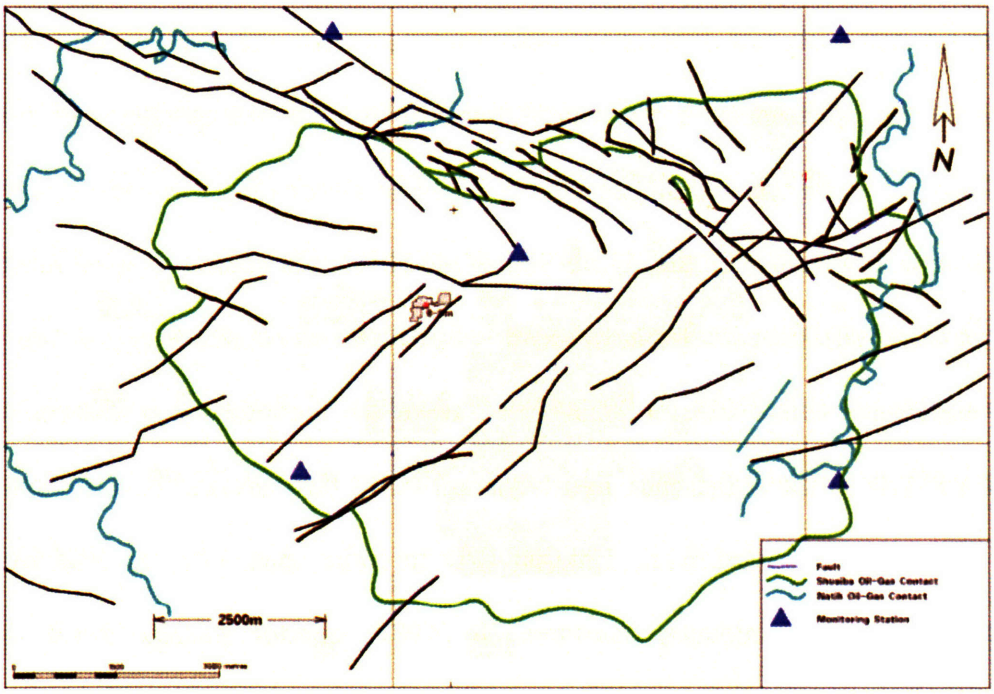

Figure A.5. Structure map of the Field.

Like Natih Field and Fahud Field, gas production from Natih has been extracted by depletion drive. Production of the Natih gas commenced in 1971 to supply lift gas for

the Shuaiba oil. Gas supply to the government gas grid was initiated in 1978. The Natih gas reservoir in Yibal is currently a depleting gas reservoir and pressure has dropped from 10,120 KPa to 7,920 KPa since 1973 (van Driel et al., 2000). Currently, there are 14 dedicated wells producing gas from the Natih.

Annual oil production in the Yibal field rose gradually since 1969. The Shuaiba oil reservoir was initially production by natural depletion, and thus the field has suffered from rapid reservoir pressure depletion. Water injection based on a five-spot lateral water flooding pattern development was introduced in 1972 to maintain reservoir pressure. It was subsequently expanded to an inverted nine spot pattern (500 m well spacing) infilling. Water injection serves the dual purpose of pressure management and produced water disposal. Water was initially injected into the oil column but was converted to deep injectors, injecting water into the aquifer below the 50% water saturation level in Shuaiba (Litsey et al., 1986). Past studies have identified uneven vertical and lateral sweep due to uneven subsurface water distribution as a result of the complicated fracture and fault patterns as well as the subsurface hydrodynamics and flow mechanisms. In 1986, the field's output was boosted from 120,000 B/D to more than 140,000 B/D with the installation of water injection facilities. In 1989, quarter pattern in-fill drilling commenced on the crest of the field to increase production and improve sweep.

Production was increased further following the completion of a $200 million development project, called Yibal Shuaiba Phase II, in 1994. The project involved drilling 96 wells, mostly horizontal, and modifications to production stations which

included the installation of gas injection facilities. Production reached to a peak of approximately 225,000 B/D in 1997 and began to decline rapidly afterwards. Since then, production has fallen at an annual rate of about 12 percent, that is, more than twice the normal rate of 5 percent in the region. Oil production has decreased to approximately 95,000 B/D in 2002. As the field matured, production wells experience co-production of oil and water. This rise in oil-water contact and process of water injection contributed into further increase of water-cut in producers. Water production has accelerated since 1997 to a gross rate of approximately 850,000 B/D in 2002 (Mijnssen et al., 2003). Production costs has increased due to the increase in the amount of water in the extracted oil to as much as 90 percent of the total volume. Since 1999, new well results have been disappointing, and drilling was suspended in early 2001. Current recovery factor in the field is 40%. Initial reservoir pressure was 15,700 KPa with a bubble point pressure of 14,900 KPa. Current reservoir pressure is slightly lower varying between 13,000 and 15,000 KPa across the field. Following decades of production, it proves difficult to accurately predict the exact location of remaining oil in Yibal. Key uncertainties with respect to ultimate recovery are expected to be waterflood sweep efficiency and residual oil saturation.

A.3 References

Al-Khodhori, S., 2001, The Challenges and Way Forward of Horizontal Dual Lateral Wells in Fahud Matrix Reservoir: SPE Middle East Oil Show , 17-20 March, Bahrain.

Al-Mugheiry, M.A., Mueller, G., Braas, M., Materna, T., Davies, H., Hsu, C.F., Keating, J., 2003, Al-Huwaisah Reservoir: The Long Journey to Improved Oil Recovery!: Middle East Oil Show, 9-12 June, Bahrain.

Baumann, A., 1983, Application of Sedimentological Studies in the Reservoir Geological Modeling of the Al Huwaisah Field, Oman: Middle East Oil Technical Conference and Exhibition, 14-17 March, Bahrain.

Blaskovich, F.T., Thurber, S.S., Echois, D.P., Al-Hinai, K.B.M., 1985, Reservoir Management of the Yibal Field in North Oman: A Simulation Approach: Middle East Oil Technical Conference and Exhibition, 11-14 March, Bahrain.

Brennan, P., 1985, Middle Cretaceous carbonate reservoirs, Fahud field and northwestern Oman: Discussion: American Association Petroleum Geologist Bulletin, **69**, 809 – 818.

Droste, H.J., 1997, Stratigraphy of the Lower Paleozoic Supergroup of Oman: GeoArabia, **2**, 419 – 471.

Edgell, H.S., 1991, Proterzoic salt basins of the Persian Gulf area and their role in hydrocarbon generation: Precambrian Research, **54**, 1 – 14.

Eikmans, H. and Hitchings, V.H., 1999, Using 3D Integrated Modelling to Manage the Fractured Natih Field (Oman): Middle East Oil Show and Conference, 20-23 February, Bahrain.

Gorin, G.E., Racz, L.G., and Walter, M.R., 1982, Late Precambrian-Cambrian sediments of Huqf Group, Sultanate of Oman: American Association Petroleum Geologist Bulletin, **66**, 2609 – 2627.

Harris, P.M., and Frost, S.H., 1984, Middle Cretaceous carbonate reservoirs, Fahud field and northwestern Oman: American Association Petroleum Geologist Bulletin, **68**, 649 – 658.

Heward, A.P., 1990, Salt removal and sedimentation in southern Oman, *in* Robertson, A.H.F., Searle, M.P., and Ries, A.C., eds., The Geology and Tectonics of the Oman Region: Geological Society of London Special Publication 49, 637 – 651.

Hitchings, V.H. and Potters, H., 2000, Production and geologic implications of the Natih 9-C, 3-D seismic survey: The Leading Edge, **19**, 1117 – 1122.

Hughes-Clarke, M.W., 1998, Stratigraphy and rock unit nomenclature in the oil-producing area of interior Oman: Journal of Petroleum Geology, **11**, 5 – 60.

Husseini, M.I. and Husseini, S.I., 1990, Origin of the Infracambrian Salt Basins of the Middle East, *in* Brooks, J. (ed), Classic Petroleum Provinces, Geological Society of London Special Publication No. 50, 279 – 292.

Levell, B.K., Braakman, J.H., and Rutten, K.W., 1988, Oil-bearing sediments of the Gondwana glaciation in Oman: American Association Petroleum Geologist Bulletin, **72**, 775 – 796.

Litsey, L.R., MacBride Jr., W.L., Al-Hinai, K.M., and Dismukes, N.B., 1986, Shuaiba reservoir geological study, Yibal field, Oman: J. Petroleum Geology, **38**, 651-661.

Loosveld, R.J.H., Bell, A. and Terken, J.J.M., 1996, Tectonic evolution of north Oman: GeoArabia, **1**, 28 – 51.

Mattes, B.W., and Conway-Morris, S., 1990, Carbonate/evaporite deposition in the Late Precambrian-Early Cambrian Ara Formation of southern Oman, *in* , A.H.F., Searle, M.P., and Ries, A.C. (eds), The Geology and Tectonics of the Oman Region, Geological Society Special Publication No. 49, 617 – 636.

Mijnssen, F.C.J., Davies, A.H., Grondin, K., Keating, J., Hsu, C.F., Amthor, J., 2003, Bringing Al Huwaisah's Volume to Value: SPE Annual Technical Conference and Exhibition, 5-8 October, Denver, Colorado.

Mijnssen, F.C.J., Rayes, D.G., Ferguson, I., Al Abri, S.M., Mueller, G.F., Razali, P.H.M.A, Nieuwenhuijs, R., Henderson, G.H., 2003, Maximizing Yibal's remaining value: SPE Reservoir Evaluation & Engineering, **6**, 255 – 263.

Nicholls, C.A., Boom, W. , Geel, J., Al Khodori, S. , Al Lawati, M., 1999, Fracture Modeling as a Key to Waterflood Development of the Fahud Field Natih-E Reservoir: Middle East Oil Show and Conference, 20-23 February, Bahrain.

O'Neil, N., 1988, Fahud field review: A switch from water to gas injection: J. Petroleum Technology, 609 – 618.

Pollastro, R.M., 1999, Ghaba salt basin province and Fahud salt basin province, Oman – geological overview and total petroleum systems: U.S.G.S. Open-File Report 99-50D.

Searle, M.P., 1988, Structure of the Musandam culmination and the Straits of Hormuz Syntaxis: Journal of the Geological Society, London, **145**, 831 – 845.

Scotese, C.R., Bambach, R.K., Barton, C., van der Voo, R., and Ziegler, A.M., 1979, Paleozoic base maps: Journal of Geology, **87**, 217 – 277.

Sharief, F.A.M., 1982, Lithofacies distribution of the Permian-Triassic rocks of the Middle East: Journal of Petroleum Geology, **5**, 203 – 206.

Terken, J.M.J. and Frewin, N.L., 1999, The Q petroleum system of Oman: AAPG Bulletin, **83**, 1343.

Vail, P.R., Audemard, F., Bowman, S.A., Eisner, P.N., and Perez-Cruz, C., 1991, The stratigraphic signature of tectonics, eustasy, and sedimentology — An overview, *in* Einsele, G., Ricken, W., and Seilacher, A., eds., Cycles and Events in Stratigraphy, Springer-Verlag, Berlin Heidelberg, 617 – 659.

Van Dijkum, C.E. and Walker, T., 1991, Fractured Reservoir Simulation and Field Development, Natih Field, Oman: SPE Annual Technical Conference and Exhibition, 6 – 9 October, Dallas, Texas.

Willetts, J.M., Hogarth, R.A.M., 1987, Lekhwair Pilot Waterflood, North Oman: Middle East Oil Show, 7-10 March, Bahrain

Appendix B

Hypoinverse-2000 Microearthquake Locations

YR/MM/DD	HR/MIN	SEC	LAT	LONG	DEPTH	RMS
991029	0102	56.16	22.131833	56.006500	1.82	0.02
991103	0733	50.41	22.134000	56.007500	2.89	0.05
991107	2333	25.49	22.136167	56.021167	2.84	0.03
991115	0212	47.35	22.131500	56.005667	2.68	0.04
991115	1541	22.37	22.131333	56.007167	1.99	0.03
991115	1657	52.37	22.133833	56.007667	2.07	0.04
991119	0333	11.65	22.169333	55.985667	0.62	0.06
991121	0922	31.28	22.130333	56.005500	2.62	0.03
991121	1923	29.01	22.135667	56.016500	2.66	0.01
991125	1836	32.65	22.139500	56.014167	2.61	0.02
991125	1838	52.40	22.138667	56.014167	2.63	0.04
991211	0248	15.12	22.155500	56.033000	2.74	0.02
991214	1450	40.79	22.150167	56.020333	1.43	0.02
991217	1826	14.22	22.130833	56.003667	2.91	0.05
991220	1911	29.71	22.152500	55.962667	2.90	0.02
991222	2045	46.74	22.129500	56.003500	0.95	0.02
991222	2212	18.34	22.124000	55.998667	2.81	0.04
991223	0524	16.90	22.150333	56.028833	0.95	0.02
991223	1501	14.54	22.131000	56.012167	1.60	0.08
000101	0454	5.86	22.133667	56.013000	2.31	0.01
000102	1745	17.95	22.132167	56.007833	1.77	0.01
000106	2225	21.93	22.151000	56.028833	1.10	0.01
000108	1432	35.90	22.131500	56.004833	2.75	0.03
000109	1645	0.33	22.169000	56.041333	1.57	0.06
000109	2300	31.65	22.146833	56.023667	1.53	0.05
000229	1637	49.01	22.147833	56.018833	1.05	0.02
000302	0528	47.55	22.133500	56.018500	2.73	0.05
000307	0958	19.02	22.177667	56.049667	2.86	0.05
000310	1316	28.49	22.148667	56.016333	0.90	0.05
000311	1215	19.33	22.148500	56.016167	0.68	0.03
000312	1634	43.90	22.128000	55.996667	2.41	0.02
000320	0805	40.08	22.131833	56.008667	2.58	0.03
000320	1013	39.71	22.128500	56.003000	2.84	0.03
000320	1015	40.05	22.130167	56.006333	2.77	0.04
000320	1016	20.07	22.133167	56.006500	2.66	0.02
000414	0029	29.32	22.134000	56.007667	2.02	0.01
000416	0151	31.68	22.142500	56.007333	1.01	0.01
000416	0937	1.60	22.159500	56.037833	2.95	0.04

YR/MM/DD	HR/MIN	SEC	LAT	LONG	DEPTH	RMS
000422	0136	27.60	22.144833	56.013333	0.93	0.01
000422	1155	59.37	22.132000	56.006000	2.60	0.01
000424	0345	44.67	22.132667	56.007833	2.84	0.04
000424	0432	7.83	22.133000	56.007167	2.84	0.03
000424	0501	39.84	22.131667	56.005667	2.79	0.03
000429	1303	10.12	22.130500	56.008833	1.12	0.01
000429	2248	10.58	22.145333	56.013667	1.18	0.03
000501	1601	9.61	22.132500	56.006667	2.79	0.02
000503	0043	3.59	22.130500	56.004833	2.99	0.03
000503	0435	33.46	22.129833	56.004333	2.76	0.01
000504	1151	50.44	22.156833	56.011167	2.65	0.01
000505	1740	2.11	22.132833	56.008667	2.03	0.03
000506	0942	4.01	22.126833	56.007333	1.51	0.01
000507	0022	7.73	22.131000	56.003167	3.40	0.01
000513	0757	41.24	22.130000	55.993667	1.48	0.08
000513	1450	5.67	22.131167	55.997000	0.47	0.04
000514	1023	11.51	22.160167	56.062833	3.73	0.03
000515	0046	19.94	22.125500	56.001667	2.71	0.03
000516	0631	6.57	22.136500	56.007667	1.84	0.03
000516	1507	25.54	22.132000	56.009667	2.33	0.08
000518	0557	52.94	22.132000	56.007000	2.60	0.03
000519	1445	15.58	22.146833	56.013667	1.02	0.01
000521	0309	23.15	22.144333	56.009500	1.05	0.01
000522	2108	25.20	22.146833	56.007833	1.40	0.03
000522	2256	30.68	22.143333	56.010667	0.90	0.02
000522	2334	27.81	22.131833	56.008333	2.57	0.06
000529	0041	10.64	22.134000	56.007167	3.03	0.01
000530	0850	28.88	22.147500	56.026333	1.08	0.02
000530	0852	40.64	22.144667	56.025667	0.99	0.04
000603	2009	1.94	22.128833	56.002333	2.39	0.05
000606	1421	3.20	22.135167	56.008167	2.40	0.02
000607	0314	0.74	22.134500	56.008833	1.95	0.04
000613	1109	23.65	22.144667	56.011667	1.05	0.04
000613	2140	16.07	22.146333	56.015167	1.18	0.01
000617	1155	54.42	22.132333	56.005833	2.95	0.05
000618	0934	48.23	22.134000	56.004667	2.99	0.07
000620	1932	42.55	22.129167	55.994167	2.05	0.01
000626	0946	34.14	22.134333	56.009833	2.98	0.04
000627	1647	55.44	22.124167	55.991500	1.53	0.03
000702	1502	13.57	22.131333	55.998333	1.49	0
000705	0216	46.50	22.152500	56.029333	2.84	0.01
000714	0554	14.59	22.131667	56.006667	2.88	0.04
000717	1443	13.91	22.159500	56.028167	1.01	0.02
000718	0148	22.85	22.161333	56.025333	2.76	0.02
000718	1240	47.26	22.163333	56.028167	1.52	0.04
000719	1702	1.71	22.142500	56.009333	1.05	0.02

YR/MM/DD	HR/MIN	SEC	LAT	LONG	DEPTH	RMS
000723	1336	35.78	22.133333	56.007667	2.90	0.01
000725	0405	29.30	22.148500	55.981333	2.91	0.06
000726	0822	36.61	22.129167	55.995667	1.39	0.01
000726	1314	3.17	22.145333	56.009500	1.13	0.02
000727	2308	21.26	22.148500	56.026667	0.82	0.01
000728	0700	42.71	22.146833	56.024667	1.59	0.06
000728	0917	42.12	22.148000	55.983333	2.79	0.04
000728	0923	16.92	22.148167	55.981667	2.86	0.04
000731	2143	25.95	22.176167	56.046667	1.29	0.08
000802	2020	23.43	22.148667	56.026500	1.09	0.03
000804	0523	23.30	22.150167	56.021500	1.31	0.03
000806	1148	48.15	22.144833	56.013667	0.68	0.01
000809	0459	29.17	22.132833	56.007333	2.82	0.02
000809	0712	53.64	22.134500	56.006833	2.57	0.01
000815	1448	52.69	22.128333	56.005333	2.69	0.02
000823	1809	20.52	22.149167	55.980667	2.41	0.05
000905	0731	22.81	22.134000	56.009167	2.76	0.01
000905	2102	9.93	22.160833	56.028500	2.13	0.01
000907	0430	28.10	22.148833	56.027833	1.22	0.04
000907	1039	56.53	22.149000	56.028333	1.09	0.03
000909	1157	56.48	22.151500	56.030167	2.44	0.03
000910	1005	1.17	22.144500	56.023167	0.76	0.03
000911	0003	52.55	22.144833	56.023667	0.68	0.03
000911	0027	18.90	22.143000	56.023833	1.00	0.03
000912	1101	7.10	22.146000	56.023500	1.54	0.06
000912	2229	32.70	22.145667	56.025833	0.91	0.03
000912	2317	1.82	22.143167	56.018333	3.40	0.01
000913	1429	5.33	22.147500	56.027500	2.07	0.06
000915	2322	3.83	22.139667	56.008833	3.80	0.01
000917	0826	32.57	22.133167	56.006667	2.01	0.05
001001	0447	58.23	22.131833	56.008333	0.90	0.03
001001	2041	43.65	22.148500	55.982000	2.30	0.06
001001	2034	40.03	22.148833	55.981000	1.54	0.05
001003	2028	21.59	22.152333	55.980833	1.74	0.07
001009	0658	56.10	22.133667	56.009167	2.90	0.02
001009	1740	9.17	22.133000	55.997833	1.76	0.05
001012	2257	19.68	22.134167	56.007667	1.24	0.02
001012	2313	46.57	22.135500	56.010500	2.04	0.02
001013	0017	55.57	22.146667	55.973167	1.59	0.06
001013	2151	38.37	22.132333	56.008167	2.30	0.05
001013	2153	15.13	22.132000	56.007167	2.68	0.04
001013	2339	31.87	22.133667	56.006000	2.86	0.02
001017	0140	16.30	22.142167	56.008667	0.94	0.06
001017	0805	36.39	22.135167	56.004000	2.84	0.04
001017	1119	17.83	22.131000	56.006500	1.56	0.02
001017	2041	44.87	22.148333	55.982000	2.77	0.06

YR/MM/DD	HR/MIN	SEC	LAT	LONG	DEPTH	RMS
001018	0726	13.72	22.127167	56.003667	2.71	0.06
001020	1942	34.66	22.133000	56.007500	2.32	0.02
001023	0640	41.86	22.135000	56.008833	2.31	0.02
001024	0749	32.79	22.136333	56.009500	2.37	0.03
001024	0834	58.75	22.129333	56.007500	0.91	0.05
001027	2124	46.36	22.152000	56.037333	1.53	0.02
001028	2232	17.83	22.134000	56.007667	2.18	0.04
001028	2345	21.69	22.136000	56.020500	3.07	0.01
001030	0707	47.35	22.134333	56.007833	1.51	0.03
001031	0227	27.54	22.132833	56.008667	2.79	0.02
001101	0918	31.63	22.132500	56.007000	2.02	0.02
001104	2201	9.93	22.164333	56.040167	2.58	0.08
001105	0541	47.86	22.162500	56.040667	2.50	0.08
001107	0303	23.35	22.131833	56.006833	2.43	0.01
001107	1804	0.88	22.145333	56.024333	1.07	0.03
001107	2309	6.58	22.164000	56.041833	2.97	0.06
001107	2337	31.90	22.164167	56.041000	2.47	0.08
001110	0219	18.62	22.148833	56.013667	0.91	0.03
001110	0251	47.28	22.151000	56.014333	1.27	0.05
001110	1758	58.02	22.163667	56.041167	2.98	0.06
001111	0657	22.72	22.164667	56.042833	2.67	0.08
001111	0729	22.16	22.164167	56.040333	1.58	0.08
001111	0729	30.79	22.165333	56.042667	2.93	0.07
001113	2144	22.04	22.134333	56.013500	2.75	0.03
001114	0649	18.03	22.162333	56.032167	2.55	0.03
001120	2247	18.79	22.130500	56.006167	2.04	0.02
001121	0601	22.81	22.131500	56.006167	3.04	0.02
001121	1508	17.27	22.134000	56.007500	2.36	0.02
001123	0601	27.02	22.132333	56.013833	3.11	0.03
001126	0104	56.73	22.153333	56.036667	2.94	0.05
001126	0255	59.52	22.131667	56.007167	2.45	0.03
001126	0952	26.47	22.154333	56.032167	2.80	0.03
001126	1618	54.13	22.152833	56.032500	2.76	0.02
001127	1215	58.80	22.143500	56.009000	1.26	0.04
001128	1833	25.17	22.129667	55.995333	1.52	0.01
001130	1753	26.55	22.143333	56.023500	0.72	0.02
001203	2012	22.34	22.158333	56.034500	3.13	0.04
001204	0213	59.80	22.160667	56.028167	1.50	0.03
001210	0041	28.43	22.144667	56.013000	1.31	0.01
001212	0217	24.77	22.124000	55.990667	2.04	0.03
001213	1115	14.41	22.135833	56.006500	3.22	0.09
001216	0114	57.89	22.140500	56.010000	1.27	0.04
001218	1512	1.34	22.139167	56.009667	1.08	0.03
001218	1513	21.16	22.143333	56.012500	1.23	0.05
001222	2151	14.05	22.134167	56.007833	2.10	0.02
001222	2159	10.29	22.132333	56.010833	2.01	0.03

YR/MM/DD	HR/MIN	SEC	LAT	LONG	DEPTH	RMS
010104	2226	14.28	22.177000	56.048333	1.37	0.04
010105	0710	26.05	22.175500	56.046500	1.28	0.08
010106	0629	11.06	22.177500	56.050667	1.48	0.07
010106	2159	58.00	22.135167	56.006000	2.94	0.05
010109	0748	32.49	22.135500	56.007833	2.80	0.04
010109	1208	2.11	22.134500	56.009833	1.58	0.05
010110	1334	23.61	22.138167	56.011667	2.68	0.06
010112	0916	39.25	22.138500	56.011833	2.62	0.05
010112	2142	22.90	22.139167	56.013667	2.65	0.03
010114	1720	57.44	22.139333	56.014000	2.57	0.05
010114	1722	6.76	22.139167	56.012333	2.95	0.03
010116	2339	38.99	22.127500	55.994167	1.32	0.02
010116	2342	26.40	22.129333	55.992833	2.15	0.01
010118	1511	3.38	22.126333	55.992333	1.52	0.03
010119	0543	12.09	22.134333	56.010667	2.68	0.01
010122	2040	49.13	22.132833	56.008167	2.91	0.02
000122	2104	14.84	22.133667	56.010333	0.04	0.12
010123	1906	56.61	22.141500	56.010167	1.51	0.04
010202	0313	35.42	22.143500	56.014833	4.20	0
010204	0039	10.98	22.128667	55.995333	2.29	0.02
010204	0106	55.67	22.127333	55.991167	1.48	0.07
010204	0115	57.76	22.128667	55.994500	1.55	0.04
010204	0728	21.18	22.129000	55.995167	1.51	0.07
010204	1242	27.72	22.145333	56.015000	1.28	0.02
010204	1243	28.31	22.145667	56.015500	1.23	0.02
010204	1243	44.87	22.145833	56.015500	1.30	0.01
010204	1757	33.10	22.130167	56.005167	2.68	0.01
010204	1809	23.53	22.130167	56.003833	2.72	0.03
010205	2230	47.60	22.136000	56.007833	2.93	0.04
010206	1052	56.05	22.137667	56.011333	2.65	0.05
010206	1151	29.25	22.141333	56.014500	2.71	0.04
010206	1154	16.24	22.140833	56.016000	2.48	0.04
010206	1710	39.33	22.139167	56.007833	3.27	0.04
010207	0240	32.70	22.127667	56.003667	2.83	0.03
010207	1610	59.85	22.137667	56.008833	2.94	0.03
010208	1856	48.12	22.132333	56.006667	2.92	0.04
010210	1945	55.66	22.134167	56.015000	2.91	0.01
010211	2342	18.84	22.140000	56.011667	1.26	0.01
010211	2342	29.70	22.140667	56.010667	1.16	0.02
010212	0611	9.88	22.146333	56.016333	1.22	0.01
010212	1523	49.77	22.141333	56.009333	1.39	0.01
010219	1628	33.45	22.150333	56.021667	1.17	0.01
010219	1635	3.96	22.150167	56.021333	1.15	0.02
010219	2039	35.76	22.152000	56.023000	1.19	0.01
010223	1820	44.44	22.144500	56.018500	0.85	0.06
010223	1841	57.47	22.139667	56.009833	1.12	0.04

YR/MM/DD	HR/MIN	SEC	LAT	LONG	DEPTH	RMS
010224	2230	22.24	22.148167	56.020500	1.26	0.03
010224	2342	1.22	22.134500	56.007833	2.42	0.02
010225	0239	30.58	22.145167	56.015500	1.12	0.03
010227	0056	14.05	22.128167	55.993500	2.38	0
010304	2114	17.79	22.146500	56.015667	1.27	0.02
010304	2254	50.86	22.146500	56.016667	1.00	0.02
010305	1436	35.97	22.123000	55.986500	2.67	0.06
010306	0909	59.40	22.122833	55.985500	1.73	0.02
010308	1253	25.28	22.149000	56.017500	1.35	0.04
010311	1251	51.37	22.147000	56.015833	1.18	0.02
010311	1444	8.21	22.143000	56.009667	1.30	0.05
010311	2207	56.92	22.144167	56.014667	1.03	0.02
010313	0319	40.35	22.129167	55.994833	2.80	0.05
010313	1802	48.30	22.142833	56.011000	1.38	0.02
010315	2108	36.54	22.147667	56.019833	1.34	0.03
010316	0954	16.51	22.149000	56.021167	0.98	0.04
010318	0402	45.22	22.147500	56.015833	0.80	0.03
010318	0711	33.92	22.148833	56.016500	1.02	0.02
010318	1448	46.71	22.167000	56.041333	3.01	0.05
010318	2124	8.44	22.147833	56.017667	1.16	0.02
010318	2149	30.61	22.145667	56.016333	1.25	0.01
010319	1807	54.81	22.147333	56.016167	1.36	0.01
010320	0052	54.21	22.132000	56.005333	2.88	0.03
010320	0128	35.06	22.144833	56.014500	1.17	0.01
010320	0143	29.20	22.133833	56.006167	2.85	0.02
010320	0157	48.24	22.134000	56.007000	2.55	0.01
010320	0312	44.63	22.141667	56.004667	2.61	0.04
010320	0446	46.15	22.132167	56.005500	2.58	0.04
010321	0844	46.19	22.132333	56.005833	2.66	0.02
010321	1420	12.32	22.147667	56.013000	1.03	0.01
010323	0440	37.73	22.134000	56.008000	2.85	0.02
010323	0957	37.23	22.145000	56.016167	1.19	0.01
010323	1231	41.65	22.145833	56.015667	1.33	0.01
010323	1441	5.84	22.146167	56.016500	1.27	0.01
010324	0256	50.74	22.135833	56.009167	2.59	0.02
010324	0347	13.76	22.143833	56.012667	1.38	0.01
010324	2035	18.59	22.130833	56.003833	2.86	0.01
010325	1530	13.72	22.131833	55.999667	1.49	0.03
010325	1934	58.85	22.141000	56.011833	1.38	0.02
010326	2148	36.96	22.141333	56.010500	1.34	0.02
010328	1105	16.80	22.142000	56.009667	1.09	0.04
010328	2232	19.59	22.142000	56.011333	1.32	0.01
010329	0844	24.54	22.144667	56.014333	1.36	0.01
010330	1256	16.70	22.160000	56.024000	1.87	0.01
010330	1522	48.06	22.149833	56.023333	1.16	0.03
010330	2218	10.02	22.150333	56.020000	0.99	0.03

YR/MM/DD	HR/MIN	SEC	LAT	LONG	DEPTH	RMS
010331	0049	42.75	22.153167	56.021167	0.84	0.01
010331	2348	29.16	22.148667	56.020333	0.79	0.02
010401	0016	29.44	22.148667	56.018333	1.05	0.03
010401	1303	18.30	22.143667	56.014333	1.32	0.01
010401	1441	5.72	22.151667	56.019500	1.09	0.02
010402	0550	42.14	22.161500	56.041833	2.92	0.04
010402	0551	18.16	22.162500	56.043000	2.92	0.05
010402	0624	43.48	22.146333	56.016000	1.27	0.01
010402	0949	40.57	22.144333	56.014667	1.32	0.04
010402	1802	9.52	22.130333	56.005833	2.60	0.03
010402	2154	30.29	22.155333	56.027167	1.04	0.04
010403	1115	27.46	22.136000	56.011333	2.90	0.05
010404	0133	35.28	22.141167	56.012000	1.23	0.02
010404	0930	59.13	22.146000	56.016000	1.26	0.01
010406	1759	29.35	22.149833	56.019000	1.36	0.04
010407	1215	13.04	22.146000	56.011167	0.87	0.01
010407	2250	28.15	22.132167	55.999000	2.97	0.04
010408	2346	5.23	22.146000	56.011833	1.06	0.02
010409	0358	58.30	22.146000	56.012167	1.14	0.01
010409	2358	35.95	22.144333	56.010167	1.06	0.02
010410	1121	34.93	22.147500	56.012333	1.32	0.05
010410	2125	38.43	22.147333	56.016167	1.14	0.02
010410	2348	1.35	22.145667	56.013333	1.30	0.01
010412	1622	26.71	22.144667	56.015333	1.17	0.01
010412	1943	41.57	22.145500	56.012667	1.22	0.05
010412	2254	6.21	22.146333	56.015167	1.30	0.02
010414	2201	25.14	22.151000	56.020000	0.82	0.02
010415	1402	38.88	22.160500	56.026333	2.35	0.02
010416	0807	10.39	22.147500	56.018833	1.10	0.01
010416	1140	41.50	22.149833	56.017000	1.12	0.01
010416	1502	18.67	22.159667	56.027667	1.90	0.04
010418	0133	31.80	22.134833	56.015667	2.72	0.02
010419	0830	1.99	22.141167	56.010000	1.50	0.07
010421	0249	46.33	22.133333	56.007500	2.94	0.01
010421	0249	52.80	22.134167	56.007333	2.67	0.02
010421	0518	43.97	22.174500	56.044500	2.66	0.04
010421	0539	42.93	22.173000	56.040833	1.84	0.05
010421	1551	33.65	22.154167	56.033000	2.55	0.02
010422	0946	4.14	22.157333	56.036500	2.95	0.03
010422	1254	1.97	22.143167	56.012500	1.16	0.01
010426	1517	2.89	22.133667	56.006500	2.92	0.03
010426	2359	7.42	22.161500	56.032333	2.17	0.04
010427	1026	58.64	22.176167	55.986833	1.07	0.06
010427	1940	29.04	22.132500	56.013667	2.87	0.01
010428	0637	30.14	22.135333	56.009500	2.66	0.02
010428	0659	6.57	22.132667	56.007667	2.39	0.01

YR/MM/DD	HR/MIN	SEC	LAT	LONG	DEPTH	RMS
010429	0345	16.67	22.131833	56.012667	3.20	0.01
010429	0609	40.66	22.134500	56.006500	1.93	0.02
010501	1919	0.58	22.146167	56.016833	1.24	0.03
010501	2231	19.27	22.170667	56.039833	1.56	0.03
010502	0443	45.82	22.145500	56.013833	1.08	0.01
010504	2230	13.92	22.145500	56.010333	0.99	0.01
010505	0946	14.32	22.144000	56.011333	1.01	0.03
010505	1823	50.31	22.146333	56.017500	1.08	0.04
010505	2125	10.52	22.150333	56.020333	1.25	0.03
010506	0537	4.11	22.149333	56.037833	3.06	0.04
010507	1103	32.75	22.133500	56.008833	2.84	0.01
010508	1643	40.37	22.137000	56.009333	3.48	0
010510	0336	3.74	22.134500	55.998833	2.77	0.04
010512	1948	43.03	22.146500	56.015333	1.30	0.02
010512	2015	33.68	22.133333	56.007167	2.89	0.01
010514	1047	1.74	22.130167	55.993167	2.31	0.03
010514	1917	25.89	22.143333	56.012667	1.14	0.01
010515	1418	39.11	22.128833	55.992333	1.09	0.07
010515	2028	51.83	22.128833	55.992333	0.96	0.06
010515	2229	32.43	22.146500	56.015667	1.32	0.02
010516	1053	3.28	22.148333	56.015500	1.06	0.01
010517	0113	3.65	22.133000	56.012667	2.26	0.04
010517	0120	0.17	22.133167	56.012000	2.49	0.04
010518	2258	29.72	22.149000	56.018500	1.09	0.02
010519	0542	28.08	22.147833	56.014000	1.10	0.03
010519	0714	42.62	22.148000	56.015833	0.92	0.01
010520	0439	11.04	22.135833	56.011500	2.58	0.02
010521	0111	22.57	22.142667	56.010833	0.96	0.01
010521	0111	40.19	22.143833	56.010833	1.09	0.02
010521	1848	44.54	22.143500	56.008167	1.12	0.02
010521	2021	42.91	22.149000	56.012167	1.12	0.02
010521	2353	59.45	22.150833	56.021167	1.16	0.02
010523	0445	18.66	22.147333	56.014333	1.06	0.02
010523	1250	33.94	22.145833	56.012167	1.17	0.03
010523	1419	28.20	22.147000	56.012833	1.10	0.02
010523	2124	45.43	22.145000	56.010833	1.04	0.04
010524	1306	33.01	22.145667	56.012833	1.27	0.01
010525	0423	17.03	22.140167	56.008333	1.09	0.02
010530	0526	45.71	22.133500	56.000833	2.52	0.02
010531	1915	57.60	22.133500	56.007333	2.90	0.01
010531	2049	13.48	22.135333	56.006500	1.85	0.01
010603	0424	20.82	22.145333	56.023667	0.77	0.02
010603	1356	9.36	22.128833	55.991500	1.20	0.09
010603	1408	25.74	22.112333	55.974833	3.86	0.11
010605	1433	15.10	22.136333	56.014333	2.68	0.01
010605	1854	49.67	22.138167	56.012667	2.87	0.05

YR/MM/DD	HR/MIN	SEC	LAT	LONG	DEPTH	RMS
010606	0648	20.69	22.142667	56.011833	1.08	0.01
010606	1630	55.09	22.146833	56.015167	1.50	0.02
010606	1741	36.53	22.145667	56.016167	1.30	0.02
010606	1835	55.78	22.146500	56.016500	1.20	0.01
010607	0858	34.65	22.135500	56.008167	2.82	0.02
010608	0136	46.94	22.132500	56.000833	1.86	0.04
010608	0137	2.69	22.133667	56.000167	1.89	0.02
010608	1320	18.94	22.152167	56.020167	0.83	0.02
010608	1425	38.64	22.153167	56.020167	0.88	0.02
010609	1807	21.34	22.132000	56.006167	2.79	0.01
010610	0735	57.00	22.153167	56.020833	0.86	0.02
010610	1246	51.46	22.150667	56.020000	0.92	0.03
010611	0403	18.03	22.144000	56.024000	0.80	0.01
010611	0516	49.78	22.163833	56.044000	2.92	0.05
010611	2029	32.17	22.144167	56.013500	1.22	0.03
010612	1042	49.15	22.134333	56.009000	2.92	0.03
010612	1605	3.71	22.134833	56.009833	2.82	0.02
010612	1606	26.39	22.158833	56.027500	1.17	0.02
010612	1757	0.39	22.152333	56.031500	1.08	0.01
010612	1757	25.66	22.152833	56.030500	1.56	0.03
010613	0917	54.05	22.133667	56.007667	1.18	0.03
010613	1656	47.50	21.623333	55.801333	2.01	0.34
010613	1905	41.85	22.130667	56.007667	2.72	0.03
010613	2251	10.22	22.131833	56.006833	2.29	0.03
010614	0054	29.13	22.130500	56.003500	1.93	0.03
010614	0054	34.39	22.132500	56.006833	2.89	0.02
010614	0303	32.76	22.146500	56.014500	1.21	0.01
010614	0527	3.25	22.145667	56.025000	0.67	0.01
010614	0752	22.18	22.133833	56.006667	2.83	0.02
010614	1949	4.17	22.124833	55.987833	2.12	0.07
010614	2021	15.87	22.135500	56.008167	1.94	0.01
010614	2029	9.30	22.134667	56.008000	2.51	0.03
010614	2249	57.30	22.132833	56.007000	2.64	0.01
010615	0634	23.59	22.139500	56.021500	2.76	0.02
010615	1856	58.12	22.140333	56.008667	1.27	0.04
010615	1857	1.01	22.141167	56.010167	1.31	0.02
010616	0157	25.57	22.174667	56.041833	2.72	0.03
010616	1349	58.06	22.133833	56.021000	2.70	0.04
010616	1854	55.95	22.137167	56.020167	3.44	0.02
010616	2215	56.14	22.149000	56.016500	1.15	0.03
010617	0320	12.40	22.153000	56.020833	1.10	0.02
010617	0720	59.33	22.134833	56.011167	2.63	0.02
010617	1640	39.64	22.132500	56.007167	2.81	0.03
010618	0108	11.49	22.146833	56.015833	1.30	0.01
010618	1157	8.64	22.141833	56.010667	1.11	0.02

Appendix C

Nonlinear Grid-Search Microearthquake Locations

YR/MM/DD	HR/MIN	SEC	LAT	LONG	DEPTH	RMS
991029	01 02	56.13644	22.13711	56.01068	2.3	0.014266
991103	07 33	50.38408	22.13829	56.01086	3.24	0.034421
991107	23 33	25.41062	22.13812	56.02319	0.76	0.010288
991115	02 12	47.34418	22.13644	56.00977	2.74	0.021426
991115	15 41	22.35976	22.1361	56.01122	2.16	0.019447
991115	16 57	52.36753	22.13863	56.01195	2.18	0.028253
991119	03 33	11.72782	22.1731	55.9913	0.9	0.042006
991121	09 22	31.27279	22.13559	56.00977	2.72	0.013353
991121	19 23	29.01496	22.14065	56.02029	2.62	0.008678
991125	18 36	32.64601	22.14403	56.01794	2.76	0.01964
991125	18 38	52.38452	22.14268	56.01721	2.92	0.025297
991211	02 48	15.12142	22.15922	56.03553	2.74	0.011333
991214	14 50	40.79086	22.15399	56.02374	1.4	0.00949
991217	18 26	14.22152	22.1361	56.00832	2.9	0.037578
991220	19 11	29.7096	22.15807	55.9679	2.98	0.01558
991222	20 45	46.73062	22.13458	56.00778	0.96	0.017568
991222	22 12	18.33473	22.12901	56.00324	2.86	0.034201
991223	05 24	16.89579	22.15416	56.03172	0.9	0.01552
991223	15 01	14.41335	22.13593	56.01557	0.92	0.023977
000101	04 54	5.843914	22.13897	56.01703	2.42	0.005333
000102	17 45	17.91914	22.13711	56.01195	1.36	0.000898
000106	22 25	21.92612	22.155	56.03172	1.06	0.015674
000108	14 32	35.91694	22.13796	56.0105	2.74	0.08802
000109	16 45	0.311145	22.17256	56.04443	2.1	0.039432
000109	23 00	31.56247	22.15028	56.02737	1.02	0.019461
000122	21 04	14.81773	22.14133	56.01322	0.24	0.037329
000229	16 37	49.02262	22.15214	56.02211	1.12	0.014439
000302	05 28	47.53519	22.13913	56.02174	1.2	0.029953
000307	09 58	19.03581	22.17965	56.05151	2.9	0.043332
000310	13 16	28.50631	22.15298	56.01957	1	0.031713
000311	12 15	19.33972	22.15265	56.01975	0.78	0.007015
000312	16 34	43.88943	22.13374	56.00125	2.56	0.008342
000320	08 05	40.05642	22.13677	56.01285	1.22	0.014262
000320	10 13	39.70672	22.13374	56.00742	2.86	0.026465
000320	10 15	40.05047	22.13525	56.01068	2.72	0.031341
000320	10 16	20.06908	22.13846	56.01068	2.64	0.011631
000414	00 29	29.30277	22.13914	56.01195	2.24	0.005797
000416	01 51	31.68755	22.14741	56.01159	1.06	0.003383

YR/MM/DD	HR/MIN	SEC	LAT	LONG	DEPTH	RMS
000416	09 37	1.608049	22.16293	56.04061	3.04	0.022281
000422	01 36	27.61032	22.14927	56.01703	0.96	0.008354
000422	11 55	59.35961	22.13745	56.01032	2.76	0.005804
000424	03 45	44.67624	22.13796	56.01159	2.78	0.015173
000424	04 32	7.834921	22.1388	56.01141	2.82	0.018401
000424	05 01	39.83751	22.13745	56.01032	2.8	0.017717
000429	13 03	10.19432	22.1366	56.01358	1.5	0.034412
000429	22 48	10.58005	22.14994	56.0174	1.24	0.020695
000501	16 01	9.597576	22.13711	56.01104	2.84	0.011082
000503	00 43	3.602748	22.13644	56.00905	2.98	0.014281
000503	04 35	33.46152	22.13526	56.00868	2.76	0.005926
000504	11 51	50.44693	22.16042	56.01523	2.72	0.003903
000505	17 40	2.051294	22.13745	56.01267	1.14	0.006607
000506	09 42	4.01078	22.13204	56.01158	1.5	0.00842
000507	00 22	7.722039	22.1361	56.00778	3.62	0.013828
000513	07 57	41.14072	22.13273	55.99708	2.98	0.055221
000513	14 50	5.661705	22.13627	56.00143	0.44	0.025233
000514	10 23	11.66151	22.16275	56.05548	2.94	0.061569
000515	00 46	19.93611	22.13154	56.00633	2.68	0.016186
000516	06 31	6.572127	22.14083	56.01195	1.8	0.018883
000516	15 07	25.37369	22.13643	56.01376	0.62	0.03236
000518	05 57	52.91477	22.13627	56.0114	2.88	0.020112
000519	14 45	15.5942	22.1513	56.01721	1.04	0.002661
000521	03 09	23.14902	22.14893	56.01395	1.04	0.006542
000522	21 08	25.1988	22.1513	56.01196	1.4	0.015631
000522	22 56	30.68805	22.14792	56.01467	0.96	0.012403
000522	23 34	27.76841	22.13711	56.01285	1.1	0.030233
000529	00 41	10.64492	22.13914	56.01177	3.12	0.00643
000530	08 50	28.8803	22.15146	56.02936	1.06	0.018456
000530	08 52	40.64968	22.14926	56.02864	1.08	0.027385
000603	20 09	1.918663	22.13475	56.00687	2.54	0.033909
000606	14 21	3.179099	22.14015	56.01231	2.7	0.013537
000607	03 14	0.728085	22.13914	56.01304	2.2	0.023725
000613	11 09	23.6571	22.14961	56.01594	1.1	0.022334
000613	21 40	16.06915	22.15062	56.01885	1.18	0.012321
000617	11 55	54.4127	22.13627	56.00923	3	0.04418
000618	09 34	48.22824	22.13796	56.00887	3.18	0.042683
000620	19 32	42.5315	22.13425	55.99871	2.38	0.006919
000626	09 46	34.13909	22.13863	56.01358	2.98	0.025157
000627	16 47	55.43616	22.12935	55.9969	1.5	0.02332
000702	15 02	13.55759	22.13661	56.00307	2	0.004287
000705	02 16	46.5114	22.15602	56.03227	2.84	0.004334
000714	05 54	14.60331	22.13677	56.01086	2.76	0.02036
000717	14 43	13.93117	22.16294	56.031	1.1	0.012188
000718	01 48	22.83563	22.1648	56.02847	2.92	0.012236
000718	12 40	47.27406	22.16683	56.03137	1.5	0.019233

YR/MM/DD	HR/MIN	SEC	LAT	LONG	DEPTH	RMS
000719	17 02	1.704627	22.14724	56.01359	1.06	0.015187
000723	13 36	35.77637	22.13796	56.01177	2.96	0.006645
000725	04 05	29.30598	22.15317	55.98585	3.16	0.042404
000726	08 22	36.61453	22.13458	56.00053	1.42	0.004241
000726	13 14	3.178841	22.15012	56.01413	1.16	0.010845
000727	23 08	21.25961	22.15264	56.02973	0.82	0.007504
000728	07 00	42.59881	22.15027	56.02864	1	0.023084
000728	09 17	42.12432	22.15283	55.98803	3.02	0.029325
000728	09 23	16.96192	22.15317	55.98621	2.78	0.023423
000731	21 43	25.90487	22.17982	56.05024	1.94	0.03546
000802	20 20	23.44726	22.15281	56.02918	1.18	0.020701
000804	05 23	23.29639	22.15416	56.02483	1.3	0.024438
000806	11 48	48.13401	22.1491	56.01776	0.62	0.002722
000809	04 59	29.17326	22.13779	56.01159	2.82	0.007833
000809	07 12	53.62456	22.13998	56.01123	2.72	0.007584
000815	14 48	52.68038	22.13357	56.00977	2.72	0.01169
000823	18 09	20.59312	22.15486	55.98404	1.82	0.027382
000905	07 31	22.81688	22.13897	56.01376	2.72	0.005385
000905	21 02	9.92825	22.16412	56.03137	2.22	0.007131
000907	04 30	28.09679	22.15314	56.03081	1.2	0.035953
000907	10 39	56.54107	22.15348	56.031	1.1	0.023725
000909	11 57	56.46901	22.15551	56.03299	1.28	0.013978
000910	10 05	1.160295	22.14909	56.02646	0.74	0.029829
000911	00 03	52.56335	22.14926	56.027	0.72	0.024696
000911	00 27	18.8948	22.1474	56.02736	1	0.014917
000912	11 01	6.983118	22.14994	56.02737	0.9	0.026668
000912	22 29	32.6657	22.15011	56.029	0.78	0.013002
000912	23 17	1.82904	22.14741	56.02174	3.46	0.00153
000913	14 29	5.243571	22.15112	56.03117	1.02	0.028026
000915	23 22	3.834621	22.14404	56.01358	3.82	0.010757
000917	08 26	32.58452	22.1388	56.01141	2.08	0.030643
001001	04 47	58.19068	22.13711	56.01267	0.8	0.026009
001001	20 34	40.06197	22.15418	55.98531	1.5	0.025494
001001	20 41	43.62461	22.15317	55.98621	2.9	0.035068
001003	20 28	21.55673	22.15705	55.98621	1.5	0.009841
001009	06 58	56.09994	22.13812	56.0134	2.92	0.011976
001009	17 40	9.118269	22.13796	56.00252	1.2	0.042736
001012	22 57	19.66815	22.13897	56.01195	1.16	0.01527
001012	23 13	46.5504	22.14083	56.01449	2.42	0.013392
001013	00 17	55.59702	22.15182	55.97733	1.5	0.033291
001013	21 51	38.2817	22.1366	56.01195	0.96	0.020432
001013	21 53	15.11712	22.13711	56.0114	1.24	0.019406
001013	23 39	31.86884	22.13813	56.01014	2.78	0.051313
001017	01 40	16.32786	22.14809	56.01232	1.08	0.041458
001017	08 05	36.38762	22.13948	56.00851	2.96	0.022172
001017	11 19	17.82488	22.13559	56.01068	1.5	0.008917

YR/MM/DD	HR/MIN	SEC	LAT	LONG	DEPTH	RMS
001017	20 41	44.87056	22.15283	55.98712	3.1	0.036117
001018	07 26	13.70653	22.1312	56.00904	2.74	0.035663
001020	19 42	34.62781	22.13812	56.01177	2.78	0.015942
001023	06 40	41.84559	22.13964	56.01286	2.48	0.010076
001024	07 49	32.76333	22.141	56.01304	2.78	0.02203
001024	08 34	58.71858	22.1339	56.01195	0.86	0.026272
001027	21 24	46.36101	22.15601	56.04006	1.5	0.009284
001028	22 32	17.82687	22.1388	56.01177	2.32	0.025571
001028	23 45	21.68159	22.14116	56.02428	3.32	0.009998
001030	07 07	47.34975	22.13897	56.01177	1.5	0.018885
001031	02 27	27.541	22.13779	56.01304	2.74	0.01304
001101	09 18	31.60808	22.13813	56.01122	2.44	0.013625
001104	22 01	9.921573	22.16766	56.04406	3	0.043206
001105	05 41	47.86013	22.16614	56.04424	3	0.041251
001107	03 03	23.33926	22.13694	56.0114	2.6	0.00727
001107	18 04	0.879392	22.14977	56.02755	1.02	0.026612
001107	23 09	6.586795	22.16732	56.04443	3.22	0.03882
001107	23 37	31.87048	22.16766	56.04533	3.22	0.052196
001110	02 19	18.62725	22.15332	56.0174	0.98	0.020486
001110	02 51	47.30376	22.15569	56.0174	1.32	0.025366
001110	17 58	58.04081	22.16715	56.04388	3	0.038702
001111	06 57	22.70613	22.16884	56.04606	3.46	0.061481
001111	07 29	22.10206	22.16817	56.04515	3	0.046008
001111	07 29	30.80771	22.16867	56.0457	3	0.03832
001113	21 44	22.05042	22.13897	56.01775	2.56	0.018875
001114	06 49	18.02356	22.16547	56.03463	1.24	0.022876
001120	22 47	18.76052	22.13593	56.0105	2.56	0.017804
001121	06 01	22.7929	22.13644	56.0105	3.32	0.014633
001121	15 08	17.26114	22.13897	56.01177	2.58	0.011597
001123	06 01	27.0233	22.13643	56.01793	3.12	0.020477
001126	01 04	56.74754	22.15702	56.03952	3	0.033336
001126	02 55	59.44529	22.13492	56.0114	0.98	0.006091
001126	09 52	26.47225	22.15804	56.03481	2.84	0.027339
001126	16 18	54.13174	22.15669	56.03481	2.76	0.011766
001127	12 15	58.80518	22.14809	56.01341	1.26	0.029817
001128	18 33	25.16448	22.13543	55.99998	1.74	0.005824
001130	17 53	26.55686	22.14724	56.02646	0.72	0.008432
001203	20 12	22.33921	22.16142	56.03789	3.36	0.030247
001204	02 13	59.75046	22.16379	56.03137	1.24	0.00996
001210	00 41	28.42402	22.1491	56.01667	1.3	0.008471
001212	02 17	24.70372	22.128	55.99472	2.74	0.023272
001213	11 15	14.26593	22.13593	56.01213	0.48	0.02862
001216	01 14	57.90297	22.14556	56.01395	1.32	0.024112
001218	15 12	1.337868	22.1442	56.01395	1.02	0.01895
001218	15 13	21.17881	22.14876	56.01576	1.34	0.037914
001222	21 51	14.02447	22.13897	56.01195	1.32	0.008219

YR/MM/DD	HR/MIN	SEC	LAT	LONG	DEPTH	RMS
001222	21 59	10.29391	22.1361	56.01503	1.6	0.026798
010104	22 26	14.27752	22.17982	56.05006	1.62	0.007177
010105	07 10	25.97379	22.18252	56.05406	2.64	0.030684
010106	06 29	11.01008	22.17998	56.05224	2.08	0.028434
010106	21 59	58.00336	22.13965	56.01032	3.16	0.031418
010109	07 48	32.50187	22.13998	56.01159	2.76	0.023756
010109	12 08	2.070641	22.13931	56.01376	1.5	0.012321
010110	13 34	23.60239	22.1415	56.01485	3	0.037821
010112	09 16	39.23129	22.14218	56.01521	2.88	0.030378
010112	21 42	22.89382	22.14353	56.01757	2.76	0.024206
010114	17 20	57.42891	22.14336	56.01775	2.92	0.03263
010114	17 22	6.762298	22.14336	56.01648	3.04	0.020029
010116	23 39	39.00653	22.13222	55.99835	1.5	0.010814
010116	23 42	26.39853	22.13475	55.99781	2.24	0.007265
010118	15 11	3.345153	22.13138	55.99654	2.34	0.025159
010119	05 43	3.934818	22.1415	56.01576	2.88	0.037986
010119	05 43	12.07782	22.13914	56.01449	2.78	0.006341
010122	20 40	49.13357	22.13779	56.01249	2.9	0.009695
000122	20 41	49.12962	22.13779	56.01249	2.8	0.013583
010123	19 06	56.5504	22.14555	56.0154	1.22	0.003864
010202	03 13	35.41558	22.13677	56.01793	0.5	0.001321
010204	00 39	10.94175	22.1334	55.9998	2.8	0.012119
010204	01 06	55.70443	22.13594	55.99473	1.5	0.03298
010204	01 15	57.76302	22.1334	55.99962	1.5	0.027782
010204	07 28	21.15526	22.13374	56.00035	1.5	0.040695
010204	12 42	27.71806	22.14961	56.01866	1.26	0.009969
010204	12 43	28.32531	22.15028	56.01921	1.26	0.011266
010204	12 43	44.87286	22.15011	56.01921	1.3	0.00437
010204	17 57	33.08886	22.13509	56.00941	2.74	0.004644
010204	18 09	23.5168	22.13542	56.00814	2.76	0.014895
010205	22 30	47.60496	22.14015	56.01177	3.02	0.026393
010206	10 52	56.00944	22.14015	56.01467	3.02	0.042615
010206	11 51	29.2269	22.14488	56.01902	2.92	0.032977
010206	11 54	16.20971	22.14505	56.01866	2.92	0.040422
010206	17 10	39.40723	22.14032	56.01177	1.34	0.017851
010207	02 40	32.68219	22.13407	56.0085	1.1	0.018167
010207	16 10	59.84717	22.14218	56.01376	3.04	0.029613
010208	18 56	48.12096	22.13745	56.01086	2.96	0.025177
010210	19 45	55.66422	22.13897	56.01884	2.92	0.005013
010211	23 42	18.83918	22.14488	56.01558	1.28	0.006777
010211	23 42	29.7096	22.14555	56.01449	1.2	0.01271
010212	06 11	9.886459	22.15079	56.01975	1.24	0.015598
010212	15 23	49.78039	22.14623	56.0134	1.4	0.01174
010219	16 28	33.45488	22.1545	56.02483	1.18	0.006216
010219	16 35	3.96825	22.15433	56.02447	1.2	0.018334
010219	20 39	35.76338	22.15602	56.0261	1.18	0.003771

YR/MM/DD	HR/MIN	SEC	LAT	LONG	DEPTH	RMS
010223	18 20	44.39063	22.14893	56.02265	0.7	0.055117
010223	18 41	57.48969	22.14488	56.01358	1.24	0.027904
010224	22 30	22.23373	22.1523	56.02411	1.24	0.027837
010224	23 42	1.221125	22.13964	56.01195	2.46	0.008958
010225	02 39	30.58114	22.14977	56.01921	1.14	0.020401
010227	00 56	14.02746	22.13323	55.99817	2.64	0.005046
010304	21 14	17.78294	22.15062	56.01939	1.28	0.010787
010304	22 54	50.85706	22.15079	56.02048	1	0.010544
010305	14 36	35.97167	22.12851	55.99182	2.74	0.044983
010306	09 09	59.33971	22.12733	55.98929	2.28	0.020314
010308	12 53	25.27634	22.15298	56.02102	1.38	0.026103
010311	12 51	51.36634	22.15113	56.01975	1.14	0.01661
010311	14 44	8.215184	22.14724	56.01377	1.26	0.030978
010311	22 07	56.92001	22.14876	56.01884	1.04	0.011436
010313	03 19	40.35291	22.13425	55.99944	2.86	0.034182
010313	18 02	48.29441	22.14724	56.01504	1.34	0.009361
010315	21 08	36.54322	22.15163	56.02356	1.32	0.021762
010316	09 54	16.51784	22.15315	56.02429	1	0.037369
010318	04 02	45.22819	22.15214	56.01975	0.84	0.022602
010318	07 11	33.92266	22.15315	56.01994	1.06	0.013812
010318	14 48	46.71607	22.1707	56.04407	3.34	0.027779
010318	21 24	8.43746	22.15214	56.02139	1.14	0.012994
010318	21 49	30.61621	22.15028	56.01993	1.28	0.007033
010319	18 07	54.80619	22.15146	56.01975	1.36	0.004298
010320	00 52	54.21628	22.13711	56.00995	2.76	0.016408
010320	01 28	35.06742	22.14961	56.01812	1.18	0.010935
010320	01 43	29.19658	22.13846	56.01068	2.92	0.018856
010320	01 57	48.21423	22.1388	56.01141	2.86	0.010453
010320	03 12	44.61554	22.14573	56.00869	2.92	0.024297
010320	04 46	46.14449	22.13728	56.00977	2.66	0.022123
010321	08 44	46.17378	22.13711	56.01014	2.9	0.0117
010321	14 20	12.31507	22.15197	56.01685	1.02	0.017938
010323	04 40	37.7319	22.13846	56.01195	2.86	0.009139
010323	09 57	37.22884	22.14944	56.01957	1.22	0.017026
010323	12 31	41.64908	22.15045	56.01903	1.36	0.021332
010323	14 41	5.837782	22.15062	56.01993	1.28	0.00914
010324	02 56	50.72842	22.14066	56.01286	2.78	0.021001
010324	03 47	13.7521	22.14826	56.01667	1.36	0.016259
010324	20 35	18.59094	22.1361	56.00832	2.92	0.008037
010325	15 30	13.686	22.13712	56.00452	1.5	0.005046
010325	19 34	58.85036	22.14555	56.01576	1.36	0.014823
010326	21 48	36.97222	22.14657	56.01485	1.36	0.014426
010328	11 05	16.81185	22.14724	56.01377	1.18	0.024543
010328	22 32	19.58867	22.14674	56.01522	1.32	0.002438
010329	08 44	24.53639	22.14893	56.01812	1.34	0.006223
010330	12 56	16.7222	22.16362	56.02774	1.5	0.006028

YR/MM/DD	HR/MIN	SEC	LAT	LONG	DEPTH	RMS
010330	15 22	48.05919	22.15365	56.02664	1.16	0.027682
010330	22 18	10.03186	22.1545	56.0232	1.04	0.02407
010331	00 49	42.75247	22.15737	56.02447	0.84	0.012413
010331	23 48	29.14155	22.15298	56.02356	0.78	0.004808
010401	00 16	29.44607	22.15315	56.02175	1.1	0.020681
010401	13 03	18.29526	22.14775	56.01794	1.28	0.007894
010401	14 41	5.72384	22.15535	56.02284	1.12	0.011086
010402	05 50	42.15711	22.16428	56.04424	2.98	0.02603
010402	05 51	18.17833	22.16563	56.04533	3	0.027243
010402	06 24	43.48665	22.15096	56.01957	1.3	0.005872
010402	09 49	40.58131	22.14927	56.01812	1.38	0.034475
010402	18 02	9.467324	22.13407	56.0105	1	0.005947
010402	21 54	30.31492	22.15889	56.02973	1.18	0.027767
010403	11 15	27.46921	22.14066	56.01521	3.08	0.032348
010404	01 33	35.2937	22.14623	56.01594	1.26	0.011031
010404	09 30	59.1302	22.15028	56.01957	1.28	0.009699
010406	17 59	29.33761	22.15349	56.02284	1.28	0.032644
010407	12 15	13.0357	22.15062	56.01522	0.86	0.005505
010407	22 50	28.1595	22.13728	56.00379	3	0.022731
010408	23 46	5.226345	22.15028	56.01595	1.04	0.01276
010409	03 58	58.30073	22.15028	56.01613	1.1	0.005282
010409	23 58	35.9473	22.14876	56.01449	1.02	0.011403
010410	11 21	34.93639	22.15332	56.01631	1.38	0.032782
010410	21 25	38.42615	22.15146	56.01975	1.14	0.01585
010410	23 48	1.345465	22.14994	56.01721	1.26	0.008671
010412	16 22	26.71397	22.1491	56.01885	1.2	0.006961
010412	19 43	41.56314	22.14994	56.01685	1.1	0.034561
010412	22 54	6.212153	22.15079	56.01903	1.3	0.010068
010414	22 01	25.13881	22.15501	56.0232	0.8	0.020171
010415	14 02	38.88322	22.16379	56.02955	2.3	0.015108
010416	08 07	10.38735	22.1518	56.02247	1.08	0.009835
010416	11 40	41.50092	22.154	56.02066	1.1	0.005434
010416	15 02	18.63126	22.16345	56.031	1.28	0.016558
010418	01 33	31.80492	22.14015	56.01956	2.74	0.019817
010419	08 30	1.896442	22.1442	56.0134	0.92	0.003472
010421	02 49	46.32649	22.13829	56.01195	2.98	0.004275
010421	02 49	52.79729	22.13762	56.01213	1.2	0.009498
010421	05 18	43.96058	22.17729	56.04806	3	0.021367
010421	05 39	42.94755	22.1751	56.0419	1.5	0.023599
010421	15 51	33.65601	22.1577	56.03589	2.5	0.009826
010422	09 46	4.145188	22.16108	56.03952	3	0.019072
010422	12 54	1.969671	22.14775	56.01631	1.16	0.006097
010426	15 17	2.89198	22.13829	56.01032	3	0.020516
010426	23 59	7.382355	22.16497	56.03481	1.2	0.01489
010427	10 26	58.66306	22.17918	55.99202	1.1	0.067601
010427	19 40	29.03808	22.13745	56.01739	2.92	0.004964

YR/MM/DD	HR/MIN	SEC	LAT	LONG	DEPTH	RMS
010428	06 37	30.13427	22.14015	56.01376	2.68	0.014723
010428	06 59	6.557863	22.13762	56.01195	2.48	0.005633
010429	03 45	16.66981	22.13626	56.01648	3.22	0.006529
010429	06 09	40.65517	22.13931	56.01086	1.98	0.012692
010501	19 19	0.577861	22.15011	56.0203	1.2	0.01819
010502	04 43	45.8187	22.14994	56.01758	1.06	0.006186
010504	22 30	13.91348	22.14961	56.01449	0.94	0.008801
010505	09 46	14.33351	22.14893	56.01522	1.06	0.021877
010505	18 23	50.32289	22.15079	56.0212	1.12	0.036559
010505	21 25	10.51822	22.15416	56.02393	1.24	0.026317
010506	05 37	4.114706	22.15331	56.04042	3.24	0.027203
010507	11 03	32.74341	22.13812	56.01322	2.9	0.006761
010508	16 43	40.37289	22.14167	56.0134	3.54	0.000948
010510	03 36	3.738045	22.13914	56.00361	2.82	0.028651
010512	19 48	43.0202	22.15045	56.01939	1.26	0.017344
010512	20 15	33.67698	22.13812	56.01177	2.98	0.009606
010514	10 47	1.695419	22.13442	55.99763	2.9	0.023574
010514	19 17	25.88542	22.14792	56.01649	1.14	0.002551
010515	14 18	39.05607	22.13087	55.99346	2.74	0.060124
010515	20 28	51.78206	22.12969	55.99273	2.72	0.04442
010515	22 29	32.43102	22.15096	56.01921	1.34	0.012769
010516	10 53	3.271905	22.15231	56.01921	1.04	0.008303
010517	01 13	3.581856	22.13778	56.01666	1.1	0.018554
010517	01 20	0.130466	22.13795	56.0163	1.16	0.020931
010518	22 58	29.72571	22.15332	56.02175	1.12	0.012912
010519	05 42	28.08313	22.15248	56.01794	1.08	0.019755
010519	07 14	42.61852	22.15231	56.01939	0.9	0.018601
010520	04 39	11.03721	22.14083	56.01558	2.66	0.008973
010521	01 11	22.56775	22.14707	56.01504	0.94	0.007771
010521	01 11	40.18587	22.14843	56.01504	1.08	0.011611
010521	18 48	44.54426	22.14809	56.0125	1.12	0.011073
010521	20 21	42.91891	22.15299	56.01595	1.1	0.012018
010521	23 53	59.44069	22.1545	56.02483	1.12	0.019918
010523	04 45	18.65949	22.15163	56.0183	1.02	0.010249
010523	12 50	33.94242	22.15011	56.01631	1.12	0.023223
010523	14 19	28.18987	22.15113	56.01685	1.06	0.011203
010523	21 24	45.42189	22.14893	56.01449	1	0.015328
010524	13 06	33.00579	22.14994	56.01667	1.24	0.010469
010525	04 23	17.04225	22.14556	56.01232	1.14	0.011841
010530	05 26	45.68465	22.13847	56.00542	2.88	0.013919
010531	19 15	57.58994	22.13812	56.01177	2.96	0.010434
010531	20 49	13.47338	22.14049	56.0105	2.14	0.005066
010603	04 24	20.80906	22.14977	56.027	0.76	0.011952
010603	13 56	9.288229	22.1307	55.99273	2.76	0.083063
010603	14 33	15.09881	22.14133	56.0183	2.78	0.004721
010605	18 54	49.67876	22.14251	56.01667	2.94	0.033707

YR/MM/DD	HR/MIN	SEC	LAT	LONG	DEPTH	RMS
010605	06 48	20.6953	22.14741	56.01576	1.1	0.006478
010606	16 30	55.07101	22.15079	56.01903	1.38	0.008265
010606	17 41	36.52165	22.14994	56.01993	1.26	0.008827
010606	18 35	55.77741	22.15079	56.02012	1.18	0.003931
010607	08 58	34.65731	22.14015	56.01231	2.84	0.013891
010608	01 36	46.90737	22.13745	56.0056	1.34	0.029836
010608	01 37	2.649273	22.1388	56.00524	1.3	0.004812
010608	13 20	18.94704	22.15602	56.02375	0.84	0.015951
010608	14 25	38.63222	22.15703	56.02356	0.86	0.012515
010609	18 07	21.33733	22.13677	56.01068	2.86	0.007424
010610	07 35	57.00794	22.1572	56.02429	0.88	0.009466
010610	12 46	51.45518	22.15467	56.02338	0.9	0.024121
010611	04 03	18.02428	22.14842	56.02737	0.78	0.003662
010611	05 16	49.79541	22.16681	56.04642	3	0.02667
010611	20 29	32.18196	22.1491	56.01721	1.26	0.016152
010612	10 42	49.14952	22.13964	56.01322	3.14	0.017107
010612	16 05	3.711993	22.13931	56.01358	2.86	0.009438
010612	16 06	26.39431	22.16244	56.03046	1.2	0.018636
010612	17 57	0.400716	22.15652	56.03426	1.1	0.008432
010612	17 57	25.58737	22.15652	56.03372	1.12	0.008189
010613	09 17	54.05694	22.13897	56.01195	1.24	0.023201
010613	16 56	58.27536	22.13762	56.01141	2.44	0.005123
010613	19 05	41.84364	22.13576	56.01177	2.74	0.016902
010613	22 51	10.18082	22.13694	56.0114	1.24	0.014644
010614	00 54	29.10122	22.13627	56.00778	2.56	0.023054
010614	00 54	34.38831	22.13745	56.01104	2.92	0.012801
010614	03 03	32.75322	22.15079	56.0183	1.2	0.010319
010614	05 27	3.230562	22.14994	56.02827	0.62	0.006749
010614	07 52	22.17272	22.1388	56.01122	2.88	0.010195
010614	19 49	4.109614	22.12851	55.99146	2.74	0.046629
010614	20 21	15.86733	22.14032	56.01231	2	0.00797
010614	20 29	9.293342	22.13948	56.01195	2.72	0.017087
010614	22 49	57.28901	22.13813	56.01141	2.78	0.003559
010615	06 34	23.59381	22.14437	56.02501	2.82	0.011377
010615	18 56	58.11771	22.14488	56.01304	1.24	0.025111
010615	18 57	1.022228	22.14606	56.01395	1.36	0.014093
010616	01 57	25.59203	22.17712	56.04353	2.62	0.018614
010616	13 49	58.03791	22.13913	56.02446	1.18	0.019518
010616	18 54	55.92813	22.14251	56.02392	3.64	0.012989
010616	22 15	56.13421	22.15332	56.01994	1.18	0.020092
010617	03 20	12.40771	22.15687	56.02411	1.14	0.018715
010617	07 20	59.31698	22.13931	56.01503	2.9	0.015829
010617	16 40	39.64683	22.13812	56.01159	2.74	0.016579
010618	01 08	11.49456	22.15129	56.01957	1.32	0.012841
010618	11 57	8.648526	22.14691	56.01467	1.14	0.012268

Appendix D

Double-Difference Microearthquake Locations

YR/MM/DD	HR/MIN	SEC	LAT	LONG	DEPTH	RMS
99 12 14	14 50	40.78	22.15316	56.02367	1.354	0.022
99 12 23	5 24	16.86	22.15451	56.03188	0.957	0.015
00 1 6	22 25	21.9	22.15496	56.03198	1.092	0.015
00 1 9	23 0	31.56	22.14992	56.02729	0.918	0.016
00 2 29	16 37	49.03	22.15175	56.02278	0.947	0.023
00 3 10	13 16	28.53	22.15252	56.0203	0.83	0.019
00 3 11	12 15	19.34	22.15222	56.02007	0.709	0.021
00 4 16	1 51	31.69	22.1464	56.01195	0.907	0.01
00 4 22	1 36	27.63	22.14846	56.01757	0.802	0.018
00 4 29	22 48	10.56	22.14915	56.01759	1.17	0.02
00 5 19	14 45	15.6	22.15056	56.01772	0.878	0.018
00 5 21	3 9	23.15	22.14812	56.01427	0.931	0.015
00 5 22	21 8	25.2	22.15066	56.01159	1.326	0.006
00 5 22	22 56	30.7	22.14649	56.0148	0.786	0.019
00 5 30	8 50	28.86	22.15167	56.02985	1.055	0.02
00 5 30	8 52	40.63	22.14871	56.0287	1.022	0.021
00 6 13	11 9	23.66	22.14915	56.01652	0.991	0.016
00 6 13	21 40	16.06	22.15009	56.01911	1.082	0.02
00 7 17	14 43	13.95	22.16397	56.03168	0.897	0.01
00 7 19	17 2	1.72	22.14591	56.01366	0.844	0.021
00 7 26	13 14	3.18	22.14946	56.01433	1.094	0.014
00 7 27	23 8	21.22	22.1528	56.02962	0.856	0.021
00 7 28	7 0	42.57	22.15018	56.02851	1.033	0.025
00 8 2	20 20	23.44	22.15271	56.03006	1.064	0.021
00 8 4	5 23	23.29	22.15322	56.02566	1.17	0.02
00 8 6	11 48	48.13	22.14797	56.01772	0.519	0.014
00 9 7	4 30	28.08	22.15319	56.03129	1.164	0.024
00 9 7	10 39	56.52	22.15345	56.03125	1.129	0.015
00 9 9	11 57	56.45	22.15561	56.03334	1.313	0.015
00 9 10	10 5	1.13	22.14902	56.02652	0.741	0.017
00 9 11	0 3	52.53	22.14948	56.02668	0.724	0.008
00 9 11	0 27	18.87	22.14753	56.02734	0.989	0.016
00 9 12	11 1	6.96	22.15006	56.02757	0.881	0.022
00 9 12	22 29	32.64	22.1504	56.02866	0.773	0.023
00 9 13	14 29	5.22	22.15187	56.03186	1.001	0.021
00 10 17	1 40	16.42	22.14489	56.0141	0.746	0.014
00 11 7	18 4	0.88	22.14958	56.02747	0.908	0.019
00 11 10	2 19	18.63	22.15287	56.01786	0.86	0.02
00 11 14	6 49	18.04	22.16618	56.03625	0.998	0.012

YR/MM/DD	HR/MIN	SEC	LAT	LONG	DEPTH	RMS
00 11 27	12 15	58.83	22.14568	56.01255	0.982	0.022
00 11 30	17 53	26.52	22.14828	56.02669	0.758	0.016
00 12 4	2 13	59.78	22.16518	56.03248	0.941	0.01
00 12 10	0 41	28.42	22.14848	56.01703	1.17	0.022
00 12 16	1 14	57.93	22.14331	56.01381	1.031	0.028
00 12 18	15 12	1.33	22.14402	56.01431	0.989	0.017
00 12 18	15 13	21.16	22.14878	56.01549	1.322	0.018
01 1 23	19 6	56.54	22.14453	56.01548	1.105	0.02
01 2 4	12 42	27.69	22.15284	56.01916	1.494	0.006
01 2 4	12 43	28.33	22.15	56.01977	1.163	0.02
01 2 4	12 43	44.86	22.14996	56.01981	1.232	0.022
01 2 11	23 42	18.84	22.1435	56.01557	1.125	0.019
01 2 11	23 42	29.72	22.1441	56.01456	1.02	0.026
01 2 12	6 11	9.88	22.15042	56.02051	1.13	0.021
01 2 12	15 23	49.8	22.14436	56.01328	1.206	0.021
01 2 19	16 28	33.47	22.15201	56.02488	0.913	0.016
01 2 19	16 35	3.97	22.15383	56.02537	1.056	0.021
01 2 19	20 39	35.76	22.15534	56.02667	1.13	0.022
01 2 23	18 20	44.3	22.15034	56.01982	1.213	0.014
01 2 23	18 41	57.52	22.14276	56.01338	0.976	0.022
01 2 24	22 30	22.24	22.15153	56.02467	1.135	0.022
01 2 25	2 39	30.6	22.14869	56.01971	0.934	0.02
01 3 4	21 14	17.78	22.14988	56.02004	1.148	0.023
01 3 4	22 54	50.88	22.15043	56.02123	0.852	0.025
01 3 8	12 53	25.26	22.15295	56.02116	1.364	0.023
01 3 11	12 51	51.37	22.15083	56.02045	1.041	0.018
01 3 11	14 44	8.24	22.14555	56.014	1.05	0.006
01 3 11	22 7	56.92	22.14803	56.01892	0.934	0.015
01 3 13	18 2	48.32	22.14564	56.01502	1.164	0.02
01 3 15	21 8	36.52	22.15045	56.02361	1.251	0.015
01 3 16	9 54	16.54	22.15219	56.02489	0.803	0.019
01 3 18	4 2	45.21	22.1519	56.02037	0.797	0.019
01 3 18	7 11	33.93	22.15279	56.02047	0.889	0.022
01 3 18	21 24	8.44	22.15179	56.02206	1.009	0.021
01 3 18	21 49	30.62	22.14975	56.02034	1.187	0.016
01 3 19	18 7	54.8	22.15099	56.02019	1.269	0.016
01 3 20	1 28	35.07	22.14885	56.01858	1.013	0.02
01 3 21	14 20	12.31	22.15119	56.01716	0.882	0.013
01 3 23	9 57	37.22	22.14887	56.01998	1.093	0.018
01 3 23	12 31	41.65	22.14938	56.01955	1.215	0.017
01 3 23	14 41	5.83	22.15006	56.02069	1.144	0.019
01 3 24	3 47	13.74	22.14733	56.01684	1.259	0.014
01 3 25	19 34	58.84	22.14416	56.01578	1.223	0.022
01 3 26	21 48	36.98	22.14577	56.01544	1.232	0.018
01 3 28	11 5	16.83	22.14544	56.0138	0.969	0.021
01 3 28	22 32	19.58	22.14555	56.01535	1.192	0.019

YR/MM/DD	HR/MIN	SEC	LAT	LONG	DEPTH	RMS
01 3 29	8 44	24.54	22.14804	56.01868	1.201	0.023
01 3 30	15 22	48.05	22.15289	56.02714	1.091	0.023
01 3 30	22 18	10.04	22.15395	56.02393	0.883	0.024
01 3 31	0 49	42.73	22.15697	56.02466	0.813	0.02
01 3 31	23 48	29.12	22.15311	56.02349	0.815	0.014
01 4 1	0 16	29.46	22.15237	56.02229	0.861	0.018
01 4 1	13 3	18.3	22.14709	56.01837	1.176	0.017
01 4 1	14 41	5.72	22.15514	56.02355	0.96	0.023
01 4 2	6 24	43.48	22.15018	56.02016	1.176	0.017
01 4 2	9 49	40.58	22.14703	56.01683	1.152	0.022
01 4 2	21 54	30.32	22.16008	56.03039	1.063	0.003
01 4 4	1 33	35.29	22.14518	56.0159	1.133	0.021
01 4 4	9 30	59.13	22.14974	56.02008	1.16	0.019
01 4 6	17 59	29.36	22.15255	56.02332	1.094	0.02
01 4 7	12 15	13.04	22.14952	56.01554	0.764	0.014
01 4 8	23 46	5.22	22.14949	56.01609	0.896	0.02
01 4 9	3 58	58.3	22.1495	56.01632	0.978	0.02
01 4 9	23 58	35.94	22.14786	56.0146	0.925	0.022
01 4 10	11 21	34.96	22.15056	56.01662	0.987	0.007
01 4 10	21 25	38.42	22.15109	56.02043	1.029	0.021
01 4 10	23 48	1.34	22.14924	56.01737	1.156	0.016
01 4 12	16 22	26.72	22.14808	56.01936	1.039	0.019
01 4 12	19 43	41.6	22.14916	56.01749	0.836	0.008
01 4 12	22 54	6.2	22.14968	56.01877	1.222	0.026
01 4 14	22 1	25.12	22.15438	56.02352	0.751	0.019
01 4 16	8 7	10.37	22.15114	56.02275	0.998	0.022
01 4 16	11 40	41.51	22.15386	56.0215	0.94	0.028
01 4 16	15 2	18.67	22.16472	56.03281	0.994	0.014
01 4 19	8 30	1.9	22.14369	56.01374	0.795	0.011
01 4 22	12 54	1.97	22.14676	56.01647	1.034	0.018
01 4 26	23 59	7.4	22.16542	56.03631	0.9	0.008
01 5 1	19 19	0.56	22.14969	56.02033	1.146	0.025
01 5 2	4 43	45.84	22.14926	56.01785	0.871	0.014
01 5 4	22 30	13.92	22.14902	56.01484	0.854	0.015
01 5 5	9 46	14.36	22.14741	56.01495	0.828	0.025
01 5 5	18 23	50.34	22.14897	56.02079	1.028	0.025
01 5 5	21 25	10.52	22.15346	56.0247	1.124	0.02
01 5 12	19 48	43.02	22.1498	56.0201	1.127	0.026
01 5 14	19 17	25.88	22.14715	56.01673	1.049	0.018
01 5 15	22 29	32.44	22.15002	56.02024	1.162	0.016
01 5 16	10 53	3.28	22.15179	56.01969	0.885	0.018
01 5 18	22 58	29.72	22.15299	56.02233	0.973	0.017
01 5 19	5 42	28.08	22.15199	56.01843	0.945	0.013
01 5 19	7 14	42.62	22.15172	56.01973	0.822	0.02
01 5 21	1 11	22.57	22.14624	56.01531	0.827	0.022
01 5 21	1 11	40.19	22.14714	56.01514	0.916	0.024

YR/MM/DD	HR/MIN	SEC	LAT	LONG	DEPTH	RMS
01 5 21	18 48	44.56	22.14676	56.01248	0.947	0.014
01 5 21	20 21	42.92	22.15317	56.01669	0.989	0.019
01 5 21	23 53	59.44	22.1536	56.0253	1.012	0.017
01 5 23	4 45	18.66	22.15129	56.0189	0.902	0.021
01 5 23	12 50	33.95	22.14928	56.01673	0.933	0.024
01 5 23	14 19	28.19	22.15048	56.01706	0.931	0.018
01 5 23	21 24	45.44	22.1482	56.01475	0.877	0.027
01 5 24	13 6	33.01	22.14927	56.01702	1.115	0.018
01 5 25	4 23	17.05	22.14438	56.01247	1	0.017
01 6 3	4 24	20.78	22.14973	56.0269	0.745	0.015
01 6 6	6 48	20.69	22.14637	56.01618	0.968	0.018
01 6 6	16 30	55.07	22.14988	56.01945	1.234	0.019
01 6 6	17 41	36.52	22.14957	56.02002	1.222	0.022
01 6 6	18 35	55.76	22.15034	56.0203	1.109	0.023
01 6 8	13 20	18.93	22.15587	56.02411	0.815	0.02
01 6 8	14 25	38.62	22.15687	56.02412	0.807	0.02
01 6 10	7 35	57.01	22.15667	56.02471	0.823	0.017
01 6 10	12 46	51.44	22.15425	56.02359	0.897	0.023
01 6 11	4 3	17.98	22.14879	56.02729	0.848	0.02
01 6 11	20 29	32.18	22.14834	56.01733	1.149	0.021
01 6 12	16 6	26.45	22.1637	56.03162	0.789	0.005
01 6 12	17 57	0.38	22.15676	56.03471	1.135	0.004
01 6 12	17 57	25.56	22.15722	56.03447	1.112	0.009
01 6 14	3 3	32.75	22.15024	56.01878	1.072	0.022
01 6 14	5 27	3.19	22.15014	56.02815	0.675	0.015
01 6 15	18 56	58.12	22.1435	56.01337	1.079	0.016
01 6 15	18 57	1.04	22.14445	56.0139	1.188	0.02
01 6 16	22 15	56.16	22.1526	56.02064	1.035	0.019
01 6 17	3 20	12.4	22.15664	56.02494	1.026	0.014
01 6 18	1 8	11.48	22.15088	56.02012	1.217	0.016
01 6 18	11 57	8.66	22.14552	56.01484	0.976	0.022
99 10 29	1 2	56.12	22.13674	56.0108	2.132	0.018
99 11 15	2 12	47.34	22.1353	56.00928	2.763	0.025
99 11 15	15 41	22.36	22.1347	56.01132	2.075	0.013
99 11 15	16 57	52.36	22.1372	56.01167	1.936	0.02
99 11 21	9 22	31.28	22.13493	56.0094	2.841	0.023
99 11 21	19 23	29.02	22.13923	56.02045	2.594	0.014
99 11 25	18 36	32.64	22.14277	56.01805	2.609	0.02
99 11 25	18 38	52.36	22.14283	56.01715	2.732	0.009
99 12 17	18 26	14.22	22.13542	56.00726	2.872	0.019
99 12 22	20 45	46.76	22.13374	56.00774	0.781	0.015
99 12 23	15 1	14.38	22.13585	56.0155	1.015	0.006
00 1 1	4 54	5.84	22.13765	56.0175	2.347	0.008
00 1 8	14 32	35.94	22.13585	56.00862	2.737	0.021
00 3 20	8 5	40.07	22.13492	56.01239	1.004	0.02
00 3 20	10 13	39.72	22.13222	56.00623	2.915	0.016

YR/MM/DD	HR/MIN	SEC	LAT	LONG	DEPTH	RMS
00 3 20	10 15	40.06	22.13406	56.01017	2.77	0.021
00 3 20	10 16	20.08	22.13738	56.01032	2.681	0.026
00 4 14	0 29	29.3	22.13892	56.01216	2.176	0.019
00 4 22	11 55	59.37	22.13607	56.01011	2.821	0.02
00 4 24	3 45	44.68	22.13676	56.01148	2.93	0.023
00 4 24	4 32	7.85	22.1371	56.01158	2.993	0.023
00 4 24	5 1	39.86	22.13615	56.01022	2.968	0.023
00 5 1	16 1	9.6	22.13638	56.01048	2.856	0.022
00 5 3	0 43	3.64	22.13507	56.0084	3.438	0.01
00 5 3	4 35	33.49	22.13354	56.00834	2.965	0.02
00 5 5	17 40	2.08	22.13637	56.01265	0.99	0.023
00 5 15	0 46	19.96	22.12936	56.00527	2.972	0.007
00 5 16	6 31	6.57	22.14024	56.01173	1.6	0.01
00 5 16	15 7	25.29	22.13604	56.01388	0.827	0.009
00 5 18	5 57	52.9	22.1362	56.01149	2.694	0.021
00 5 22	23 34	27.84	22.13538	56.01259	0.625	0.015
00 5 29	0 41	10.65	22.13847	56.01193	3.179	0.017
00 6 3	20 9	1.98	22.13255	56.00567	3.323	0.011
00 6 6	14 21	3.17	22.13955	56.0125	2.491	0.019
00 6 7	3 14	0.71	22.13839	56.01293	2.09	0.026
00 6 17	11 55	54.39	22.13693	56.00999	2.683	0.011
00 6 18	9 34	48.21	22.1389	56.00937	2.747	0.018
00 6 26	9 46	34.13	22.13829	56.01346	2.858	0.022
00 7 14	5 54	14.61	22.13562	56.01046	2.774	0.03
00 7 23	13 36	35.78	22.13754	56.01168	2.876	0.013
00 8 9	4 59	29.18	22.13659	56.01155	2.886	0.022
00 8 9	7 12	53.62	22.13952	56.01143	2.733	0.023
00 8 15	14 48	52.71	22.13184	56.0095	2.963	0.009
00 9 5	7 31	22.82	22.13822	56.01376	2.755	0.018
00 9 15	23 22	3.92	22.1473	56.01359	4.319	0.004
00 9 17	8 26	32.6	22.13672	56.01056	2.117	0.018
00 10 1	4 47	58.15	22.13798	56.01267	0.87	0.017
00 10 9	6 58	56.1	22.13772	56.01312	2.849	0.019
00 10 12	22 57	19.64	22.1395	56.0119	1.236	0.015
00 10 12	23 13	46.52	22.14032	56.01469	2.225	0.016
00 10 13	21 51	38.26	22.13637	56.01235	0.898	0.016
00 10 13	21 53	15.14	22.13533	56.01126	1.068	0.023
00 10 13	23 39	31.88	22.13706	56.01005	2.961	0.016
00 10 17	8 5	36.38	22.1401	56.00817	2.806	0.019
00 10 18	7 26	13.6	22.13437	56.00317	2.825	0.007
00 10 20	19 42	34.6	22.13718	56.01194	2.402	0.015
00 10 23	6 40	41.83	22.13888	56.01296	2.341	0.021
00 10 24	7 49	32.73	22.14004	56.01309	2.365	0.016
00 10 24	8 34	58.61	22.13558	56.01151	1.413	0.001
00 10 28	22 32	17.8	22.13775	56.01146	2.033	0.026
00 10 31	2 27	27.55	22.13575	56.01276	2.898	0.02

YR/MM/DD	HR/MIN	SEC	LAT	LONG	DEPTH	RMS
00 11 1	9 18	31.61	22.13755	56.01122	2.333	0.021
00 11 7	3 3	23.34	22.13635	56.01142	2.61	0.023
00 11 13	21 44	22.08	22.13697	56.01817	2.786	0.012
00 11 20	22 47	18.74	22.13527	56.01067	2.143	0.007
00 11 21	6 1	22.78	22.1358	56.01084	2.934	0.01
00 11 21	15 8	17.26	22.13841	56.01194	2.502	0.023
00 11 23	6 1	27.02	22.13653	56.01808	2.843	0.012
00 11 26	2 55	59.42	22.13473	56.01145	0.949	0.017
00 12 13	11 15	14.23	22.13628	56.01219	0.579	0.007
00 12 22	21 51	14	22.13907	56.01147	1.306	0.013
00 12 22	21 59	10.38	22.13584	56.01407	0.95	0
01 1 6	21 59	58	22.14002	56.01017	2.908	0.018
01 1 9	7 48	32.5	22.13825	56.01115	2.83	0.031
01 1 10	13 34	23.58	22.14174	56.01528	2.55	0.016
01 1 12	9 16	39.22	22.14224	56.0151	2.622	0.021
01 1 12	21 42	22.88	22.14248	56.0175	2.527	0.013
01 1 14	17 20	57.4	22.14375	56.01785	2.7	0.011
01 1 14	17 22	6.76	22.14369	56.01693	2.84	0.014
01 1 19	5 43	3.96	22.14301	56.01399	2.992	0.009
01 1 19	5 43	12.08	22.13889	56.01495	2.745	0.021
01 1 22	20 40	49.14	22.13686	56.01217	2.9	0.015
01 1 22	20 41	49.12	22.13706	56.01295	2.378	0.011
01 2 2	3 13	35.36	22.137	56.0178	0.603	0.001
01 2 4	18 9	23.56	22.13361	56.00758	3.201	0.013
01 2 5	22 30	47.6	22.14082	56.01198	2.845	0.026
01 2 6	10 52	55.96	22.142	56.01456	2.484	0.016
01 2 6	11 51	29.2	22.14585	56.01883	2.685	0.008
01 2 6	11 54	16.17	22.14525	56.01918	2.533	0.009
01 2 6	17 10	39.44	22.13879	56.013	0.985	0.012
01 2 7	2 40	32.66	22.13232	56.00803	1.183	0.015
01 2 7	16 10	59.85	22.14289	56.0136	2.944	0.01
01 2 10	19 45	55.68	22.13742	56.01927	2.977	0.012
01 2 24	23 42	1.22	22.13855	56.01169	2.448	0.024
01 3 20	0 52	54.21	22.13579	56.00949	2.736	0.027
01 3 20	1 43	29.19	22.13868	56.01076	2.763	0.025
01 3 20	1 57	48.2	22.13874	56.01167	2.678	0.025
01 3 20	4 46	46.15	22.13565	56.00918	2.75	0.025
01 3 21	8 44	46.17	22.13714	56.00965	2.816	0.016
01 3 23	4 40	37.74	22.13831	56.01271	2.904	0.024
01 3 24	2 56	50.7	22.1395	56.01305	2.545	0.021
01 3 24	20 35	18.64	22.1355	56.00749	3.297	0.015
01 4 2	18 2	9.44	22.13406	56.01022	1.008	0.016
01 4 3	11 15	27.46	22.1416	56.0152	2.736	0.019
01 4 7	22 50	28.16	22.13736	56.00287	2.881	0.008
01 4 18	1 33	31.81	22.1384	56.02008	2.839	0.01
01 4 21	2 49	46.33	22.1375	56.01208	3.074	0.022

YR/MM/DD	HR/MIN	SEC	LAT	LONG	DEPTH	RMS
01 4 21	2 49	52.78	22.13681	56.01207	1.163	0.014
01 4 26	15 17	2.89	22.13832	56.01007	2.859	0.023
01 4 27	19 40	29.04	22.13649	56.01757	2.86	0.018
01 4 28	6 37	30.15	22.13969	56.01442	2.781	0.018
01 4 28	6 59	6.56	22.13675	56.01206	2.392	0.023
01 4 29	3 45	16.68	22.13546	56.01662	3.198	0.006
01 4 29	6 9	40.65	22.13809	56.01087	1.691	0.017
01 5 7	11 3	32.75	22.13771	56.01326	2.893	0.017
01 5 8	16 43	40.45	22.14484	56.01431	4.078	0.004
01 5 12	20 15	33.68	22.13747	56.01194	2.911	0.021
01 5 17	1 13	3.61	22.13586	56.0159	0.867	0.014
01 5 17	1 20	0.15	22.13594	56.01581	0.987	0.017
01 5 30	5 26	45.66	22.13869	56.00439	2.494	0.008
01 5 31	19 15	57.6	22.13801	56.01197	2.928	0.018
01 5 31	20 49	13.48	22.14039	56.01044	2.099	0.016
01 6 5	14 33	15.1	22.13992	56.01832	2.665	0.013
01 6 5	18 54	49.68	22.14302	56.01682	2.76	0.015
01 6 7	8 58	34.65	22.13933	56.01242	2.66	0.022
01 6 9	18 7	21.34	22.1361	56.01073	2.836	0.02
01 6 12	10 42	49.15	22.13988	56.01366	2.963	0.023
01 6 12	16 5	3.7	22.13887	56.01379	2.636	0.018
01 6 13	9 17	54.09	22.13699	56.01176	0.89	0.021
01 6 13	16 56	58.29	22.13669	56.01152	2.409	0.02
01 6 13	19 5	41.84	22.13464	56.01129	2.799	0.019
01 6 13	22 51	10.2	22.13536	56.01067	0.996	0.019
01 6 14	0 54	34.38	22.13645	56.01099	2.927	0.021
01 6 14	7 52	22.18	22.13757	56.01114	2.95	0.023
01 6 14	20 21	15.86	22.13968	56.01246	1.874	0.024
01 6 14	20 29	9.3	22.13829	56.01187	2.545	0.028
01 6 14	22 49	57.28	22.13695	56.01166	2.831	0.023
01 6 17	7 20	59.27	22.13805	56.01534	2.295	0.012
01 6 17	16 40	39.66	22.13671	56.01123	2.789	0.033
00 4 16	9 37	1.61	22.16366	56.0404	2.899	0.027
00 11 4	22 1	9.92	22.168	56.04454	3.147	0.07
00 11 5	5 41	47.86	22.16627	56.04451	2.961	0.086
00 11 7	23 9	6.56	22.16686	56.04419	2.966	0.067
00 11 7	23 37	31.88	22.16774	56.04553	3.064	0.072
00 11 10	17 58	58.04	22.16707	56.04381	2.902	0.089
00 11 11	6 57	22.69	22.16914	56.04661	3.261	0.041
00 11 11	7 29	22.1	22.1685	56.04495	2.933	0.062
00 11 11	7 29	30.82	22.16826	56.0453	2.996	0.063
00 12 3	20 12	22.34	22.16094	56.03703	3.258	0.027
01 3 18	14 48	46.75	22.17039	56.04399	3.515	0.026
01 4 2	5 50	42.15	22.16443	56.04399	2.868	0.078
01 4 2	5 51	18.18	22.16578	56.04516	2.854	0.075
01 4 22	9 46	4.15	22.16117	56.03924	3.139	0.035

YR/MM/DD	HR/MIN	SEC	LAT	LONG	DEPTH	RMS
01 6 11	5 16	49.79	22.16669	56.04608	2.88	0.07
00 3 12	16 34	43.89	22.13438	56.00153	2.688	0.025
00 5 13	7 57	41.14	22.13229	55.99802	3.017	0.005
00 6 20	19 32	42.54	22.13439	55.99896	2.454	0.043
00 12 12	2 17	24.72	22.12908	55.99521	3.009	0.03
01 1 16	23 42	26.4	22.13483	55.99832	2.47	0.043
01 1 18	15 11	3.34	22.13126	55.99704	2.417	0.036
01 2 4	0 39	10.96	22.13113	55.99857	2.325	0.007
01 2 27	0 56	14.03	22.13321	55.99841	2.779	0.041
01 3 5	14 36	35.97	22.12831	55.9913	2.756	0.028
01 3 13	3 19	40.33	22.13446	55.99885	2.733	0.033
01 5 14	10 47	1.7	22.13459	55.99825	2.936	0.031
01 5 15	14 18	39.05	22.13097	55.99344	2.647	0.029
01 5 15	20 28	51.76	22.12924	55.99337	2.567	0.032
01 6 3	13 56	9.3	22.13032	55.9918	2.787	0.038
01 6 14	19 49	4.12	22.12791	55.99086	2.837	0.027
00 7 2	15 2	13.55	22.13639	56.00279	2.133	0.015
00 7 26	8 22	36.6	22.13383	56.00048	1.361	0.008
00 10 9	17 40	9.08	22.13754	56.00283	1.178	0.032
00 11 28	18 33	25.16	22.13444	55.99987	1.947	0.015
01 2 4	7 28	21.14	22.13333	56.0002	1.425	0.008
01 6 8	1 36	46.89	22.13719	56.0052	1.264	0.031
01 6 8	1 37	2.63	22.13856	56.00535	1.309	0.025
99 12 11	2 48	15.11	22.15956	56.03583	2.703	0.057
00 7 5	2 16	46.5	22.15545	56.03174	2.793	0.052
00 11 26	9 52	26.47	22.15739	56.03497	2.766	0.075
00 11 26	16 18	54.14	22.15694	56.03488	2.862	0.051
01 4 21	15 51	33.66	22.15787	56.03561	2.562	0.069
00 7 25	4 5	29.3	22.15311	55.98556	3.133	0.06
00 7 28	9 17	42.11	22.1532	55.98757	2.966	0.079
00 7 28	9 23	16.98	22.15274	55.98773	3.055	0.075
00 10 1	20 41	43.6	22.1532	55.9859	2.848	0.054
00 10 17	20 41	44.88	22.15296	55.98707	2.98	0.072
00 3 7	9 58	19.04	22.17987	56.05174	2.872	0.061
01 1 5	7 10	25.97	22.18236	56.05381	2.655	0.061
00 7 31	21 43	25.9	22.17971	56.05014	1.916	0.027
01 1 4	22 26	14.28	22.17991	56.0503	1.609	0.011
01 1 6	6 29	11.01	22.18007	56.05215	2.096	0.025
00 8 23	18 9	20.6	22.15487	55.98398	1.779	0.034
00 10 3	20 28	21.56	22.15713	55.98623	1.488	0.034
99 11 7	23 33	25.42	22.13846	56.02293	0.772	0.078
00 3 2	5 28	47.53	22.13909	56.02198	1.185	0.087
01 6 16	13 49	58.04	22.13895	56.02441	1.173	0.087
00 10 28	23 45	21.68	22.14142	56.02426	3.312	0.074
01 6 16	18 54	55.92	22.14226	56.02395	3.649	0.074
00 9 5	21 2	9.92	22.16408	56.03142	2.22	0.017

YR/MM/DD	HR/MIN	SEC	LAT	LONG	DEPTH	RMS
01 4 15	14 2	38.88	22.16383	56.02958	2.3	0.017